

2-9-2011

Aerosol Synthesis and Electrochemical Analysis of Niobium Mixed-Metal Oxides for the Ethanol Oxidation Reaction in Acid and Alkaline Electrolyte

Daniel Konopka

Follow this and additional works at: https://digitalrepository.unm.edu/cbe_etds

Recommended Citation

Konopka, Daniel. "Aerosol Synthesis and Electrochemical Analysis of Niobium Mixed-Metal Oxides for the Ethanol Oxidation Reaction in Acid and Alkaline Electrolyte." (2011). https://digitalrepository.unm.edu/cbe_etds/5

This Dissertation is brought to you for free and open access by the Engineering ETDs at UNM Digital Repository. It has been accepted for inclusion in Chemical and Biological Engineering ETDs by an authorized administrator of UNM Digital Repository. For more information, please contact disc@unm.edu.

Daniel A. Konopka

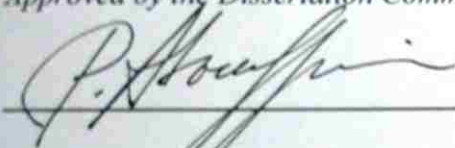
Candidate

Chemical and Nuclear Engineering

Department

This dissertation is approved, and it is acceptable in quality and form for publication:

Approved by the Dissertation Committee:

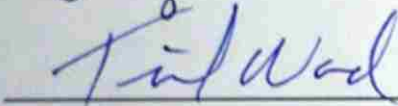


Plamen Atanasov, Ph.D.

, Chairperson



Abhaya Datye, Ph.D.



Timothy Ward, Ph.D.



Claudia Luhrs, Ph.D.



Boris Kiefer, Ph.D.

**AEROSOL SYNTHESIS AND ELECTROCHEMICAL
ANALYSIS OF NIOBIUM MIXED-METAL OXIDES FOR THE
ETHANOL OXIDATION REACTION IN ACID AND
ALKALINE ELECTROLYTE**

BY

DANIEL A. KONOPKA

B.S., Chemical Engineering, 2006
M.S., Nanoscience and Microsystems, 2009

DISSERTATION

Submitted in Partial Fulfillment of the
Requirements for the Degree of

**Doctor of Philosophy
Engineering**

The University of New Mexico
Albuquerque, New Mexico

September 2010

© 2010, Daniel A. Konopka

**AEROSOL SYNTHESIS AND ELECTROCHEMICAL
ANALYSIS OF NIOBIUM MIXED-METAL OXIDES FOR THE
ETHANOL OXIDATION REACTION IN ACID AND
ALKALINE ELECTROLYTE**

BY

DANIEL A. KONOPKA

ABSTRACT OF DISSERTATION

Submitted in Partial Fulfillment of the
Requirements for the Degree of

**Doctor of Philosophy
Engineering**

The University of New Mexico
Albuquerque, New Mexico

September 2010

Aerosol Synthesis and Electrochemical Analysis of Niobium Mixed-Metal Oxides for the Ethanol Oxidation Reaction in Acid and Alkaline Electrolyte

By

Daniel A. Konopka

B.S., Chemical Engineering, University of Colorado at Boulder, 2006
M.S., Nanoscience and Microsystems, University of New Mexico, 2009
Ph.D., Engineering, University of New Mexico, 2010

Abstract

Direct ethanol fuel cells are especially important among emerging electrochemical power systems with the potential to offset a great deal of the energy demand currently met through the use of fossil fuels. Ethanol can be refined from petroleum sources or attained from renewable biomass, and is more easily and safely stored and transported than hydrogen, methanol or gasoline. The full energy potential of ethanol in fuel cells can only be realized if the reaction follows a total oxidation pathway to produce CO_2 . This must be achieved by the development of advanced catalysts that are electrically conductive, stable in corrosive environments, contain a high surface area on which the reaction can occur, and exhibit a bi-functional effect for the ethanol oxidation reaction (EOR). The latter criterion is achievable in mixed-metal systems.

Platinum is an effective metal for catalyzing surface reactions of many adsorbates and is usually implemented in the form of Pt nanoparticles supported on inexpensive carbon.

This carbon is believed to be neutral in the catalysis of Pt. Instead, carbon can be replaced with carefully designed metals and metal oxides as co-catalysis or support structures that favorably alter the electronic structure of Pt slightly through a strong metal support interaction, while also acting as an oxygen source near adsorbates to facilitate the total oxidation pathway.

Niobium mixed-metal-oxides were explored in this study as bi-functional catalyst supports to Pt nanoparticles. We developed a thermal aerosol synthesis process by which mesoporous powders of mixed-metal-oxides decorated with Pt nanoparticles could be obtained from liquid precursors within ~5 seconds or less, followed by carefully refined chemical and thermal post-treatments. Exceptionally high surface areas of 170-180m²/g were achieved via a surfactant-templated 3D wormhole-type porosity, comparable on a per volume basis to commercial carbon blacks and high surface area silica supports.

For the first time, in situ FTIR measurements in acid electrolyte showed that highly dispersed Pt nanoparticles (2-5nm) on NbRu_yO_z (at% 8Nb:1Ru) catalyze the formation of CO₂ from ethanol in greater yield, and 0.35-0.4V lower, than Pt(111). Compared to conventional Pt/carbon, this indicates that, (1) Pt supported on NbRu_yO_z can be more effective at splitting the C—C bond in ethanol and, (2) the scission occurs at potentials more ideal for a higher efficiency fuel cell anode.

Ex situ-microscopy revealed the polarization-induced two- and three-dimensional formation of Pt-NbO_x interfacial adsorption sites responsible for the facilitation of the total oxidation pathway of ethanol. The results show that synthesis and post-treatment of niobia supports can bias the utility of Pt/niobia systems towards the ethanol oxidation

reaction at the anode or the oxygen reduction reaction at the cathode. Experimental and computational-theoretical analyses indicate that the mechanism of interfacial site formation is dependent upon the local oxygen concentration, as well as the availability of multiple, energetically accessible oxidation states like those inherent to niobia. Future directions for the development of highly active, niobium-based materials tailored for efficient catalysis of the total oxidation pathway of ethanol are discussed.

Table of Contents

Abstract	v
Table of Contents	viii
List of Figures	xv
List of Tables	xxv
List of Appendices	xxvi
CHAPTER 1 - Introduction	1
1.1 Fuel Cell Concept.....	3
1.2 Fuel Cell Design.....	5
1.3 Properties of Potential Fuels	7
1.3.1 Hydrogen (H ₂).....	8
1.3.2 Methanol (CH ₃ OH).....	9
1.3.3 Ethanol	11
1.4 Economic Factors	12
1.4.1 Catalysts and Support Materials	12
1.4.2 Ethanol from Biomass.....	14
1.5 Spray Pyrolysis Aerosol Synthesis.....	16
CHAPTER 2 - Electrocatalysts: Stability and Performance.....	22
2.1 Aqueous Electrocatalysis	22
2.2 Ethanol Oxidation in Alkaline Fuel Cells	29

2.3	Catalyst and Support Durability	30
2.4	Theory of Pt and Pt-Alloys.....	32
2.5	Niobia for Alcohol Oxidation or Oxygen Reduction	35
CHAPTER 3 - Problem Statement		38
CHAPTER 4 - Experimental Methodology		41
4.1	Spray Pyrolysis Reactor System	41
4.2	Conductance Testing	47
4.3	Structural and Compositional Analysis.....	50
4.3.1	Electron Microscopy (EM)	50
4.3.2	Elemental Analysis (EDS & EELS)	51
4.3.3	X-ray Diffraction Spectroscopy (XRD).....	52
4.3.4	X-ray Photoelectron Spectroscopy (XPS)	52
4.3.5	X-ray Absorption Spectroscopy (XAS).....	54
4.3.6	Gas Adsorption-Desorption Analysis	56
4.3.7	Thermogravimetric Analysis (TGA).....	57
4.4	Computational Method: Density Functional Theory	57
4.5	Electrochemistry Studies.....	59
4.5.1	The Half Cell.....	59
4.5.2	Cyclic Voltammetry	61
4.5.3	CO Stripping	62

4.5.4	In situ Infrared Reflection Absorption Spectroscopy (IRRAS)	63
4.5.5	Rapid Electrode Aging.....	65
CHAPTER 5 - Synthesis of Mixed Metal Oxides		68
5.1	Multiphysics Simulations of Reactor Conditions.....	68
5.2	Synthesis of Niobium Intermetallic Compounds at Low Temperature.....	74
5.2.1	Titanium.....	74
5.2.2	Nickel, Iron, and Tin	76
5.2.3	Platinum, Ruthenium and Carbon.....	80
5.2.4	Tin and Ruthenium	84
CHAPTER 6 - Mesoporous Niobia Supports		89
6.1	Changing Properties with Variations in Synthesis	91
6.1.1	Single-Metal Niobium Oxide.....	92
6.1.2	Ru-Modified Niobium Oxide.....	94
6.1.3	Effect of Acid-Wash Post-Treatment.....	95
6.1.4	Optimized NbRu _y O _z Support	96
6.1.5	Porous Structure of Supports	97
6.1.6	Crystalline Structure of Supports.....	98
6.1.7	Surface Analysis	100
6.1.8	Thermal Behavior of Support Materials	104
6.1.9	Electrochemical Characterization	107

6.2	Discussion	108
CHAPTER 7 - Platinum Catalyst on NbRu _y O _z		113
7.1	Synthesis of Electrocatalysts	113
7.2	Verification of Pt with Electron Microscopy	116
7.2.1	30% Pt/NbRu _y O _z (Pt-DI)	116
7.2.2	60% Pt/NbRu _y O _z (Pt-SP)	118
7.3	X-ray Studies	120
7.3.1	X-ray Diffraction of the Pt Structure	120
7.3.2	X-ray Photoelectron Spectroscopy	123
7.3.3	X-ray Absorption Spectroscopy	125
7.4	Electrochemical Surface Studies	129
7.4.1	IRRAS	129
7.4.2	Reaction Kinetics	133
7.4.3	Pt-Monolayer Deposition	136
7.4.4	Support Crystallization	139
CHAPTER 8 - Electrochemical Studies and DFT Analysis of Suppressed Exchange Current Density of Pt Supported on NbRu _y O _z		146
8.1	Pt/NbRu _y O _z Electrocatalyst	146
8.2	Electrochemical Aging Studies	146
8.3	Electron Energy Loss Spectroscopy	151

8.4	Sequential Oxidation Cyclic Voltammetry	153
8.5	Chrono-potentiostatic Analysis	158
8.6	CO Stripping	162
8.7	Open Circuit Potential Studies in Alkaline Electrolyte.....	165
8.8	Density Functional Theory Studies Adsorbates on the Pt Surface.....	170
8.9	60%Pt/NbRu _y O _z Treated at 300°C and 650°C	171
CHAPTER 9 - Non-Aerosol Synthesis of Composite Crystalline Oxides		179
9.1	Electro-catalytic Value of Tin	179
9.1.1	Batch Deposition of Catalyst onto Supports	179
9.1.2	IRRAS Studies	181
9.2	Micro-Emulsion Silica Template	187
9.3	Silica-Templated Pt/NbSn _x Ru _y O _z	189
9.4	Niobium-Ruthenium-Carbide as a Support.....	198
CHAPTER 10 - Conclusions		207
	<i>Synthesis of Mixed Metal Oxides</i>	207
	<i>Mesoporous Niobia Supports.....</i>	207
	<i>Platinum Catalyst on NbRu_yO_z</i>	208
	<i>Electrochemical Studies and DFT Analysis of Suppressed Exchange Current Density of Pt Supported on NbRu_yO_z</i>	210
	<i>Non-Aerosol Synthesis of Composite Crystalline Materials.....</i>	211

Appendix A:.....	212
Corrosion Stability of Ruthenium Oxide Materials	212
Experimental Approach	214
Results and Discussion	216
Physical Characterization.....	216
Electrochemical Characterization	225
Conclusion	229
Appendix B:	230
Niobium Oxide as a Cathode Catalyst	230
Experimental	233
Results and Discussion	235
Materials Characterization	235
Electrochemical Characterization	237
Oxygen Reduction Reactivity in the Presence of Methanol	247
Conclusions	254
Appendix C:	256
Cyclic Voltammetry: Charging Response to Increasing Polarization Rates	256
30wt% Platinum Supported on XC-72 (commercial, Etek).....	257
60wt% Pt/NbRu _y O _z Treated to 300°C	257
60wt% Pt/NbRu _y O _z Treated to 650°C	258

60wt% Pt/NbRu _y O _z (silica templated) Treated to 900°C.....	258
References	259

List of Figures

Figure 1.1: (Left) Schematic of a single fuel cell with emphasized components and chemical processes. (Right) Fuel cells can be connected in various configurations of series (shown) and parallel stacks to produce the necessary volts and amps for a particular application.....	6
Figure 1.2: Hydrogen and carbon ratios (oxygen not shown) in relevant materials for chemical energy storage.....	7
Figure 1.3: Bulk cost of pure raw earth elements. Open circles indicate promising elements of interest for PEMFC electrodes.....	13
Figure 1.4: Logarithmic elemental abundance on earth. Open circles indicate promising elements of interest for PEMFC electrodes.....	14
Figure 1.5: Fractional area of irrigated grass in the continental United States of America	16
Figure 1.6: Spray Pyrolysis reactor setup.....	17
Figure 1.7: The effect of SP reactor conditions and precursor characteristics on A) Particle Morphology, and B) composite particle microstructure.....	19
Figure 1.8: Common solvent and solute concentration profiles in a droplet during SP.....	22
Figure 2.1: Potential-pH equilibrium diagram for platinum in water at 25°C.....	25
Figure 2.2: Helmholtz interpretation (simplification) of potential distribution from the surface into the ionic electrolyte.....	26
Figure 2.3: Fundamental electrode processes. Note that the Faradaic process (a) illustrates oxidation. (b) is applicable when K^+ cannot be reduced at the applied potential of the catalyst.....	27
Figure 2.4: The changing concentration profile of oxidation and reduction species with time relative to the electrode surface.....	28
Figure 2.5: (Left) DFT calculated adsorption energies of O_2 as a function of d-band center energy from E_{Fermi} on altered noble metal surfaces. (Right) Volcano-type relationship between the rate (current) of the methanol oxidation reaction versus the binding energy on different transition metals.....	33

Figure 2.6: Pourbaix diagram for niobium showing the equilibrium species in an aqueous environment of varying pH and potential (V) at 25°C, 75°C, and 95°C.....	36
Figure 4.1: (Top) Mesoporous Nb ₂ O ₅ film deposited as a film after SP processing at 190°C followed by post treatment at 400°C to remove P123 surfactant. (Bottom Left) Cross section of 60%Pt/Nb ₂ O ₅ powder which has been pressed into a film at 5,000 lb/in ² . (Bottom Right) Fractured particle of mesoporous Nb ₂ O ₅ synthesized by SP at 200°C showing a precipitation layer at the outer edge.....	42
Figure 4.2: Heat of vaporization of relevant elements with d-orbitals. Open circles mark especially relevant elements considered in this study.....	43
Figure 4.3: Heat of fusion of relevant elements with d-orbitals. Open circles mark especially relevant elements considered in this study.....	44
Figure 4.4: Imposed photo and schematic of the compression-conduction device used to test powders synthesized by SP.....	48
Figure 4.5: Example effect of reduction temperature on conductance using Ru/RuO ₂	49
Figure 4.6: Incident x-rays excite core electron levels causing the ejection of photoelectrons with elementally specific, measureable kinetic energies.....	53
Figure 4.7: Qualitative depiction of the excitation potential of different core electron levels.....	55
Figure 4.8: Behavior of an adsorption-desorption isotherm for a mesoporous structure experiencing capillary condensation from the adsorbate.....	56
Figure 4.9: Three-electrode electrochemical test cell setup.....	61
Figure 4.10: Cyclic voltammetry behavior, a) triangular potential waveform produced by the potentiostat and b) resulting current behavior of a redox process at the WE.....	62
Figure 4.11: In situ IRRAS apparatus at Brookhaven National Laboratory Dept. of Chemistry. The IR beam reflects off of the surface of the WE while probing bond vibrations of species adsorbed onto the catalyst surface.....	64
Figure 4.12: The process of preparing a catalyst onto an Au TEM grid for rapid aging studies. The grid serves as a WE and can be examined before and after electrochemical testing.....	66

Figure 5.1: Simulated temperature and flow profiles in heated reactor tubes, 1” and 3” in diameter. Temperature is reported in °C.....	68
Figure 5.2: Profiles for temperature, velocity and heat flux at each point in the reactor furnace calculated from the COMSOL multi-physics models in Fig.5.1. The bold line in each plot represents the average value at each position in the tube furnace.....	69
Figure 5.3: Total energy imparted from the furnace to the gas/aerosol by convection and conduction heat transfer.....	70
Figure 5.4: SEM images of Nb ₅₆ Ti ₁₄ O ₃₀ (from TiCl ₄), (Top Left) from the filter paper, (Top Right) after calcination at 400°C, and (Bottom Left) wash in 0.3M H ₂ SO ₄ followed by calcination at 400°C. (Bottom Right) TEM image of the same sample taken from the filter paper, possibly showing the vaporization and nucleation of TiO ₂ nano-particles.....	74
Figure 5.5: TEM image of Nb ₅₅ Ti ₁₆ O ₂₉ (from Ti(OEt) ₄) directly from the filter paper.	75
Figure 5.6: NiCl ₂ and P123 surfactant (1:1) processed by SP at 260°C in N ₂ (Left) off the filter paper and (Right) after reduction at 400°C for 4hr.....	77
Figure 5.7: SEM images of niobia composite materials synthesized by SP at 250°C in N ₂ . (Top Left) Nb-Fe (5:2). Nb-Mo (3:1) (Top Right) off the filter paper, (Bottom Left) reduced at 400°C for 4hrs, and (Bottom Right) washed in 0.3M H ₂ SO ₄ and thermally reduced.....	79
Figure 5.8: Nb-Pt-C (1:1:0.5) processed by SP with metal-chloride and sucrose precursors at 250°C in N ₂ . (Left) wide view SEM and (Right) TEM of a granular edge).....	81
Figure 5.9: TEM images of Nb-Ru-C (2:1:1) processed by SP with metal-chloride and sucrose precursors at 250°C in N ₂ . (Left) Droplet morphology is maintained while (Right) incoherent lattice fringes indicate a mixed, crystalline structure throughout the sample.....	82
Figure 5.10: 60wt% Pt on Niobia processed by SP with metal-chloride precursors and P123 surfactant at 240°C in N ₂	83
Figure 5.11: Nb-Sn and Nb-Sn-Ru species processed by SP with metal-chloride precursors and P123 surfactant at 200°C in N ₂ . (Top-Left) Nb-Sn (1:1) reduced at 400°C for 4hrs in 10%H ₂ /N ₂ , (Top Right) and the same sample washed in 0.3M H ₂ SO ₄ and thermally reduced. (Bottom) Nb-Ru-Sn (2:1:1) after the same wash and thermal post-treatments.....	84

Figure 5.12: Nb-Sn (1:1) processed by SP with metal-chloride precursors and P123 and Brij-35 (1:1) surfactants at 200°C in N₂.....85

Figure 5.13: NbSnC (1:1:0.5) processed by SP with metal-chloride precursors, sucrose and P123 surfactant at 260°C in N₂ before post-treatments. (Top) Mixed component particles which appear amorphous by the absence of any electron diffraction pattern. (Bottom) The same particles after intense stimulation by the electron beam. The niobia matrix and P123 remain intact while tin precursor separates into a semi-crystalline phase.....86

Figure 5.14: NbSnC (1:1:0.5): Continued evolution/transformation transformation of tin-based particles with constant exposure to the electron beam of the TEM.....87

Figure 6.1: TEM showing (A) the 5-6 nm diameter mesopores of NbO_x-Dry-Air, and (B) lattice fringes of crystalline niobia formed in NbO_x-Dry-N₂/H₂. SEM of (C) NbRu_yO_z calcined in air without a washing step (NbRu_yO_z-Dry-Air), and (D) with a washing step (NbRu_yO_z-Wash-Air).....93

Figure 6.2: Adsorption-desorption isotherms in N₂ (solid, top and right axes) and corresponding pore size distributions calculated by the BJH method (dotted, bottom and left axes) for NbO_x-Wash-Air (dark) and NbRu_yO_z-Wet-N₂/H₂ (light).....97

Figure 6.3: X-ray diffraction patterns from 10 to 90° 2θ for (A) NbRu_yO_z-Wet-N₂/H₂ and (B) NbO_x-Wash-Air, as well as (C, D) both samples after additional heating at 900°C for 5 h in N₂, respectively.....99

Figure 6.4: High-resolution XPS spectra: (A) Nb 3d spectrum of NbRu_yO_z-Wet-N₂/H₂, (B) Nb 3d spectrum of NbO_x-Wash-Air, (C) O 1s spectrum of NbRu_yO_z-Wet-N₂/H₂, and (D) O 1s spectrum of NbO_x-Wash-Air.....101

Figure 6.5: High-resolution Ru 3d and C 1s XPS spectra of (A) NbRu_yO_z-Wet-N₂/H₂ and (B) NbO_x-Wash-Air.....103

Figure 6.6: Thermogravimetric analysis of NbO_x-Wash and NbRu_yO_z-Wet under the same conditions experienced during post-treatment. Samples were ramped at 10°C/min to 400°C in their respective atmospheres, where they were held for 4 h. All samples were then exposed to a N₂ atmosphere during heating from 400 to 1500°C at the same ramp rate. At temperatures of 400°C and below, (A) NbO_x-Wash was in air, (B) NbRu_yO_z was in N₂/10%H₂, (C) previously post-treated NbO_x-Wash-Air was in air and (D) N₂/10%H₂, and (E) previously post-treated NbRu_yO_z-Wash-N₂/H₂ and (F) NbRu_yO_z-Wet-N₂/H₂ were both in N₂.....105

Figure 6.7: Cyclic voltammograms of 128 $\mu\text{g}/\text{cm}^2$ NbRu_yO_z -Wet- N_2/H_2 initially in 1 M KOH solution, and then with 1 M methanol added. Scan rate of 10 mV/s vs Hg/HgO reference electrode.....107

Figure 6.8: Schematic depiction of transformations that occur during spray pyrolysis of Nb/Ru precursor solution containing a surfactant template, followed by post-treatment. (A) Evaporation begins as a vapor layer forms around the droplet. (B) Precipitation of the outer surface. (C) Outer layers begins to dry faster than interior moisture diffuses to the surface, resulting in formation of vesicles from surfactant. (D) Entire droplet eventually dries. (E) Thermolysis of chloride precursors into porous metal oxides. (F) Proper post-treatment exposes the intact mesoporous structure.....108

Figure 6.9: TEM of (A) NbRu_yO_z -Dry-Air (calcined without a washing step), and (B) STEM of NbRu_yO_z -Wet- N_2/H_2 (calcined with a preceding acid washing step). (C) NbRu_yO_z particles of various sizes before any post-treatment, showing a 3D wormhole porous structure in the particle interior and 2-3 exterior lamellar layers. (D) Higher-magnification clarifies the separate structures.....110

Figure 6.10: SEM image of a particle fragment of NbRu_yO_z -Dry-Air. During spray pyrolysis or thermal processing, particle surfaces may become nearly impermeable before volatile species can escape to the atmosphere. The pressure developed by these trapped volatiles is sometimes sufficient to fracture some particles.....111

Figure 7.1: SEM images showing large platinum nanoparticles in Pt-DI utilizing Secondary Electron (A,C) and Backscattered Electron (B,D) detectors. (E) TEM image of a particle showing some visible catalyst penetration into the mesoporous support interior. Overall, a range of Pt particle sizes are visible, from 5nm nanoparticles to 200nm nanoparticles/clusters.....117

Figure 7.2: (Top) TEM image of 60%Pt/ NbRu_yO_z immediately after spray pyrolysis. The inset shows the presence of Pt nanoparticles 2nm in diameter. (Bottom) SEM image of the same material after post-treatment, showing some catalyst clustering on the porous support surface.....118

Figure 7.3: (A) The NbRu_yO_z support of Pt-DI is mostly amorphous after spray pyrolysis. (B) There is some increase in ordered structure after post-treatment, possibly due to uptake of moisture/carbon species in the form of RuO_2 (triangle), RuO_4 (square), and RuCO_4 (star). These features mostly disappear after wet impregnation of Pt. (C) Pt peaks (circle) are distinct due to larger nanoparticles visible in SEM, shown on the next slide.....120

Figure 7.4: Pt-SP: (A) Broad Pt peaks are visible and indicative of nanoparticles in the amorphous niobia matrix after spray pyrolysis. (B) After calcination at 400°C for 4hrs in

10% H₂/N₂. Both (A) & (B) show a range of low intensity peaks from 20-35(2 θ) associated with RuO_x at various oxidation states, and possibly also PtO_x species.....122

Figure 7.5: XPS Spectra of (A) Ru 3d/C 1s and (B) Pt 4f for Pt-DI, and (C) Ru 3d/C 1s and (D) Pt 4f for Pt-PS.....123

Figure 7.6: XANES spectra of Pt L3 edge from PtNbRuO_x nanoparticles prepared by the wet impregnation (blue) and spray pyrolysis (green) methods, together with that from a Pt reference foil (red).....126

Figure 7.7a: Fourier-transformed EXAFS spectra of Pt L3 edge from PtNbRuO_x nanoparticles prepared by spray pyrolysis method (blue), together with a fitted line (red) based on Pt-Pt and Pt-O paths.....127

Figure 7.7b: Fourier-transformed EXAFS spectra of Pt L3 edge from PtNbRuO_x nanoparticles prepared by wet impregnation method (blue), together with a fitted line (red) based on Pt-Pt and Pt-O paths.....127

Figure 7.8a: XANES spectra of Nb K edge from PtNbRuO_x nanoparticles prepared by the wet impregnation (blue) and spray pyrolysis (green) methods, together with that from a Nb reference foil (red).....128

Figure 7.8b: XANES spectra of Ru K edge from PtNbRuO_x nanoparticles prepared by the wet impregnation (blue) and spray pyrolysis (red) methods, together with that from a Ru reference foil (green).....129

Figure 7.9: *In situ* IRRAS spectra recorded during ethanol oxidation on: (a) 30%Pt/NbRu_yO_z (Pt-DI); (b) 60%Pt/NbRu_yO_z (Pt-PS).....131

Figure 7.10: IR band intensities of CO₂, C=O and CO_L during ethanol oxidation at different electrode potentials (data from Fig.7.9): a) Pt-DI, b) Pt-SP. c) The ratio of CO₂ band intensity to C=O band intensity versus applied potentials.....132

Figure 7.11: (Left) Cyclic voltammograms for Pt-C (commercial), Pt-DI, Pt-SP, and Pt-TM. Scans performed at 10mV/s in 0.1M HClO₄. (Right) Ethanol oxidation performance of the same samples at 50mV/s in 0.5M EtOH and 0.1M HClO₄.....134

Figure 7.12: Cyclic voltammograms of Pt-DI before and after secondary Pt-monolayer deposition. (A) 50mV/s in 1M KOH. (B) 10mV/s in 1M KOH and 0.5M EtOH. (C) 10mV/s in 0.1M HClO₄. (D) 10mV/s in 0.1M HClO₄ and 0.5M EtOH.....137

Figure 7.13: Cyclic voltammograms of Pt/NbRu_yO_z (wt% - 60:10:10:20) after different heat treatments including immediately after spray pyrolysis heating to 300°C and 650°C in 10% H₂/N₂ for 4hrs. (A) 50mV/s in 1M KOH. (B) 50mV/s in 1M KOH and 0.5M EtOH. (C) 10mV/s in 0.1M HClO₄. (D) 50mV/s in 0.1M HClO₄ and 0.5M EtOH.....140

Figure 8.1: Cyclic voltammograms of (A) 30% Pt/XC-72 and (B) 60% Pt/NbRu_yO_z in 0.1M HClO₄ at a scan rate of 10mV/s (Ag/AgCl). Each plot shows the 10th cycle measured before and after the electrode was exposed to 3600 cycles at 1V/s.....147

Figure 8.2: TEM images of particles of 30% Pt/XC-72 (A) before and (B) after 3600 cycles at 1V/s in 0.1M HClO₄. Migration of Pt nanoparticles after aging is apparent.....148

Figure 8.3: TEM images of particles of 60% Pt/NbRu_yO_z (A) before and (B) after 3600 cycles at 1V/s in 0.1M HClO₄. The aging treatment evolves a thin oxide film around the particles.....150

Figure 8.4: TEM image of 60%Pt/NbRu_yO_z after 3600 cycles at 1V/s in 1M KOH. The oxide film appears to form as a disordered lamellar layer growing in a traverse manner at layer edges. Inset shows the FFT pattern of darker lattice fringes, verifying the atomic spacing (2.235-2.405Å) of Pt(111).....152

Figure 8.5: Radial oxygen concentration profile from the center (0nm) to the surface (~40nm) of the particle in Fig.8.4, measured using EELS O-Kα₂.....153

Figure 8.6: Cyclic voltammograms of 30%Pt/XC72 in 0.1M HClO₄ at a scan rate of 20mV/s with step-increases of 0.1V/cycle from 0.3V to 1.6V (solid), then back to 0.3V (dashed).....154

Figure 8.7: Cyclic voltammograms of 30%Pt/XC72 in 1M KOH at a scan rate of 20mV/s with step-increases of 0.1V/cycle from 0.3V to 1.6V (solid), then back to 0.3V (dashed).....155

Figure 8.8: Cyclic voltammograms of 60%Pt/NbRu_yO_z in 0.1M HClO₄ at a scan rate of 20mV/s with step-increases of 0.1V/cycle from 0.3V to 1.6V (solid), then back to 0.3V (dashed).....155

Figure 8.9: Cyclic voltammograms of 60%Pt/NbRu_yO_z in 1M KOH at a scan rate of 20mV/s with step-increases of 0.1V/cycle from 0.3V to 1.6V (solid), then back to 0.3V (dashed). Inset shows growth of the H_{des} peak.....156

Figure 8.10: Chrono-potentiostatic coulometry measurements of (A) 30%Pt/XC72 and (B) 60%Pt/NbRu_yO_z. Electrodes were held at 0.0V, 1.2V, and 0.0V for 20 min periods in 0.1M HClO₄ (A1-A3) and 1M KOH (B1-B3).....159

Figure 8.11: Hydrogen desorption peaks from cyclic voltammograms taken in 1M KOH at 50mV/s for (A) 30%Pt/XC72 and (B) 60%Pt/NbRu _y O _z before and after each potential holding period in Fig.8.10.....	161
Figure 8.12: CO stripping cyclic voltammetry in 0.1M HClO ₄ at 100mV/s on (A) 30%Pt/XC72 and (B) 60%Pt/NbRu _y O _z	163
Figure 8.13: Open-circuit potential measurements in the presence of 1M KOH electrolyte, electrolyte and bubbled O ₂ (sparging), and electrolyte and 1M ethanol.....	165
Figure 8.14: Post OCP cyclic voltammograms at 50mV/s in 1M KOH for 30%Pt/XC72. Showing cycles 1, 10, 20, 30, 40 and 50. Labels correspond to those of Fig.8.13.....	168
Figure 8.15: Post OCP cyclic voltammograms at 50mV/s in 1M KOH for 60%Pt/NbRu _y O _z . Showing cycles 1, 10, 20, 30, 40 and 50. Labels correspond to those of Fig.8.13.....	169
Figure 8.16: (Left) Grey spheres represent Pt atoms. The arrow indicates the transition path between the hollow fcc and hcp sites. (Right) Energetics along the transition path: squares, circles, and triangles, for surface diffusion of elemental C, O, and Nb, respectively.....	171
Figure 8.17: Cyclic voltammograms of Pt-300 (A) and Pt-650 (B) in 0.1M HClO ₄ and 1M KOH at a scan rate of 20mV/s with step-increases of 0.1V/cycle from 0.3V to 1.6V (solid), then back to 0.3V (dashed).....	172
Figure 8.18: Chrono-potentiostatic coulometry measurements of Pt-300 (left) and Pt-650 (right). Electrodes were held at 0.0V, 1.2V, and 0.0V for 20 min periods in 0.1M HClO ₄ (A1-A3) and 1M KOH (B1-B3).....	174
Figure 8.19: CO stripping cyclic voltammetry in 0.1M HClO ₄ at 100mV/s on Pt-300 (A) and (B) Pt-650. CO _{des} peak is shaded in blue.....	177
Figure 9.1: Cyclic voltammograms for 30%Pt (A,B) and 22%Pt-11%Ru (C,D) on crystalline NbO ₂ , NbRuSnO _x (8:1:1), and NbRuO _x (8:1). The total catalyst loading in each case was 50ug to completely cover the surface of a glassy carbon electrode.....	180
Figure 9.2: in situ IRRAS of 30%Pt/NbRu _y O _z : (Left) CVs taken at a rate of 10mV/s in 0.1M HClO ₄ . (Right) Corresponding FTIR time-resolved spectra (taken at 1mV/s). The red spectra indicates the start of CO ₂ evolution.....	182
Figure 9.3: in situ IRRAS of 30%Pt/NbO ₂ : (Left) CVs taken at a rate of 10mV/s in 0.1M HClO ₄ . (Right) Corresponding FTIR time-resolved spectra (taken at 1mV/s). The red spectrum indicates the start of CO ₂ evolution.....	182

Figure 9.4: in situ IRRAS of 30%Pt/NbO ₂ : (Left) CVs taken at a rate of 10mV/s in 0.1M HClO ₄ . (Right) Corresponding FTIR time-resolved spectra (taken at 1mV/s). The red spectrum indicates the start of CO ₂ evolution.....	183
Figure 9.5: Cyclic voltammograms for 60%Pt/Nb _x Ru _y O _x (1:1:2) after thermal reduction at 300°C and 650°C. (Left) 0.1M HClO ₄ and (right) 0.1M HClO ₄ + 0.5M EtOH.....	185
Figure 9.6: TEM analysis of 60%Pt/Nb _x Ru _y O _x (1:1:2) after thermal reduction at 300°C (top) and 650°C (middle). Insets are selected area diffraction patterns which reveal the crystalline nature of the latter. Comparative EDS analysis from both samples is also shown (bottom).....	186
Figure 9.7: Flowchart of the impregnation process of metal precursors into the micro-emulsion silica template.....	188
Figure 9.8: (Top) TEM bright-field (left) and dark-field (right) images of a Pt ₄ Nb ₁ Ru ₁ Sn _{1.3} O ₂ C ₂₄ particle after thermal decomposition with the silica template still present. (Bottom) SEM images of the same material after the silica template has been etched away.....	190
Figure 9.9: Cyclic voltammograms of Pt ₄ Nb ₁ Ru ₁ Sn _{1.3} O ₂ C ₂₄ taken in 0.1M HClO ₄	191
Figure 9.10: (Top) X-ray diffraction spectra of Pt ₄ Nb ₁ Ru ₁ Sn _{1.3} O ₂ C ₂₄ taken after dry impregnation of sucrose and metal salts into the silica template, after heating to 900°C for 4hrs, and after chemical removal of the silica template.....	192
Figure 9.11: Chrono-potentiostatic coulometry measurements of Pt ₄ Nb ₁ Ru ₁ Sn _{1.3} O ₂ C ₂₄ . Electrodes were held at 0.0V, 1.2V, and 0.0V for 20 min periods in 0.1M HClO ₄ (A1-A3) and 1M KOH (B1-B3).....	194
Figure 9.12: Cyclic voltammograms of Pt ₄ Nb ₁ Ru ₁ Sn _{1.3} O ₂ C ₂₄ in 0.1M HClO ₄ (top) and 1M KOH (bottom) at a scan rate of 20mV/s with step-increases of 0.1V/cycle from 0.3V to 1.6V (solid), then back to 0.3V (dashed).....	195
Figure 9.13: CO stripping cyclic voltammetry in 0.1M HClO ₄ at 100mV/s on Pt ₄ Nb ₁ Ru ₁ Sn _{1.3} O ₂ C ₂₄ . The CO desorption peak area is highlighted in blue.....	196
Figure 9.14: JCPDS Patterns Comparing the crystalline structure of NbRu ₃ C to various Pt _x Sn _y species.....	199
Figure 9.15: DFT calculations of relaxed structures of cubic Nb-Ru with increasing fractions of C occupying the center of the unit cell.....	200

Figure 9.16: Electronic Density of States calculated for various catalyst structures using DFT.....	201
Figure 9.17: SEM and TEM of NbRu ₃ C after heating in 10% H ₂ /N ₂ for 3 hrs at 600°C (top) and 800°C (bottom).....	203
Figure 9.18: X-ray diffraction (XRD) studies of NbRu ₃ C crystallization after heating from 200-800°C at ramp rates of 1°C/min in 10% H ₂ /N ₂	205

List of Tables

Table 1.1: Energy Density of Potential PEMFC Fuels Compared to Gasoline.....	8
Table 5.1: Total Imparted Energy as Related to Aerosol Residence Time.....	71
Table 6.1: Summary of Post-Treatments and Resulting Material Properties of All Samples.....	91
Table 7.1: XPS Elemental Composition (wt%).....	124
Table 7.2: Relative Elemental Moieties (at%).....	124
Table 7.3: In situ IRRAS Spectra Band Assignments.....	131
Table 7.4: Total Charge Density and 0.5M Ethanol Oxidation Peak Dimensions (CV) Before and After Secondary Pt Deposition on Pt-DI.....	137
Table 7.5: Total Charge Density and 0.5M Ethanol Oxidation Peak Dimensions (CV) for Pt/NbRu _y O _z (wt% - 60:10:10:20) Before and After Heat Treatments.....	140
Table 8.1: Calculation of Electrochemical Surface Area on Pt for CO and H (soln) species from Fig.8.12.....	162
Table 8.2: CO Stripping Results Calculated from Fig.8.19.....	176
Table 9.1: Comparative JCPDS Structure Data of Active EOR catalysts	199

List of Appendices

Appendix A: Corrosion Stability of Ruthenium Oxide Materials

Ruthenium oxide materials were evaluated as possible non-carbon-based supports for fuel cell catalysts. The effects of composition and morphology of ruthenium oxide materials on the conductivity and corrosion stability in the gas-diffusion electrode (GDE) configuration were thoroughly investigated. The compositions of the bulk and surface of three ruthenium oxide materials, along with the surface area and surface morphology, were compared. We have found that all tested ruthenium oxide powders exhibited higher corrosion stability compared to carbon. Full conversion of $\text{RuO}_2 \cdot n\text{H}_2\text{O}$ to the RuO_2 phase by postreduction in a hydrogen atmosphere leads to improved conductivity and corrosion stability.

Appendix B: Niobium Oxide as a Cathode Catalyst

Composite electrocatalysts consisting of platinum nanophase supported on carbon black decorated with niobium oxide phase were prepared by a two step precipitation/reduction procedure. The intrinsic catalytic activity of these materials was evaluated for the oxygen electroreduction, measured in the absence and presence of methanol. It was found that in the presence of Nb_xO_y materials are more hydrophilic and thus initially have lower intrinsic catalytic activity for oxygen reduction. However, materials containing Nb_xO_y offer better overall platinum mass utilization, achieved through much better dispersion of the platinum nanophase. Such advantageous dispersion is observed even for high metal loadings. Another advantage of these materials is minimal effect on the poisoning with the intermediates formed during methanol oxidation that results in the enhanced methanol tolerance.

Appendix C: Cyclic Voltammetry: Charging Response to Increasing Polarization Rates

Cyclic Voltammograms of important samples in this study are shown at increasing polarization rates. CV's are normalized by the polarization rate so that the double layer of each sweep is equal and comparable. This shows how the redox features shift at increasing polarization rates.

CHAPTER 1 - Introduction

Chemical reactions which involve the release of stored energy potential usually have an activation barrier which must first be overcome, either by environmental changes, or some other carefully controlled activation process. The latter is especially important for the controlled release of energy from fuels which can follow multiple reaction pathways, possibly leading to different final products. Some of these might be less favorable, either because a portion of the chemical energy remains unharnessed, or they pose environmental or health hazards in proximity to people.

Catalysis is generally known as the phenomena in which the energy of an activation barrier is lowered through temporary electron exchange with a renewable material (catalyst), increasing the rate, conversion, or selectivity of an interesting reaction. But catalysis is also the science by which we can control otherwise difficult or dangerous reactions for our benefit, and in the case of this study, tailor a process for a particular application with unique design parameters. An example is the catalytic oxidation of ethanol inside a fuel cell, which should proceed at a temperature of 60-80°C and in the presence of moderate levels of water. Catalytic materials are often designed to be stable at much higher temperatures than this while maintaining the highest surface area possible on which reactions can occur. This can be achieved by dispersion of catalyst particles onto a rough, inert substrate which remains stable under reaction conditions. Such an approach is usually more cost-effective than introducing a high surface area, nano-scale structure into the catalyst, itself.

Electro-catalysts and electrocatalytic systems primarily involve Faradaic reactions in which a charge is transferred to the catalyst, while a counter-charge in the form of an ion is also formed. If such a catalyzed reaction is occurring at the anode in a fuel cell, then the catalyst and support must both be capable of conducting the negative charge away from the catalyst surface for the overall reaction to continue. While most heterogeneous catalysis processes are concerned with the steady supply of reactants to and removal of products from the catalyst surface, fuel cell electro-catalysis is similarly concerned with the conduction of electrons and ions from the anode to the cathode in order to affect useful current and voltage potentials between the two. This is the basis for powering devices in any electrochemical storage system.

Though they are co-dependent, catalysis and ion conduction are separate sciences unto themselves within fuel cell design. The same catalyst that is efficient for hydrogen oxidation may not be optimal for ethanol oxidation. Moreover, the resulting ions can be positively or negatively charged depending upon the pH of the ionic barrier between the anode and cathode. It is evident from this simple introduction to fuel cell systems that great advances in the technology require coordinated efforts across multiple fields.

The Department of Energy began implementing programs to support the research and development of fuel cell systems in 1984. Most of the effort since this time has focused on catalysis in acidic electrolyte with proton charge transfer due to DuPont's introduction of Nafion over ten years prior as the most stable and effective ionomer available¹. The fluorocarbon chain structure of Nafion is resistant to most forms of chemical degradation, except in the presence of alkali metals such as sodium or potassium. The chain contains sulfonic acid ions which can conduct $\text{H}^+/\text{H}_3\text{O}^+$ ions when hydrated. This property

inherently limits Nafion to acidic chemistry and lower operating temperatures at which water remains a liquid. Lower operating temperatures limit the kinetics of reaction on the catalyst. To compensate, larger amounts of catalyst are required. The most effective catalysts known are platinum and platinum-ruthenium alloys in quantities which have traditionally been prohibitively expensive to implement. The most notable exception has been the implementation of alkaline fuel cells as part of NASA's manned spaceflight missions for nearly the past five decades. These systems have used compressed oxygen and hydrogen free of impurities to produce drinking water as well as energy ².

The delay in widespread implementation of fuel cells might be partially attributable to this restricted approach and will most certainly continue until a decrease in the materials expense is achieved. One promising approach is the development of more effective catalysts which utilize less expensive materials with similar or complimentary properties to platinum, tailored towards the oxidation reaction pathways of domestically producible alcohols.

1.1 Fuel Cell Concept

The years that have elapsed since the introduction of the internal combustion engine (ICE) and its widespread implementation to fulfill the energy requirements of a growing world have been filled with great technological advancements and increasingly complicated applications. In fact, it is difficult to provide an adequate picture of the profound changes, and complications, caused by ICE technology and the availability of cheap fossil fuels most widely consumed. To most people the fuel cell concept is understood to be a progressive response to modern problems: environmental degradation and pollution, energy efficiency, and increasingly expensive, imported petroleum, to

name a few. People can also generally appreciate the clumsier aspects of ICE technology: engines are noisy, smelly, and unwieldy for smaller applications. But for most energy needs, electrical transmission lines separate the user from the aforementioned unpleasanties.

Efficiency and simplicity are fundamental towards understanding why fuel cells represent a favorable alternative to heat engines for many applications. Ethanol is a simple alcohol which could easily be combusted inside an automotive engine, or oxidized inside a fuel cell to power an electric motor. In both cases, the stored energy potential of ethanol is the same, initially.

Power Generation: Chemical Energy → Thermal Energy → Mechanical Energy → Electrical Energy

Automotive: Chemical Energy → Thermal Energy → Mechanical Energy

Fuel Cell: Chemical Energy → Electrical Energy → Mechanical Energy

Each step in the above processes represents a loss in efficiency. Thermal energy capture is especially inefficient, with a conventional automotive vehicle achieving as high as 20%. Alternatively, a fuel cell vehicle might achieve ~55% because, unlike a heat engine, its efficiency can exceed the thermodynamic Carnot limit.

Because their efficiency is not based entirely upon the capture of thermal energy, the fuel cell concept can theoretically be designed around a larger range of temperatures, usually anywhere from 80°C to 1200°C. Similar to batteries, fuel cells can also vary greatly in size for portable and stationary applications, including personal electronics, automotive transportation, remote and backup power supply, and power for infrastructure in urban and industrial environments. Advantages over batteries include the ability to refuel very quickly as well as the potential for an air breathing cathode, resulting in less carried

weight. Supercapacitors (also known as ultracapacitors) are another emerging form of energy storage, offering high power density at lower energy densities than batteries or fuel cells. Many mobile applications such as automotive, as well as uninterruptible power supply (UPS) schemes benefit from systems utilizing combinations of these technologies, where the strengths of one can supplant the shortcomings of another. The performance properties of these devices relative to one another are usually well described in Ragone plots.

1.2 Fuel Cell Design

A polymer electrolyte membrane fuel cell (PEMFC) is an electrochemical device which utilizes oxidation and reduction processes specific to a given fuel to release chemical energy that can be used to perform work. A fuel is first fed to the anode where it passes through the gas diffusion layer (GDL) and is broken down into three components after adsorbing onto the catalyst: electrons, hydrogen-based ions, and oxidized byproducts. In the case of hydrogen as a fuel in an acidic ion-membrane, H_2 is broken down into H^+ and e^- , with no byproducts from the anode assuming the fuel is entirely consumed. Electrons travel from the anode to the cathode by way of a complete circuit to and from an electrical device to which power is provided. H^+ charge carriers also traverse an ion-conductive membrane as H_3O^+ . Both charged species recombine at the cathode along with O_2 to form H_2O . This last process is referred to as the oxygen reduction reaction (ORR).

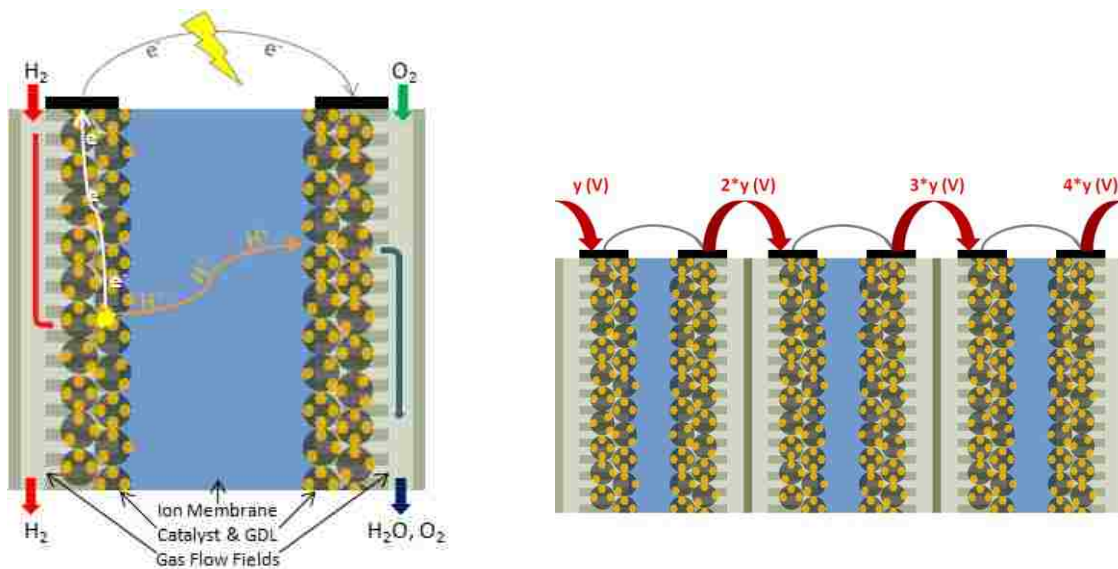


Figure 1.1: (Left) Schematic of a single fuel cell with emphasized components and chemical processes. (Right) Fuel cells can be connected in various configurations of series (shown) and parallel stacks to produce the necessary volts and amps for a particular application.

Reactions occurring on both electrodes are conventionally catalyzed by platinum nanoparticles dispersed onto high surface area carbon support particles. The carbon is amorphous with a graphitic surface that is relatively stable and hydrophobic.

To yield useful amounts of power for most devices, multiple cells must be connected in series to produce higher voltages. This constitutes a fuel cell stack, which warrants further design considerations: a system for balanced hydration regulation, effective heat dissipation, and even disbursement of reactant gasses across the entire surface area of the electrode using bipolar plates with carefully patterned channels. Each one of these systems helps address an efficiency sink within the system. The commonality of such losses in fuel cell stacks is why it is especially important for a catalyst to be designed around a particular fuel and ion-membrane chemistry.

1.3 Properties of Potential Fuels

In addition to their potential efficiency and scalability, much of the political and technological appeal of PEMFCs is based upon the variety of chemicals which can be used as fuels. The ideal fuels of the future and the accompanying infrastructure necessary to distribute them will likely prove to be regionally specific, unlike the systems currently in place for petroleum consumption. Even though domestic oil production can only provide about 5 million barrels of oil per day (mB/d), an advanced, global land and sea infrastructure allows for the importing of an additional 11 mB/d for transportation and 6.5 mB/d for industrial processes³. A feasible infrastructure is an indispensable criterion for new energy sources, though an alternative fuel which could be distributed on this scale is not currently available.

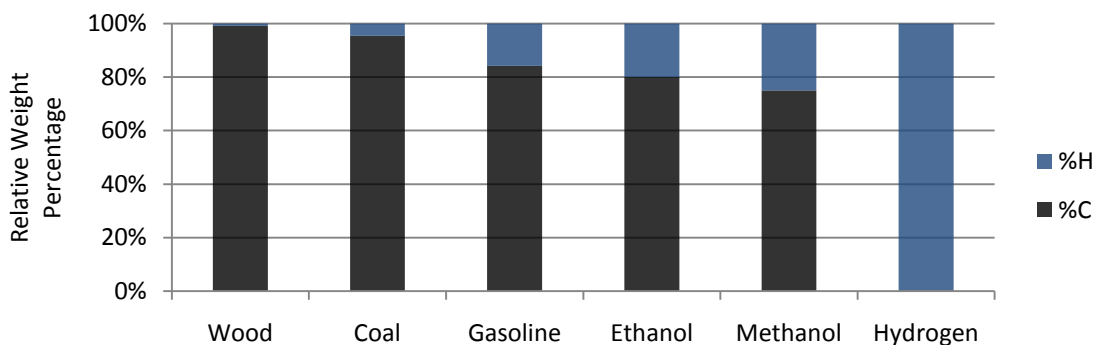


Figure 1.2: Hydrogen and carbon composition (oxygen not shown) in relevant materials for chemical energy storage.

Electro-catalytic oxidation of large hydrocarbons is considerably more difficult than for hydrogen and lighter alcohols. Generally, it is helpful to associate energy density of a fuel with its hydrogen content. H^+ ions are the smallest species to associate with electrons, and the kinetics of oxidation are relatively fast. Of the fuels listed in Fig.1.2,

hydrogen, methanol, and ethanol have the highest hydrogen content and involve simpler catalysis. Fuels which appear farther left are better suited for heat-driven energy production, while those farther to the right have the most potential for efficiency electro-catalytic oxidation.

Table 1.1: Energy Density of Potential PEMFC Fuels Compared to Gasoline ⁴

Fuel	H₂	H₂ Tank (~1.5wt%)	Methanol	Ethanol	Gasoline
kWh/kg	32.8	0.42	6.1	8.1	12.7

The energy density of gasoline is 156% that of ethanol. Yet considering the relative efficiency of heat engines and fuel cells alone, an ethanol fuel cell would only need to operate at about 35% efficiency to deliver the same energy per mass as a gasoline internal combustion engine.

1.3.1 Hydrogen (H₂)

Hydrogen is easily oxidized over Pt and has an excellent energy density until one considers attainment and storage. Storage as a compressed gas is currently the most practical method, but the energy loss per weight is obvious in Table 1.1. Alternative storage techniques involve reversible absorption of hydrogen into a substrate to form metal hydrides ^{5,6} or adsorption onto the surface of carbon nano-tubes ⁷, both at lower pressures than compressed H₂ gas (~15-35 MPa). It is usually obtained from steam reforming of methane, natural gas or coal, or from electrolysis of water ¹. And all these sources involve high emissions of CO_x species with current reforming methods (except in the case of solar-driven electrolysis). Hydrogen is also difficult to store for long periods due to a high diffusion rate through most tank materials. And because of its high

flammability and the significant losses incurred during transport from Source Material>Refined State>Stored State>Vehicle Tank, an entirely new infrastructure is necessary for its implementation.

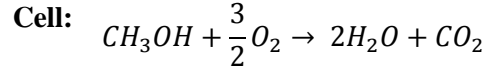
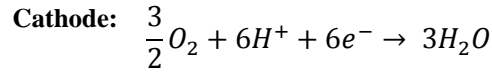
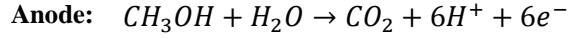
Acid Electrolyte	Base Electrolyte
Anode: $H_2 \rightarrow 2H^+ + 2e^-$	Anode: $H_2 + 2(OH^-) \rightarrow 2H_2O + 2e^-$
Cathode: $\frac{1}{2}O_2 + 2H^+ + 2e^- \rightarrow H_2O$	Cathode: $\frac{1}{2}O_2 + H_2O + 2e^- \rightarrow 2(OH^-)$
<hr/>	<hr/>
Cell: $H_2 + \frac{1}{2}O_2 \rightarrow H_2O$	Cell: $H_2 + \frac{1}{2}O_2 \rightarrow H_2O$
Eqn.1.1	Eqn.1.2

Despite these complications, the hydrogen oxidation reaction has been well studied and remains the simplest fuel for which a PEMFC can be designed.

1.3.2 Methanol (CH₃OH)

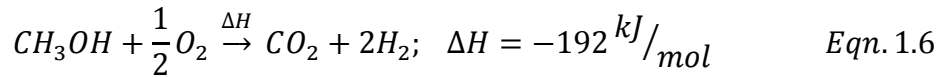
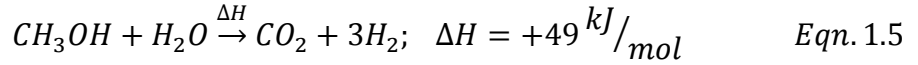
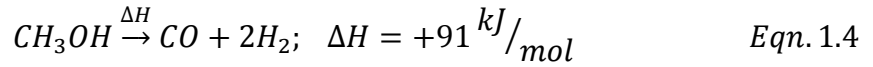
Methanol is usually obtained from coal or natural gas, both of which are abundant in the United States, resulting in significant emissions of greenhouse gasses. Zero emissions processes from renewable biomass are possible, but not currently established. Storage requires tanks and lines made of corrosion resistant plastic and metal. If these are available, then methanol is easily stored as a liquid under ambient conditions for stationary and mobile applications. However, its use for smaller devices is questionable due to the fuel's toxicity and potential to be absorbed through the skin.

Acid Electrolyte



Eqn.1.3

There has been extensive time and money invested into the development of direct methanol fuel cells ^{8,9} and methanol reformers which subsequently produce hydrogen ¹⁰ mainly because of the ease with which it can be stored, as well as its substantially higher energy density compared to compressed hydrogen.



Decomposition of methanol (Eqn.1.4) is undesirable for PEMFCs because of the high concentrations of CO produced. The reaction for steam reforming of methanol to produce hydrogen (Eqn.1.5) is similar to the anode reaction in Eqn.1.3. However, in PEMFCs where steam is unsuitable, the reaction instead proceeds exothermically using Pt catalyst. An exothermic partial oxidation reaction (Eqn.1.6) can be considered to avoid the need for an external heating source which is otherwise required and

complicates the design of smaller devices ¹¹, but this represents a significant loss of efficiency.

At the PEMFC anode, the methanol oxidation reaction is complicated by slower kinetics, and the formation of CO with its strong adsorption affinity for the Pt surface that can lead to poisoning of the catalyst. If CO_{ads} and O_{ads} occupy adjacent Pt surface sites, then the energy of formation and desorption of CO₂ is about 95 kJ/mol, compared to 259 kJ/mol to desorb CO_{ads} otherwise ¹². Nafion ionomer is also somewhat permeable to methanol, allowing some of the fuel to traverse the membrane and react on the cathode catalyst. The result is a decrease in the potential between the anode and cathode.

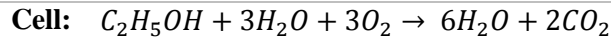
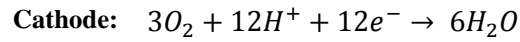
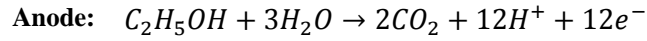
1.3.3 Ethanol

Ethanol shares the same storage benefits and precautions as methanol. It is less toxic than either methanol or gasoline, and established processes already exist in the United States and elsewhere for the attainment of ethanol from bio-renewable sources, including corn, wood, and grass and others ¹³. Currently, manufacturing processes are still energy intensive, similar to hydrogen.

The high energy density of ethanol can only be realized inside a fuel cell with the complete oxidation of both carbon atoms, leading to the formation of CO₂. This requires that partially oxidized, double-carbon intermediate species remain bonded to the catalyst surface long enough for scission of the C—C bond to occur. Conventional catalysts for PEMFCs such as Pt/C and PtRu/C fail at achieving a high yield of CO or CO₂. Much work has been spent designing Pt-alloys, especially variations of PtRu in which the

ruthenium helps stabilize the Pt surface against poisoning by CO. However, this approach might not necessarily be conducive to C—C scission of multi-carbon fuels.

Acid Electrolyte



Eqn.1.7

The mechanism of ethanol oxidation in alkaline electrolyte is more complicated than in acid. This is partially due to the formation of soluble carbonates from CO₂ production. But ethanol also has a greater variety of partial oxidation products than methanol, including acetic acid and acetaldehyde. Similar to oil, ethanol is a commodity for chemical products as well as energy, with varying value for each depending upon whether it is obtained from biomass or fossil fuel ¹⁴. However, with regard to stability of storage and toxicity (including oxidation by-products), ethanol is most optimal.

1.4 Economic Factors

1.4.1 Catalysts and Support Materials

Platinum based catalysts are the conventional standard for both oxidation and oxygen reductions in low temperature fuel cells. The cost of this material, alone, greatly defines the overall expense of fuel cells. To be economically competitive, the cost must decrease roughly five times for the implementation of fuel cell stacks for automotive applications ¹⁵. Alternatively, systems which require similarly smaller amounts of Pt with enhanced

durability must be developed. One approach being pursued is the use of ultra-low Pt loadings, wherein monolayer amounts of Pt are deposited onto a substrate ¹⁶. Another method is the synthesis of nanoparticles with carefully controlled morphologies which promise greater stability ^{17, 18}. Corrosion of the carbon support also leads to a loss of platinum, and carbon nanotubes are being pursued as a more stable alternative ¹⁹.

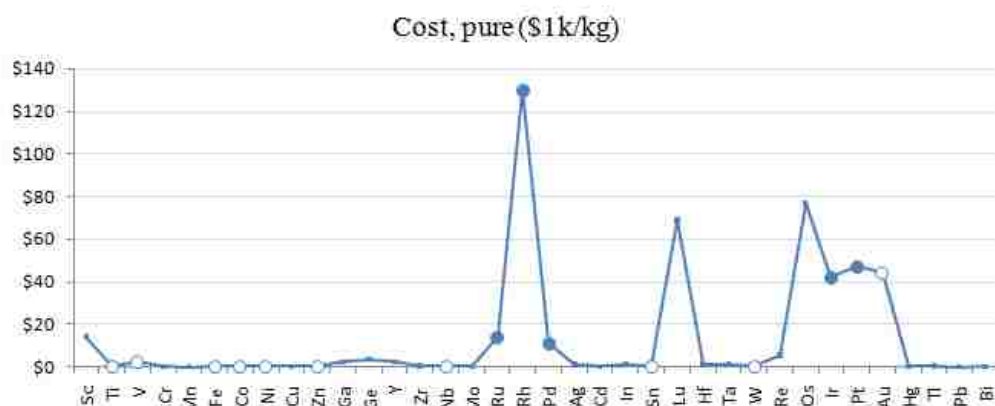


Figure 1.3: Bulk cost of pure raw earth elements. Open circles indicate promising elements of interest for PEMFC electrodes.

Yet another approach involves replacing the carbon support, entirely, with an alternative material that offers better stability while simultaneously enhancing the stability and/or performance of platinum. But because activated carbons tend to be very inexpensive, any replacement must be appreciably better on both counts. The figure above shows the average bulk prices of various elements in 2009 (relative prices can vary from those associated with gram-amount purchases). Elements with open circles indicate some promising alternatives with notable electrochemical behavior.

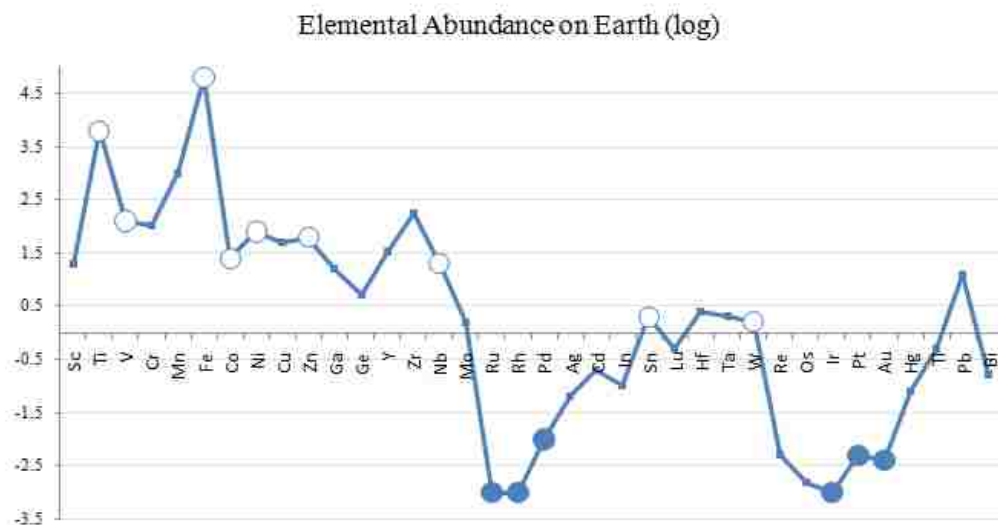


Figure 1.4: Logarithmic elemental abundance on earth. Open circles indicate promising elements of interest for PEMFC electrodes.

The elemental abundance of potential support materials is especially relevant. Platinum is relatively rare, with most mines centralized in South Africa and Russia. The market price can be inconsistent and subject to severe fluctuations. Materials with a positive logarithmic abundance would help ensure a more stable production price, and allow fuel cells to be more easily implemented.

1.4.2 Ethanol from Biomass

As mentioned previously, ethanol has value in multiple markets including energy as well as food. This is especially true in the United States where gasoline is blended to contain 10% ethanol (E10) in order to reduce automotive emissions. Government subsidizing of ethanol is intended to support this practice and add stability to the energy market by guaranteeing corn-farmers a minimum annual demand. This inflates the \$/bushel value of corn by 15-30% depending upon the state²⁰. Gasoline refiners also receive an income tax credit of \$0.51 per gallon of E10 sold²¹. These subsidies ultimately cost the

government \$2.00-\$3.00 per gallon of ethanol produced from biomass in addition to what is paid by the consumer. The benefit of this system is clearly relative to the market value of petroleum. Fossil fuels are used in the production of most biomass derived chemicals. This includes hydrogen and alcohols, in which the energy contained in the fossil fuel consumed is usually greater than that of the chemical produced. But when the ethanol market is considered in its entirety, including all energy inputs involved in growing the corn, refining, transporting, and marketing, it can be shown that the ethanol produced contains more energy than the fossil fuels used in its production²². Alternatively, the energy obtained from gasoline by the user is 80% of that in the fuels used in its production²³.

Subsidization of corn also affects the food market. Arguments against corn ethanol often discuss the adverse impact on food prices that could result because corn products are more common than any other in refined foods in the United States. It is estimated that an increase of 50-80 million acres of cropland would be necessary to displace gasoline consumption with biomass-derived fuels for energy. Currently the United States utilizes roughly 430 million acres for all grown crops. But the main obstacle in realizing such an increase is not land, but instead, the water required for irrigation. It was recently reported from analysis of NASA satellite imagery that the single largest irrigated crop in the U.S. is grass (32 million acres), covering an area three times greater than that of all irrigated corn^{24, 25}.



Figure 1.5: Fractional area of irrigated grass in the continental United States of America²⁵

The discussion of the economics of ethanol is intimately related to intelligent water management. With this revelation, it is notable that Food vs. Fuel arguments are not limited to ethanol, and instead encompass the growth of biomass-derived chemicals, in general.

1.5 Spray Pyrolysis Aerosol Synthesis

The spray pyrolysis process is also referred to in the literature as aerosol decomposition, evaporative decomposition, spray roasting, spray calcination, and liquid aerosol thermolysis²⁶. The concept involves a liquid mixture containing precursors which are soluble in a particular solution. This liquid is atomized to produce droplets by one of several aerosol generation techniques also involving a carrier gas. Depending upon the

desired oxidation state of the final material, the carrier gas is commonly air, H_2/N_2 mixes, or other inert gasses. Suspended in the gas, the droplets are carried through a furnace reactor where they eventually dry into particles and the precursors thermally decompose, most often into metals or metal oxides. These particles are collected on a surface, in a solution, or on a filter paper that traps only the desired product.

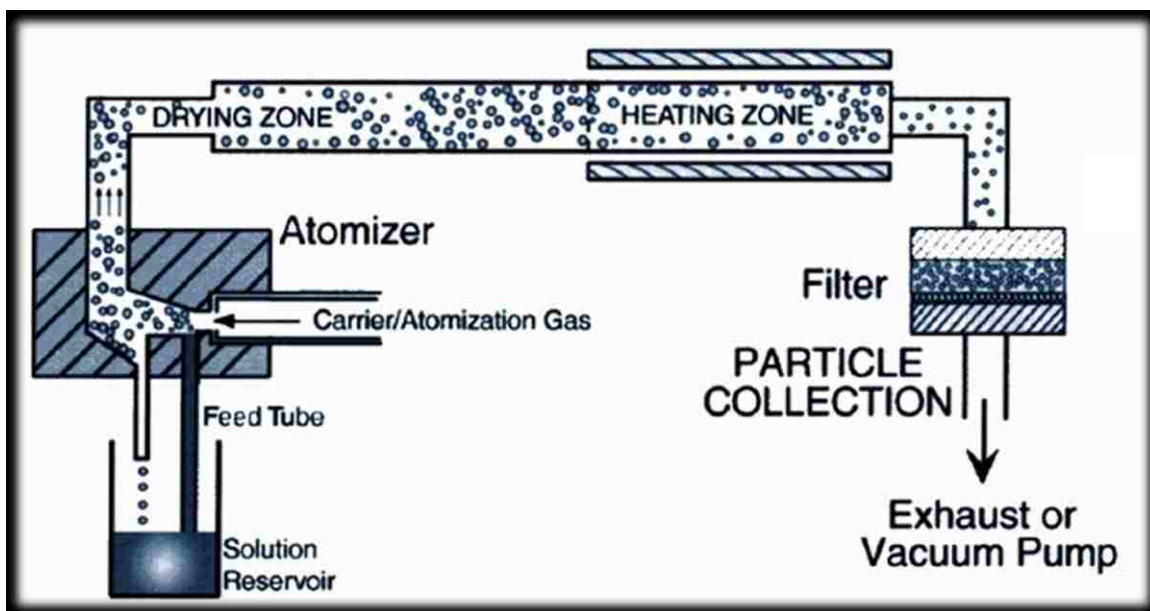


Figure 1.6: Spray Pyrolysis reactor setup ²⁷.

The advantages of spray pyrolysis are considerable for synthesis of catalyst materials:

- Simple precursors dissolved into solution
- Homogeneous mixing in which droplets act as individual micro-reactors
- Rapid processing time on the order of several seconds
- Utilize evaporation-induced self-assembly of surfactants (EISA)
- Consolidated processing of multiple thermal decomposition stages and atmospheres into a single scheme

- Excellent scalability from bench-top to industrial processes

Sufficient solubility of precursors in the initial solution ensures that each droplet will have a homogeneous composition. Droplets are usually poly-dispersed and vary depending upon the atomization method, though diameters c.a. 0.2-0.3 μ m are common. With compatible precursors, this type of aerosol synthesis technique can be used to produce metals and metal-oxides, ceramics, and composite materials involving non-metals. Surfactants can be used to template materials with meso or nano sized features. In addition, sol-gel chemistries in the literature can be easily adapted to spray pyrolysis to achieve products of equal composition over much faster processing periods.

The type of solvent used depends upon the precursor and template of interest, and is often aqueous or alcohol-based. Other potential solvents or additives such as NH_3OH , benzene, or similar have hazardous byproducts which must be scrubbed or thermally decomposed from the exhaust gas downstream of the main reactor. Such solvents are usually avoided for industrial scale processes when possible. Typical precursors include metal carboxylates, halides, nitrates, and alkoxides. Nitrates are useful in place of carboxylates when carbon contamination in the product is of concern. However, carboxylates usually break down to CO and CO_2 , whereas nitrates and halides can result in more hazardous or reactive byproducts, such as HNO_3 and NO_x ^{26, 28, 29}. Chlorides can be useful precursors because many metals exhibit similar solubility in aqueous solutions. Byproducts are usually H_2 , HCl , and Cl_2 which deposit into the collected sample at low concentrations and are easily removed by washing or thermal post-processing. Chlorides will decompose in aqueous solutions into metals or metal oxides when pH is increased beyond a certain threshold, often above pH 2-3. Such a change can be induced by

evaporation of solvent with solvated Cl^- from a droplet. The ability to coordinate the decomposition of metal precursors in near simultaneous fashion is especially helpful for achieving homogeneous materials of components with varying volatilities. The independent nature of each droplet in SP is particularly useful for heterogeneous catalysts because it is easy to maintain a high level of dispersion for metallic nanoparticles within a metal oxide matrix³⁰.

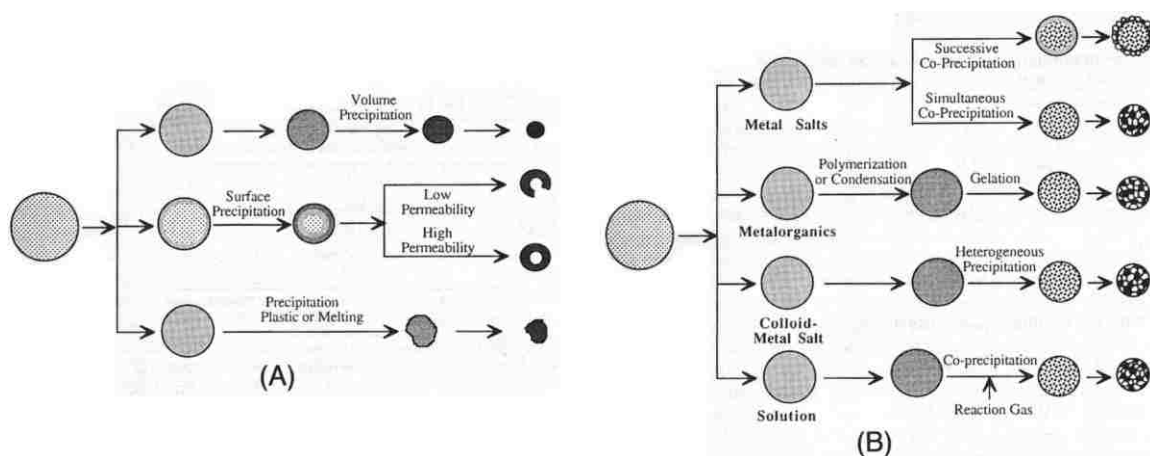


Figure 1.7: The effect of SP reactor conditions and precursor characteristics on A) Particle Morphology, and B) composite particle microstructure³¹.

Another attractive feature of SP is the scalability. Control over the various droplet-reaction phenomena described above, along with consolidation of sequential post-treatments, can be economically achieved in large, multi-zone reactors carefully designed for a specific type of material. Multi-physics simulations of such reactors (see Ch.5) can help ensure specifications before any significant financial investment into a pilot system. Simulated flow patterns and residence times for different reactor designs can be coupled with kinetics models of a droplet to predict the state of the end product, so long as properties of the material are known.

Depending upon the concentration of the precursor solution, the solvent will provide 90% or more of the droplet's initial mass. The change in mass initially correlates to the evaporation rate of solvent at the droplet surface^{31, 32}:

$$\frac{dm}{dt} = \frac{4\pi R D_v M}{R_g} \left(\frac{p_\infty}{T_\infty} - \frac{p_d}{T_d} \right) \quad \text{Eqn. 1.8}$$

R_g is the universal gas constant, D_v is the diffusion constant of vapor, R is the droplet radius, p_∞ and p_d are the ambient vapor pressures far from and at the droplet surface, T_∞ and T_d are the reactor and droplet temperatures, and M is the molecular weight of the carrier gas. The equation above neglects changes in droplet radius, which is also assumed to be greater than 50nm and moving at a vector equal to that of the ambient carrier gas.

The rate of temperature change at the droplet surface is a factor of loss of energy to the latent heat of evaporation of solvent, as well as heating from the ambient gas.

$$4\pi R K (T_\infty - T_d) + \lambda \frac{dm}{dt} = m S \frac{dT_d}{dt} \quad \text{Eqn. 1.9a}$$

$$\text{condition: } \frac{4R\sigma T_\infty^3}{K} \ll 1 \quad \text{Eqn. 1.9b}$$

K is the ambient thermal conductivity, S is the specific heat of the solvent, and σ is the Stefan-Boltzmann constant. This model applies assuming Eqn.1.9b is true, indicating negligible contribution from radiant heating.

The solute concentration in the droplet decreases from the surface to the interior as solvent evaporates from the surface. This involves a concentration gradient, the mathematical solution for which varies greatly for different systems:

$$\frac{\partial C}{\partial t} = \frac{D_s}{r^2} \frac{\partial}{\partial r} \left(r^2 \frac{\partial C}{\partial r} \right) \quad \text{Eqn. 1.10}$$

Eqn.1.10 assumes a constant particle radius. When the evaporation rate from the surface is similar to the diffusion rate of solvent from the droplet interior, this model becomes inaccurate. It can instead be modified to account for changes in concentration ³³:

$$u = \frac{c_A}{c}, z = \int C r^2 dr, s = D_s C^2;$$

$$\frac{\partial u}{\partial z} = \frac{\partial \left(r^4 s \frac{\partial u}{\partial z} \right)}{\partial z} \quad \text{Eqn. 1.11}$$

D_s is the diffusion constant of the solvent, and r is the radius (now variable) of the droplet.

Once most of the solvent has evaporated and the droplet is better described as a particle, solvent diffusion-limited drying can be taken in the place of Eqn.1.8 ³⁴:

$$\frac{dm}{dt} = \frac{4\pi R_c D_v}{1 + \frac{D_v}{D_{cr}} \frac{\delta}{R_c - \delta}} (\gamma_d - \gamma_\infty) \quad \text{Eqn. 1.12}$$

R_c is the droplet radius at the point of precipitation, δ is the thickness of the precipitation layer at the surface, D_{cr} is the diffusivity of vapor through the precipitation layer, and γ is the mass concentration of solvent vapor. Eqn.1.12 assumes a constant rate of diffusion through a uniform precipitate layer of unchanging thickness.

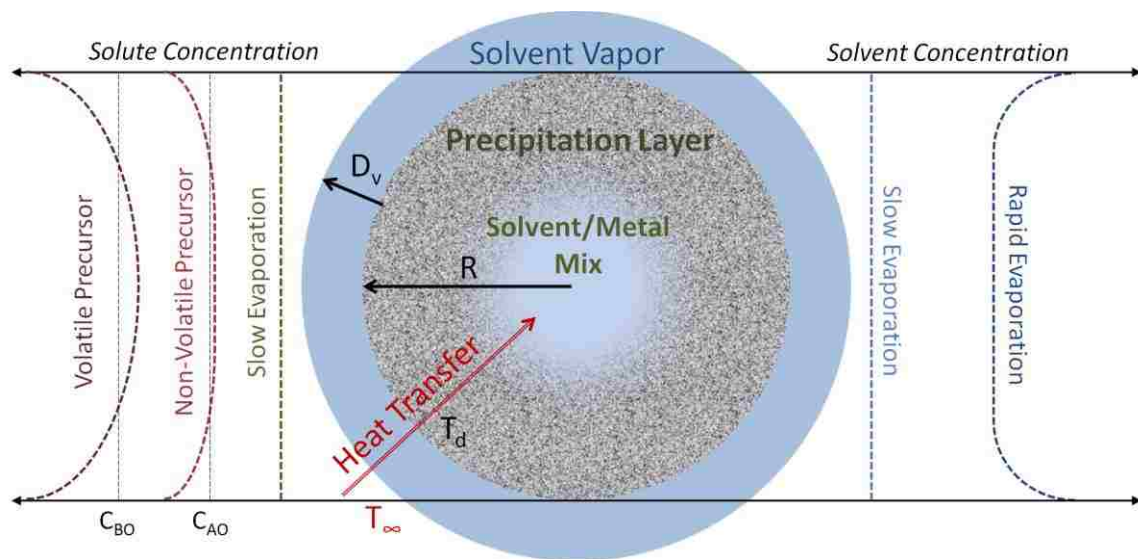


Figure 1.8: Common solvent and solute concentration profiles in a droplet during SP.

Common droplet behavior similar to what might be modeled by Egn.1.8-1.12 is depicted in Fig.1.8. The actual concentration gradients of metal precursors and solvent will vary depending the materials and temperature profile of the reactor.

CHAPTER 2 - Electrocatalysts: Stability and Performance

2.1 Aqueous Electrocatalysis

When two electrodes are connected by an electron and an ion conducting medium, each will exhibit Faradaic behavior in which a charge transfer occurs. This involves a redox process in which reduction and oxidation reactions are simultaneously proceeding at equilibrium. One function of the catalyst is to shift this equilibrium to favor one redox process over the other, altering the charge transfer measured as exchange current density. The value of this term reflects electro-catalytic activity at the electrode. Oxidation behavior is assigned to the anode, and reduction to the cathode. The difference between

the exchange current density of each electrode constitutes the total potential of the circuit, referred to as the cell.

$$\Delta E = E_{anode} - E_{cathode} \quad Eqn. 2.1$$

In the absence of an externally applied potential, the natural redox behavior of each electrode will proceed proportionally to the magnitude of the negative Gibbs energy of reaction until equilibrium is reached:

$$\Delta G_{rxn}^o = -nFE_{redox} \quad Eqn. 2.2$$

where ΔG_{rxn}^o is Gibb's free energy of reaction. n is the number of electrons transferred. F is Faraday's constant, 96,489 C/mol e^- . E_{redox} is the reversible potential of the cell. In this case, ΔE of Eqn.2.1 represents the open circuit potential (OCP) of the system. The value of OCP can be useful for determining how similar an electrode's natural redox processes are to its intended operating potential inside a fuel cell. For a hydrogen/oxygen fuel cell run under standard conditions, the OCP is known to be 1.23V. This is the theoretical potential limit of such fuel cells.

The Nernst Equation is useful for describing the electrochemical activity of a cell when an external potential is applied and the response of one electrode is based upon a predictable, measureable reference redox couple (E^o):

$$E_{cell} = E^o - \frac{RT}{nF} \ln K_{eq} = E^o - \frac{RT}{nF} \ln \frac{[red]}{[ox]} \quad Eqn. 2.3$$

where E_{cell} is an externally applied potential. R is the universal gas constant, 8.314J/mol-K. T is the temperature of the system. K_{eq} is the equilibrium constant between reduction

and oxidation processes at the electrode of interest. In this way, Eqn.2.3 is an analogue of Eqn.2.1. If the response of one electrode (E^0) to the applied cell potential (E_{cell}), then the activity of an unknown electrode can be described.

The nature of the electrolyte affects the operating potential range of the cell. Aqueous systems must operate within the potential range at which H_2O is relatively stable without evolving hydrogen or oxygen. These boundaries are reflected in the potential-pH diagram of Figure 2.1, denoted by the dotted lines, (a) $[\text{H}_2/\text{H}^+]$ and (b) $[\text{O}_2/\text{H}_2\text{O}]$.

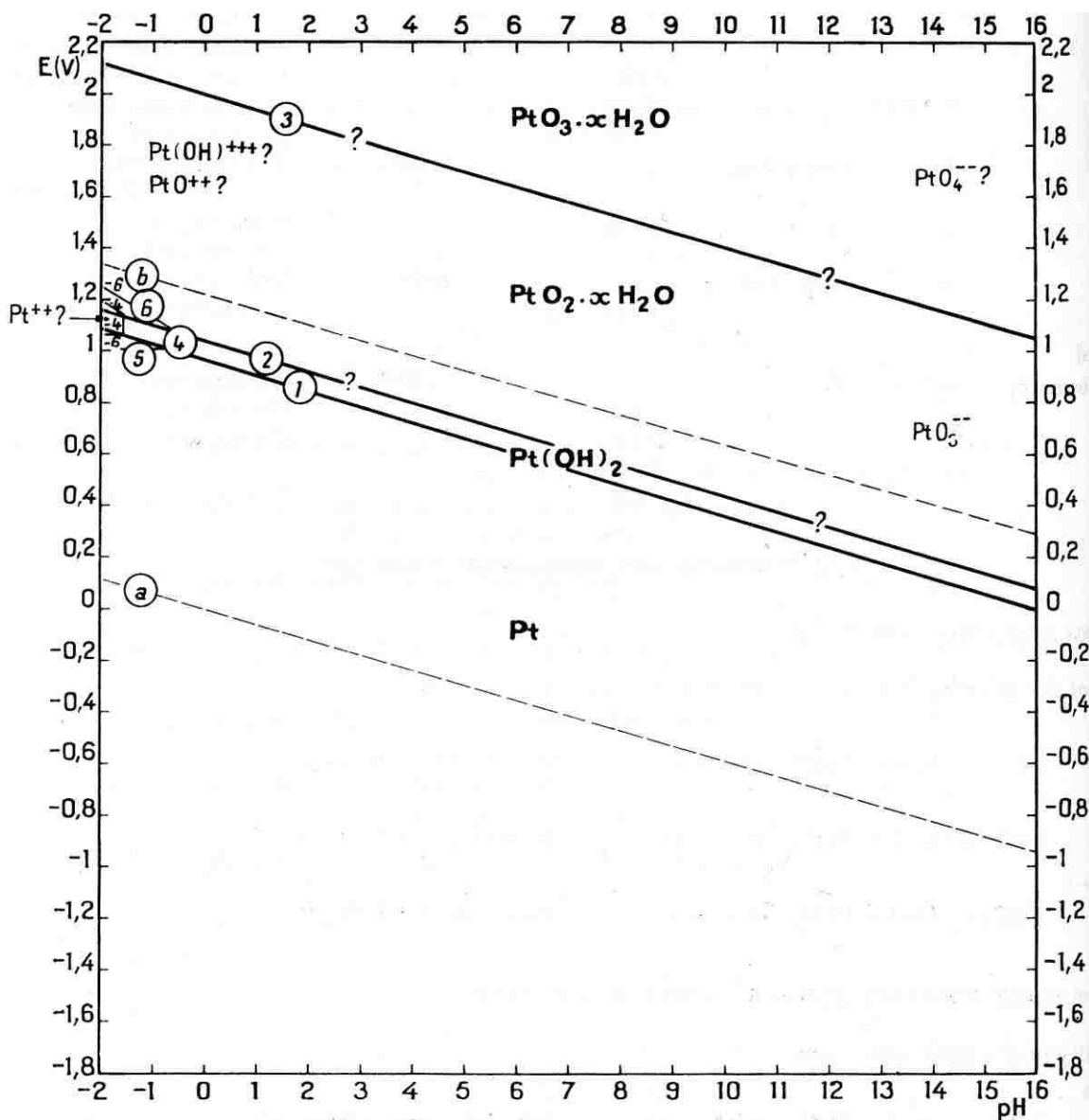


Figure 2.1: Potential-pH equilibrium diagram for platinum in water at 25°C ³⁵.

The state of the catalyst surface between (a) and (b) is of interest. In this range, platinum is largely metallic, which is a desirable property. Through interaction with the electrolyte, platinum can also form hydrides, oxides, and hydrous phases. During a Faradaic process, the composition of the catalyst/electrolyte interface can be simply described in terms of these charged species.

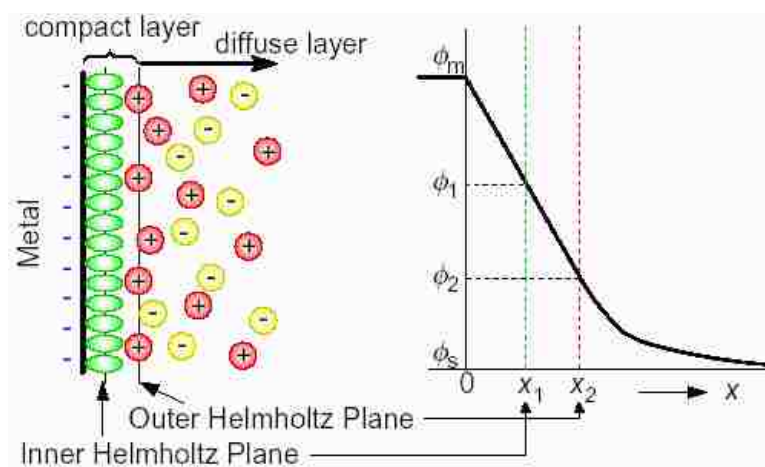


Figure 2.2: Helmholtz interpretation (simplification) of potential distribution from the surface into the bulk electrolyte ³⁶.

The Helmholtz model is a simple description of the change in potential across the interface from the polarized electrode to the bulk electrolyte. The charge which is externally applied to the surface of the electrode, ϕ_m , causes an opposing response from the electrolyte in the formation of a compact layer of charged H_2O molecules. In the case of a negatively charged catalyst, H_2O molecules will orient to bring their more positive hydrogen atoms into contact with the surface as opposed to negatively charged oxygen, and vice versa. The Inner Helmholtz Plane (IHP) passes through the center of these molecules. Ions from the solution will collect atop the IHP to form the Outer Helmholtz Plane (OHP). Beyond this plane and into the bulk electrolyte, positive and negative ions exist in a more homogeneous state. The IHP and OHP together form the electrical double layer, across which the potential drop ($\phi_m > \phi_{IHP} > \phi_{OHP} > \phi_s$) is a measurable phenomena. The actual interface is more complicated than the Helmholtz model describes due to a variety of ionic behaviors depending upon the system. Three fundamental processes which occur at the electrode-electrolyte interface are shown in Figure 2.3.

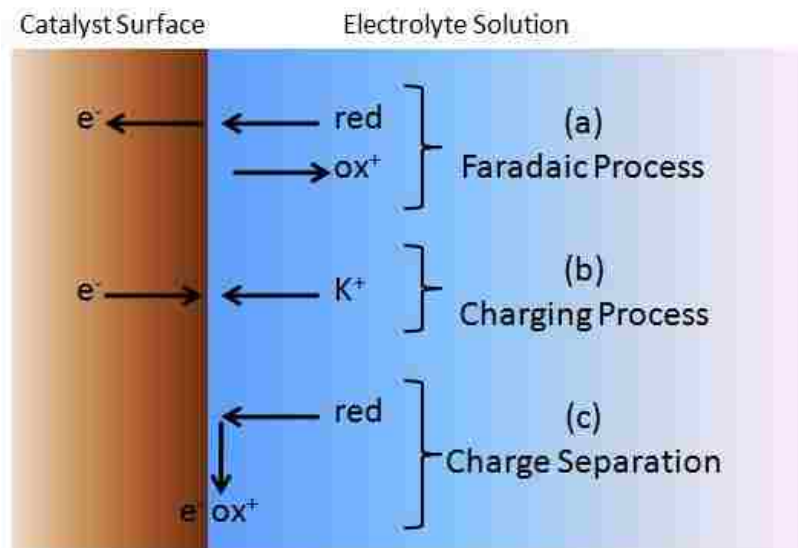


Figure 2.3: Fundamental electrode processes. Note that the Faradaic process (a) illustrates oxidation. (b) is applicable when K^+ cannot be reduced at the applied potential of the catalyst.

Ethanol oxidation and oxygen reduction reactions are Faradaic and contribute to the exchange current density. The double layer forms by a charging process which is apparent in most electrochemical measurements. Such measurements become more complicated when all three processes occur simultaneously. When an electrochemical experiment is designed so that it can be reasonably assumed that most of the electrode activity is from Faradaic reactions, the following equation can be used to quantify the mass activity on the electrode surface:

$$\text{Moles Reacted} = \frac{Q}{nF} = \frac{1}{nF} \int I dt \quad \text{Eqn. 2.4}$$

where I is a measured current taken in amperes, and Q is the cumulative current over time, or total charge passed across the electrode. This relation is the basis for many forms of electrochemical analysis.

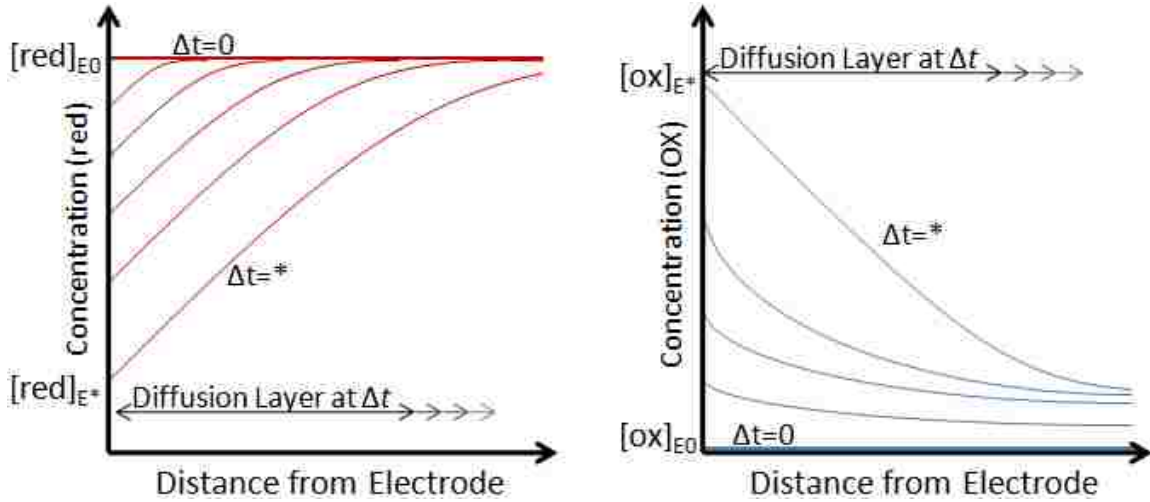


Figure 2.4: The changing concentration profile of oxidation and reduction species with time relative to the electrode surface.

When ethanol or a similar hydrogen-containing molecule is oxidized at the electrode, the concentration, $[red]_E$, will naturally decrease at a rate which is dependent upon the kinetics of the reaction as well as the diffusion of more ethanol from the bulk to the electrode. At the same time, the byproduct of EOR, $[ox]_E$, will begin to form at the electrode. At a constant current, linear concentration gradients will develop across a diffusion layer, the length of which begins at the electrode and ends at the point when both concentrations in solution stabilize. This diffusion layer represents the point at which the reaction becomes limited by mass-transfer. The time-dependent flux of reactant towards the electrode can be modeled as³⁷:

$$\varphi_E = A([red]_{soln} - [red]_{E*}) \left(\frac{D_{red}}{\pi t} \right)^{\frac{1}{2}} \quad \text{Eqn. 2.5}$$

where D_{red} is the diffusion coefficient of ethanol through the electrolyte. A is the area of the electrode surface. Two modifications can be made to relate this equation to Eqn.2.4. The current can be found by multiplying Eqn.2.5 by nF . In addition, under steady state

operation at constant current, the rate of the charge transfer reaction will become negligible compared to mass transfer. In this case, Eqn.2.5 can be written as:

$$I = nF\varphi_E = nF \left(\frac{D_{red}}{\pi t} \right)^{\frac{1}{2}} [red]_{soln} \quad \text{Eqn. 2.6}$$

2.2 Ethanol Oxidation in Alkaline Fuel Cells

Liquid electrolyte alkaline fuel cells (AFCs) are far more practical than those which use an ionomer, referred to as AMFCs. The latter type can operate at temperatures of 80°C, though are usually limited to 50-60°C due to instability of the membrane. Anion conducting membranes usually fail after several days of use and require aqueous KOH to maintain ion conductivity. This fact has traditionally made it difficult to manufacture reliable membrane electrode assemblies (MEA) for comparative studies against acid PEMFCs. Carbonate buildup at the cathode from interactions between CO/CO₂ and KOH is another problem which hinders AFCs and AMFCs.

These drawbacks are overlooked by researchers who recognize alkaline electrolyte as a more efficient environment for the oxidation of alcohols and other organic fuels^{38,39}. It is apparent from the anode process for ethanol oxidation of Eqn.1.7 that the forward reaction is favored in more basic environments. This would seem to be verified by the experimental observation using in situ spectroscopic techniques that ethanol appears to oxidize more completely to CO₂ on a Pt surface in alkaline media⁴⁰. Some researchers have noted that the kinetics of oxidation of organic molecules at the anode as well as the oxygen reduction reaction (ORR) are easier in KOH electrolyte⁴⁰⁻⁴². Others question the

idea of improved kinetics, citing a lack of clear evidence to this point. Instead, there is better evidence to show that the alkaline environment is less corrosive towards catalyst metals and that less poisoning occurs due to the easier oxidation and removal of impurities⁴³. This allows for the use of a wider variety of metals on the electrode, such as nickel⁴⁴, iron or aluminum⁴⁵ that would otherwise dissolve into solution at certain potentials. Though the most active catalysts in AFCs still use Pt and Pd⁴⁶, many other transition metals have been shown to enhance EOR and ORR activity by altering the electronic structure of noble metal binding sites⁴¹ or forming oxides which allow oxygen species to form in proximity of bound ethanol and subspecies⁴⁷⁻⁵¹.

2.3 Catalyst and Support Durability

At the anode, the current state of the art utilizes decorated nanoparticles of PtRu alloy supported on high-surface-area carbon blacks⁵². It is generally believed that the improved fuel oxidation and enhanced resistance to CO poisoning seen with PtRu is a result of the bifunctionality of the material^{18, 53}. Carbon blacks have traditionally been used as the catalytic support for PtRu due to their excellent electronic conductivity and high surface areas ranging from 150 to 1200 m²/g. The outer surface of the most commonly used carbons is graphitic with a low degree of oxidation, whereas the interior remains amorphous and especially susceptible to corrosion^{54, 55}. There are three primary means of failure of carbon as a catalytic support. The first develops from percolation effects in the conductive carbon matrix as the material shifts and its simple morphology is unable to maintain as many points of electrical contact among particles, resulting in ohmic losses. Because carbon does not interact with the catalyst, kinetic losses also occur when platinum particles agglomerate and migrate around and off of the support surface,

leading to sintering and loss of catalyst/support contact. Consequently, platinum and ruthenium have been shown to detach from the carbon and migrate across the ion exchange membrane⁵⁶⁻⁵⁸. Finally, carbon forms surface oxides that create a hydrophilic interface and lead to flooding of the support, ultimately hindering fuel flow to the catalyst. Carbon supports do not participate in the catalytic oxidation/ reduction reactions and offer low stability, leading to degradation of the fuel cell. For these reasons, noncarbon supports are being explored as an alternative. Transition metal oxides possessing variable oxidation states are one class of noncarbon material that offers promise as electrocatalyst supports because of the generally superior stability, and reasonable electrical conductivity associated with substoichiometric oxides. This class of materials for electrocatalyst supports has been recently reviewed⁵⁹. One challenge with these materials is the need for the oxide to be partially reduced to provide electronic conductivity while maintaining high surface area⁶⁰. In some cases, incorporating a second oxide element, such as Nb into titanium oxide^{61, 62}, can enhance electronic conductivity. Alternatively, small to moderate weight percents of metal oxides supported on carbon have also been implemented as pseudo supports for catalyst^{18, 63}.

Niobium oxide, when modified to enhance electrical conductivity, is one of several potentially suitable materials for replacing carbon as a catalytic support in membrane fuel cells^{61, 64}. Literature has shown that niobia can play a complementary role in the catalysis of oxygen reduction^{62, 63}, hydrogen oxidation⁶⁵, and methanol oxidation^{18, 61}, wherein Pt activity is enhanced depending upon the form and quantity of the metal oxide. The design requirements of alternative electrocatalyst support materials are rigorous. A competitive replacement must have a reasonably high surface area, exhibit a degree of catalyst

stabilization, have minimal gas transport resistance, be electrically conductive, and have the proper balance of hydrophobic surface chemistry so as to avoid inhibiting levels of hydration.

2.4 Theory of Pt and Pt-Alloys

Platinum is an excellent oxidation catalyst because of its crystalline surface structure and moderate adsorption energies with CO_x, H₂ and O₂ due to the element's noble electronic structure. This concept is described by the Sabatier Principle⁶⁶. While the energies of sp-band electrons are relatively stable across the periodic table⁶⁷, those of d-band electrons in transition elements vary considerably and are responsible for the improved catalytic performance of platinum-group metals compared to others. D-bands are localized closer to the Fermi level, which can make them well suited for bonding in addition to exhibiting conductivity from an occupied valence band. An optimum catalytic rate occurs when the surface-bond strength is rate limited neither by the dissociative adsorption or by desorption of by-products. Of course, real systems are biased toward one or the other. This bias can be visualized using volcano plots which compare the adsorption energy of a species onto a surface relative to the d-band center of that surface.

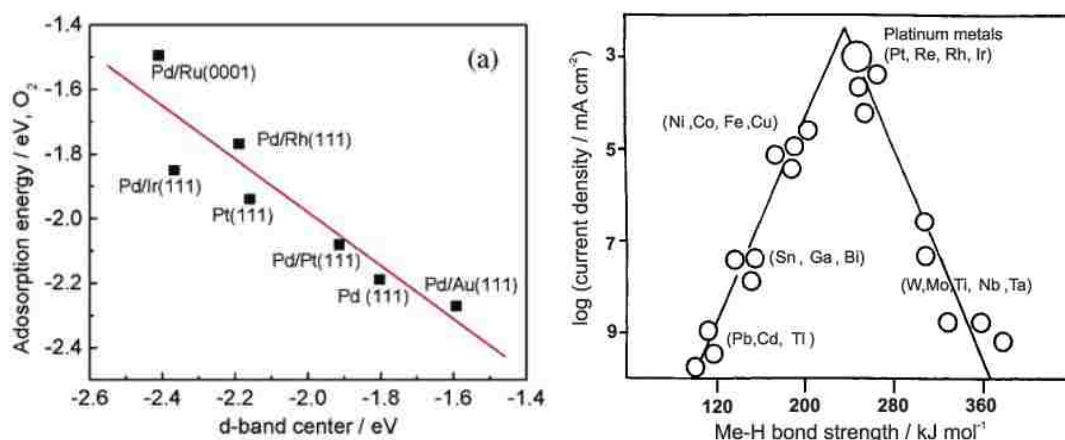


Figure 2.5: (Left) DFT calculated adsorption energies of O_2 as a function of d-band center energy from E_{Fermi} on altered noble metal surfaces ⁶⁸. (Right) Volcano-type relationship between the rate (current) of the methanol oxidation reaction versus the binding energy on different transition metals ⁶⁹.

Nearly full d-orbitals result in a stable atom which is better able to form bonds strong enough to hold an intermediate at the surface for the duration of the reaction, and weak enough to release the product when the reaction is complete. In the case of methanol oxidation, binding with Pt lowers the activation energy necessary to break the O—H and C—H bonds. This occurs as CH_3OH approaches the Pt surface and begins to interact with the broad sp-band (lower energy) at the surface, which lowers and broadens the energy of the sp-bands of the methanol. The molecule also interacts with the Pt d-band (higher energy near E_{Fermi}). This dual-orbital interaction causes the shared electrons of O—H to split into bonding (low energy) and anti-bonding (high energy) orbitals. If the latter is occupied by electrons, then the internal bonds within the molecule weaken, leading to dissociation ⁷⁰. The hydroxyl hydrogen is the first bond to break, followed by the remaining hydrogen bonds from carbon. The molecule dissociates as methanol > methoxy intermediate > formaldehyde >> CO. The same mechanism is not effective for the C—O bond which becomes more stabilized, contributing to CO/Pt poisoning. The

ethanol oxidation reaction is more complex than that of methanol, but the activation energy of splitting the same C—O group is comparable⁷¹⁻⁷³. Pt-group alloys, such as PtRu and Pt₃Sn, and other intermetallic compounds are an attempt to fill the spaces between elements in a volcano plot and obtain the most desirable binding energies for a specific reaction^{67, 74-76}.

The specific structure of the d-band of a Pt atom depends upon its coordination number as well as the atomic spacing. The Pt(111) surface is recognized as the most catalytically active due its close-packed structure. The optimal size of Pt nanoparticles is between 2-5nm diameter, after which there is no gain in active surface area or exposure of Pt(111) from dispersion. But this size also implies a ratio of surface and edge atoms which exhibit different binding energies. An edge atom with a low coordination number will compensate by forming stronger bonds with adsorbates. Therefore, stronger binding will occur on the less dense Pt(110) face than on Pt(111), while the latter exhibits the fastest kinetics. This behavior illustrates reactions which proceed with varying degrees of structure sensitivity. In a PEMFC with electrolyte of pH similar to that of typical Nafion, hydrogen will preferentially adsorb/desorb on Pt surfaces at different operating voltages (potentials): 0.35-0.45V on Pt(111), 0.3-0.4V on Pt(100), and 0-0.2V for Pt(110)⁷⁷. Pt-alloys and homogeneous intermetallic compounds are ideally designed with a modified electronic structure specific to the anode or cathode reaction of species anticipated to be present in a system. The design of new, more effective electro-catalysts for the ethanol oxidation reaction must be approached in this way.

2.5 Niobia for Alcohol Oxidation or Oxygen Reduction

There has been some disagreement in the literature about the catalytic nature of niobium/niobia and whether it is best suited for alcohol oxidation or oxygen reduction. The question is hardly as simple as this because niobia can be implemented in different oxidation states, amorphous or crystalline morphologies, and in various amounts with other metals. Conventional PEMFCs utilize platinum at both electrodes which is problematic when fuel crosses the membrane and is able to adsorb and oxidize at the cathode. Although crossover issues seen with hydrogen and methanol should be less with a larger molecule like ethanol, the overall cell potential would be improved if the electrodes were intrinsically different to suppress the primary reactions of one from occurring on the other. Therefore, it is important to identify the primary functionality of niobia as a bi-functional electrocatalyst. Nb(V) is the most representative form to consider due to the instability of more reduced forms in the presence of aqueous electrolyte.

Fuel cells are usually limited by the kinetics of oxygen dissociative adsorption onto Pt at the cathode. The cathode is more sensitive to ionized species derived from the aqueous electrolyte than is the anode. At the anode, adsorbed HO^- surface species can assist in the oxidation of alcohol intermediates. But this same species at the cathode acts as a major inhibitor of O_2 adsorption. Reduced forms of niobia at the cathode would ideally donate electrons to Pt in order to weaken its binding energy with undesired hydroxyls.

Alternatively, more oxidized niobia at the anode might help oxidize neighboring Pt and adsorbed intermediates to exhibit a similar effect. It is known that the niobia surface is acidic in aqueous electrolyte by the formation of $\text{Nb}_2\text{O}_5 \cdot n\text{H}_2\text{O}$ species. It is not clear

whether HO^- species would spillover from niobia on the Pt surface, or if hydroxyls on the more noble Pt surface would react to form H_2O from a similar spillover effect. The prevalence of one effect over the other is highly circumstantial. Pourbaix diagrams can be used to approximate the stable niobia species present in different electrolyte conditions. But nano-particle or nano-structured niobia likely exhibits behavior which deviates from such figures. Experimental or computation studies are required to examine the binding energies in each case and begin associating the properties of niobia with either electrode.

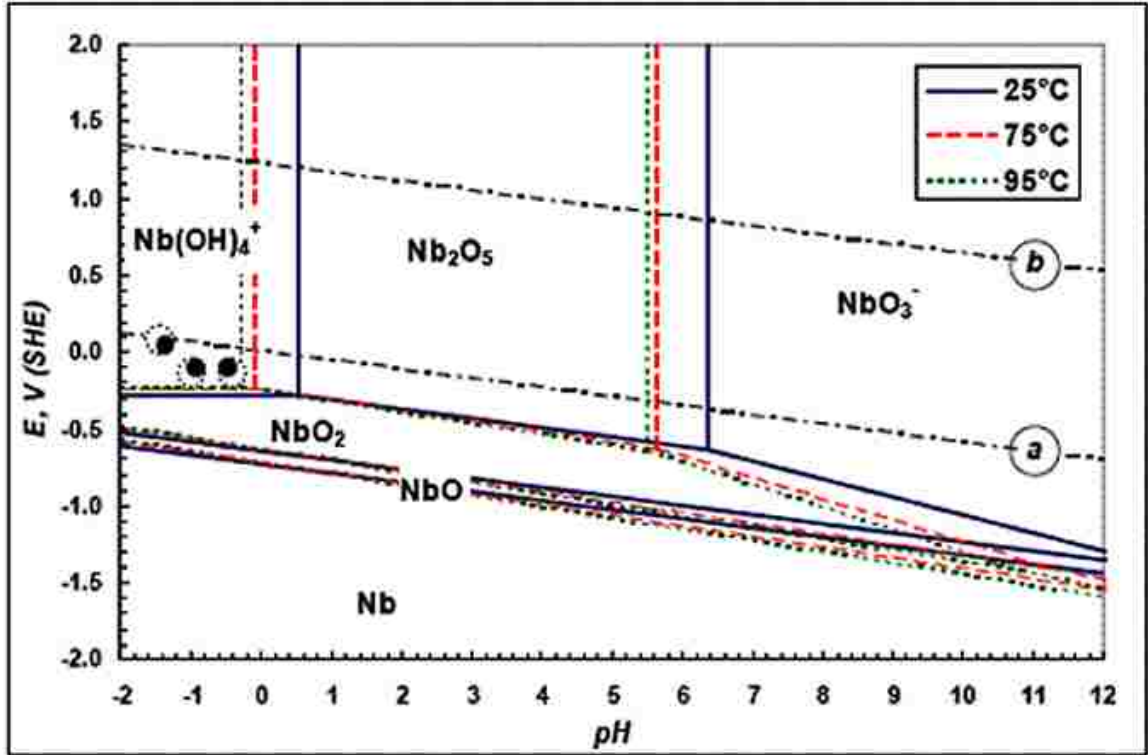
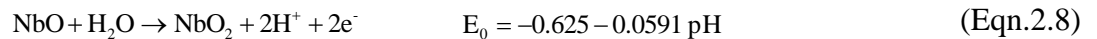
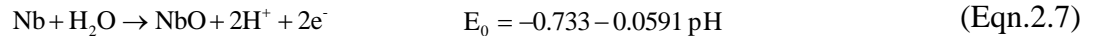
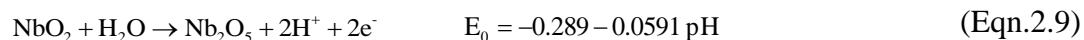


Figure 2.6: Pourbaix diagram for niobium showing the equilibrium species in an aqueous environment of varying pH and potential (V) at 25°C, 75°C, and 95°C⁷⁸.





Equations 2.7-2.9 demonstrate that Nb(V) is the dominant form of niobia at cathode and anode potentials, 0-1.2V. Though Fig.2.6 shows how niobia at the charge transfer interface on an electrode can be influenced by temperature, possibly to stabilize perniobate species that could lower the barrier to CO oxidation.

Another important property relating to the sensitivity of the cathode comes from the fact that dissociative adsorption is more complex than adsorption followed by decomposition. The former requires availability of adjacent surface sites with partially filled d-orbitals which exhibit a long bonding radius. Platinum and other 5d elements are best at meeting this last criterion, whereas the orbitals of 3d elements are generally too small. This rule is relaxed somewhat in electrolyte of higher pH, which is why a wider range of transition metals may be catalytically active in an alkaline environment. Niobia is a 4d element, and is not clearly suited to either electrode by this standard.

CHAPTER 3 - Problem Statement

The efficient electrocatalytic oxidation of ethanol requires the use of more carefully considered composite catalysts tailored for the specific environment of interest. This research seeks to develop aerosol synthesis routes with promising alternative metals and metal-oxides that could be used to form alloys or intermetallic compounds with platinum as catalysts tailored specifically for the ethanol oxidation reaction. Due to its relative stability at high temperatures and in corrosive environments, niobia is of interest to supplant carbon as a support material. It can also improve upon carbon with the added benefits of a stabilizing strong metal support interaction (SMSI) with Pt nanoparticles and multivalent oxide compounds which could lower energy barriers associated with oxidizing adsorbed Pt surface species.

- **Objective 1:** *Experiment with the aerosol spray pyrolysis system to identify a stable surfactant/solvent/metal precursor system using niobium as the primary metal.*

The bench-top spray pyrolysis system will be refined for synthesis of intermetallic niobia compounds also utilizing promising transition metals previously identified. The synthesis process will utilize block co-polymer surfactants to impart a porous mesostructure into the metal oxide matrix. The large surface area which results will enhance mass transfer characteristics and maximize the number of accessible reaction sites.

- **Objective 2:** *Develop a protocol for quickly testing the conductance of bulk powders which can be used to ascertain their suitability as an electrode material.*

A device which measures the conductance of bulk powder (500mg or less) will be constructed. Synthesized intermetallic compounds will be compared against commercial powders of other conductive materials typically found in conventional electrodes, including carbon XC72, Ru/RuO₂, NbO₂, and Nb₂O₅ to establish an acceptable level of conductance.

- **Objective 3:** *Synthesize an electrically conductive intermetallic compound primarily composed of niobia with a nanostructured network of pores 4-7nm in diameter.*

The entire synthesis process, including the bench top spray pyrolysis apparatus as well as additional post processing steps, will be refined to produce 1g or more of conductive powder of consistently homogeneous composition. An emphasis is placed on engineering porous nanostructures using templating surfactants to attain high surface area morphology, as only surface atoms directly lend themselves to electrocatalytic activity. Both chemical and thermal post-processing steps will be evaluated until a powder of this description based upon niobia is obtained.

- **Objective 4:** *Achieve highly dispersed platinum on the surface or within the matrix of the intermetallic support.*

A variety of techniques will be explored for the deposition of platinum onto mesoporous niobia mixed-metal-oxides. These will include in situ formation of Pt nanoparticles on the metal-oxide matrix during spray pyrolysis, wet and dry impregnation methods in which varying amounts of Pt dissolved in solution is dried on the support, and galvanic electrochemical deposition. Materials which

successfully meet all of the aforementioned criteria will undergo basic electrochemical analysis for EOR.

- **Objective 5:** *Achieve a catalyst which catalyzes the total oxidation pathway of the ethanol oxidation reaction.*

Half cell cyclic voltammetry, as well as in situ electrochemical FTIR will be used to monitor the adsorption and formation of species on the catalyst surface correlated to the time-dependent potential of a polarized electrode. The potential and relative concentration of evolving species provides evidence which will be used to describe the reaction mechanism of EOR in the context of the bi-functional effect.

- **Objective 6:** *Elucidate the nature of the catalyst's EOR performance and characterize and improve upon the stability of the catalyst in the electrochemical environment.*

Half cell analysis, including ex situ electron microscopy methods, will be used to study the degradation behavior of platinum supported on niobia-based oxides at the operating potential limits of anode and cathode conditions. Mechanisms of support and catalyst degradation will be compared to that of Pt supported on carbon. Half cell experiments using acid and alkaline electrolyte allow for more comprehensive comparisons to other literature studies.

Computational Density Functional Theory will be used to model the interface of Pt(111) with common species encountered in a PEMFC utilizing niobia supports. These species include C, O₂, H₂, Nb, and similar compounds. These studies will be

used to determine the binding energy and better explain the state of the Pt(111) surface.

- **Objective 7:** *Recommend a continued direction of research for the primary objective beyond the scope of the dissertation.*

Once a stable catalyst system has been developed, alternative pore-templating techniques will be pursued using similar precursor chemistry. Low temperature aerosol synthesis will result in amorphous materials for many transition metal oxides. Crystalline materials achieved by heating to temperatures above 500°C will be explored for the potential to better stabilize reduced oxides in aqueous environments. Specifically, porous structures will be achieved using silica-based templates which are stable at 900°C or higher.

CHAPTER 4 - Experimental Methodology

4.1 Spray Pyrolysis Reactor System

Spray pyrolysis (SP) is a versatile synthesis approach capable of producing spherical, mesoporous oxide particles that, when incorporated into a well-engineered electrode architecture, could provide an attractive electrocatalyst support system. In particular, SP is well-suited to effectively utilize evaporation induced self-assembly (EISA) of amphiphilic templates to synthesize mesoporous materials with controlled pore size and mesostructure and relatively high internal surface area⁷⁹⁻⁸¹. The purity, composition, and uniformity of precursor solutions for SP are highly controllable, and that control is also reflected in the properties of aerosol droplets produced from the solution^{82, 83}. Each

droplet within such an aerosol can be viewed as an independent microreactor with homogeneously mixed components and minimal internal diffusion resistance³¹. Total reaction time is relatively short in SP reactor systems, usually in the range of seconds or tens of seconds. SP also has excellent potential as a scalable process.

Products of a particular composition can be collected as a powder or as a film deposited onto a substrate, shown in Fig.4.1. Individual particles of a powder can form a variety of different morphologies depending upon temperature, composition, and energy of vaporization and crystallization of subcomponents.

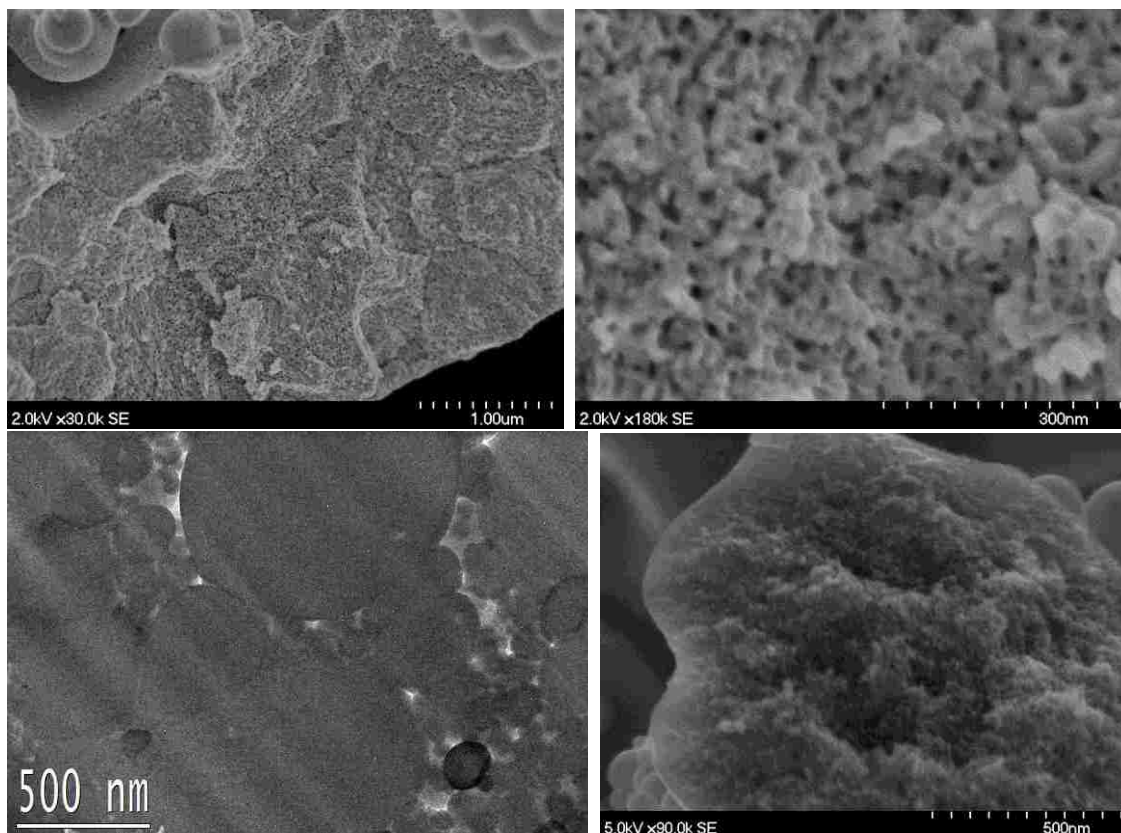


Figure 4.1: (Top) Mesoporous Nb₂O₅ film deposited as a film after SP processing at 190°C followed by post treatment at 400°C to remove P123 surfactant. (Bottom Left) Cross section of 60%Pt/Nb₂O₅ powder which has been pressed into a film at 5,000 lb/in². (Bottom Right) Fractured particle of mesoporous Nb₂O₅ synthesized by SP at 200°C showing a precipitation layer at the outer edge.

Porous films can be achieved in two primary forms by spraying directly onto a substrate. The reactor temperature can be held slightly lower ($\sim 10^{\circ}\text{C}$) than the thermal decomposition temperature of the precursors so that approaching particles coalesce into an indistinguishable layer which is then calcined in air at the appropriate temperature to remove the employed surfactant. Alternatively, higher reactor temperatures allow each particle to maintain a spherical shape. After deposition, the sample can be calcined at temperatures appropriate to induce sintering of the particles into a solid structure, or the powder can be pressed at high pressure using an appropriately shaped die.

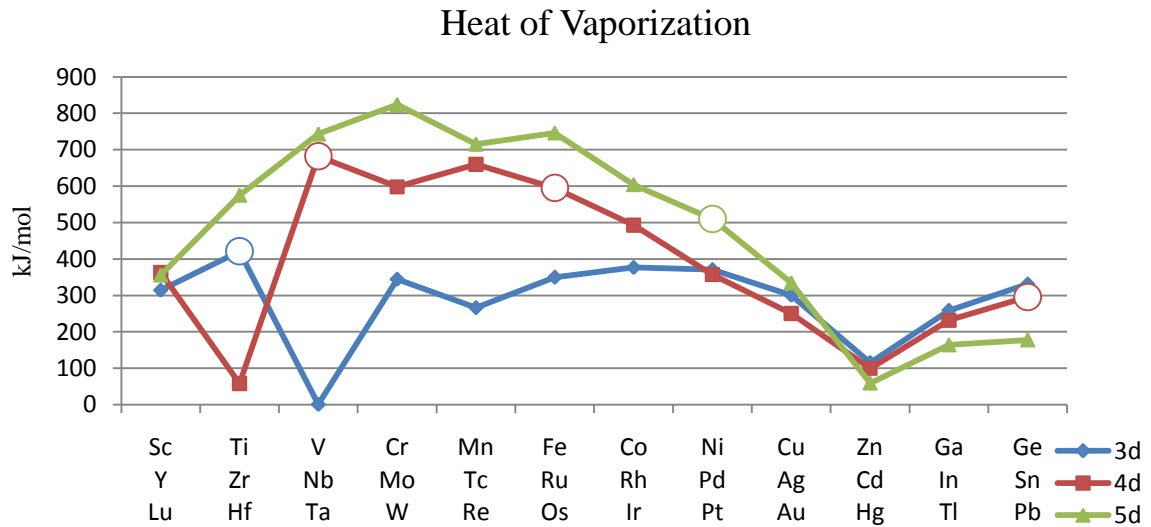


Figure 4.2: Heat of vaporization. Open circles mark especially relevant elements considered in this study.

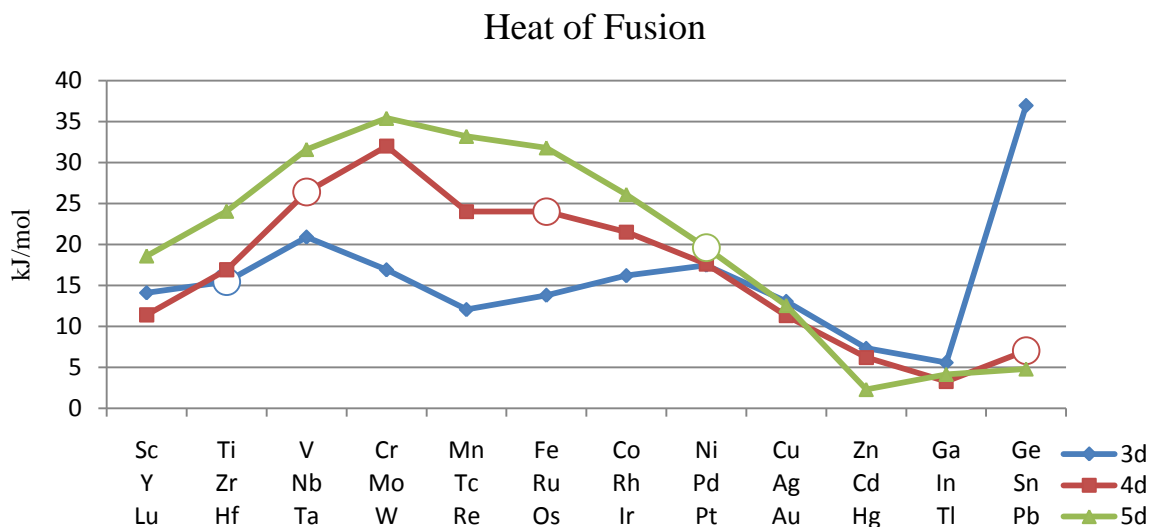


Figure 4.3: Heat of fusion. Open circles mark especially relevant elements considered in this study.

Synthesis of intermetallic compounds containing one element which is only weakly soluble in the other at ambient conditions is usually achieved by heating to extremely high temperatures of 800°C or greater or through high pressure extrusion processing⁸⁴. Homogeneous intermetallic compounds from volatile precursors would be extremely difficult to obtain in an aerosol process at such temperatures, and the mesostructure is easily compromised at high pressures. To obtain intermetallic compounds at lower temperatures, it is necessary to choose precursors with similar volatility and reactivity in cases when the precursors exhibit significantly different heats of vaporization. For example, some species such as ruthenium become more volatile as they are increasingly oxidized, $\text{Ru} < \text{RuO}_2 < \text{RuO}_3 < \text{RuO}_4$ ⁸⁵⁻⁸⁷. The same is true of Pt-oxides, which can form a vapor phase in an oxygen atmosphere, or mobile atoms/clusters restricted to surface migration in H_2/N_2 atmospheres^{88, 89}. However, a chloride precursor of the same base-metal can be considerably more stable. $\alpha\text{-RuCl}_3$ is not volatile until temperatures above

600°C⁹⁰. An optimal SP system will utilize precursors with similar thermal properties designed to induce thermal decomposition of all components to achieve co-precipitation shown in Fig.1.7.

The bench-top SP system used for the materials described in this work is represented in Fig.1.6. The atomizer is of the collision type (TSI model 3076). The drying zone is exaggerated in the figure to emphasize that most of the solvent evaporation modeled by Eqn.1.8 will occur in the piping leading from the atomizer to the furnace, or shortly after entering the heating zone. The result of this effect is the formation of structured surfactant (3D wormhole type) within the droplet (just before or after the entrance of the heating zone) before thermal decomposition of metal precursors begins farther downstream into the furnace. If the thermodynamic shift of surfactant structure formation were to occur at temperatures much greater than the ambient, the motion of the surfactant would augment the overall fluidity of material throughout the droplet, especially when ~50% of the droplet volume is occupied by surfactant. This would lower the diffusion barrier across the droplet radius for all components, allowing especially volatile reactants to segregate. Upon cooling, these phases condense on the particle surface to form a decorated surface type structure through a process of successive co-precipitation (if liquid intermediate phase exists) or nucleation, seen in Fig.1.7. Useful catalysts exhibiting a bi-functional effect for the ethanol oxidation reaction are expected to result from intermetallic compounds⁴⁶, which is why the reaction process must be carefully considered and designed to avoid the type of component segregation of more volatile components described here.

The processes occurring in the reactor are described in the following steps for Nb, Ru, and Pt chloride precursors:

1. Metal chloride precursors (NbCl_5 , RuCl_3 , $\text{H}_2\text{PtCl}_6 \cdot 6\text{H}_2\text{O}$) and surfactant (P123) are dissolved in an ethanol/water solution in a container and stirred until well mixed. The container is then attached to a collision aerosol generator.
2. An inert gas, N_2 , is fed into an inlet on the aerosol generator (atomizer) at 30psi. The gas passes through an orifice, causing an increase in velocity. This results in a pressure decrease in a tube downstream of the orifice. The effect draws solution from the container (Bernoulli effect).
3. Aerosol flows from the atomizer into a horizontal tube furnace set at 220°C . Most of the solvent has evaporated shortly downstream of the furnace entrance.
4. The aerosol is comprised of droplets which absorb ambient heat up as they travel down the furnace. Each droplet contains stoichiometric amounts of solvent, metal chlorides, and P123 surfactant relative to the original precursor solution. One end of the linear P123 molecule is more soluble in solution. As solvent evaporates, these like ends stick together, eventually forming 3D organic scaffolding within the $\text{Pt/NbRu}_y\text{O}_z$ bulk. Afterwards, the heat causes metal chlorides to decompose into HCl , Cl_2 gas, and dry metal oxide particles (formerly droplets) containing the structured P123 surfactant.
5. Particles are collected on a filter at the end of the furnace, while N_2 , vaporized solvent, and chlorine byproducts pass through the filter into an exhaust filtration system. Collection rate varies from 0.1 to 3g per hour for the bench top SP system.

The relatively low temperature of the furnace provides just enough heat transfer to droplets so as to thermally oxidize the chloride precursors without substantial vaporization of volatile ruthenium. Surfactant removal requires higher temperatures.

6. The particles are heated to 400°C at 5°C/min, a much slower rate than that imparted to the aerosol upon entering the furnace (~12500°C/min). Oxygen from the metal-oxide surface reacts with surfactant to form volatile CO_x species which are carried away in a flowing gas of 10% H₂/N₂. Surface oxygen removal, along with the flowing hydrogen, simultaneously reduces the metal oxide to a lower oxidation state, held stable to various degrees by the formation of metal-metal or shared metal-oxygen-metal bonds.
7. P123 surfactant byproducts enter the exhaust filtration system.
8. Remaining mixed metal-oxide particles have a mesoporous structure resulting from the voids left by the P123 surfactant.

4.2 Conductance Testing

Conductivity is a necessary requirement for electrode materials to efficiently pass electrons with minor loss to heat generation. Graphitic carbon exhibits excellent conductivity across planar networks of pi-bonds connecting carbon atoms. Once the carbon is oxidized, these electrons are locked in the hybrid band of the C—O bond at a lower energy with a greater band gap. Only electrons occupying the conduction band can move freely across atoms. The band gap is the energy barrier necessary to activate this electron mobility through some form of excitation. The process is directly related to the way in which materials exhibit color properties, or photon responses to excitation by

visible and non-visible electromagnetic radiation (EMR). A conductive material like graphite will have a very small band gap, and a proportionally minor transmission (reflection) of EMR excitation, i.e. conductive materials will appear to be darker than semiconducting or insulating materials.

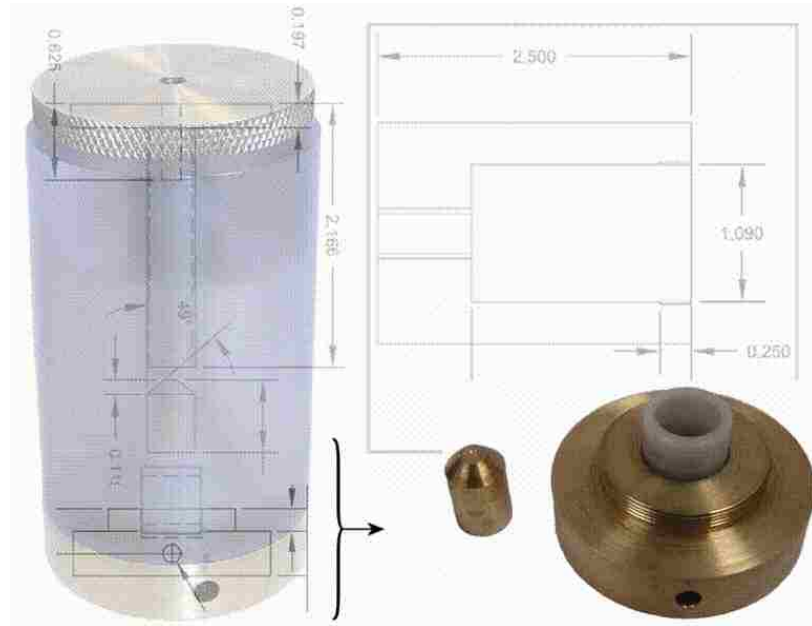


Figure 4.4: Imposed photo and schematic of the compression-conduction device used to test powders synthesized by SP.

Therefore, powders produced by spray pyrolysis which are lighter in color are not feasible electrode materials. Post-SP thermal reduction of these powders in hydrogen gas can reduce some materials to a conductive state, which may be reversible upon exposure to the oxygen in open air. It is also possible for atoms near the surface to reduce, resulting in a dark appearance, while those in the bulk remain oxidized. To adequately determine the true conductance of various powders, a compression-conductance device was fabricated from brass. A measured amount of powder is placed into a small cavity inside a base-plate. A small, fitted insert is placed over the powder into the cavity. The

base-plate is then affixed into a plastic, cylindrical housing with contains a variable height, brass hammer at the opposite end. The hammer and base-plate are each connected to a resistance-meter. As the head of the hammer is rotated, complimentary threading in the housing moves the hammer towards the base-plate until a complete electrical circuit is formed. As the pressure is increased between contact points, the bulk-density of the powder decreases while intra-particle contact points increase, improving conduction. The resistance can be simultaneously measured. For materials of similar composition, this test provides a reliable comparison of conductance [Ω^{-1}] between different samples and is more expedient than measuring true conductivity [$(\Omega\text{-cm})^{-1}$]. Some results for Ru/RuO₂ are shown below:

	RuO2 at 150		RuO2 at 250		RuO2 at 350
Weight (g)	0.0003	Weight (g)	0.0003	Weight (g)	0.0003
Touch (1/ Ω)	0.0353	Touch (1/ Ω)	1.25E+001	Touch (1/ Ω)	1.25E+001
Press (1/ Ω)	10.0000	Press (1/ Ω)	1.25E+001	Press (1/ Ω)	1.25E+001

Figure 4.5: Example effect of reduction temperature on conductance using Ru/RuO₂.

“Touch” represents the first reading at which electrical contact is made, while “Press” represents compaction of the powder. Ruthenium which was reduced at higher temperatures exists in a more metallic state, resulting in higher conductance values.

Powders which did not exhibit similar values to those shown here were not considered for further electrochemical testing.

4.3 Structural and Compositional Analysis

4.3.1 Electron Microscopy (EM)

Scanning electron microscopy (SEM) and transmission electron microscopy (TEM) provide visual means of examining the particle size distribution, micro-structure, and homogeneity of a powder. Both techniques probe a sample using an accelerated beam of electrons. SEMs detect electrons which are scattered off of the sample surface at different angles from a beam accelerated at 2-20keV. A TEM beam is accelerated at 100keV-300keV and detects electrons which pass through the sample. The resulting image depicts the silhouette of a cross section from within the sample's depth corresponding to the point at which the beam is focused. The technique requires very small amounts of a sample compared to other characterization methods. TEM, in particular, can provide a great deal of information in addition to external morphology. The ordered atomic structure of crystalline samples will diffract electrons to form a pattern which can be analyzed to determine lattice structure, as well as single crystal or poly-crystalline nature. The high spatial resolution (0.2nm) of TEM allows for analysis of individual nanoparticles apart from the surrounding material. Elemental analysis due to sample excitation from the electron beam is also discussed. TEM requires that samples be sufficiently thin so as to allow enough electrons to pass through to provide detectable contrast. In both techniques, the sample chamber is under vacuum. Highly conductive samples can partially absorb some of the electron beam resulting in sporadic electron emission. This is known as charging, and can lead to apparent drifting of the sample from the detector's frame of reference. In this study, both EM techniques serve as a primary means of materials characterization.

4.3.2 Elemental Analysis (EDS & EELS)

Elemental analysis is a useful subcomponent of EM which benefits from the high detection resolution, allowing a user to distinguish between nano and micro-sized areas of a sample. A material which is exposed to an electron beam will emit x-rays as an excitation response, the energies of which are characteristic of individual elements within the sample. The detection and measurement of these x-rays is known as energy-dispersive spectroscopy (EDS). The penetration depth surveyed depends upon the accelerating voltage of the beam, but is typically limited to $\sim 1\mu\text{m}$. Elements present at concentrations below 1% or of mass below carbon ($Z < 12$) are undetectable. The resolution limits in the plane orthogonal to the electron beam are usually about 800nm and 50nm for SEM-EDS and TEM-EDS, respectively.

When electrons from the higher energy beams employed in TEMs pass through the sample, many are inelastically scattered, resulting in an energy loss. The reduced energies of scattered electrons will also be characteristic of specific elements and can be quantitatively measured. This technique is known as electron energy loss spectroscopy (EELS). More powerful electron beams allow for the excitation of higher energy orbitals closer to the atomic nucleus.

EDS and EELS are both useful for elemental analysis of different regions inside a single frame of reference. EELS will tend to allow for better spatial resolution because electrons travel a more direct path through the sample, whereas a significant amount of x-ray scattering occurs throughout a volume within the sample bulk before traveling towards the detector.

4.3.3 X-ray Diffraction Spectroscopy (XRD)

XRD utilizes a monochromatic x-ray emission source to probe a sample in an attempt to identify crystalline structures from diffracted x-rays. The incident angle of the beam relative to the plane of the sample begins at $\sim 10^\circ$ and is increased at a steady rate sufficient to obtain a high number of counts at each point. The number of counts at any particular angle can be correlated to the known x-ray wavelength from the source to determine the lattice spacing of a crystalline structure according to the Bragg equation. When a “Bragg angle” is reached, x-rays will diffract in a coherent manner, resulting in an increase in the magnitude of x-rays reaching the detector. In a plot of Counts vs 2θ (Bragg angle), this will result in peaks of various aspect ratio depending upon the distribution of crystallite sizes. Amorphous materials will result in low detection, and a steady baseline decrease in signal with increasing angle absent of any features. Detection limits vary with materials, the source emission, and detector quality. Because platinum exhibits a distinct pattern and crystallizes by 200°C , it can be a simple matter to identify changes in its structure due to modification by other elements.

4.3.4 X-ray Photoelectron Spectroscopy (XPS)

XPS utilizes an x-ray source to irradiate a sample surface and induce the emission of photoelectrons with energies (eV) characteristic of the elements within the sample. Specifically, UNM operates a Kratos Axis Ultra XPS with a monochromatic Al KR (1486.6 eV) source running at 300 W. This approach is especially useful for complex, intermetallic compounds because small shifts from the expected emission energy for a pure element indicate chemical bonding with other elements. The probing depth depends upon the mass of the sample and the incident angle of the beam, usually between 3-10nm.

For powders consisting of nanoparticles, XPS can be taken as a bulk-measurement technique which can yield relevant information about the oxidation state of platinum nanoparticles and any accompanying metal oxides.

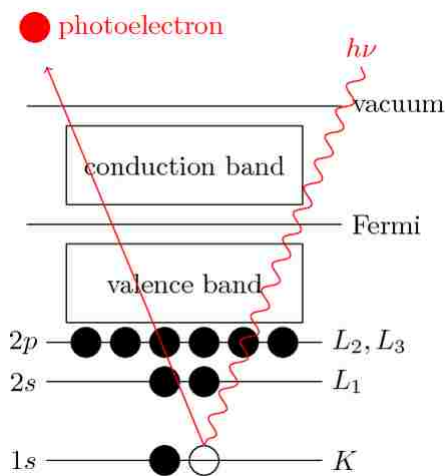


Figure 4.6: Incident x-rays excite core electron levels causing the ejection of photoelectrons with elementally specific, measureable kinetic energies.

Limitations include the shallow sample penetration of the low energy x-rays, the need for larger sample areas with diameters on the order of several millimeters, and sample compatibility with ultra-high vacuum conditions. The last limitation is rarely a problem with metal and metal-oxide powders unless degassing of the sample occurs to any significant degree inside the chamber, or if one wishes to study the properties of a surface under any significant atmosphere. Otherwise, XPS also offers a great deal of additional versatility in which the sample can be simultaneously imaged, or ion sputtering can be used to bore into the sample and increase the x-ray penetration to perform elemental depth profiling. It is a vital technique to understand how different transition metals are affected by the presence of one another as well as carbon contaminants. By using XPS to

ascertain the nature of the electronic structure of composite catalysts, the electrocatalytic can be better understood.

4.3.5 X-ray Absorption Spectroscopy (XAS)

XAS is a technique in which a monochromatic beam of incident x-rays bombards a sample while the absorption of transmitted x-rays from the sample is measured. The energy of the beam is steadily increased ($\sim 10^3$ - 10^4 eV or more) until core electrons within the sample are suddenly excited to a higher level. When this occurs, significantly more incident x-rays are absorbed, resulting in a spike in the measurement called *edges*. This region of the data is known as X-ray Absorption Near-Edge Structure (XANES). The energies at which edges occur are unique to different elements as well as the particular electron core level experiencing excitation. The shape and energy-shift of an edge relative to that from a neutral (metallic) foil of the same base element (taken as a reference) reveals information about the density and valence state of an element within the sample. This excitation results in the release of scattered photoelectrons which propagate as a spherical wave that scatters off of surrounding atoms in the structure. This effect also impacts the x-ray absorption and the shape of the spectra several hundred eV above the edge to further reveal information about the local atomic structure. This area is known as Extended X-ray Absorption Fine Structure (EXAFS). Together, these regions offer a comprehensive analysis of the sample. With post-analysis, XANES reveals the density of states, the coordination geometry, and the valence state of the excited atoms. EXAFS can yield bond length, coordination number, and types of ligands within the sample.

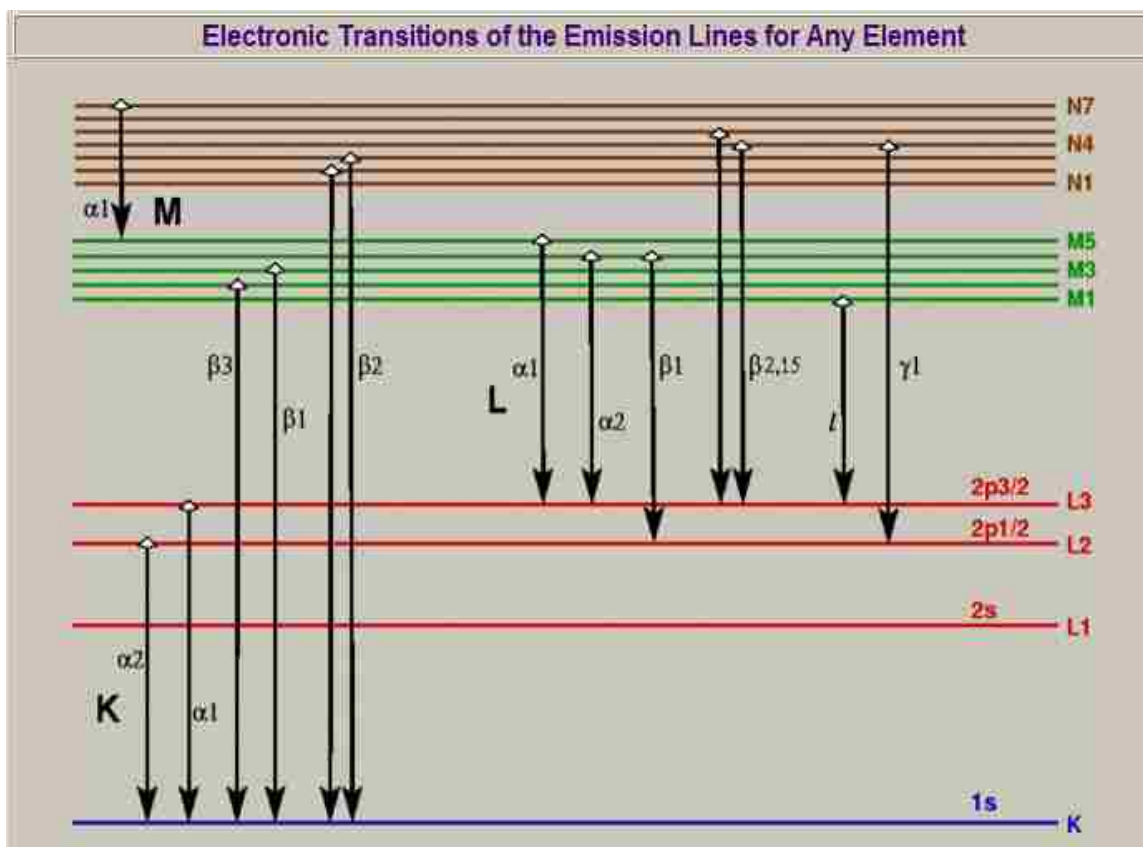


Figure 4.7: Qualitative depiction of the excitation potential of different core electron levels ⁹¹.

XAS has some similarities to TEM-EELS. A 200keV TEM electron beam can probe electron shells of energies from hundreds to several thousand eV, revealing most M-shell edges. But the energies of these edges can be very close, making them difficult to distinguish. Alternatively, XAS is usually performed using a synchrotron: an accelerated ring of electrons which is used to produce monochromatic x-rays. The National Synchrotron Light Source (NSLS) at Brookhaven National Laboratories operates at 2.8GeV and is capable of probing all remaining core shell edges with excellent elemental resolution. The NSLS was used for the analysis of several Pt/NbRu_yO_z-type materials discussed in this study.

4.3.6 Gas Adsorption-Desorption Analysis

It is usually important to determine the surface area of mesoporous materials, as well as the type of porosity imparted from the templating agent. Both questions can be answered by attaining adsorption-desorption isotherms for a sample. The pressure of inert gas such as N_2 is slowly increased inside an initially vacated chamber containing the sample until a saturation pressure is reached ($P/P_0 \sim 1$). Because a monolayer amount of N_2 adsorbs on the sample surface in this range, the measured pressure of the chamber will be less than would be expected if no adsorption were to occur. By approximating the space which each nitrogen atom occupies on the surface, a total sample area per mass can be calculated using the Brunauer-Emmet-Teller method⁹².

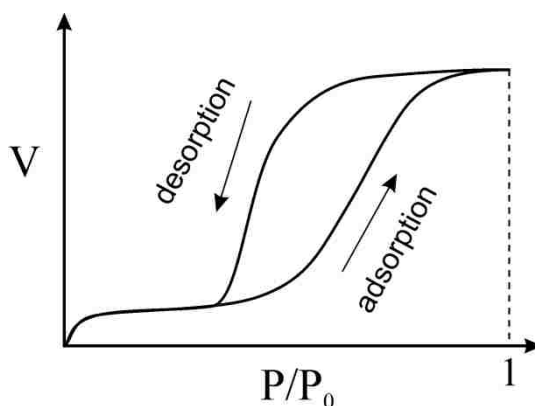


Figure 4.8: Behavior of an adsorption-desorption isotherm for a mesoporous structure experiencing capillary condensation from the adsorbate.

In mesoporous structures, the adsorption curve will often behave differently than the desorption curve. Even before the saturation pressure, some of the gas can condense beyond a single monolayer inside individual pores. Depending upon the shape of the pore, capillary effects will stabilize the adsorbate in this state until much lower pressures. Models such as the Barrett-Joyner-Halenda (BJH) method, which are based upon the

Kelvin equation for relating equilibrium vapor pressure of a liquid to the shape of the liquid/vapor interface, can be used to determine pore size distribution. But these models use either the adsorption or desorption curve without the other, and will yield different results depending upon which is used. Typically, the most accurate results are obtained using the adsorption curve, removing points closer to the saturation pressure.

4.3.7 Thermogravimetric Analysis (TGA)

TGA measures changes in the mass of a sample upon exposure to controllable temperature profiles, usually involving specified heating ramp rates, isothermal periods, and different flowing atmospheres. Measureable changes in mass occur when a sample is reduced/oxidized, desorbs water, or thermally decomposes. Heat flux is also recorded so that shifts in mass can be attributed to endo- or exothermic processes. Better accuracy requires ~10mg of sample, which is why the heating rate must be slow enough to allow for the completion of processes which involve diffusion through the sample. Otherwise, results are more easily misinterpreted. If a diffusion-dependent process is well understood, kinetic data can be determined from the rate of change in mass.

4.4 Computational Method: Density Functional Theory

Density Functional Theory is a quantum mechanics-based approach used to compute the electronic structure of atoms in a sample and predict a variety of material properties. These might include molecular structure, vibrational frequencies, ionization energy, and reaction pathways. DFT can also be used to model the behavior of molecular or elemental species on the catalyst surface. The conceptual framework provided by DFT makes no assumptions on the nature of chemical bonding in materials and is universally applicable to many-electron systems. Thus, it provides an unbiased description for

elements and element combinations across the periodic table and can be applied to improve our understanding of solid, liquid, or gaseous phases. These are some of the reasons for the success of DFT after its invention in 1964⁹³. The following provides a description of the foundation of DFT, highlighting the origin of the universal character of DFT and several ways in which we augmented and enriched the experimental content of this work.

Foundation of DFT: DFT rests on two theorems that were instrumental for its invention⁹³:

- 1) For any (electronic) system in an external potential, $V_{\text{ext}}(\mathbf{r})$ (here the combination of ion-electron interaction and the ion-ion interaction) is determined by the ground state (electronic) charge density.
- 2) The functional $E=E[n(\mathbf{r})]$ is universal in terms of the charge density and valid for any $V_{\text{ext}}(\mathbf{r})$. For any particular $V_{\text{ext}}(\mathbf{r})$ the ground state energy of the system is given by the density that corresponds to the global minimum of the energy functional.

The main purpose of the theorems are to ensure that the correct charge density can be found by minimizing the energy which makes this method accessible to efficient numerical minimization techniques. The theorems make no mention of the type of system and hence provide a universal description of many-electron systems. Therefore, DFT provides a thorough and widely applicable description of elements in the periodic table. However, this notion comes at the expense of an exchange correlation functional (E_{xc}). Since the method is universal, so is E_{xc} . Yet, the exact functional form of the functional remains unknown. Finding and formulating increasingly better exchange correlation functionals is an area of active research⁹⁴. However, it should be noted that DFT, in

principle is an exact theory, or more precisely, it can be improved systematically by virtue of the existence of a universal exchange correlation functional. This also provides DFT with a predictive power that can be used synergistically with experiment as well as independently.

For these reasons and the insights at the atomic and electronic level that can be gained from DFT, we combine experiment and theory more closely in this research. All simulations are carried out using VASP^{95, 96}. In the first case, VASP was used to simulate a Pt(111) surface with various relevant adsorbates including C, O, Nb,, NbO_x and H_xNbO_x to determine stability at the interface. The translational energy of the molecule can also be calculated as it moves from one point on the Pt surface to the next. In this way, the translational diffusion constant can be estimated. In the second case, the structure of NbRu₃C and NbRu₃ was studied to estimate the physical and electrical properties of the cubic phase as a potential support for Pt.

4.5 Electrochemistry Studies

4.5.1 The Half Cell

A three-electrode cell is used to measure the catalytic behavior of powders for the ethanol oxidation reaction. A glass cell holds 100mL or less of electrolyte and has available three ports for electrodes and one gas inlet. The Working Electrode (WE) is a glass carbon disk encased in a Teflon body with one surface exposed. Onto this surface, electrocatalyst inks are deposited in measured quantity. A Counter Electrode (CE) is needed to receive the charge imparted from Faradic processes occurring at the WE. Usually, a Pt wire is sufficient for this function. Though the surface area of the CE

should not be significantly lower than that of the catalyst on the WE in order to obtain reliable results, and a Pt-mesh may be needed. Electron exchange between these two electrodes must be measured against a reproducible potential from a known redox couple provided from a Reference Electrode (RE). The appropriate redox chemistry depends upon the nature of the electrolyte. In 0.1M HClO₄, Ag/AgCl is reliable whereas Hg/HgO is preferred in 1M KOH. Results are usually reported against the Reversible Hydrogen Electrode (RHE) which requires conversion according to the equation ⁹⁷:

$$E_{RHE} = E_{RE} + 0.059 * pH \quad \text{Eqn. 4.1}$$

The actual redox behavior of different reference electrodes of the same type can vary depending upon construction, age, etc., and must be periodically tested for reliability. For the reference electrodes used in this work, $\Delta E_{Ag/AgCl} = 0.22V$ and $\Delta E_{Hg/HgO} = 0.924V$. To test a powder for EOR performance, all three electrodes are submersed into the electrolyte and the cell is purged of oxygen by bubbling of N₂ or Ar through the gas inlet. All three electrodes are monitored by a potentiostat which applies controlled potentials to the WE depending upon the experiment at hand.

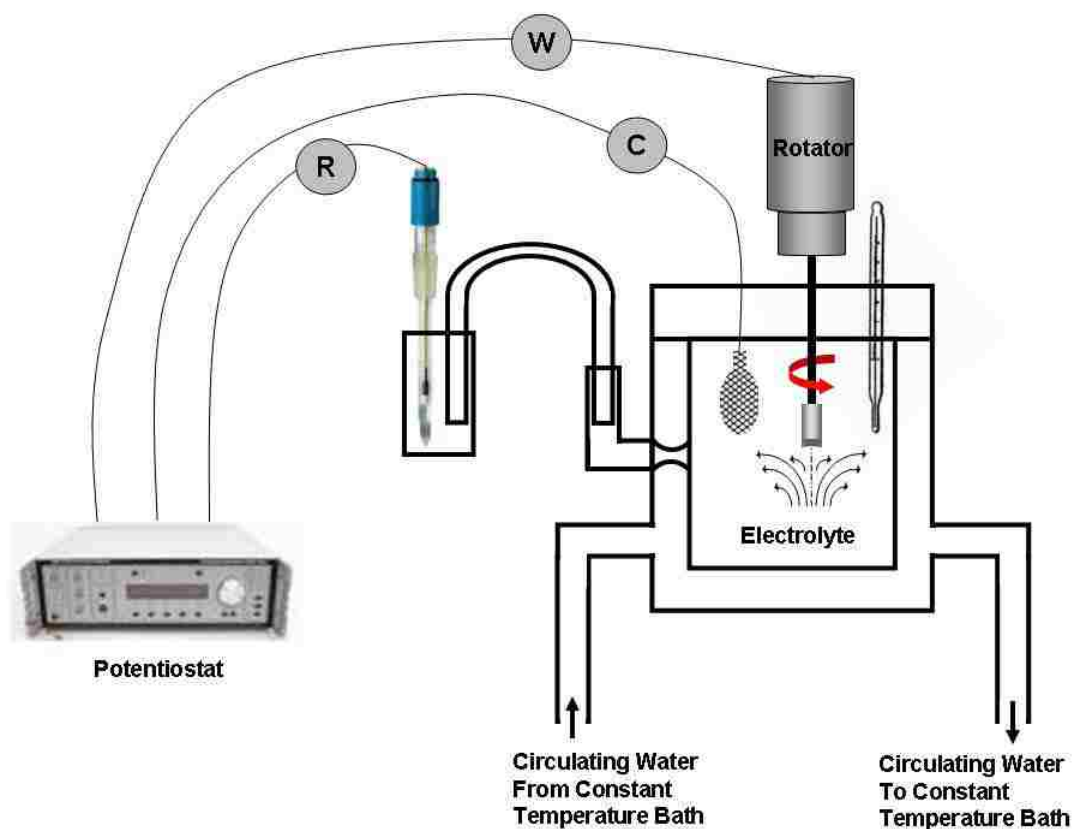


Figure 4.9: Three-electrode electrochemical test cell setup ⁹⁸.

4.5.2 Cyclic Voltammetry

Cyclic Voltammetry (CV) is the primary means of using a three-electrode test cell to determine the presence and thermodynamic and kinetic behavior of redox processes occurring on the electro-catalyst surface. The potentiostat applies a changing potential to the WE within a set potential range, following the triangular waveform of Fig.4.9(a). The exact shape of this waveform depends upon the potential range as well as the polarization rate applied. The potentiostat simultaneously measures the current exchange between the WE and CE. The initial surface of the WE must reach an equilibrium state within the electrolyte, which is why multiple cycles are typically used to obtain an accurate representation of the electro-catalyst surface.

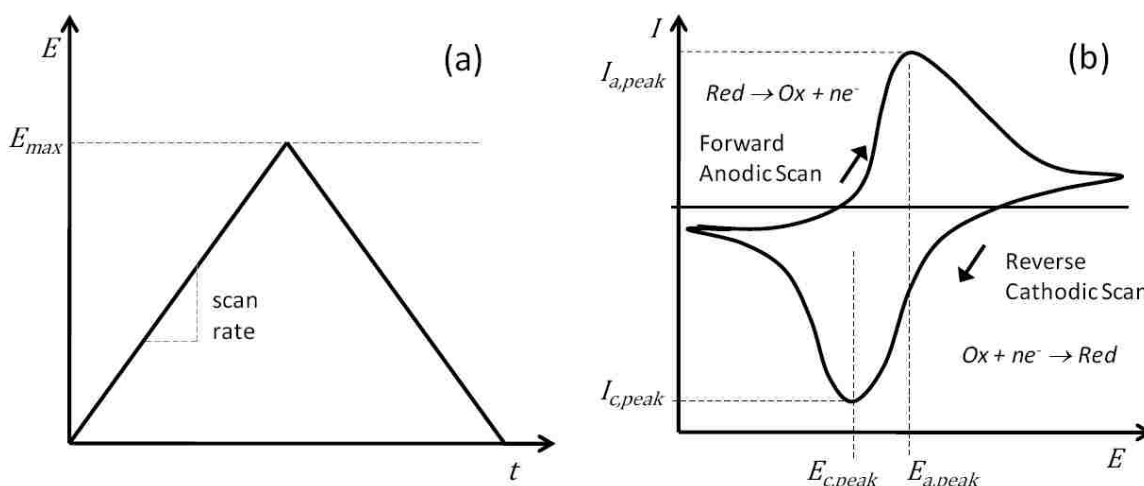


Figure 4.10: Cyclic voltammetry behavior, a) triangular potential waveform produced by the potentiostat and b) resulting current behavior of a redox process at the WE ⁹⁹.

Traversing a single leg of the waveform is known as a *sweep*, while the entire waveform represents a *cycle*. The first leg which scans to higher potentials is an anodic sweep, while the reverse is a cathodic sweep. For systems in aqueous electrolyte, the catalyst surface is oxidized accompanying the release of electrons during the anodic sweep, and reduced with the cathodic sweep. The current qualitatively indicates the presence of an active surface reaction, where intensity is proportional to reaction rate. The potential at which current is measured relates to the thermodynamic behavior of the reaction. More quantitative measurements are also possible but require additional parameters and multiple data sets ⁹⁷.

4.5.3 CO Stripping

CO stripping is performed in 0.1M HClO₄ only since CO adsorption and carbonate formation are less reliable factors in basic electrolyte. N₂ is bubbled into the electrolyte solution for 30min to purge all oxygen. 15% CO/N₂ gas is then bubbled for 30 min while the electrode was held at a constant potential of 0.32V (vs RHE) to facilitate CO/Pt

surface adsorption. The potential is held while N₂ gas is bubbled for another 30 minutes to remove dissolved CO. A cathodic sweep at 100mV/s from 0.32V to -0.02V is taken, followed by an anodic sweep to 1.2V, and a final, complete cycle across the entire range. The two anodic sweeps contrast from one another by the presence of CO oxidation current at higher potentials. The hydrogen region also exhibits adsorption/desorption behavior. The total charge of each region, $Q_{\text{CO}_{\text{des}}}$, $Q_{\text{H}_{\text{des}}}$ and $Q_{\text{H}_{\text{ads}}}$ can be calculated by integrating the area between the first and second cycles across potential ranges pertinent to each region. A polycrystalline Pt surface with an assumed value of 1.3×10^{15} atoms/cm² is typically used, along with standard Pt charge densities of 210 $\mu\text{C}/\text{cm}^2$ and 420 $\mu\text{C}/\text{cm}^2$ for single (H-region) and double (CO-region) electron exchange processes, respectively. The electrochemically active surface area (ESA) for each region is then calculated by dividing the total charge by the appropriate Pt charge density. In this way, the Pt surface area available for adsorption of each species can be revealed.

4.5.4 In situ Infrared Reflection Absorption Spectroscopy (IRRAS)

In situ monitoring of chemical species forming on the active catalyst is possible if the WE can be positioned in close proximity to a window which is transparent to a probing source of EMF. Fourier Transform Infrared Spectroscopy (FTIR) is an excellent technique for the detection of bonds with strong dipole moments that absorb infrared radiation of different wavelengths. Figure 4.10 shows a Nicolet 6300 FTIR which has been modified to divert the IR beam outside of the chassis and into a second chamber containing an electrochemical test cell. Here, the cell consists of a bottomless Teflon chamber which sits atop a ZnSe hemispherical crystal. The WE is a polished, gold disk

onto which a very thin layer of catalyst is applied. The IR beam is directed into the spherical side of the hemisphere at an incident angle which is $\sim 45^\circ$ from the crystal's planar surface. The WE is lightly pressed against the crystal which serves to reflect the beam while also ensuring that it comes into minimal contact with electrolyte. This is important because H_2O exhibits a strong absorption peak which can convolute other interesting peaks attributed to ethanol subspecies and reaction products. Upon exiting the crystal, the beam travels to an MCT detector where the absorption spectrum is processed by the FTIR.

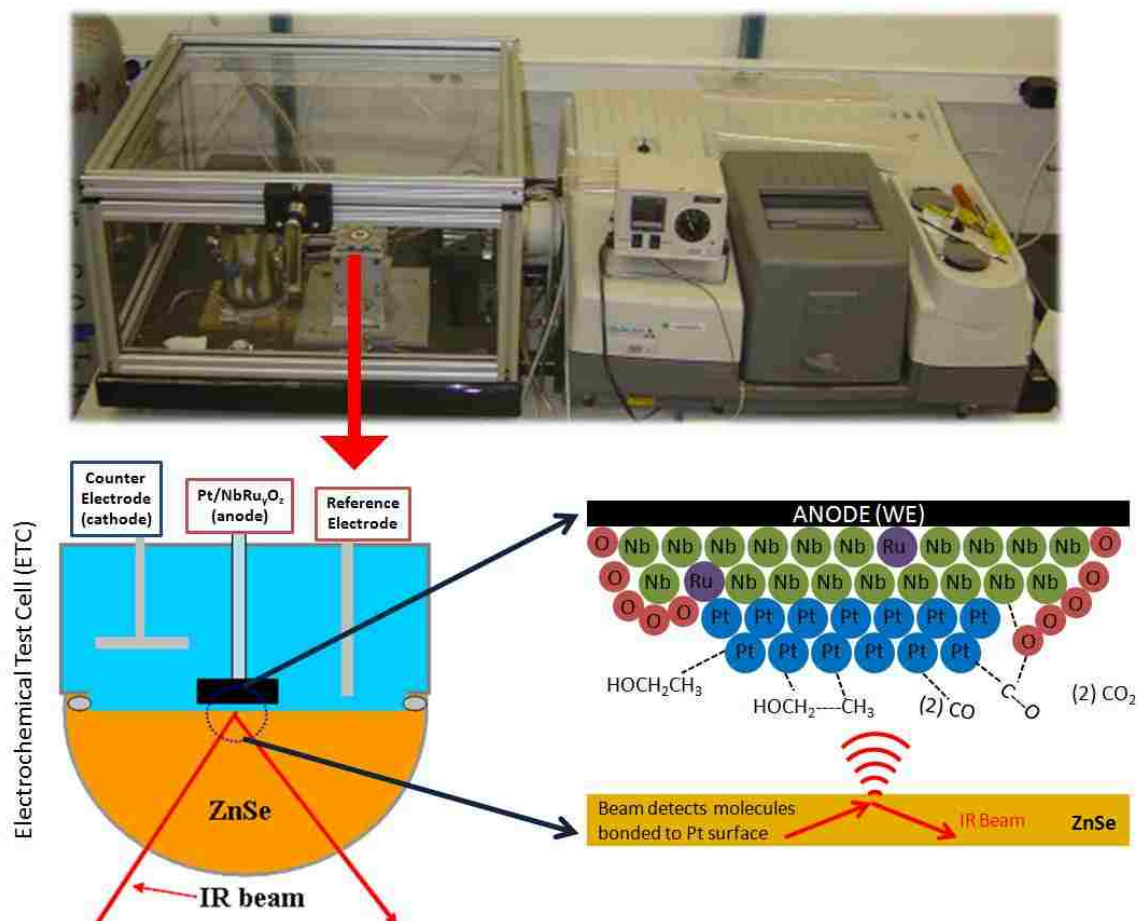


Figure 4.11: In situ IRRAS apparatus at Brookhaven National Laboratory Dept. of Chemistry. The IR beam reflects off of the surface of the WE while probing bond vibrations of species adsorbed onto the catalyst surface.

Aside from the mentioned modifications, the potentiostat and electrochemical test cell remain identical to the configuration used for standard cyclic voltammetry. *In situ* IRRAS is not useful for obtaining stand-alone CV data because too little material is deposited onto the WE in order to minimize the gap between the electrode and crystal surfaces. A gap greater than 1 μm will result in an unacceptable loss of beam intensity reaching the detector. However, resulting CV's are useful for qualitative analysis in which current behavior can be correlated to the appearance of IR absorption peaks.

In this work we are interested in monitoring the appearance of CH_3CHO (or similar), CO , and CO_2 and determining how the potentials at which these peaks appear vary among samples. Catalysts which evolve CO_2 at lower potentials might provide an environment in which the complete oxidation of ethanol is more thermodynamically favorable.

4.5.5 Rapid Electrode Aging

Aging refers to a process in which the corrosion conditions of a catalyst are enhanced to approximate its long-term performance behavior as part of a fuel cell electrode. Platinum nanoparticles supported on graphitic carbon are well studied. In some cases, separate tests are used to study Pt sintering and carbon corrosion independently. But unlike Pt/C, the behavior of $\text{Pt/NbRu}_y\text{O}_z$ involves strong metal support interactions and less known corrosion behavior.

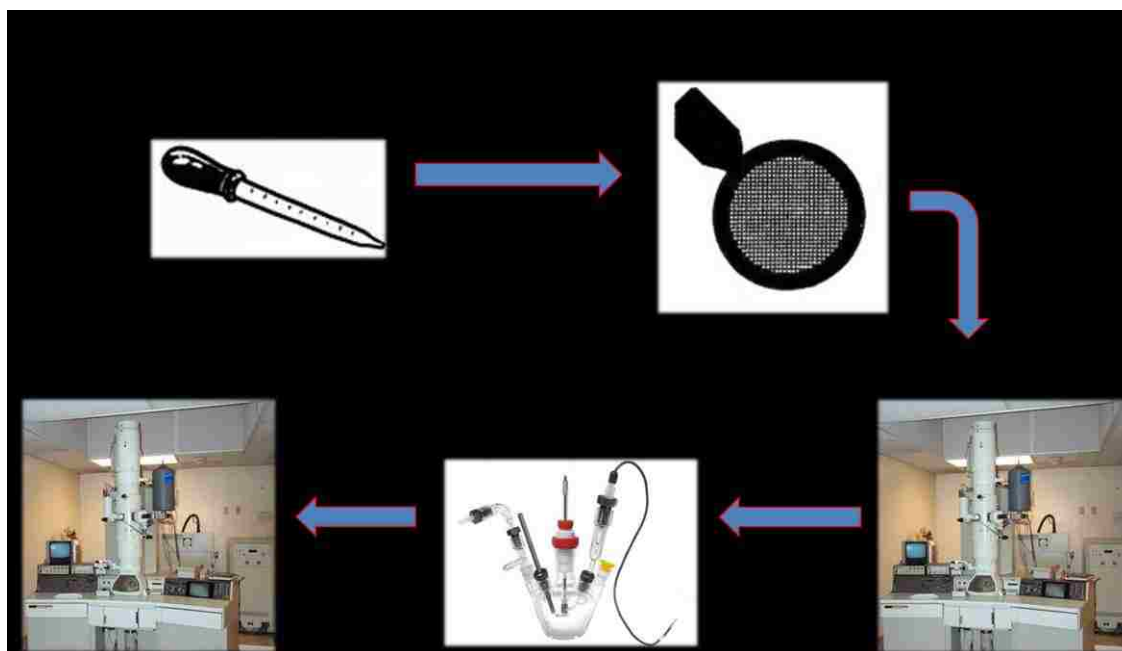


Figure 4.12: The process of preparing a catalyst onto an Au TEM grid for rapid aging studies. The grid serves as a WE and can be examined before and after electrochemical testing.

A simple rapid aging technique was used to examine the catalyst before and after activity inside an electrochemical test cell. $\text{Pt/NbRu}_y\text{O}_z$ powder was suspended in a water/acetone solution and added dropwise onto a gold TEM grid. The grid was allowed to dry, depositing catalyst particles onto the surface. A separate grid was prepared with Pt/C in the same manner. Attached to each grid was a 4mm tab that was used for handling of each sample without disturbing the deposited material. The grids were initially examined with a TEM, and several areas with deposited catalyst particles were noted and images captured. The grids were then attached to the working electrode inside an electrochemical cell, in parallel with a standard glassy carbon electrode with a more substantial amount of catalyst for the purpose of obtaining cyclic voltammogram data. A potentiostat was set to complete 3600 cycles from -0.3V to 0.9V (vs. Ag/AgCl) in 0.1M HClO_4 , or from -1.0V to 0.3V (vs Hg/HgO) in 1M KOH, both at a scan rate of 1V/s.

This subjected the catalyst and support to rapid alternation between reducing and oxidizing potentials. Once complete, each grid was again examined inside the TEM and the same areas were observed for any signs of visual degradation of the catalyst/support.

CHAPTER 5 - Synthesis of Mixed Metal Oxides

5.1 Multiphysics Simulations of Reactor Conditions

The COMSOL Multi-physics software package was used to simulate SP reactor conditions at a low temperature setting of 220°C with a flowing gas of N₂ at 1.5^L/_{min}. The furnace is designed as three sequential heating zones each 1ft in length. The effect of reactor diameter is compared between tubes of 1” and 3” ID. The models are based upon laminar, weakly compressible Navier-Stokes flow with conductive and convective heat transfer. The average pressure of each system remains near 1 atm.

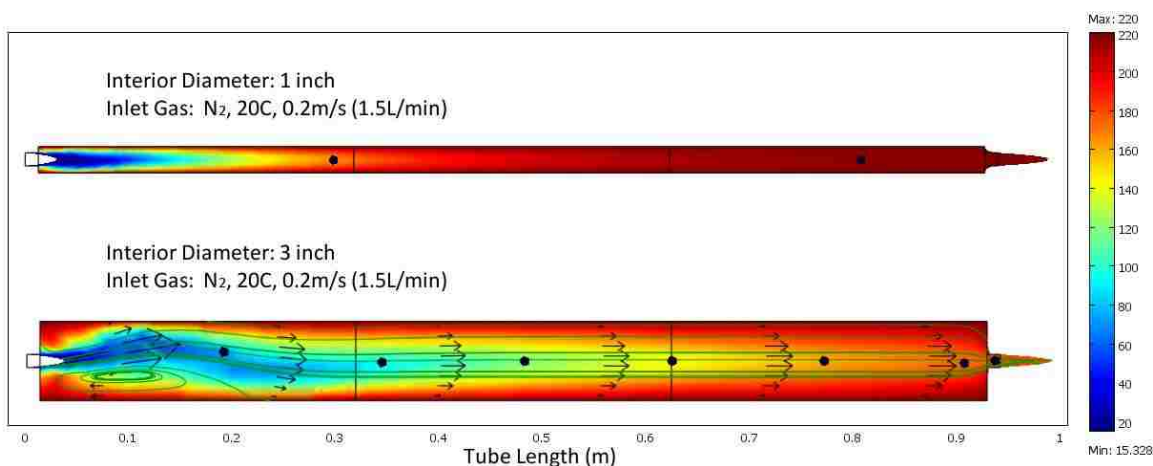


Figure 5.1: Simulated temperature and flow profiles in heated reactor tubes, 1” and 3” in diameter. Temperature is reported in °C.

Reactant behavior of multi-component precursors can be sensitive to the uniformity of the temperature and flow profile encountered by the aerosol, as previously shown in Fig.4.2. Profiles for temperature, velocity, and heat flux across the tube length for both diameters are shown below for comparison.

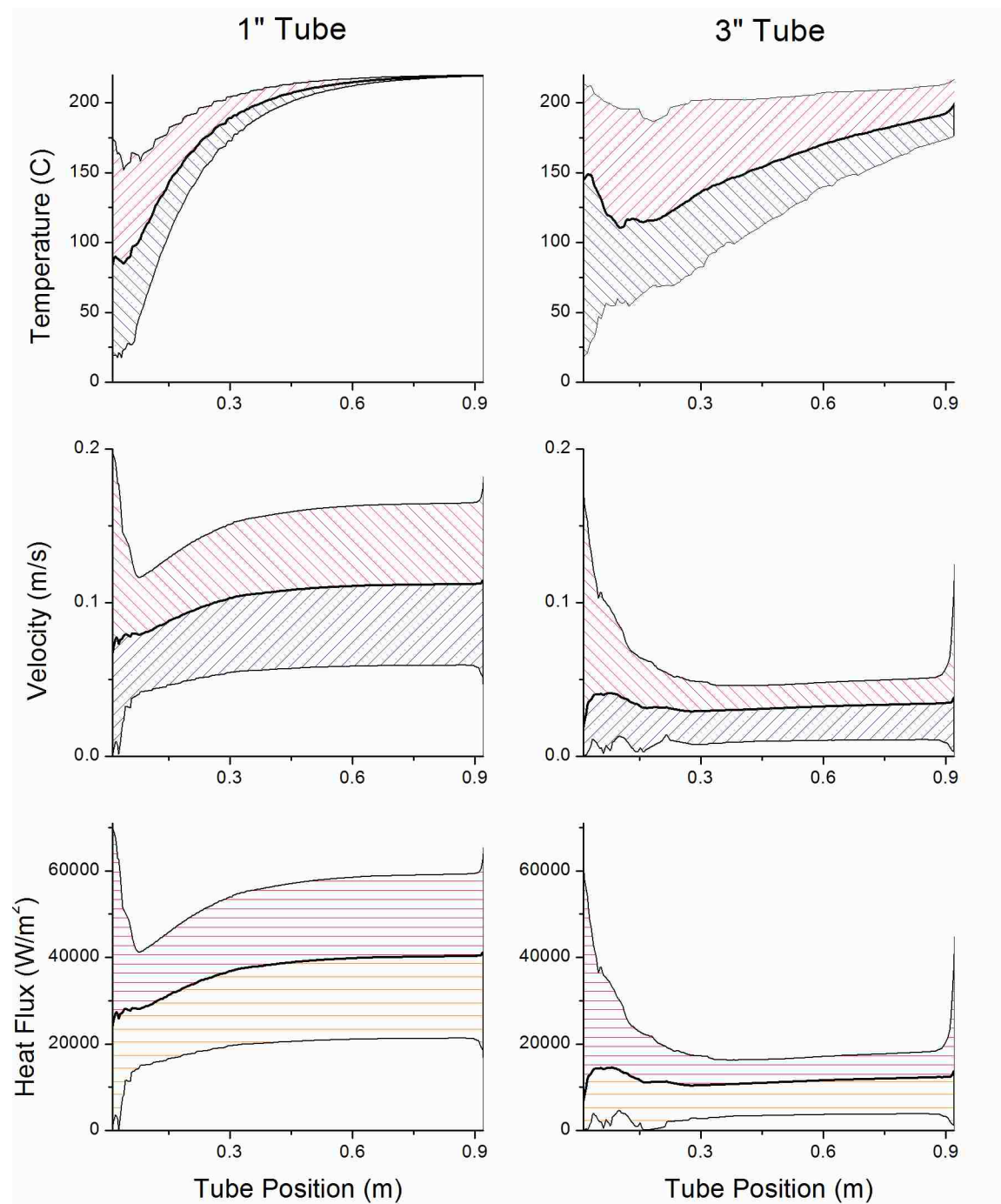


Figure 5.2: Profiles for temperature, velocity and heat flux at each point in the reactor furnace calculated from the COMSOL multi-physics models in Fig.5.1. The bold line in each plot represents the average value at each position in the tube furnace taken from nine evenly spaced trajectories.

The rate of temperature increase appears more gradual in the 3" tube, though there is more variation depending upon radial position. From the velocity profiles, points with the greatest variation between maximum and minimum values indicate where the stream is most likely to experience mixed or transitional flow. A small fraction of particles will become caught in these areas and experience significantly more time in the reactor. Heat flux is a better indicator for comparison of the energy transferred to particles, though the total residence time of the aerosol must also be taken into account.

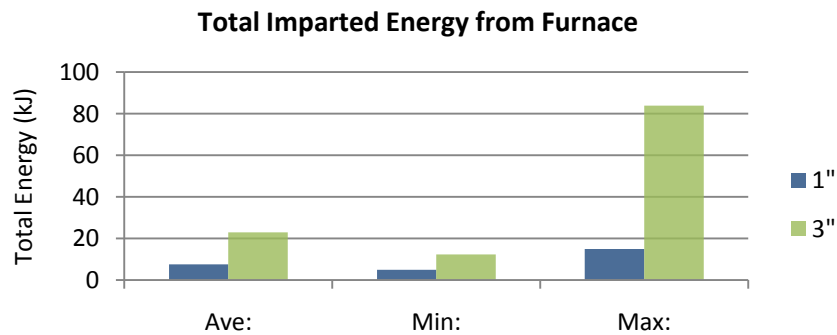


Figure 5.3: Total energy imparted from the furnace to the gas/aerosol by convection and conduction heat transfer.

The larger furnace will theoretically have greater variability in the energy imparted to particles, though smaller particles are usually assumed to be in thermal equilibrium with the transport gas. When the gas inlet is of the same diameter for both tubes with equal mass flux, the larger tube has greater potential for regions of mixed flow. There is also greater interior surface area for increased conductive heat transfer near stagnant flow.

Table 5.1: Total Imparted Energy as Related to Aerosol Residence Time

	Total Heat Flux (W)		Residence Time (s)		Total Energy (kJ)
1"	841.2	Ave:	9.01	Ave:	8
		Min:	5.94	Min:	5
		Max:	17.85	Max:	15
3"	807.35	Ave:	28.5	Ave:	23
		Min:	15.28	Min:	12
		Max:	104	Max:	84

Table 5.1 shows that the variability in energy between tube diameters is largely related to their respective residence times. This variability has much greater implications for precursor salts whose thermal decomposition behavior is weakly or completely independent of solvent evaporation rate, while the solvent/surfactant behavior is less affected. As discussed in Ch.4, this is because the majority of the solvent will evaporate shortly before or after the furnace entrance of either reactor configuration in Fig.5.1.

Castillo et al.¹⁰⁰ used COMSOL to model the evaporation and thermal decomposition of stationary, 30 μ m droplets of Ce(NO₃)₃ dissolved in H₂O. Models showed that the crust formation illustrated in Fig.1.8 is common across a wide range of temperatures and initial concentrations. This is due to salt concentrations reaching their supersaturation point at the droplet surface where solvent evaporation is rapid. Crust formation is inversely proportional to the droplet size and the volatility of the metal-salt. Its formation is also favored by higher temperatures, lower pressure, and greater atmospheric oxygen content.

The very same factors highlighted by Castillo et al. also represent important differences between SP and traditional batch sol-gel synthesis techniques. Though many of the same chemical systems are used in each process, mixed compounds of volatile precursors are

more easily achieved with sol-gel because drying and decomposition occur over several days to weeks at temperatures around 100°C or less. Additionally, the carrier gas increases the rate of solvent evaporation compared to still or convective atmospheric conditions of a batch sample. Crust formation is detrimental to achieving particles of homogeneous composition and structure. Therefore, to avoid the former process, the SP reactor system would ideally be run in a higher pressure, reducing atmosphere at the lowest temperature necessary to thermally decompose the reactants.

The flow of particles through the reactor can be modeled according to the Khan-Richardson Force equation for a body suspended in a moving fluid:

$$F_{p,fluid} = \pi r_p^2 \rho (\bar{v}_f - \bar{v}_p)^2 * (1.84 Re_p^{-0.31} + 0.293 Re_p^{0.06})^{3.45} \quad Eqn. 5.1$$

$$Re_p = \frac{2 r_p^2 \rho}{\eta} |\bar{v}_f - \bar{v}_p| \quad Eqn. 5.2$$

Where r_p^2 is the droplet/particle radius, ρ is the density of the carrier fluid, η is the fluid viscosity, Re_p is the Reynold's number of the particle, and \bar{v}_f and \bar{v}_p are the vector velocities of the fluid and the particle, respectively.

Eqn.5.1 is a single-dimension form describing the total force the carrier fluid exerts on a spherical particle. It is expanded into cylindrical coordinates within the COMSOL software package as appropriate. Particle mass is not taken into account in Eqn.5.1-5.2, although COMSOL can adapt the term using equations for the conservation of mass and momentum. However, the average mass of the droplets generated in this study is sufficiently small that the linear form of Eqn.5.1 is appropriate¹⁰¹. These equations hold across a large range of Reynolds numbers, from creeping to turbulent flow regimes¹⁰². If

a model were fitted to the temperature and velocity profiles of Fig.5.2, then Eqn.5.1 could be used with Eqns.1.8-1.12 to calculate the properties of a droplet/particle during spray pyrolysis.

5.2 Synthesis of Niobium Intermetallic Compounds at Low Temperature

5.2.1 Titanium

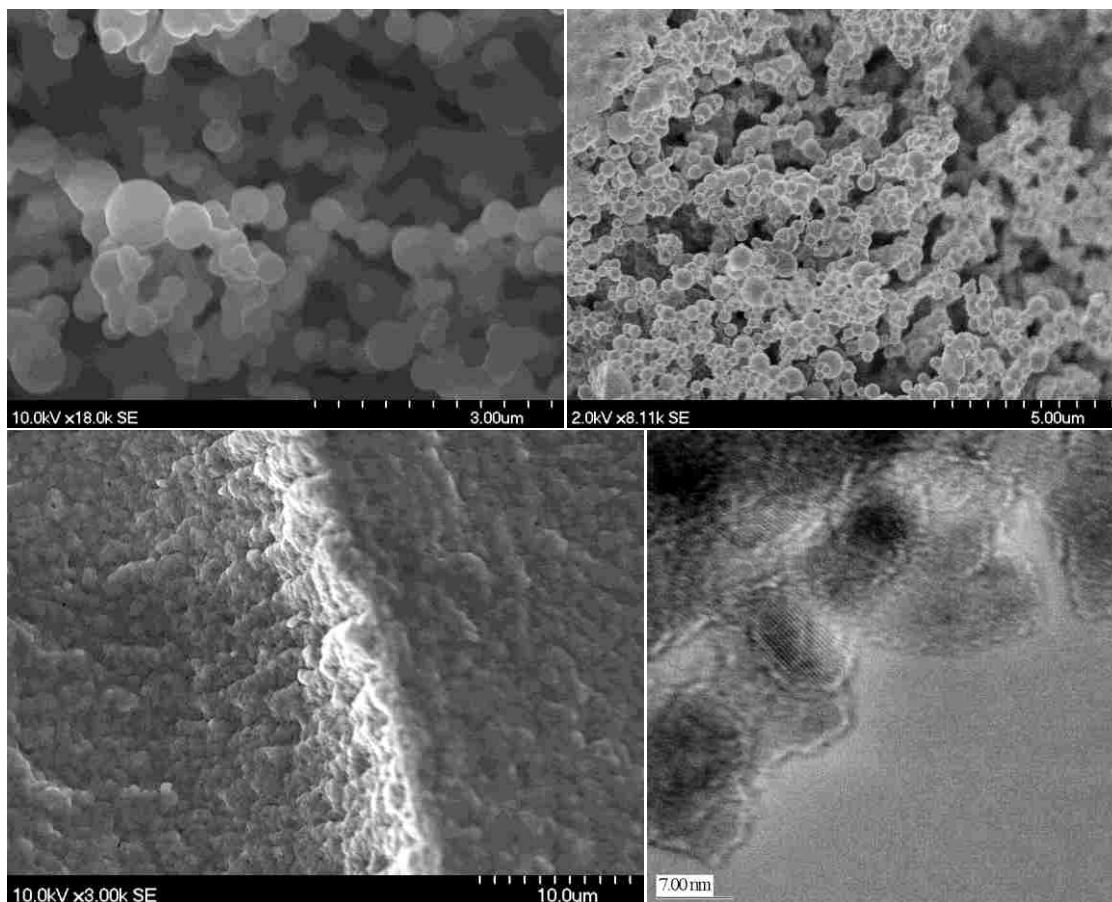


Figure 5.4: SEM images of $\text{Nb}_{56}\text{Ti}_{14}\text{O}_{30}$ (from TiCl_4), (Top Left) from the filter paper, (Top Right) after calcination at 400°C , and (Bottom Left) wash in $0.3\text{M H}_2\text{SO}_4$ followed by calcination at 400°C . (Bottom Right) TEM image of the same sample taken from the filter paper, possibly showing the vaporization and nucleation of TiO_2 nano-particles.

A precursor solution containing NbCl_5 (1.78g), TiCl_4 (0.90g), and P123 (1.10g) in ethanol solution (10.14g) was processed by SP at 200°C in a 1" quartz tube. Calcination in air was performed at 400°C for 4hrs. An optional washing step involved mixing the powder in $0.3\text{M H}_2\text{SO}_4$ for several minutes before filter-washing in DI H_2O . A spherical

particle morphology was maintained after calcination. The densification viewed after the addition of a washing step to the post-treatment is likely caused by partial dissolution of TiO_x or chlorides, since the same effect is not observed for single metal niobia particles. Closer examination in TEM (see Fig.5.4 bottom right) reveals partial segregation of Ti nanoparticles during SP, possibly through vaporization during heating followed by nucleation into nanoparticles during cooling on the filter. Despite this, the sample has a surface area of $196\text{m}^2/\text{g}$. and appears electrically resistive.

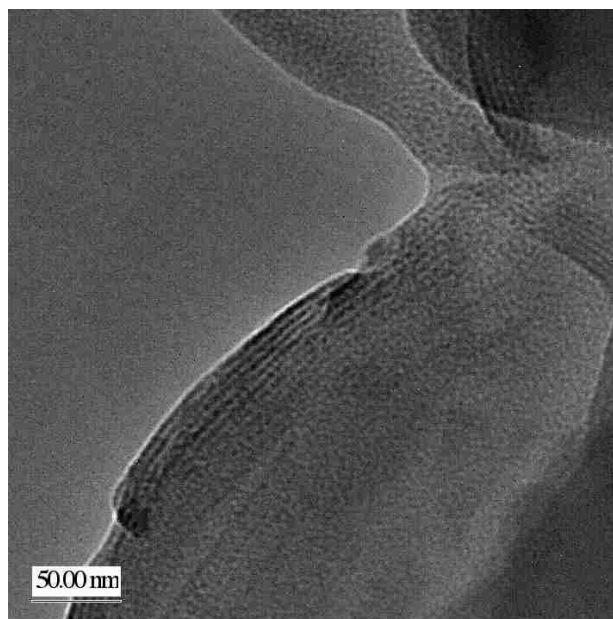


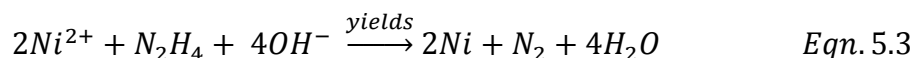
Figure 5.5: TEM image of Nb55Ti16O29 (from $\text{Ti}(\text{OEt})_4$) directly from the filter paper shows signs of tubular porosity near the thinner particle edges.

For the sample in Fig.5.5, titanium(IV) ethoxide was used in place of TiCl_4 . The particle morphology is mostly lost, suggesting that the precursors are not entirely decomposed. The sample is equally electrically resistive. Porosity is difficult to ascertain visually, but a BET surface area of $186\text{m}^2/\text{g}$ was measured before thermal post treatment. Near the edges a 1D tubular or lamellar porosity is visible. Unfortunately, the rapidly increasing

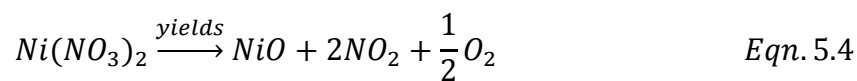
thickness of the sample prevents verification that this is the dominate structure. In Ti/Nb intermetallic compounds in the literature, niobia accounts for only a small weight percent to avoid the high electrical resistivity of Nb(V). In these systems, the same block co-polymer surfactant imparts a 3D, cubic, mesoporous structure from 0 to 75wt% Nb¹⁰³. Increased niobia content serves to stabilize the support at increasingly high temperatures.

5.2.2 Nickel, Iron, and Tin

NbO_x and TiO_x species exhibit a degree of solubility not as easily maintained with other elements during rapid synthesis processes such as SP. This issue can sometimes be resolved by altering the class of metal precursor used. Or, as in the case of nickel, issues of solubility can relate to the way the metal/metal salt behaves with surfactant or the solution. For many transition elements, surfactant can be purposely used to isolate a metal within a composite system to facilitate a desired morphology while a chemical transformation of the metal occurs. An example is the use of cationic CTAB & TC₁₂AB surfactants to produce nickel nano-particles c.a. 10nm from halide precursor¹⁰⁴. The presence of 1M or less hydrazine reduces nickel:



The size of nanoparticles depends upon the formation of nucleating atoms early in the reduction process. In a Ni/Nb halide system, nickel may begin to nucleate before niobium, which is a more stable chloride under reducing conditions. Alternatively, mixed Ni/Nb compounds may be achieved if both precursors instead form an oxide, easily achieved in aqueous solutions with nickel nitrate:



Obviously, the single-step thermal decomposition in Eqn.5.4 will be affected differently by the presence of solution compared to the hydrazine-facilitated reduction in Eqn.5.3. It has been reported that spray pyrolysis of aqueous nickel nitrate at 450°C (rapid dehydration) results in multiple speciation of NiO crystallites, hydrated nitrate, and other mixed, amorphous materials¹⁰⁵. This reaction proceeds with high yield via Eqn.5.4 which has an activation energy of 88 kJ/mol¹⁰⁶. Alternatively, the heat of fusion of nickel is about 17 kJ/mol. Only a portion of the precursor will decompose and then immediately volatilize, resulting in multiple, partially reacted nickel species. This illustrates how precursors which are solution sensitive can manifest into multiple products at high reactor temperatures. To achieve a homogeneous material, the thermal decomposition could occur at much lower temperatures for slower solvent evaporation, or at much higher temperatures (480°C and higher) to force the thermodynamics of oxidation.

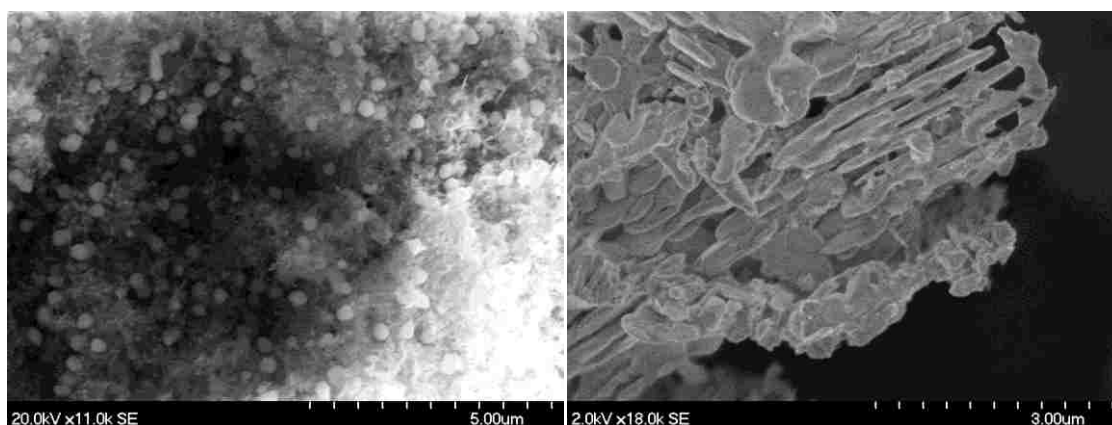


Figure 5.6: NiCl₂ and P123 surfactant (1:1) processed by SP at 260°C in N₂ (Left) off the filter paper and (Right) after reduction at 400°C for 4hr.

In this study, niobia is the primary material of interest. P123 surfactant exhibits especially predictable templating behavior with NbCl_5 . A lower reactor temperature of 260°C was used to test the impact of P123 on the morphology of NiO formation. Immediately after SP, nanoparticles of mixed morphologies are obtained wherein much of the nickel is surfactant-stabilized while some independent nucleation to form larger particles also occurred. Upon removal of surfactant the nickel undergoes a 1D crystal growth mechanism.

Niobium and nickel are known to exhibit a powerful strong metal support interaction effect¹⁰⁷⁻¹⁰⁹. Depending upon synthesis conditions, it can be so strong so as to deactivate the nickel surface for gas phase H_2 adsorption. Though it is a slightly noble metal, the surface acidity of nickel in the presence of niobia can increase substantially with increasing levels of hydration¹¹⁰. It has also been reported that the behavior of the nickel surface varies significantly between 0-15wt% loadings supported on niobia. Despite large diameters of 300-500nm, the surface of nickel nanoparticles (6wt%) is saturated with hydrogen via a spillover effect from acidic niobia within a humid vapor atmosphere¹¹¹.

The electro-catalytic behavior of nickel supported on niobia described above is likely to have implications for that of platinum (both Group VIII elements). Nickel is usually discussed as a promising catalyst for oxygen reduction in alkaline fuel cells. But it has also been shown as an effective material for borohydride oxidation¹¹², and can decrease the onset potential of EOR by 300mV as Pt-NiO/C compared to Pt/C in alkaline electrolyte⁴⁸.

Iron is less noble than nickel and has been shown to be a useful catalyst for the gas phase oxidation of small hydrocarbons ¹¹³. Its catalytic behavior has indirectly been considered for a large number of reactions because it is a by-product leftover from the catalytic formation of carbon nano-tubes using ferrocene ¹¹⁴⁻¹¹⁷. Its trivalent nature has made it a useful catalyst with Ti^{4+} in zeolite structures ¹¹⁸, and can be an active catalyst for oxidation and acid-catalyzed reactions ¹¹⁹. The niobia surface is acidic by formation of $\text{Nb}_2\text{O}_5 \cdot n\text{H}_2\text{O}$ and also exhibits unique activity and selectivity for various acid-catalyzed reactions ¹²⁰.

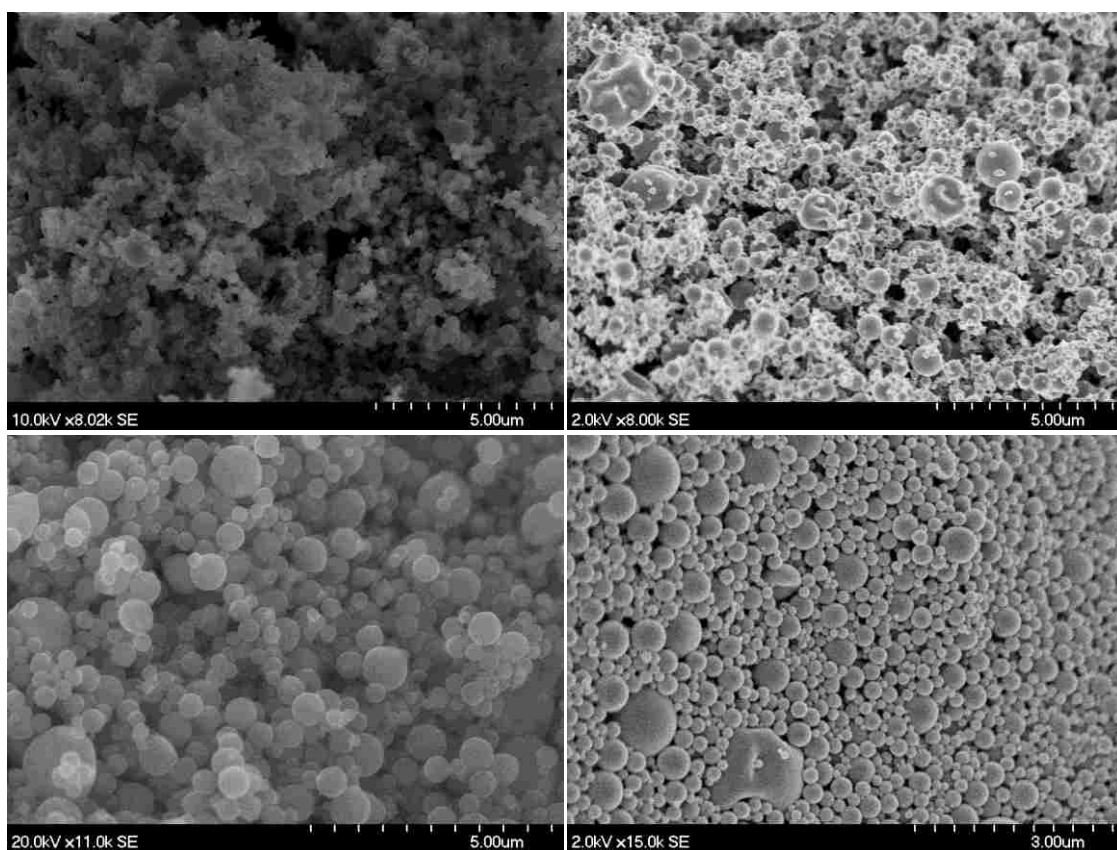


Figure 5.7: SEM images of niobia composite materials synthesized by SP at 250°C in N_2 . (Top Left) Nb-Fe (5:2). Nb-Mo (3:1) (Top Right) off the filter paper, (Bottom Left) reduced at 400°C for 4hrs, and (Bottom Right) washed in 0.3M H_2SO_4 and thermally reduced.

Molybdenum and niobium are both interesting materials for increasing the CO tolerance of Pt catalyst in PEMFC anodes. Studies have shown that only small amounts of Mo (25% or less) are useful towards this end. Otherwise, Mo begins to block too many Pt surface sites. However, Mo does not significantly lower the potential at which CO is oxidized on Pt¹²¹. And while metallic Mo is highly conductive, like niobia oxidized forms are most stable. This is why Mo would appear to be of limited use towards enhancing EOR on Pt. Alternatively, it could be used as a mixed component with niobia to dilute the significant SMSI effect seen between niobia and nickel (or other noble metal) while maintaining potential advantages.

Figure 5.7 shows that Nb-Fe and Nb-Mo maintain a homogeneous composition using the aqueous P123 surfactant system at low SP processing temperatures, even after chemical and thermal post-processing. However, resistance remains high between 7-8M Ω .

5.2.3 Platinum, Ruthenium and Carbon

The thermal decomposition of sucrose within intermetallic compounds can be used to chemically reduce metal precursors and possibly form metal-carbides. This method requires that carbon be a tolerable component in the composite. In larger quantities which vary depending upon the metal used, the carbon can also increase the overall electrical conductivity.

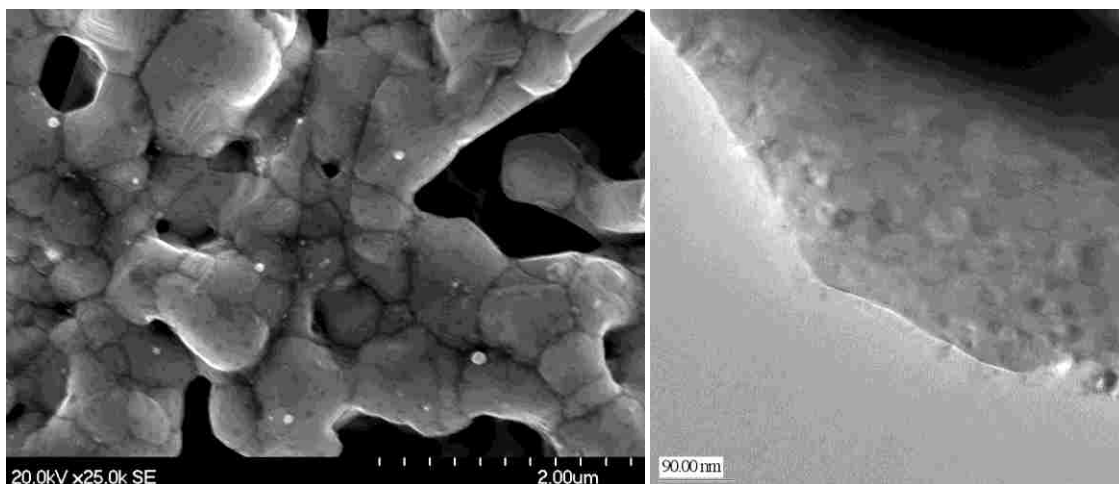


Figure 5.8: Nb-Pt-C (1:1:0.5) processed by SP with metal-chloride and sucrose precursors at 250°C in N₂. (Left) wide view SEM and (Right) TEM of a granular edge).

When niobium, platinum and carbon are synthesized by low temperature SP in the absence of any surfactant, a homogeneous material is achieved (Fig.5.8-Left). This material seems to mimic the granular morphology of Nb₂O₅, with only minor formation of some independent Pt nanoparticles. The grains appear to be 0.5-1 μm in thickness, which complicates TEM analysis. However, there appears to be some indication of hexagonal crystallites, possibly Pt, within the bulk. This could suggest a locked structure of Pt(111) that would be more stable than Pt nanoparticles under corrosive electrochemical conditions. Unfortunately, the use of P123 surfactant results in separation of Nb and Pt metals, discussed later.

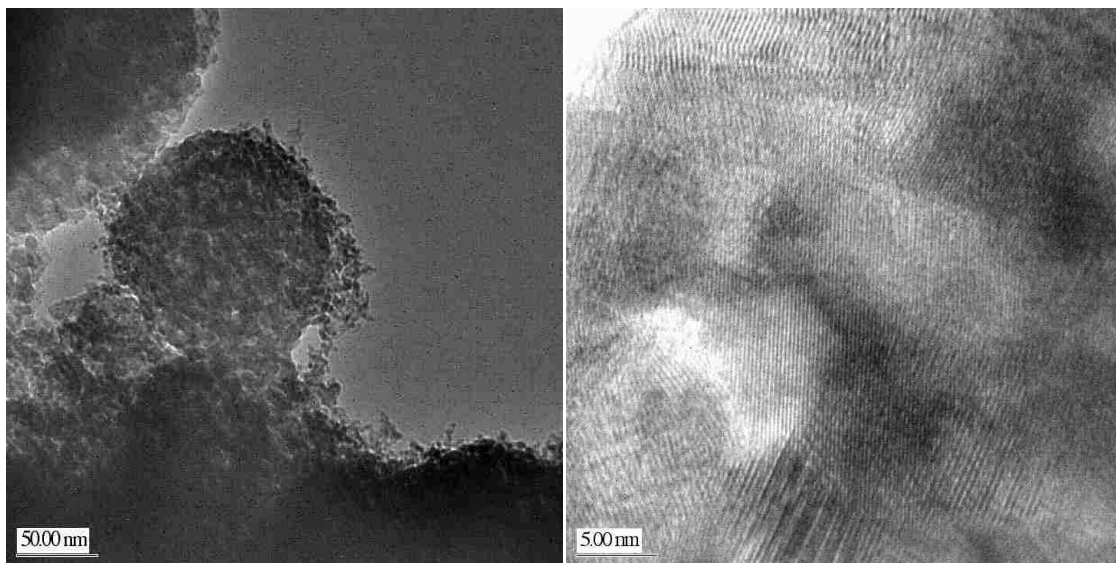


Figure 5.9: TEM images of Nb-Ru-C (2:1:1) processed by SP with metal-chloride and sucrose precursors at 250°C in N₂. (Left) Droplet morphology is maintained while (Right) incoherent lattice fringes indicate a mixed, crystalline structure throughout the sample.

A similar system using Ru in place of Pt shows that the droplet morphology appears to be maintained. Though no surfactant was used, the particles appear porous from the void left from thermal decomposition of sucrose. Loose carbon appears on the surface of particles.

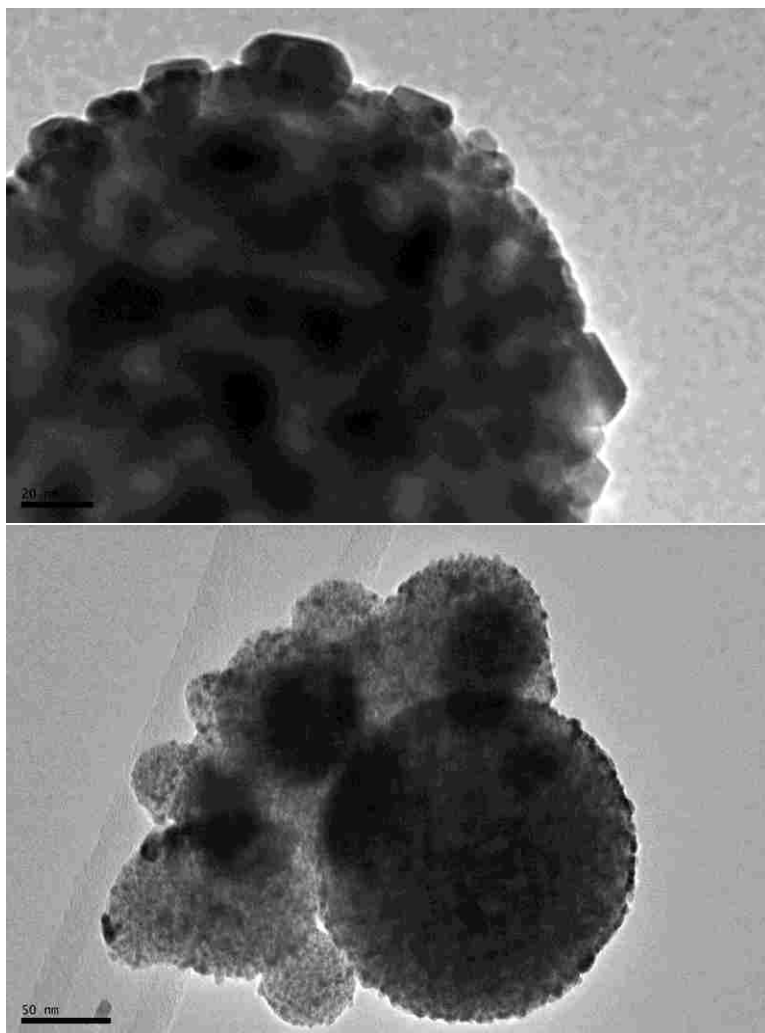


Figure 5.10: 60wt% Pt on Niobia processed by SP with metal-chloride precursors and P123 surfactant at 240°C in N₂.

Niobia generally forms a predictable oxide matrix. When P123 surfactant is used, Pt nano-particles form as a highly dispersed catalyst within the Nb₂O₅ matrix. Even at this high Pt loading, the powder exhibits a resistance of 400 Ω. A third elemental component that does not destabilize the material as sucrose does is required to further lower the material's resistance.

5.2.4 Tin and Ruthenium

Like niobia, tin is a 4d element that forms an oxide as well as multiple alloys with Pt^{46, 122, 123}. Pt-Sn has been shown to enhance the kinetics of EOR, though oxidation activity varies significantly with the ratio of Pt:Sn¹²⁴. It is not clear that even optimized alloys facilitate the total oxidation pathway of ethanol. In fact, the oxidation of CO in the gas phase (CO/H₂ mix) on Pt/Nb₂O₅ has been shown to be hindered by the addition of Sn¹²⁵. Regardless, tin remains of interest in this study as a mixed metal or oxide.

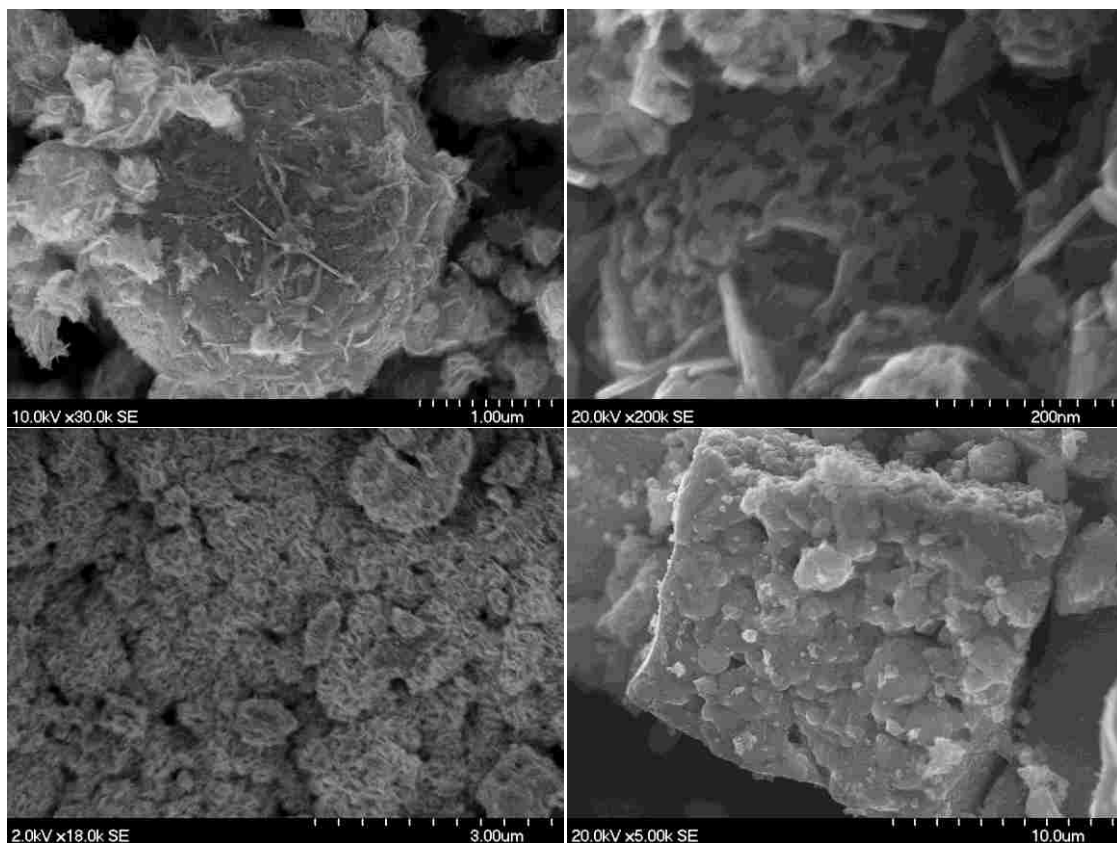


Figure 5.11: Nb-Sn and Nb-Sn-Ru species processed by SP with metal-chloride precursors and P123 surfactant at 200°C in N₂. (Top-Left) Nb-Sn (1:1) reduced at 400°C for 4hrs in 10% H₂/N₂, (Top Right) and the same sample washed in 0.3M H₂SO₄ and thermally reduced. (Bottom) Nb-Ru-Sn (2:1:1) after the same wash and thermal post-treatments.

The heat of vaporization of Sn is over 2x lower than that of niobium, which increases the importance of its chemical sensitivity to the solution and surfactant. This is reflected by the unique segregation of 1D SnO_2 crystallites in the Nb-Sn systems shown in Fig.5.11. The addition of an acid-washing step causes an increase in the pore size of the final material. This possibly indicates that the niobia was in a fluid or transitional state during the vaporization of tin and surfactant. The addition of Ru does not appear to dampen this segregation.

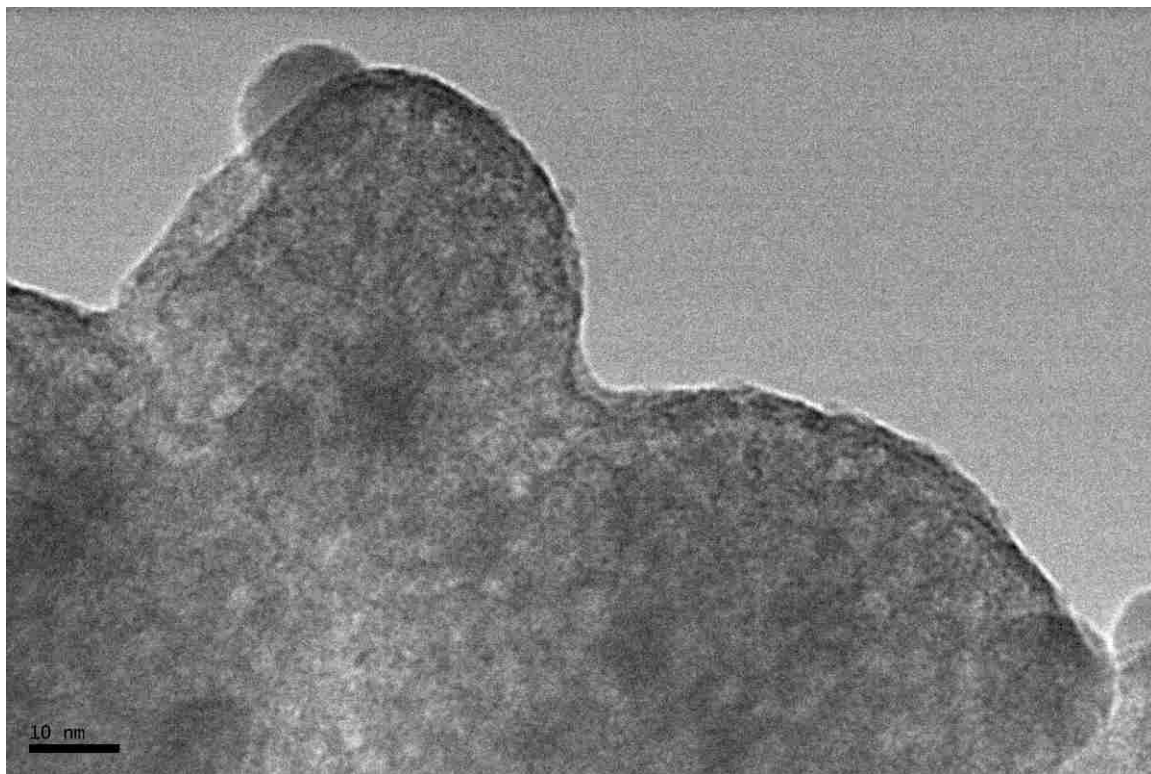


Figure 5.12: Nb-Sn (1:1) processed by SP with metal-chloride precursors and P123 and Brij-35 (1:1) surfactants at 200°C in N_2 .

When a mixed surfactant system is comprised of P123 and Brij-35, the niobium-tin precursors yield a substantially more homogeneous product. Brij-35 is a shorter nonionic

polyoxyethylene surfactant with the formula $C_{12}H_{25}EO_{23}$. Pores c.a. 4nm are visible in TEM. Yuan et al.⁷⁹ reported that this surfactant combination used with a niobia sol resulted in ordered, hexagonal mesopores c.a. 4.5nm in diameter after calcination at 400°C. While an unordered, mesoporous structure can be obtained with this multi-surfactant approach, the material exhibits near complete electrical resistance, $>10M\Omega$.

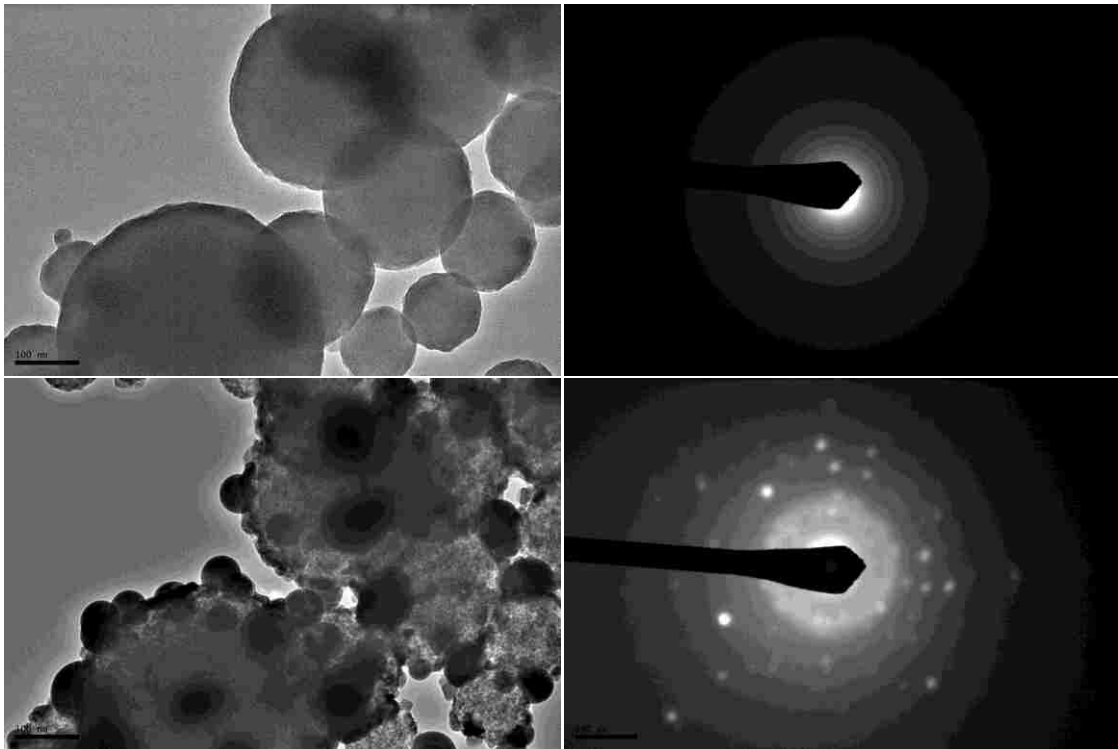


Figure 5.13: NbSnC (1:1:0.5) processed by SP with metal-chloride precursors, sucrose and P123 surfactant at 260°C in N_2 before post-treatments. (Top) Mixed component particles which appear amorphous by the absence of any electron diffraction pattern. (Bottom) The same particles after intense stimulation by the electron beam. The niobia matrix and P123 remain intact while tin precursor separates into a semi-crystalline phase.

Sucrose was added to the Nb-Sn system in an attempt to increase the conductance of the final powder. Before any post-processing steps, the powder appears to be an amorphous, mixed material in TEM (Fig.5.13). However, upon intense exposure to the electron beam

of the microscope, a secondary species appeared to separate out of the niobia matrix. Selected area diffraction of the same particles before and after intense beam exposure shows that the secondary structure is at least semi-crystalline. The morphology is spherical, and possibly indicates a fluid-like expansion into the vacuum of the chamber. It is conceivable that tin behaved similar to ruthenium by forming hydrous surface species (see Fig.6.6, App.A) that were stabilized within each particle before agitation by the beam, or that the beam energy exceeded the volatilization energy of Sn species. EDS results measured before and after the component segregation indicate mass losses of O, C, and Cl.

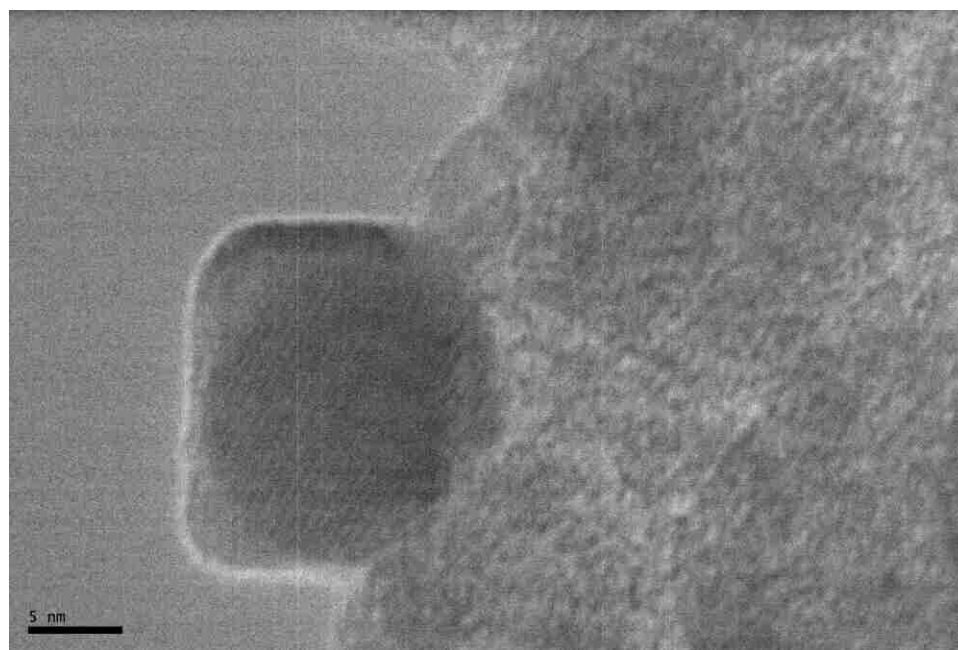


Figure 5.14: NbSnC (1:1:0.5): Continued evolution/transformation of tin-based particles with constant exposure to the electron beam of the TEM.

These newly formed droplets continue to transform with exposure to the TEM electron beam. Fig.5.14 shows a particle in which the simultaneous formation of two crystalline

structures appears to form, though only one shows visible lattice fringes. It is possible that one of these components is a carbide or Nb-Sn composite.

CHAPTER 6 - Mesoporous Niobia Supports

NbCl_5 powder was acquired from Sigma-Aldrich, RuCl_3 from Fischer Scientific, and Pluronic-123 (nonionic triblock copolymer) from BASF. All materials were used as received. In the synthesis of mesoporous NbO_x , 1 g of P123 was dissolved in 10 g of ethanol. Added to this was 2.6 g of NbCl_5 , after which the entire mixture was stirred for 10 min until all NbCl_5 was dissolved, yielding a transparent solution. A similar niobium material doped with 12% Ru by weight of metals, hereafter referred to as NbRu_yO_z , was prepared by including 1 g of H_2O and 0.385 g RuCl_3 after 22 g ethanol, 2 g P123, and 3.70 g NbCl_5 . The small amount of additional water was necessary to thoroughly dissolve the RuCl_3 into solution.

Three separate sections comprise the spray pyrolysis apparatus. A TSI Inc. aerosol generator (Model 3076) utilizes a single inert gas inlet to atomize the precursor solution, producing aerosolized liquid precursor droplets. A three-zone horizontal furnace spanned by a 3 in. outer diameter mullite tube from Coorstek, into which the aerosol stream feeds, is responsible for drying and thermal decomposition of the droplet material. The three-zone horizontal furnace with an effective heated length of 3 ft was set to provide a 200°C temperature profile, determined by thermocouple measurement at sequential points inside the tube. Precursor solutions were fed into the aerosol generator from an Erlenmeyer flask and carried through the tube as an aerosol using N_2 carrier gas at 1.5 SLM (standard liters per minute). Collection was achieved with a porous membrane filter (HT-Tuffryn 450 Disk Filter, 0.20 μm pore size) to separate the dried material from the gas stream. The filter temperature was maintained at approximately 100°C to prevent water condensation.

Once cooled to room temperature, powders were immediately collected off the filter paper. The bulk sample was divided into several smaller groups. Post-treatment given to samples containing only niobia is similar to what has previously been reported in literature for templated Nb₂O₅ via sol-gel synthesis^{64, 79, 80, 126-128}. This involved an acid wash in excess 0.3M H₂SO₄ solution followed by a water rinse, and then drying in ambient air and calcination in air (ramp at 10°C/min to 400°C, then held for 4 hr). Separate cases in the literature show acid washing and calcination to each be effective in the removal of amphiphilic surfactants, including P123^{80, 129}. In our case, both were necessary to fully expose the interior mesoporosity of the material. Post-treatment steps of samples containing ruthenium were somewhat altered compared to pure niobium oxide. The acid washing step was carried out in various degrees, including omission, to determine its true benefit. Samples are named first according to the parent sample from the filter paper, the degree of washing received, and finally the heating process. For example, NbO_x-Dry-Air, contained no Ru, received no acid wash and was calcined in air. NbRu_yO_z-Wet-N₂/H₂, initially contained 1:8 Ru to Nb (or 12 wt %), received only enough acid wash solution as to be wetted, and was reduced under N₂/H₂ atmosphere. For materials with ruthenium, a distilled water rinse was necessarily withheld until after heat treatment to ensure the stability of the mesopores and particle morphology. For all samples mentioned in this paper, calcination was done in an environment of air or in a reducing environment of N₂ with 10% H₂, both ramped at 10°C/min to 400°C, then held for 4 hr, then allowed to cool at the natural cooling rate of the furnace under the same calcination atmosphere. Hereafter, the weight percent of ruthenium is reported relative to

Ru+Nb metal content, irrespective of oxygen content. Sample names and associated treatments are summarized in Table 6.1.

Table 6.1: Summary of Post-Treatments and Resulting Material Properties of All Samples

sample ID	elemental content	wash step	heating step	BET (m ² /g)	resistance (Ω)	color
Vulcan XC-72	C, O			200–250	<0.01	black
RuO ₂ (J&J Mtrls.)	Ru, O			122	0.4	black
Nb ₂ O ₅ (HY340)	Nb, O			183	8.30 × 10 ⁶	white
NbO _x -Dry-Air	Nb, O	omitted	air 10 °C/min 400 °C 4 h	2	6.60 × 10 ⁶	white
NbO _x -Wash-Air	Nb, O	excess soln.	air 10 °C/min 400 °C 4 h	183	8.40 × 10 ⁶	white
NbO _x -Dry-N ₂ /H ₂	Nb, O	omitted	N ₂ /10 % H ₂ 10 °C/min 400 °C 4 h	2	8.10 × 10 ⁶	black
NbO _x -Wash-N ₂ /H ₂	Nb, O	excess soln.	N ₂ /10 % H ₂ 10 °C/min 400 °C 4 h	131	7.90 × 10 ⁶	gray
NbRu _y O _z -Dry-Air	Nb, Ru, O	omitted	air 10 °C/min 400 °C 4 h	2	8.20 × 10 ⁶	light green
NbRu _y O _z -Wash-Air	Nb, Ru, O	excess soln.	air 10 °C/min 400 °C 4 h	164	8.20 × 10 ⁶	green
NbRu _y O _z -Dry- N ₂ /H ₂	Nb, Ru, O	omitted	N ₂ /10 % H ₂ 10 °C/min 400 °C 4 h	10	<0.01	black
NbRu _y O _z -Wash-N ₂ /H ₂	Nb, Ru, O	excess soln.	N ₂ /10 % H ₂ 10 °C/min 400 °C 4 h	80	950	black
NbRu _y O _z -Wet-N ₂ /H ₂	Nb, Ru, O	wetted	N ₂ /10 % H ₂ 10 °C/min 400 °C 4 h	167	2.3	black

6.1 Changing Properties with Variations in Synthesis

As-produced powders of niobium oxide and Ru-modified niobium oxide appeared visually indistinguishable in SEM as collected directly from the filter paper after spray pyrolysis at 200°C. Collected particles were polydisperse, ranging from roughly 50 nm to 4 μ m. SEM-EDS indicated Ru content in NbRu_yO_z particles was in the range of 6-13%, with an average just slightly below the nominal level of 12 wt% that was in the precursor mixture. Because spray pyrolysis involves very small particles at elevated temperatures, components with significant vapor pressures at the processing conditions can undergo evaporative loss, which can result in composition changes in multi-component particles if one component is more volatile than another (20, 21). All samples mentioned hereafter originated from one of two parent samples as collected directly from the SP system, one a niobium oxide sample (NbO_x) and the other a Ru-modified niobium oxide (NbRu_yO_z). Sample names reflect the metal oxide(s) of the parent sample and the specific post-treatment received, as described further below.

6.1.1 Single-Metal Niobium Oxide

NbO_x-Dry-Air was calcined in air at 10°C/min to 400°C for 4 h, without any acid washing step. A similar sample, NbO_x-Dry-N₂/H₂, received the same treatment with heating in an N₂/10% H₂ atmosphere instead of air. BET measurements in both cases show a surface area of ~2 m²/g, with resistance readings equivalent to uncalcined Nb₂O₅. NbO_x-Dry-N₂/H₂ becomes a black powder, whereas its equivalent calcined in air remains white following heat treatment. In neither of these powders was the interior mesoporosity well-exposed (as indicated by the low surface areas), though interior mesochannels of size 5-6 nm in diameter were apparent by TEM (Figure 6.1A). The change of color to black when using the reducing calcination atmosphere in the NbO_x-Dry-N₂/H₂ treatment, perhaps combined with trapped organic material, appears to have at least partially reduced niobia during the treatment, and led to surface crystallization that is apparent from lattice fringes in TEM shown in Figure 6.1B. Analysis of these fringes (inset of Figure 6.1B) reveals reflections from (100) & (131)/(180) orthorhombic Nb₂O₅.

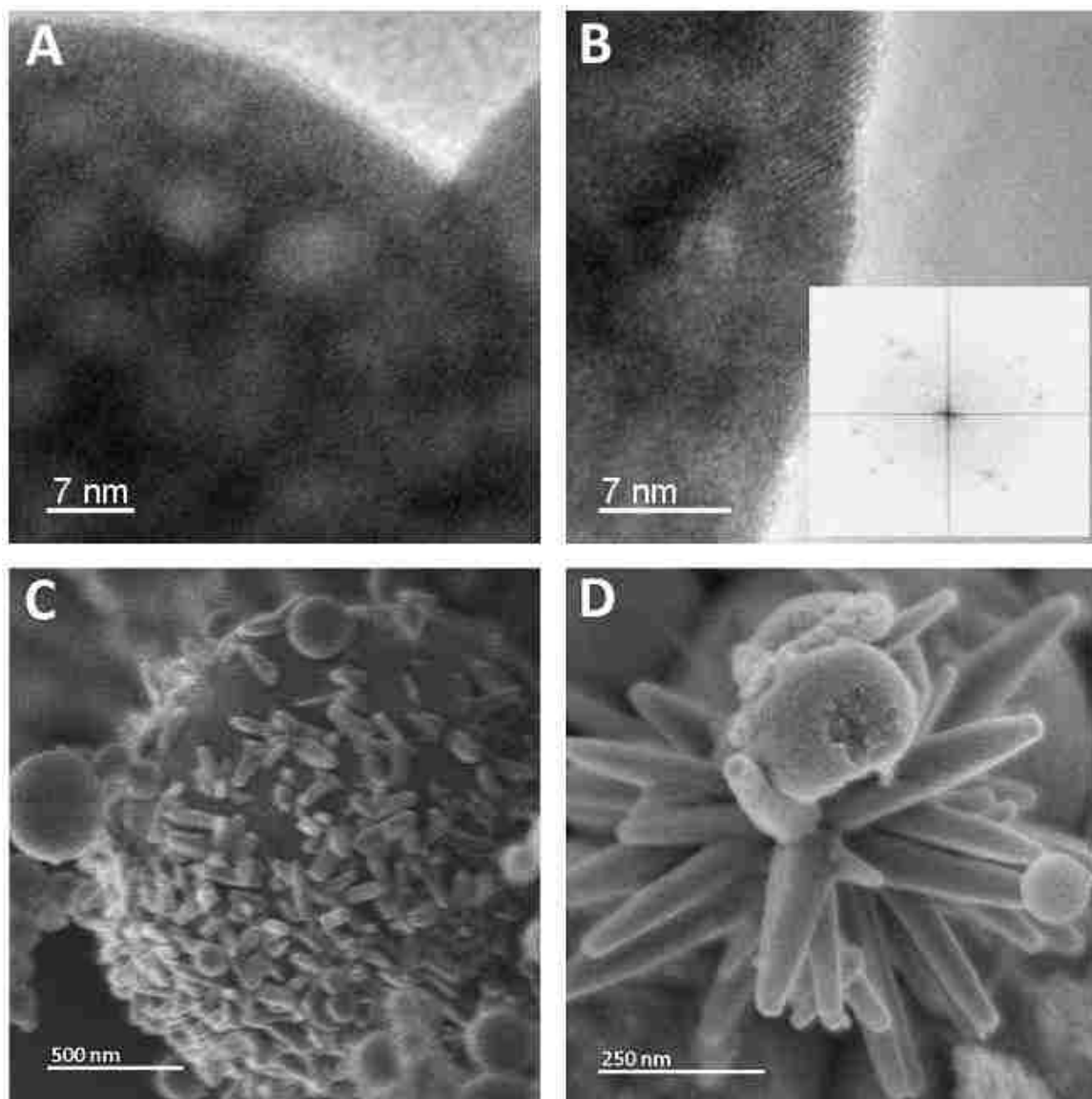


Figure 6.1: TEM showing (A) the 5-6 nm diameter mesopores of $\text{NbO}_x\text{-Dry-Air}$, and (B) lattice fringes of crystalline niobia formed in $\text{NbO}_x\text{-Dry-N}_2/\text{H}_2$. SEM of (C) NbRu_yO_z calcined in air without a washing step ($\text{NbRu}_y\text{O}_z\text{-Dry-Air}$), and (D) with a washing step ($\text{NbRu}_y\text{O}_z\text{-Wash-Air}$). (C) and (D) show nucleation of RuO_2 as surface crystallites and dendrites, respectively.

XPS results (not included here) of $\text{NbO}_x\text{-Dry-N}_2/\text{H}_2$ indicated the presence of Nb(IV) on the surface of the material, which is consistent with the color change to black, but it is likely the bulk remains as Nb(V) based on the high electrical resistance ($\sim 1 \times 10^7 \Omega$), which is consistent with reported values for Nb_2O_5 ^{60, 130}.

6.1.2 Ru-Modified Niobium Oxide

The Ru-modified niobium oxide (NbRu_yO_z) was also synthesized without an acid washing step and with calcination in air at 400°C for 4 h ($\text{NbRu}_y\text{O}_z\text{-Dry-Air}$). Close examination of the powders by SEM and EDS revealed that particles with diameters in the range of 800 nm to 1.5 μm were covered with what were apparently ruthenium oxide crystalline growths (Figure 6.1C). EDS of multiple such particles indicated an average ruthenium content of ~ 31 wt% with a range of 18-80%, much more than the expected amount, assuming RuCl_3 was homogeneously mixed in the precursor solution. NbRu_yO_z particles produced with a calcination in $\text{N}_2/10\%\text{H}_2$ ($\text{NbRu}_y\text{O}_z\text{-Dry-N}_2/\text{H}_2$) did not display the surface crystallization features by TEM that were seen with non-ruthenium containing particles under the same atmosphere. While all previous samples were electrically resistive, this material displayed no measurable resistance reading ($<0.01\ \Omega$), and had a BET surface area of $9.3\ \text{m}^2/\text{g}$. The relatively low surface area implies that much of the internal surface is still occluded; however enough of the material is apparently partially reduced to give the low resistance measurement and black color. Nevertheless, increased internal surface area is needed for a desirable support for an electrocatalyst such as Pt.

Despite the lack of an acid washing step to remove surfactant, the presence of ruthenium oxide surface crystals on the $\text{NbRu}_y\text{O}_z\text{-Dry-Air}$ samples clearly indicates that Ru species are able to permeate from the particle interiors during thermal post-processing. The ruthenium oxide surface deposition is apparently particle size dependent. In none of the Ru-modified samples produced do particles smaller than 260 nm have crystalline deposits on their surface, and EDS measurements on these particles indicates no significant Ru content. In contrast, particles that are roughly 800 nm in diameter and larger consistently

exhibit these crystals forming on their surface. It is consistent with diffusion principles that volatile Ru species would be able to diffuse to and escape from smaller particles more quickly than from larger particles during calcination. Apparently, when the system begins to cool at the end of the calcination step, the environment around the smaller particles is too depleted in Ru species to be conducive to ruthenium oxide nucleation and growth. However, the larger particles do apparently have a sufficiently high concentration of Ru vapor species near the surface to lead to nucleation and growth during cooling.

Nucleation of RuO_x on the larger particles surfaces could also be favored because of differences in surface composition. In addition, conditions are not homogeneous for particles at different locations inside the crucible during calcination/cooling, which could also contribute to our observations.

6.1.3 Effect of Acid-Wash Post-Treatment

With the introduction of an acid washing step before calcination in air at 400°C for 4 h, NbRu_yO_z -Wash-Air showed very dramatic localized Ru oxide crystalline growths. We believe that etching of the particle surfaces by the acid wash opens up internal porosity, reduces transport resistance for volatile species, and promotes the rapid evaporative loss of Ru from particle interiors during calcination. During cooling vapor Ru species apparently nucleate and grow in favored locations.

When the NbRu_yO_z is acid washed before calcination in a reducing atmosphere (NbRu_yO_z -Wash- N_2/H_2), the material was less, but still reasonably, conductive compared to NbRu_yO_z -Dry- N_2/H_2 , with a resistance of 950 Ohm, and had a much improved BET

surface area of 80 m²/g. EDS showed a reduced ruthenium content of ~6% (average over multiple particles), indicating some Ru loss relative to the solution composition, but much less loss than the NbRu_yO_z-Wash-Air material. Compared with the BET of mesoporous NbO_x-Wash-Air, there is a reduction of ~100m²/g in surface area, the reason for which is not completely clear, but it apparently related to interaction of the acid wash with the NbRu_yO_z material.

6.1.4 Optimized NbRu_yO_z Support

The initial intent of the acid wash step was to etch oxide and surfactant in the outermost, lamellar surface layers, opening up internal surface area and allowing better penetration of the reducing N₂/H₂ atmosphere into the particle interior without extensive degradation of the interior structure. On the basis of this objective, and the observation of significant surface area loss using the acid wash procedure, we tested a new etching procedure that utilized much less acid. With this treatment, NbRu_yO_z was wet by dropwise addition of 0.3M H₂SO₄ acid solution onto the powder inside a ceramic boat until all areas were wetted while maintaining the powder's original green color. The excessive acid addition associated with the "wash" step in the NbRu_yO_z-Wash-N₂/H₂ material led to a change in color from green to black before calcination, which is indicative of a change in oxidation state of the powder surface. The remaining inhibition to diffusion after the wetting procedure was apparently enough to limit significant Ru volatilization and surface area loss. After the reductive calcination, the resistance of NbRu_yO_z-Wet-N₂/H₂ was 2.3 Ohm, with a BET of 167 m²/g and ~12wt % Ru content as detected with EDS (average of multiple particles). This represented the most optimal combination of properties among powders synthesis and processing that were assessed in this work.

6.1.5 Porous Structure of Supports

Selected full N_2 adsorption-desorption isotherms were conducted to better characterize the differences in pore structure between NbO_x and $NbRu_yO_z$ powders. The pure niobia (NbO_x -Wash-Air) sample had a pore size distribution centered around 3.9 nm while the niobia/ruthenia sample ($NbRu_yO_z$ -Wet- N_2/H_2) was at 3.6 nm (Figure 6.2). Both values are similar to that of commercially available HY-340 (Nb_2O_5 , CBMM) with a mesopore diameter of 3.8 nm.

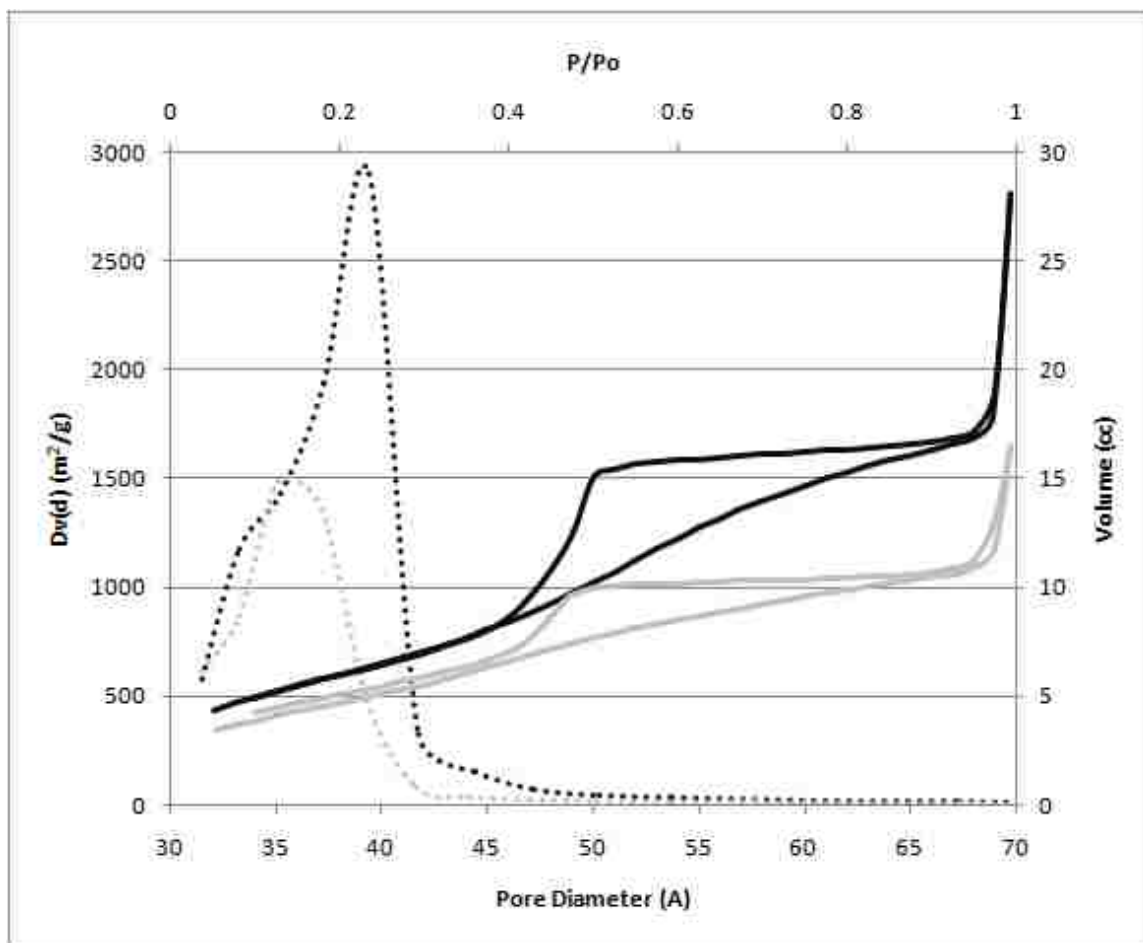


Figure 6.2: Adsorption-desorption isotherms in N_2 (solid, top and right axes) and corresponding pore size distributions calculated by the BJH method (dotted, bottom and left axes) for NbO_x -Wash-Air (dark) and $NbRu_yO_z$ -Wet- N_2/H_2 (light).

Calcination has typically been shown in the literature to cause pores to grow in size¹²⁶, which could uniquely alter the pore size distribution of different materials depending upon how they respond to thermal treatment. Despite the difference in pore size distributions, surface areas were very comparable at 183 and 167 m²/g for niobia and niobia/ruthenia samples, respectively. Both samples exhibited significant hysteresis of type H1/H2 according to the IUPAC model, common for mesoporous oxides^{79, 80, 127, 128}. Such hysteresis behavior is often indicative of pores that are necked or have restricted access. These results show that both samples are very similar structure. The observed hysteretic pore volumes were 13 and 11% for the niobia and ruthenium-modified niobia, respectively. Interestingly, the adsorption and desorption curves of NbRu_yO_z-Wet-N₂/H₂ do not merge at low pressures. This repeatable result is not fully understood, but could be due to swelling of the mesostructure during adsorption, which further exposes interior porosity that was previously inaccessible. Hysteresis then results during desorption when some N₂ is trapped within these pores.

6.1.6 Crystalline Structure of Supports

XRD was performed to determine crystallite development in selected powders. Patterns A and B in Figure 6.3 show XRD patterns for NbRu_yO_z-Wet-N₂/H₂ and NbO_x-Wash-Air. Both powders displayed poorly developed crystallinity, with no distinct crystalline component evident after calcination. However, the niobia powder had two clear broad peaks, indicating the onset of order, whereas the NbRu_yO_z sample appeared essentially completely amorphous. Both spectra are comparable to that attained by others^{64, 80} for material containing only Nb(V), though these data are insufficient to conclude on the degree of crystallinity or oxidation state. The incorporation of ruthenium in our materials

appears to delay the onset of niobia crystallization, an effect that is common for substituted or doped oxides. It can be concluded that the superior electrical conductivity of $\text{NbRu}_y\text{O}_z\text{-Wet-N}_2/\text{H}_2$ is not due to substantial crystallization of any component because the bulk of both samples was mostly amorphous.

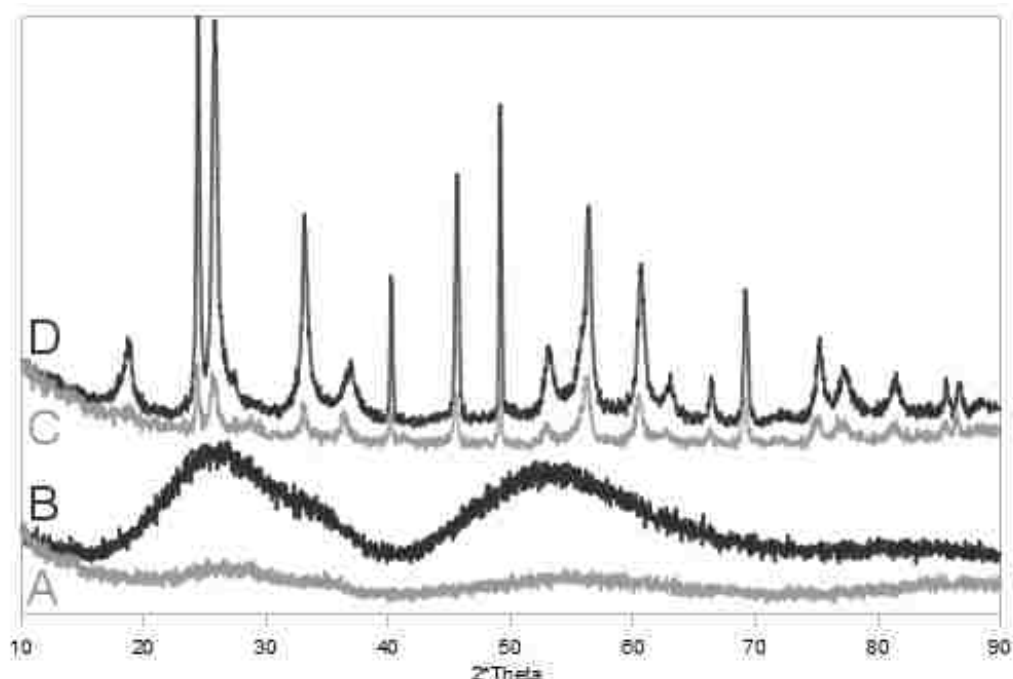


Figure 6.3: X-ray diffraction patterns from 10 to 90° 2 θ for (A) $\text{NbRu}_y\text{O}_z\text{-Wet-N}_2/\text{H}_2$ and (B) $\text{NbO}_x\text{-Wash-Air}$, as well as (C, D) both samples after additional heating at 900°C for 5 h in N_2 , respectively.

Additional heating of these samples at 900°C for 5 h in N_2 (Figure 6.3C and 6.3D) did lead to the development of well defined crystalline patterns. This is not surprising since crystallization of Nb_2O_5 into an orthorhombic structure is known to begin around 500°C^{82, 131, 132}. This is eventually followed by an irreversible transition to a monoclinic crystal state at ~900-1000°C^{64, 131}. The peaks for both powders were identically located with similar peak widths; however, the peaks for NbRu_yO_z were significantly lower in intensity. This indicates that, after heating to 900°C, the crystalline nature of NbRu_yO_z is

apparently the same as in pure NbO_x ; however, the relative amount of crystalline material is less. We were not able to index the peaks in C and D to known spectra of Nb(V), Nb(IV), or Nb(II) from the JCPDS database. However, a variety of sub-stoichiometric oxides exist for niobia-based materials that are highly dependent upon the method and conditions of preparation^{64, 131, 133}. In fact, the peaks observed in (C)/(D) are very similar to diffraction patterns published recently for single-crystal^{134, 135} and powder¹³¹ $\text{Nb}_{12}\text{O}_{29}$ and $\text{Nb}_{22}\text{O}_{54}$.

6.1.7 Surface Analysis

XPS high-resolution Ru 3d, Nb 3d, and O 1s spectra were also acquired from the NbO_x -Wash-Air and NbRu_yO_z -Wet- N_2/H_2 powders to provide oxidation state information. The Nb 3d spectrum acquired from both materials corresponded well to Nb_2O_5 (Figure 6.4B). The shape and position of Nb 3d spectra acquired from the NbRu_yO_z material (Figure 6.4A) is very similar to that of NbO_x , indicating that the oxidation states of surface niobium in each are similar. O 1s spectra and their curve-fits are shown in panels C and D in Figure 6.4. In the O 1s spectrum of the NbO_x material, the main peak is positioned at 530.6 eV and can be assigned to oxygen-bound to niobium in Nb_2O_5 . The peak at 531.6 eV can be attributed to surface OH- species. The last two components, at 532.8 and 534 eV can be assigned to adsorbed H_2O and/or CO and CO_2 species. The O 1s spectrum of the NbRu_yO_z material contains the same 4 peaks as that of the NbO_x material. The main difference between the two materials is the amount of oxygen associated with OH-, adsorbed H_2O and/or CO and CO_2 . The post reductive treatment of the material at elevated temperature in a N_2/H_2 atmosphere appears to result in a decrease in these species as compared to the post-treatment in air.

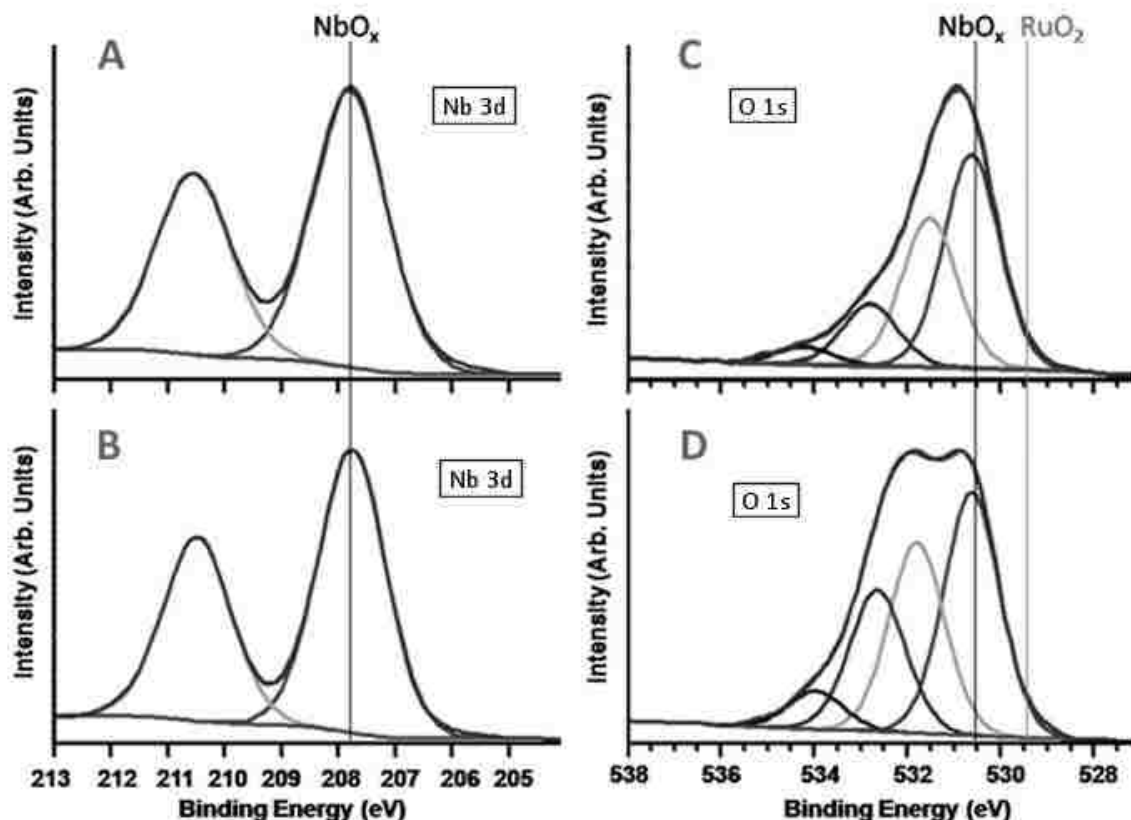


Figure 6.4: High-resolution XPS spectra: (A) Nb 3d spectrum of $\text{NbRu}_y\text{O}_z\text{-Wet-N}_2/\text{H}_2$, (B) Nb 3d spectrum of $\text{NbO}_x\text{-Wash-Air}$, (C) O 1s spectrum of $\text{NbRu}_y\text{O}_z\text{-Wet-N}_2/\text{H}_2$, and (D) O 1s spectrum of $\text{NbO}_x\text{-Wash-Air}$.

Interestingly, the peak indicative of ruthenium oxide at lower binding energies is not present. Another source of information regarding the oxidation state of ruthenium can be obtained from the Ru 3d spectrum. However, this is not straightforward because the binding energies (BE) of ruthenium and carbon species are in the same window. A high-resolution Ru 3d XPS spectrum acquired from these materials is shown in Figure 6.5. Ru 3d spectra have 2 spin-orbit components corresponding to the Ru 3d_{5/2} (lower BE side of Ru 3d) and Ru 3d_{3/2} (higher BE side). The separation between these components is 4.2 eV. Three doublet peaks in the Ru 3d spectrum correspond to ruthenium components and 5 peaks correspond to carbon components. The carbon components present in the

NbRu_yO_z material spectrum strongly coincide with carbon components present in the C 1s spectrum of the NbO_x material (Figure 6.5B), which does not have contributions from ruthenium. Typically, the BE of 5/2 component of metallic ruthenium lies in the 279.8-280.2 eV range and that of ruthenium in RuO₂ is in the range 280.5-281.0 eV. The first ruthenium component in the Ru 3d spectrum of the NbRu_yO_z material is at 281.3 eV, which is significantly higher than expected for metallic ruthenium and slightly higher than expected for RuO₂. This peak also cannot be assigned to a higher oxidation state. The second ruthenium peak in Ru 3d spectrum is around 282.3 eV, and can be assigned to hydrous ruthenium(IV) oxide. The third peak is around 284 eV and is attributed to RuO₄.

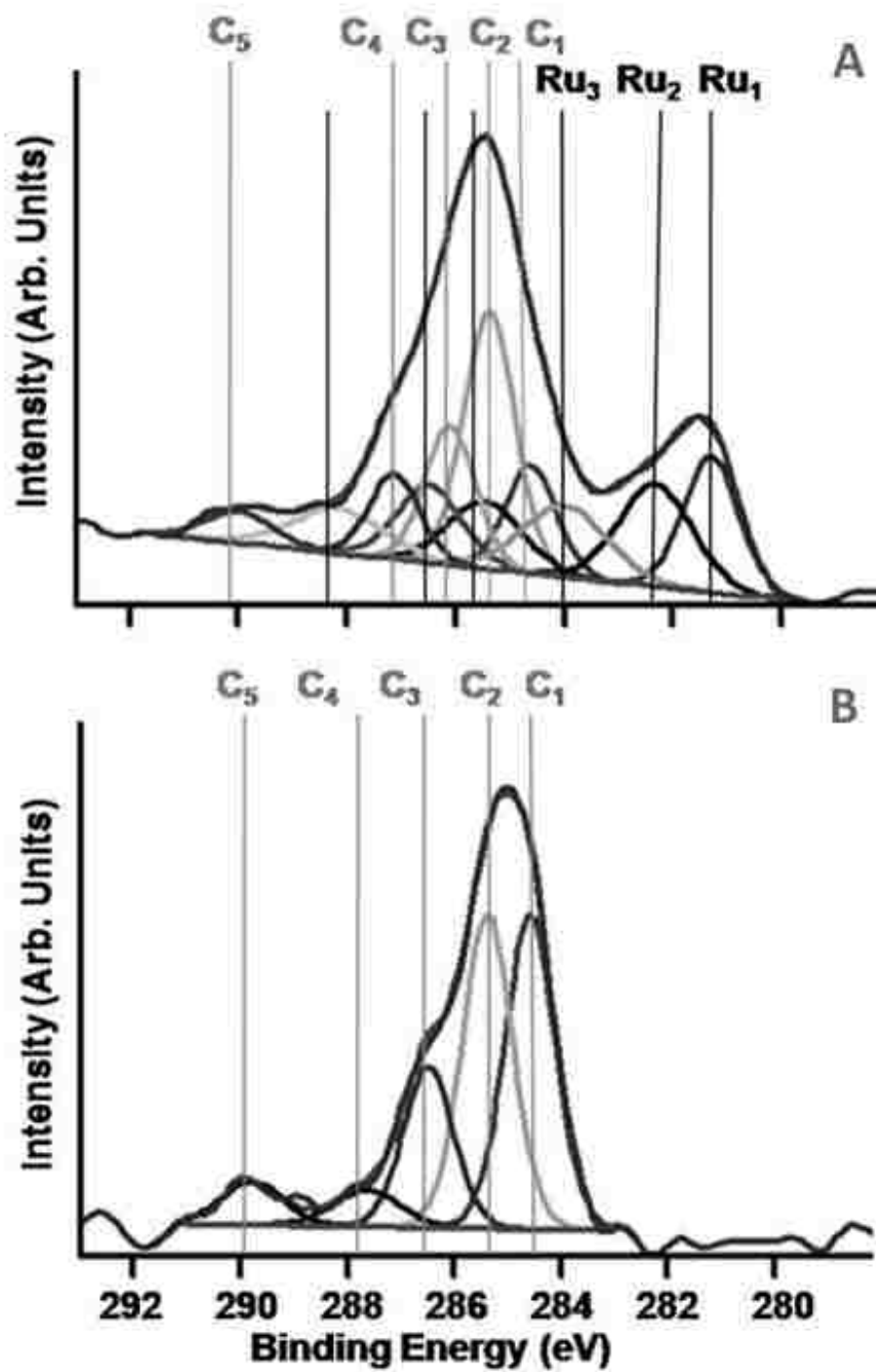


Figure 6.5: High-resolution Ru 3d and C 1s XPS spectra of (A) NbRu_yO_z-Wet-N₂/H₂ and (B) NbO_x-Wash-Air.

The absence of the RuO_2 peak in the O 1s spectrum, as well as the slightly higher than expected BE of the first ruthenium peak for RuO_2 , can be explained by the formation of a mixed Nb-Ru oxide. It is possible that incorporation of Ru(IV) into the Nb_2O_5 results in a shift of ruthenium BE to higher values, while the BE of oxygen bonded to ruthenium becomes indistinguishable from that of oxygen bound to niobium. Another observation that supports incorporation of ruthenium oxide into the niobium oxide matrix is the ratio of oxygen bound to niobium (from O1s spectrum) to niobium. In the NbO_x material O/Nb is around 2.7, which is very close to the stoichiometry of Nb_2O_5 . In comparison, the same ratio in the NbRu_yO_z material is around 1.9, and would be even lower were ruthenium content also considered. This means that the average number of oxygen atoms per metal atom in the NbRu_yO_z material is close to the stoichiometry of IV valency metal oxides.

6.1.8 Thermal Behavior of Support Materials

Thermogravimetric analysis was performed to mimic the entire post-treatment process of NbO_x -Wash-Air and NbRu_yO_z -Wet- N_2/H_2 to better understand the extent to which incompletely reacted precursors or impurities exist that may influence the powder properties, as well as to observe oxidation-reduction behaviors of the materials. After heating of the as-produced SP powders at 400°C for 4 h in their respective atmospheres in the TGA, both samples were then ramped at $10^\circ\text{C}/\text{min}$ to 1500°C in a N_2 atmosphere (Figures 6.6A and 6.6B). Weight decrease from 20 - 400°C can be attributed to loss of residual water and alcohol within the mesopores of the material, as well as much of the original surfactant. The rate of loss in NbRu_yO_z -Wet- N_2/H_2 is equivalent to that of NbO_x -Wash-Air, though delayed by roughly 60°C until $\sim 245^\circ\text{C}$ when the rate of loss from

NbO_x -Wash-Air decreases. This is possible because much of the ruthenium content is in the form of hydrous RuO_2 , wherein water remains stable slightly longer^{52, 53}.

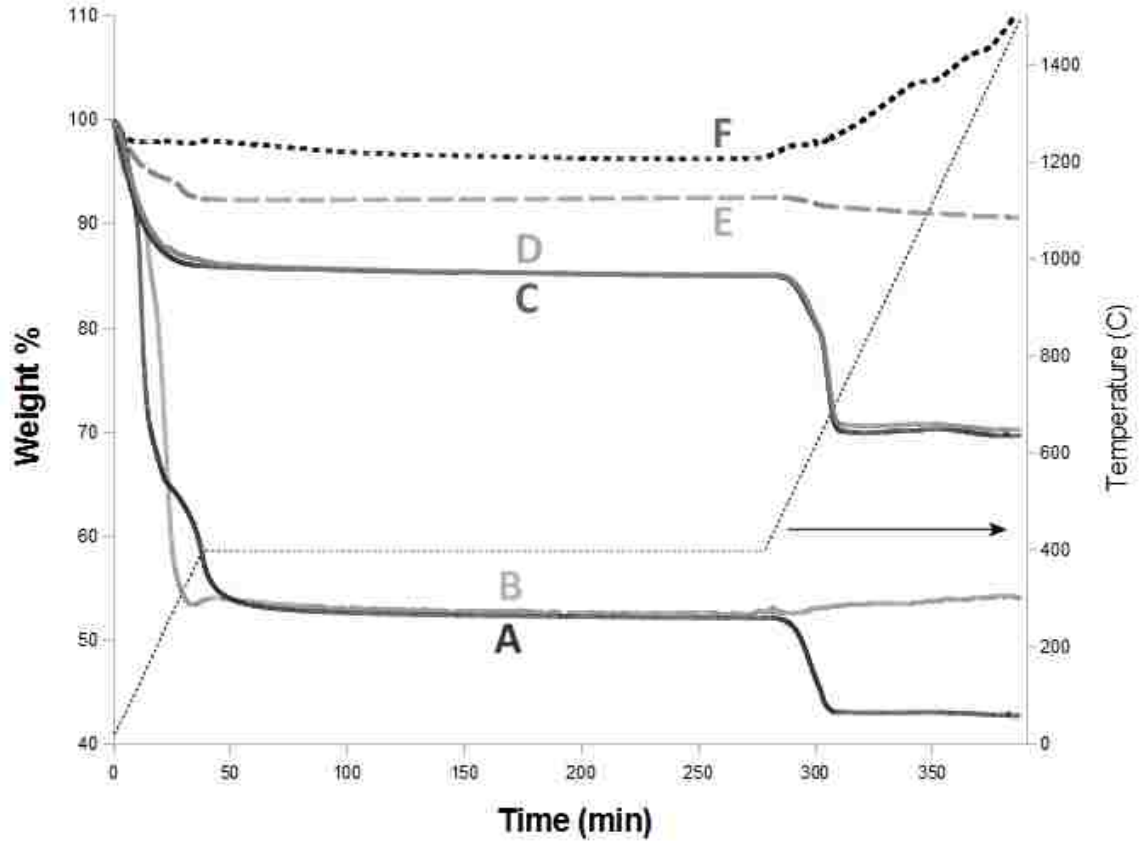


Figure 6.6: Thermogravimetric analysis of NbO_x -Wash and NbRu_yO_z -Wet under the same conditions experienced during post-treatment. Samples were ramped at $10^\circ\text{C}/\text{min}$ to 400°C in their respective atmospheres, where they were held for 4 h. All samples were then exposed to a N_2 atmosphere during heating from 400 to 1500°C at the same ramp rate. At temperatures of 400°C and below, (A) NbO_x -Wash was in air, (B) NbRu_yO_z was in $\text{N}_2/10\%\text{H}_2$, (C) previously post-treated NbO_x -Wash-Air was in air and (D) $\text{N}_2/10\%\text{H}_2$, and (E) previously post-treated NbRu_yO_z -Wash- N_2/H_2 and (F) NbRu_yO_z -Wet- N_2/H_2 were both in N_2 .

The difference in weight loss profiles A and B in Figure 6.6 seen from 0 to 50 min could be attributed to differences in the mobility of volatile species within each material, in combination with different rates of loss associated with particles of various sizes within the poly dispersed bulk. Complete dehydration may continue to 400°C and perhaps

beyond, and loss of P123 surfactant is expected to begin around 200°C and finish within the 4 h period held at 400°C. Throughout this holding period, both samples decrease equally in weight (47.9% loss for A and 47.3% loss for B), indicating that the different calcination atmospheres do not substantially affect the degree to which volatile species are removed from the materials.

Previously calcined samples of NbO_x-Wash-Air underwent the same temperature program in air (Figure 6.6C) and N₂ (Figure 6.6D). Both samples initially lost 14% of their weight, accounting for adsorbed water during their exposure to the atmosphere as collected powders. Furthermore, both samples had nearly identical weight loss profiles at all temperatures, indicating little difference between these two atmospheres for volatiles removal or oxidation state changes.

Similarly, NbRu_yO_z-Wash-N₂/H₂ (Figure 6.6E) and NbRu_yO_z-Wet-N₂/H₂ (Figure 6.6F) were heated under the same conditions as the samples in plots C and D in Figure 6.6. The NbRu_yO_z samples displayed less weight loss below 400°C than the NbO_x samples, indicating less residual water and alcohol. However, much more notable is the distinctly different behavior of the NbRu_yO_z and NbO_x samples above 400°C. All NbO_x samples in Figure 6.6 show an abrupt weight loss of roughly 17 wt% beginning at approximately 450°C, whereas all NbRu_yO_z samples show only a small weight decrease or a weight increase above 400°C. The NbO_x behavior is not yet fully understood; however, it seems likely that it may be related to the onset of crystallization since a series of crystalline structure transitions for niobia are reported to initiate at ~500°C (27). The behavior of the NbRu_yO_z samples above 400°C is likely related to slight changes in oxidation state related to the change in gas atmosphere at and above 400°C, possibly coupled with the

effect of temperature on residual volatiles or oxidation state. The sizable weight increase of NbRu_yO_z-Wet-N₂/H₂ (Figure 6.6F) is noteworthy, and supports the notion that this sample is more reduced than the other samples, which is consistent with the low resistance of that powder.

6.1.9 Electrochemical Characterization

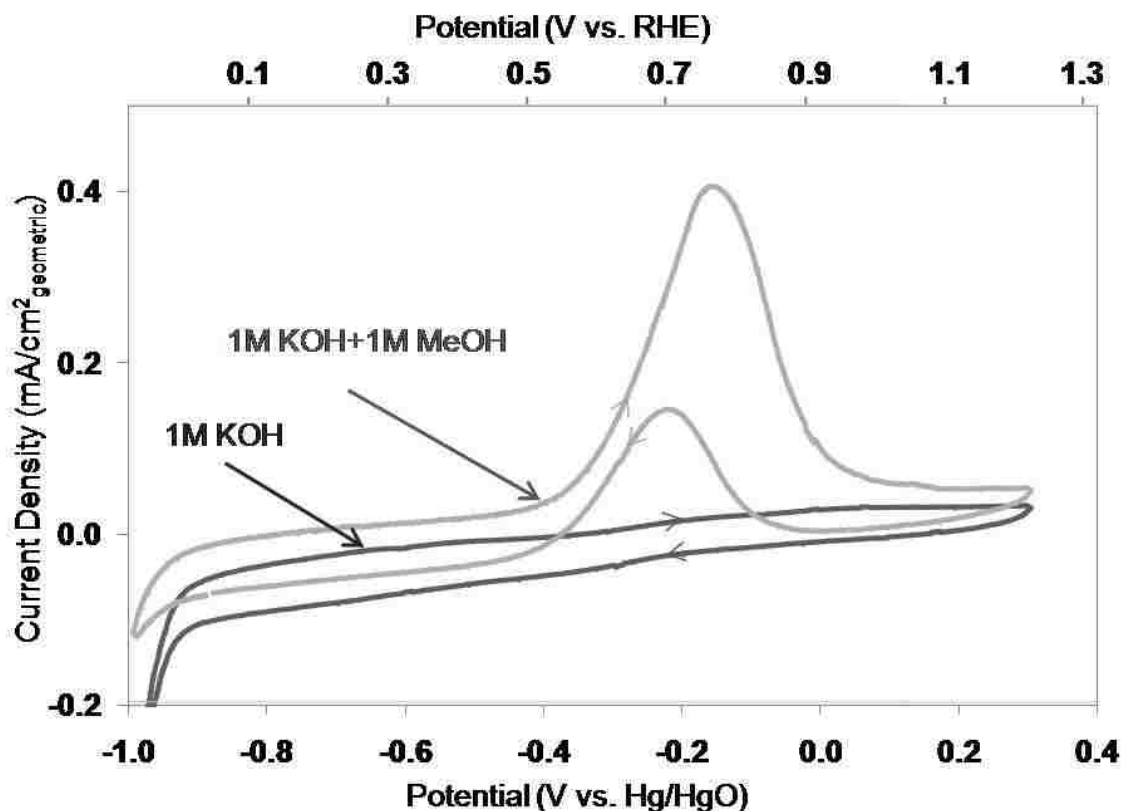


Figure 6.7: Cyclic voltammograms of 128 $\mu\text{g}/\text{cm}^2$ NbRu_yO_z-Wet-N₂/H₂ initially in 1 M KOH solution, and then with 1 M methanol added. Scan rate of 10 mV/s vs Hg/HgO reference electrode.

Based on superior surface area and low electrical resistance, the NbRu_yO_z-Wet-N₂/H₂ material was judged to have the best potential as a viable electrocatalyst support. That material was therefore selected for electrochemical characterization. Cyclic voltammetry in Ar-saturated 1 M KOH was used to address the feasibility of using NbRu_yO_z produced

by spray pyrolysis as a support for anode catalysts in fuel cells. Within the given range of potential of the cyclic voltammogram shown in Figure 6.7, there are no pronounced features until H_2 evolution at about -0.9 V. This indicates an absence of anion or cation adsorption on the electrode. Upon addition of methanol, the oxidative process indicates oxidation of the alcohol on the $NbRu_yO_z$ material. This shows that, unlike carbon, this $NbRu_yO_z$ support material does have some activity for the process of fuel oxidation. The onset of the oxidation process is expected to improve once platinum catalyst is incorporated on the support material.

6.2 Discussion

The changes experienced by a particle during the pyrolysis and post-treatment of metal-oxides are depicted in the illustration of Figure 6.8. Part of the significance of this study is derived from the control that is possible with this process.

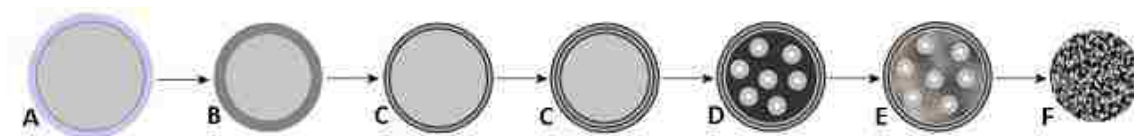


Figure 6.8: Schematic depiction of transformations that occur during spray pyrolysis of Nb/Ru precursor solution containing a surfactant template, followed by post-treatment. (A) Evaporation begins as a vapor layer forms around the droplet. (B) Precipitation of the outer surface. (C) Outer layers begins to dry faster than interior moisture diffuses to the surface, resulting in formation of vesicles from surfactant. (D) Entire droplet eventually dries. (E) Thermolysis of chloride precursors into porous metal oxides. (F) Proper post-treatment exposes the intact mesoporous structure.

Aerosolization produces homogeneous liquid droplets of the same composition as the precursor solution. Evaporation of solvents from the droplets then proceeds (A), leading to solute precipitation. Because solvent evaporation occurs from the droplet surface, solute concentration gradients develop inside droplets that typically results in precipitate

or solid formation first at the droplet surface (B). For the same reason, during EISA in evaporating droplets, concentration gradients of the surfactant (P123) will develop that trigger the surfactant liquid crystalline (LC) phase transformations, usually first at the surface of the droplet. Continued solvent evaporation leads to the propagation of surfactant LC transitions into the interior of the droplet. Because of the very short evaporation times of submicrometer droplets, much of this may happen even before droplets enter the furnace zone. The higher temperatures of the heated zone complete solvent evaporation, and drive decomposition of the precursor compounds, effectively locking in any surfactant-related mesostructure that has developed. The LC mesostructural phases that form depend on the particular phase behavior of the surfactant, and the concentrations that develop during solvent evaporation. For the case of P123 under the conditions employed here, electron microscopy indicates that a lamellar phase often forms at the surface first (C), followed by a wormlike or hexagonal mesophase in the interior of particles (C and D in Figure 6.9). As this work shows, if the collected powder receives the proper post-treatment, the process yields particles with fully exposed, mesoporous interiors (F).

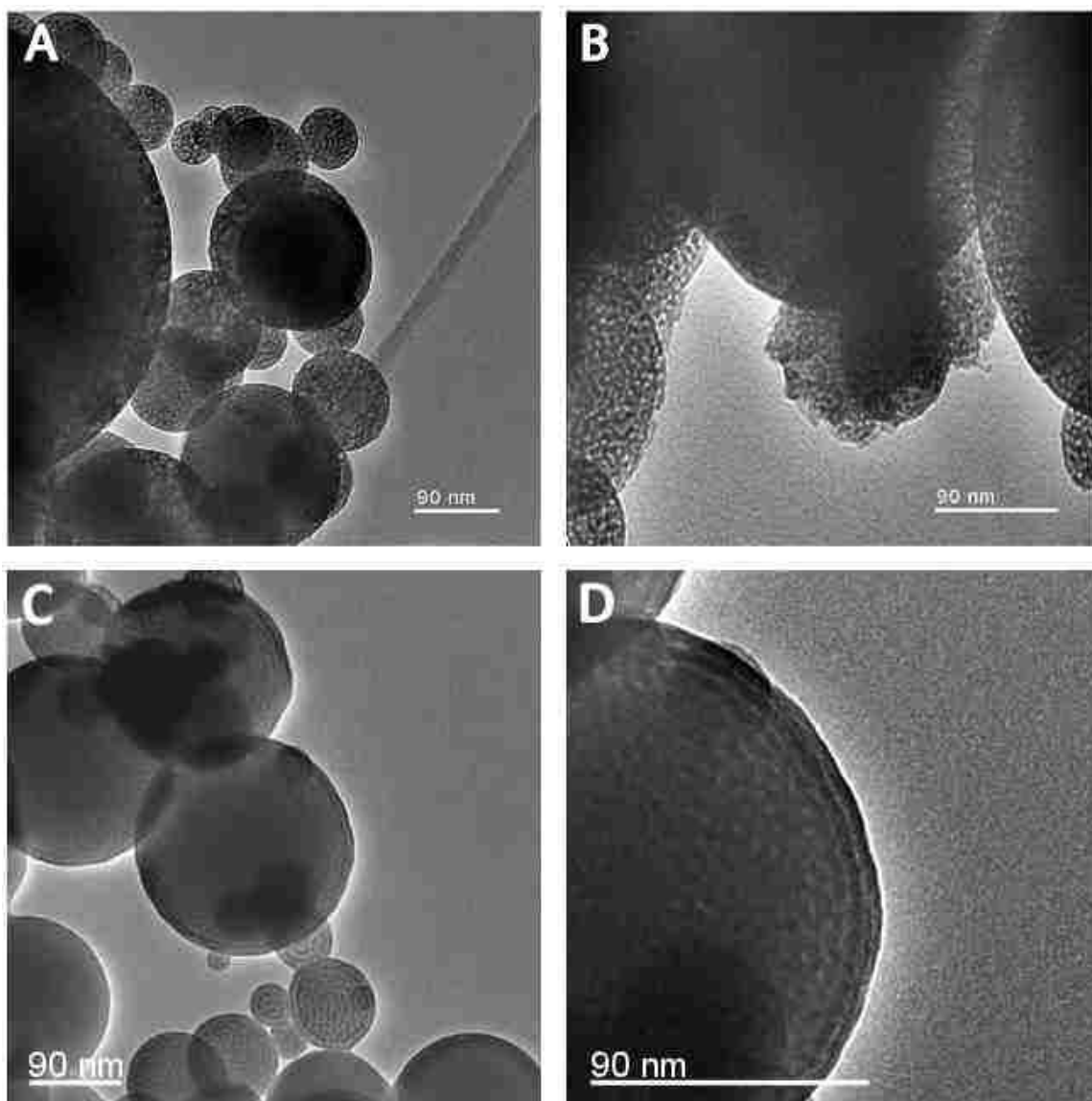


Figure 6.9: TEM of (A) NbRu_yO_z -Dry-Air (calcined without a washing step), and (B) STEM of NbRu_yO_z -Wet- N_2/H_2 (calcined with a preceding acid washing step). (C) NbRu_yO_z particles of various sizes before any post-treatment, showing a 3D wormhole porous structure in the particle interior and 2-3 exterior lamellar layers. (D) Higher-magnification clarifies the separate structures.

TEM micrographs C and D in Figure 6.9 are representative of the structure depicted in illustration (E) of Figure 6.8: NbRu_yO_z particles collected directly from the filter paper show a visible mesoporous interior isolated by 2-3 lamellar layers at the surface. Those layers apparently collapse upon removal of their surfactant scaffolding and partially

sinter when this material is calcined in air, as do the structural walls of the interior, resulting in larger, more visually distinct pores (Figure 6.9A). Interior surface area may not be fully accessible and residual organic material from any remaining surfactant may be kinetically trapped within particles under these conditions. Larger particles sometimes rupture, apparently due to interior pressure buildup associated with restrictions on the escape of volatiles (Figure 6.10). After acid etching, the lamellar surface layer appears to be gone (Figure 6.9B), and calcination effectively removes organics and opens up internal surface area, as supported by the TGA results and surface area measurements reported.



Figure 6.10: SEM image of a particle fragment of NbRu_yO_z-Dry-Air. During spray pyrolysis or thermal processing, particle surfaces may become nearly impermeable before volatile species can escape to the atmosphere. The pressure developed by these trapped volatiles is sometimes sufficient to fracture some particles.

Because of the submicrometer droplet and particle sizes in aerosol pyrolysis, and the nanoscopic dimensions of the pore structures, multicomponent aerosol-derived materials such as these can be very sensitive to evaporative loss of species that have a significant vapor pressure at the processing conditions. Preferential evaporative loss of one element

can lead to compositional deviations within the parent particles, and the volatilized material may migrate and end up elsewhere as a coating or distinct phase. Relevant to this work, it has been reported that ruthenium species possess a significantly lower energy of vaporization compared to niobium^{136, 137}. This is consistent with the observations in this work of Ru depletion in powders calcined at 400°C, though as-produced powders made at 200°C did not have substantial Ru depletion.

CHAPTER 7 - Platinum Catalyst on NbRu_yO_z

7.1 Synthesis of Electrocatalysts

H₂PtCl₆*6H₂O and NbCl₅ powder were acquired from Sigma-Aldrich, RuCl₃ from Fischer Scientific, and Pluronic-123 (nonionic triblock copolymer) from BASF. Ludox TM50 colloidal silica solution (aqueous, 20nm silica particles) was also obtained from Sigma-Aldrich.

Pt-SP: 2.0g of P123 block co-polymer surfactant (BASF) were dissolved in 22.0g of ethanol (200 proof) by mixing for 30 min. 1.1g of NbCl₅ was added to the solution and mixed until the solution changed from yellow to clear (5 min). To completely dissolve the ruthenium precursor, it was necessary to first mix 1.0g of H₂O into the solution. This was then followed by 0.12g of RuCl₃ and 1.2g of H₂PtCl₆*6H₂O. After stirring for 30 min, a black solution was obtained indicating that ruthenium was well mixed into solution.

Pt-DI: A similar process was followed, instead using 3.7g of NbCl₅, 0.385g of RuCl₃, and 0g of Pt precursor. All other steps remained unchanged.

Pt-TM: All conditions were identical to that of Pt-SP, except that carbonaceous surfactant was not used. Instead, the material was templated with TM-50 silica spheres to achieve a higher surface area support.

Pt-300 & Pt-650: The same conditions for Pt-SP were used to achieve a sample with 6Pt:1Nb:1Ru:2O wt%. This sample was then divided into halves. The two halves were separately heated to 300°C and 650°C for 3hrs in 10% H₂/N₂.

Pt-C: 30% platinum supported on XC-72 was obtained from E-Tek and used as received.

All electrocatalyst powders were synthesized using the spray pyrolysis apparatus described elsewhere¹³⁸. The precursor solutions were forced through an atomizer by an N₂ carrier gas at 30psi at a rate of 1.5 SLM (standard liters per minute). This creates a stream of liquid droplets suspended in the inert gas as an aerosol. The stream was fed through a tube furnace at 220°C, wherein droplet dehydration yielded particles. The particles underwent partial decomposition of precursor metal chlorides into metal oxides, and were collected as a bulk powder on a porous membrane filter.

Powders were collected from the filter and transferred to a crucible where they received varying post-treatments. Pt-DI received dropwise addition of 0.3M H₂SO₄ until the entirety of the powder was visually damp. Addition of excess acid solution before post-synthesis thermal treatment was detrimental to the formation of a homogeneous, mixed-metal phase. Once completely dry, the powder was placed inside a tube furnace with a flowing atmosphere of 10% H₂/N₂ and heated at a rate of 10°C/min until reaching 400°C where it was held for 4hrs. During this treatment, most of the P123 surfactant is thermally removed and the NbRu_yO_z particles reduced to a lower oxidation state. This also served to activate the surface of Pt nanoparticles in samples initially containing all three metals. Afterward, the mesoporous NbRu_yO_z powder (Pt-DI) was placed inside a clear vial. A water/acetone solution of H₂PtCl₆*6H₂O was added dropwise. The powder was allowed to dry completely between drops to facilitate penetration into the mesopores. Once a loading of 30wt% Pt was achieved, the powder was filter washed in H₂O, and

again placed in the furnace and heated to 250°C at a rate of 5°C/min in 10% H₂/N₂ and held for 2 hrs to activate the Pt catalyst.

Pt-SP and Pt-TM did not receive any dilute acid solution before receiving the same heating treatment described for Pt-DI. After heating, Pt-TM was agitated in 5M KOH solution for 4 days to etch away the Si spheres. The sample was then filter-washed in H₂O before drying in an oven at 70°C over night.

Additional platinum was deposited onto Pt-DI on a glassy carbon electrode in the absence of atmospheric oxygen using the cation-adsorption-reduction-galvanic-displacement method¹³⁹ inside a chamber purged with argon, described elsewhere¹⁶. The electrode was immersed in a solution containing Pb²⁺ stabilized at pH~11. In this environment Pb²⁺ cations only adsorb onto metallic or slightly oxidized surfaces, limited to existing Pt or Ru/RuO_x sites, while deposition onto niobia does not occur. The electrode was then immersed in a fresh, lead-free solution where previously adsorbed Pb²⁺ atoms were potentiostatically reduced to Pb⁰. The electrode was immersed in a third solution containing Pt²⁺, wherein Pb⁰ atoms were displaced by Pt atoms. The process is relatively fast and is self-terminating at approximately one monolayer of coverage. The overall effect is the restoration of the original Pt surface area free of any surface deactivating species related to the presence of oxygen. This sample, after a monolayer equivalent amount of Pt has been deposited, is referred to as Pt-ML.

7.2 Verification of Pt with Electron Microscopy

7.2.1 30%Pt/NbRu_yO_z (Pt-DI)

SEM imaging was used to visually identify the successful deposition of Pt nanoparticles on the NbRu_yO_z support (Fig.7.1). The collection of secondary electrons (SE) shows a topographical image of the spherical support morphology and verifies the polydisperse nature of the powder, with particle diameters ranging from 50nm to 4μm. A backscattered electron (BSE) detector is used to distinguish metals of different atomic number. The brighter areas in Fig.7.1B&D represent the heavier element, Pt. A range of Pt particle sizes are visible, from 5nm nanoparticles (lower resolution limits of the microscope) to 200nm nanoparticle clusters.

Pt nanoparticles 5-15nm are visible on NbRu_yO_z particles of size ~500nm or less in diameter using TEM (Fig.7.1E). Larger niobia particles may also have these smaller Pt particles on their surfaces and inside of their pores, but particle depth and weaker contrast between Nb/Ru and Pt (all large in mass) obscure their visibility. Overall penetration of Pt into the mesopores is difficult to assess. However, EDS measurements confirm a Pt loading of 30%, as well as the expected stoichiometry of the NbRu_yO_z support (8Nb:1Ru), and the removal of chlorine. The surface area decreases from 167m²/g to 70m²/g after the addition of Pt.

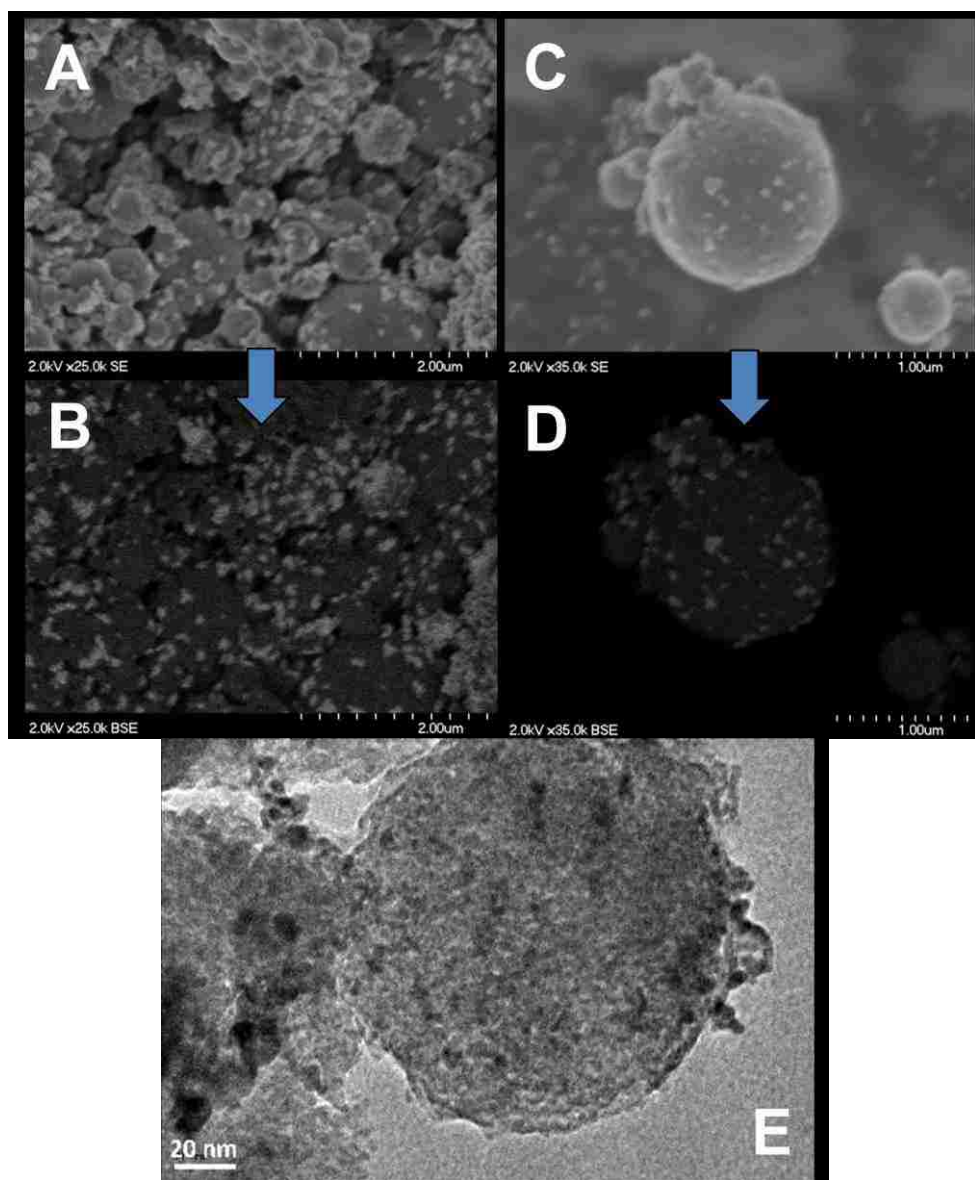


Figure 7.1: SEM images showing large platinum nanoparticles in Pt-DI utilizing Secondary Electron (A,C) and Backscattered Electron (B,D) detectors. (E) TEM image of a particle showing some visible catalyst penetration into the mesoporous support interior. Overall, a range of Pt particle sizes are visible, from 5nm nanoparticles to 200nm nanoparticles/clusters.

7.2.2 60%Pt/NbRu_yO_z (Pt-SP)

TEM images verify the formation of Pt nanoparticles from the NbRu_yO_z support (Fig.7.2). Immediately after spray pyrolysis, Pt nanoparticles of ~2nm decorate the support particles, while much of the Pt remains within the particle bulk.

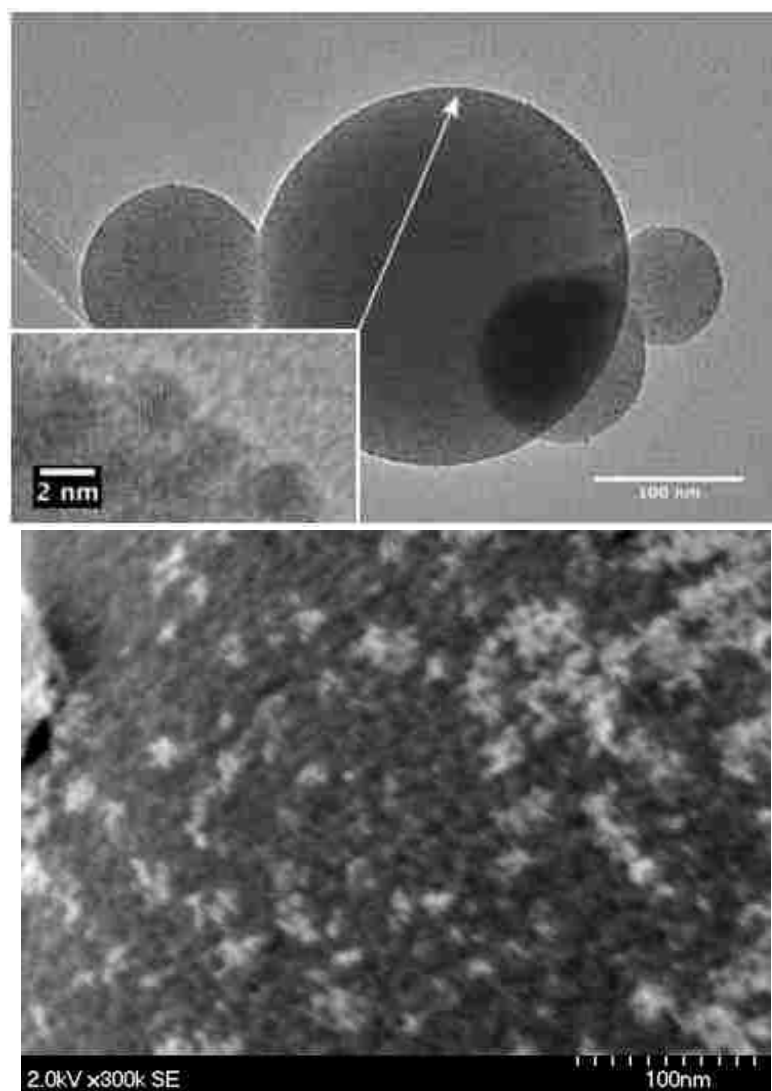


Figure 7.2: (Top) TEM image of 60%Pt/NbRu_yO_z immediately after spray pyrolysis. The inset shows the presence of Pt nanoparticles 2nm in diameter. (Bottom) SEM image of the same material after post-treatment, showing some catalyst clustering on the porous support surface.

The bottom SEM image in Fig.7.2 shows an instance of a much larger support particle (~1 micron or greater) with Pt nanoparticles decorating the surface. Unlike the impregnated sample, there are no visible Pt nanoparticles greater than ~20nm (confirmed in TEM). The rough, visually distinct surface in this micrograph is suggestive of the support's mesoporous structure similar to that observed for other high surface area samples. However, the BET surface area is reduced to $6\text{m}^2/\text{g}$. This could indicate that the mesopores of the support are largely obstructed by Pt nanoparticles.

Overall, the formation of Pt nano-particles using an in situ SP approach appears to yield much better Pt dispersion on NbRu_yO_z . The impregnated sample has much larger nanoparticles, which implies a greater ratio of bulk to surface Pt atoms and fewer in direct contact or within immediate proximity of the NbRu_yO_z support.

7.3 X-ray Studies

7.3.1 X-ray Diffraction of the Pt Structure

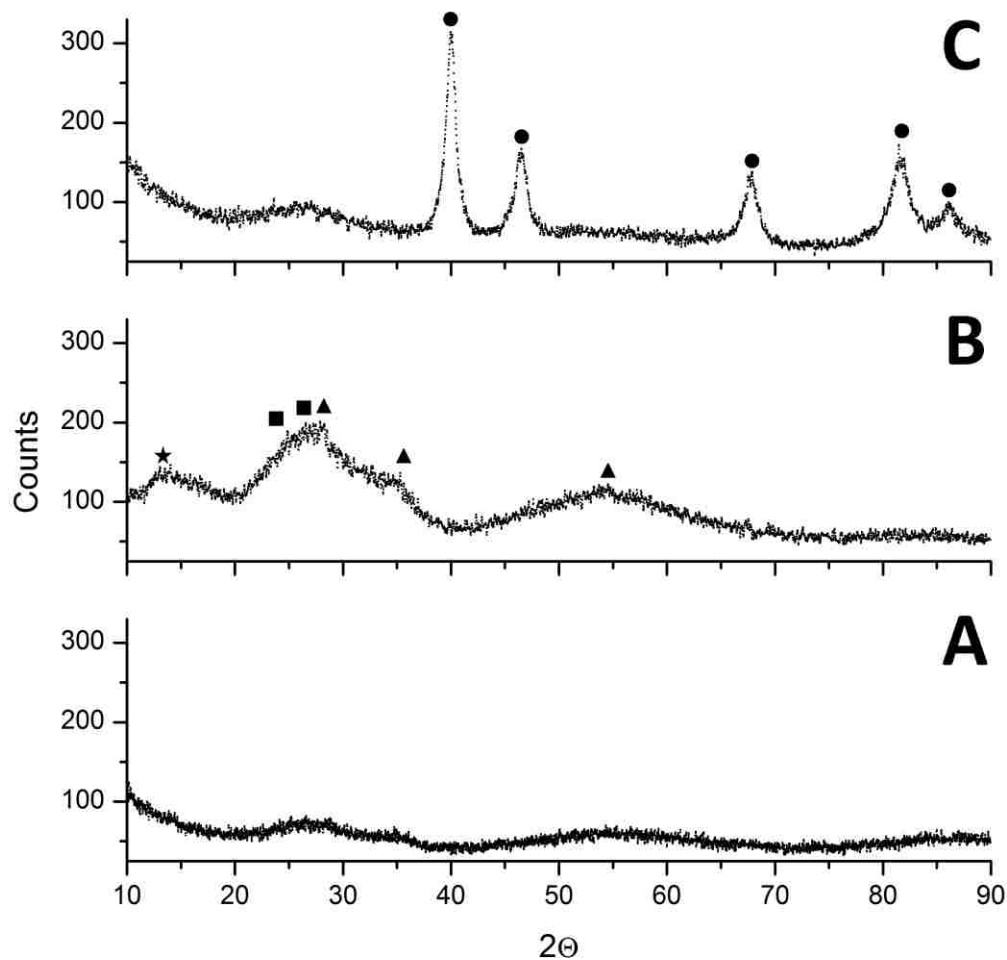


Figure 7.3: (A) The NbRuOz support of Pt-DI is mostly amorphous after spray pyrolysis. (B) There is some increase in ordered structure after post-treatment, possibly due to uptake of moisture/carbon species in the form of RuO_2 (triangle), RuO_4 (square), and RuCO_4 (star). These features mostly disappear after wet impregnation of Pt. (C) Pt peaks (circle) are distinct due to larger nanoparticles visible in SEM, shown on the next slide.

The range of temperatures to which Pt-SP and Pt-DI were exposed during synthesis was 25-400°C. This is 100°C or more below the crystallization temperature of niobia, whereas platinum and any unabsorbed ruthenium exhibit crystalline structures due to higher volatilities ⁶⁷. Therefore, x-ray diffraction can reliably monitor the formation of crystalline catalyst structures within this temperature range without interference from the support. XRD measurements were made after each step in the synthesis process.

Fig.7.3A shows that the NbRu_yO_z support is mostly amorphous immediately after spray pyrolysis. After acid-wet and thermal post-treatments some residual features are present, possibly resulting from the formation of hydrous and carbonaceous species from solution and the decomposition of surfactant, respectively (B). We previously showed that hydrous ruthenium phases can form quite easily ⁵². These features disappear after Pt impregnation, shown for Pt-DI (C). This is likely because of the thorough filter-washing process. Sharp platinum peaks are evident due to the larger nanoparticles observed in SEM. In each step, there is also evidence of an incoherent range of peaks possibly attributable to RuO₂, RuO₄, and RuCO₄. This could suggest that any RuO_x or PtRu compositions formed are small enough in size to be below the limits of the detector, while most of the ruthenium remains within the niobia matrix as a mixed metal oxide.

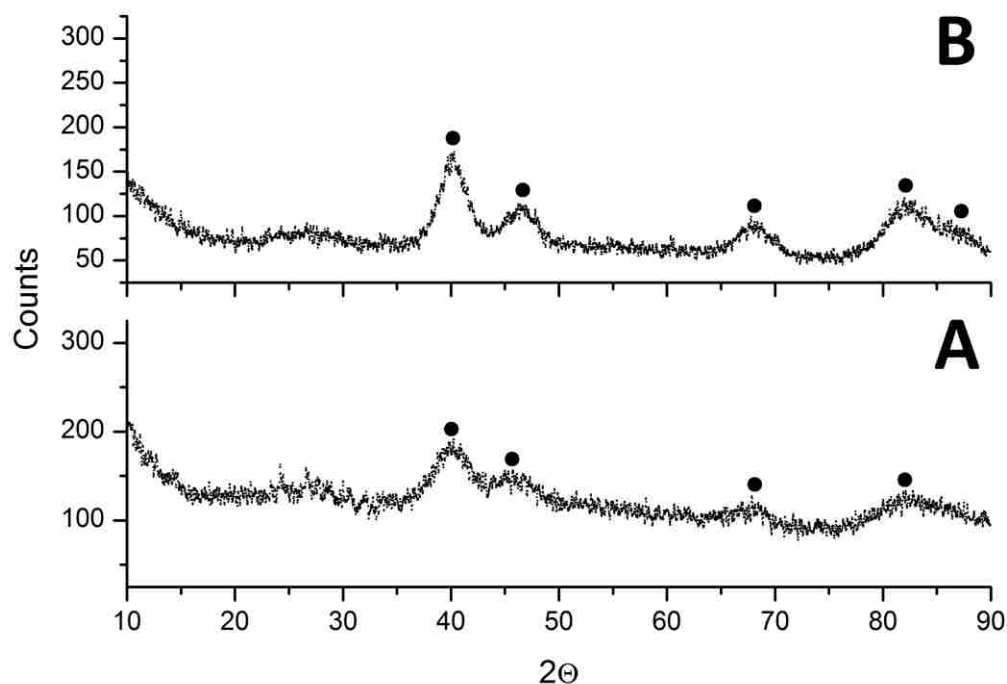


Figure 7.4: Pt-SP: (A) Broad Pt peaks are visible and indicative of nanoparticles in the amorphous niobia matrix after spray pyrolysis. (B) After calcination at 400°C for 4hrs in 10% H_2/N_2 . Both (A) & (B) show a range of low intensity peaks from 20-35(2θ) associated with RuO_x at various oxidations states, and possibly also PtO_x species.

Two spectra are shown for the Pt-SP sample in Fig.7.4, taken after spray pyrolysis (A) and again after thermal reduction (B). Though this sample contains twice the amount of platinum deposited on Pt-DI, the peaks are broader. This is consistent with the smaller diameters of Pt nanoparticles observed in TEM and SEM. After thermal treatment, the peaks increase in sharpness only slightly, while the residual peaks from 20°-35° become less coherent. The powder remains highly amorphous.

7.3.2 X-ray Photoelectron Spectroscopy

XPS provides elemental and chemical information from the sample's surface to approximately 10nm depth. Taking into account the small size of Pt nanoparticles on our samples, XPS is likely yielding information about the surface as well as the bulk composition. Table 7.1 shows the elemental compositions of Pt-DI and Pt-SP. Approximately 15% of C is present in both samples as adventitious contamination as well as from use of ethanol as solvent during synthesis. Pt-SP has almost twice as much Pt as Pt-DI sample. 30-35 % niobium is detected in both samples.

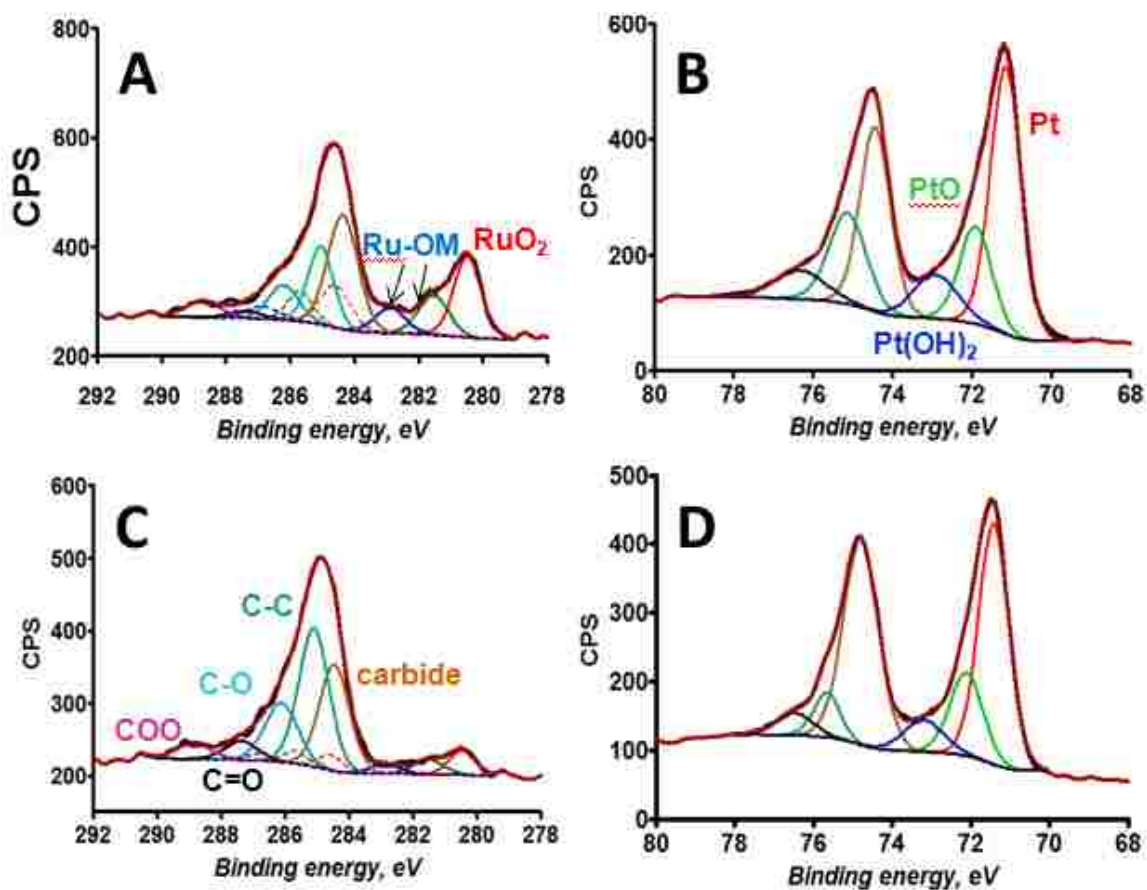


Figure 7.5: XPS Spectra of (A) Ru 3d/C 1s and (B) Pt 4f for Pt-DI, and (C) Ru 3d/C 1s and (D) Pt 4f for Pt-PS.

The ability to discriminate between different chemical environments, in addition to obtaining elemental compositions, is one of the primary advantages of XPS in the characterization of heterogeneous catalysts. Fig.7.5 shows Ru 3d/C 1s and Pt 4f high resolution spectra from two samples and Table 7.2 shows corresponding spectral curve fit results. The Nb 3d spectrum (not shown) showed one symmetrical peak for both samples at binding energy specific to Nb₂O₅.

Table 7.1: XPS Elemental Composition (wt%)

Sample	C 1s%	Nb 3d %	Ru 3d %	Pt 4f %	O 1s %
Pt-DI	13.0	36.3	5.8	18.6	26.2
Pt-PS	16.8	31.5	2.0	29.5	20.2

Table 7.2: Relative Elemental Moieties (at%)

Sample	Carbide	C-C	C-O	C=O	COOH	RuO2	Ru-OM	Pt	PtO	Pt(OH) ₂	Nb ₂ O ₅	
BE, eV	284.4	285.1	286.2	287.3	288.9	280.5	281.5	282.8	71.3	72.0	73.1	207.4
Pt-DI	40.6	34.4	16.0	3.1	5.9	68.8	19.4	11.7	58.6	30.3	11.2	100.0
Pt-PS	27.8	41.2	19.6	6.5	4.8	58.2	26.2	15.6	58.4	28.2	13.3	100.0

The Ru spectrum is overlapped with that of C 1s. A curve fit of the Ru spectrum is discussed in details in Experimental part of the article. Three peaks detected in Ru are due to RuO₂ and organometallic Ru in Ru-(C_xH_y)_z type of environment. Slightly more RuO₂ is present in the 30%Pt sample. Five peaks are used to curve fit the rest of the spectrum due to various carbon species, such as carbide, aliphatic carbon and different types of C-O moieties. There is slightly less carbide and more aliphatic carbon for Pt-SP. Pt 4f spectra of both samples are very similar. Virtually identical speciation is detected. Approximately 60% of total Pt is metallic, 30% as PtO and 10% as hydroxide. This distribution of Pt types is very similar to that of Pt on XC72R¹⁴⁰. Guerrero et al. (2009) showed that ~40% of the platinum (nanoparticles) on niobia is maintained as Pt⁺² in a

reducing atmosphere at high temperatures normally sufficient for Pt reduction to a metallic state. Interestingly, Ru, Pt and Nb are very similar for both samples, independent from carbon, which varies greatly between the two samples.

7.3.3 X-ray Absorption Spectroscopy

Fig.7.6 shows XANES spectra of the Pt L3 edge from nanoparticles prepared by dry impregnation and spray pyrolysis methods, together with that from a Pt reference foil. It is interesting to note that the spray pyrolysis method produces a smaller white line than that of the Pt foil. The intensity of the white line is inversely proportional to the d-band occupancy. This result indicates that the electron population in platinum of Pt-SP is higher than that of Pt bulk. One plausible explanation is that this may be due to defects in NbRu_yO_z surface resulting in oxygen vacancies. It is known that in some oxides electrons are trapped inside the oxygen vacancies on the surface. Thus, they can donate electrons to Pt if it is deposited on top of the oxygen vacancy.

The lower white line observed for the spray pyrolysis method suggests a decrease in Pt d-band vacancies, thereby leading to the higher d-band center¹⁴¹. As a consequence, molecule adsorption on the Pt surface can be strengthened. One may consider that the suppressed ethanol oxidation activity at potentials above 0.7V observed for Pt on NbRu_yO_z substrates synthesized by spray pyrolysis is caused by poisoning due to the strong adsorption of intermediates on the Pt surfaces.

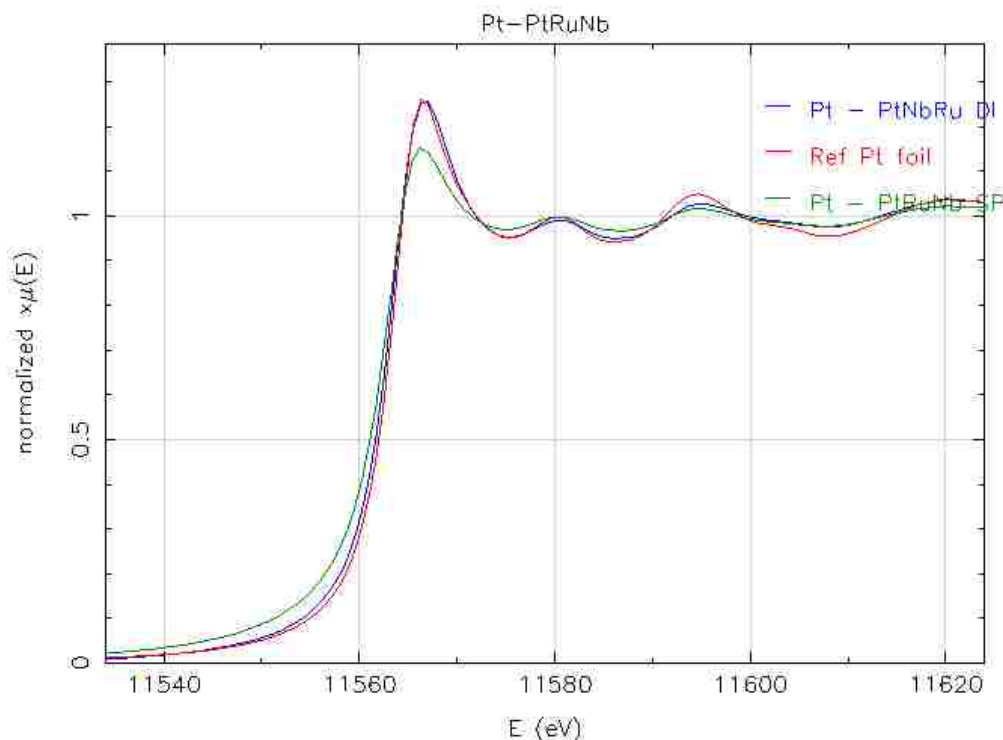


Figure 7.6: XANES spectra of Pt L3 edge from PtNbRuO_x nanoparticles prepared by the wet impregnation (blue) and spray pyrolysis (green) methods, together with that from a Pt reference foil (red).

Fig.7.7 depicts Fourier transformed EXAFS spectra of the Pt L3 edge from Pt nanoparticles prepared by dry impregnation (Fig.7.7a), and spray pyrolysis (Fig.7.7b) methods. The shoulder around 2 Å comes from oxygen contribution, so that the fitting was performed based on Pt-Pt and Pt-O paths. The presence of Pt-O bonds can be explained by formation due to the surface oxidation of Pt deposits in air and/or oxygen from NbRu_yO_z in which the Pt deposits are embedded. The coordination numbers obtained from the fittings are 7.4 ± 1.2 for the spray pyrolysis method and 10.2 ± 1.2 for the dry impregnation method; based on these coordination numbers we estimate that the average diameter of the Pt deposits by the spray pyrolysis method is smaller (ca. 2 nm) than that of the dry impregnation method (ca. 4.5 nm).

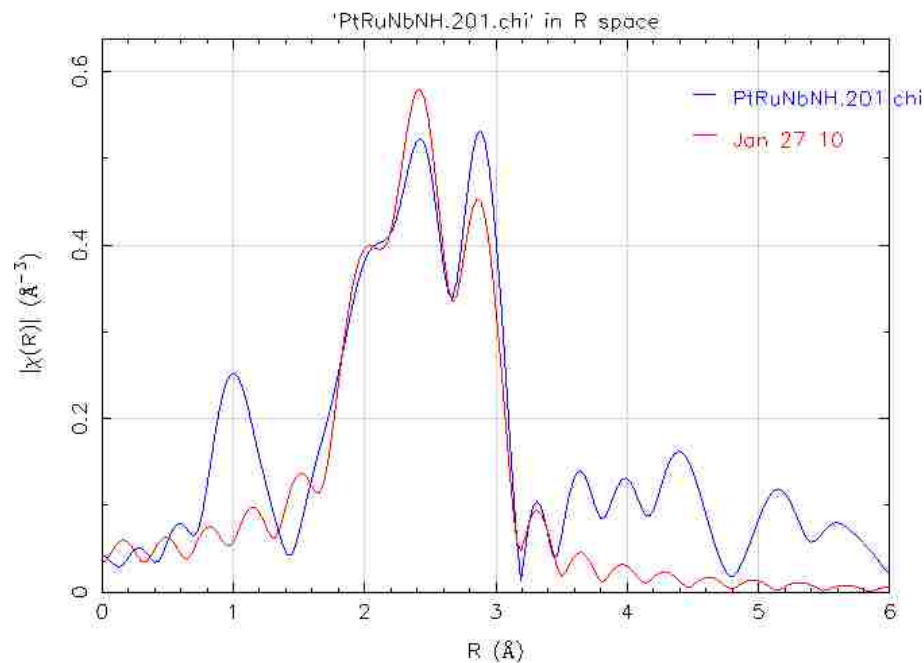


Figure 7.7a: Fourier-transformed EXAFS spectra of Pt L3 edge from PtNbRuO_x nanoparticles prepared by spray pyrolysis method (blue), together with a fitted line (red) based on Pt-Pt and Pt-O paths.

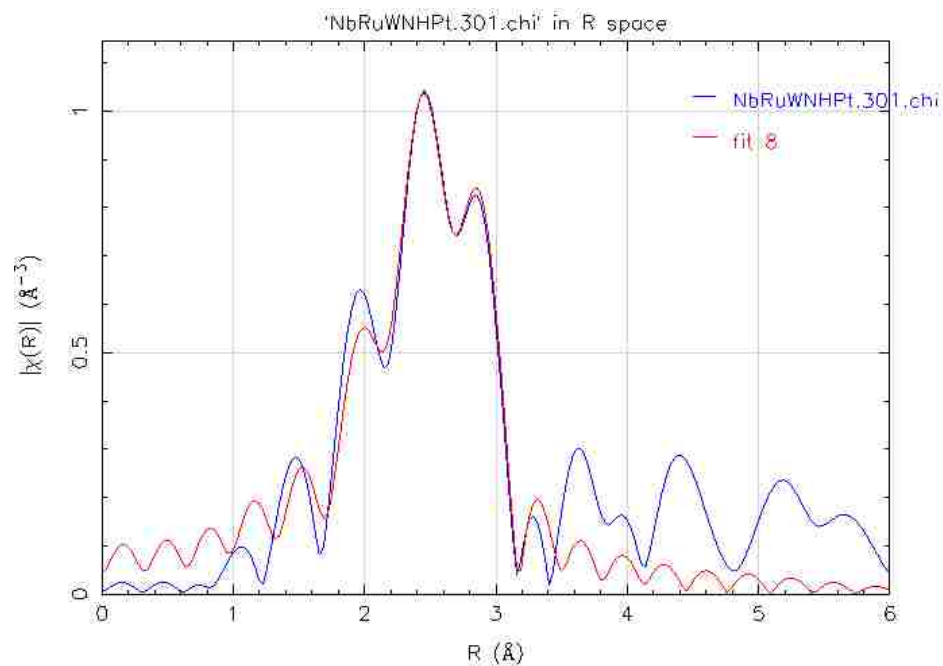


Figure 7.7b: Fourier-transformed EXAFS spectra of Pt L3 edge from PtNbRuO_x nanoparticles prepared by wet impregnation method (blue), together with a fitted line (red) based on Pt-Pt and Pt-O paths.

Fig.7.8 shows XANES spectra of the Nb K edge (Fig.7.8a) and Ru K edge (Fig.7.8b) from the nanoparticles prepared by dry impregnation and spray pyrolysis methods, together with those from respective reference foils. The XANES spectra of Nb K edge (Fig.7.8a) are independent of the preparation methods as both catalysts show almost identical spectra indicating that Nb state remains Nb_2O_5 . On the other hand, the XANES spectra of the Ru K edge (Fig.7.8b) show an increase in E_0 after Pt deposition, suggesting that Pt deposits or the condition of Pt-deposition and activation may alter the oxidation state in Ru. This is consistent with XRD results which indicated the presence of RuO_x and RuCO_x species before Pt deposition, as well as those from XPS which indicated organometallic ruthenium after Pt was deposited.

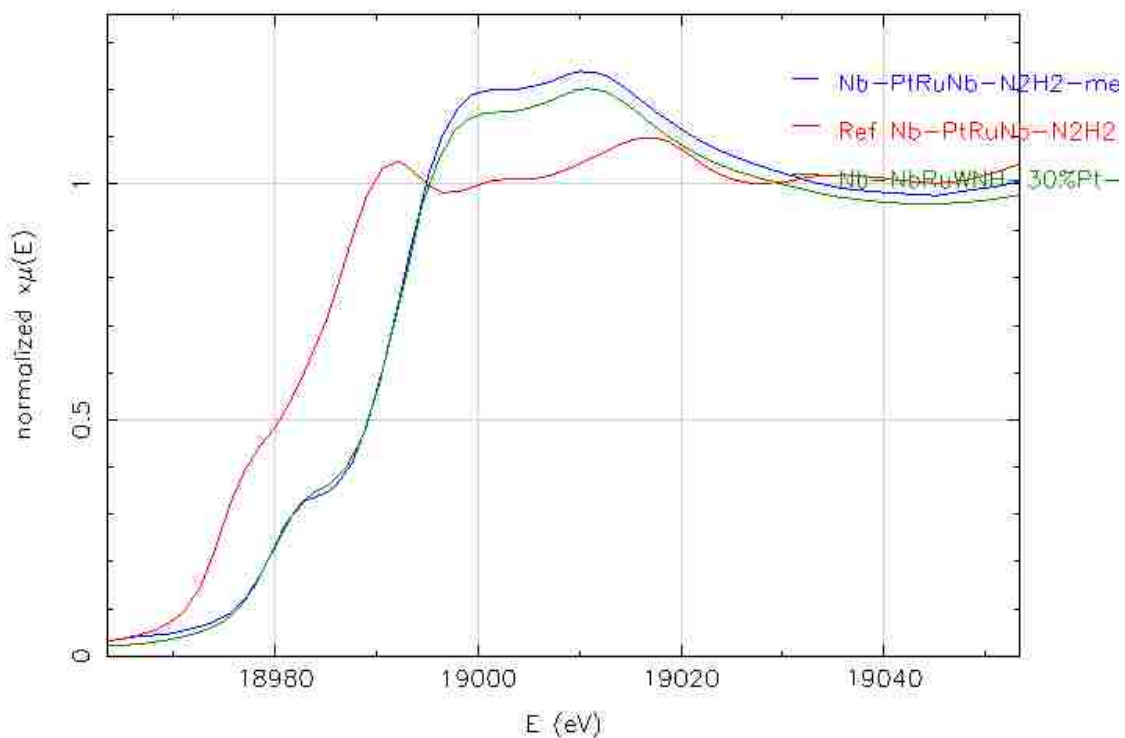


Figure 7.8a: XANES spectra of Nb K edge from PtNbRuO_x nanoparticles prepared by the wet impregnation (blue) and spray pyrolysis (green) methods, together with that from a Nb reference foil (red).

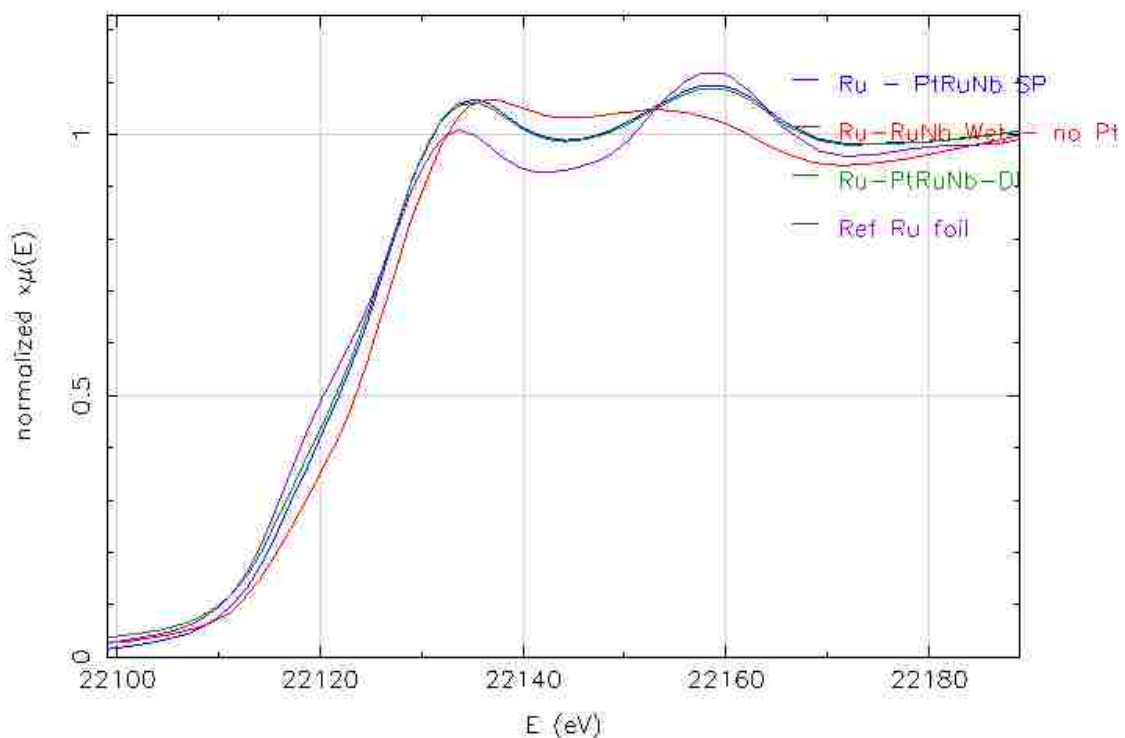


Figure 7.8b: XANES spectra of Ru K edge from PtNbRuO_x nanoparticles prepared by the wet impregnation (blue) and spray pyrolysis (red) methods, together with that from a Ru reference foil (green).

7.4 Electrochemical Surface Studies

7.4.1 IRRAS

In order to identify ethanol oxidation reaction (EOR) intermediates and products on niobia-supported platinum electrocatalysts, in situ IRRAS studies were conducted on Pt-DI and Pt-SP. The recorded spectra on both catalysts are shown in Fig.7.9 and the frequencies and band assignments are listed in Table 7.3. The IR spectra from these two catalysts suggest ethanol undergoes both total oxidation and partial oxidation pathways. Carbon dioxide (CO₂), acetic acid (CH₃COOH) and acetaldehyde (CH₃CHO) are the main EOR products. The positive-going peak near 2343cm⁻¹ is attributed to the

asymmetric stretch vibration of CO_2 . This is the product of the ethanol total oxidation pathway, and appears above 0.4V on both catalysts. The band located around 1705cm^{-1} can be assigned to the stretch vibration of the $\text{C}=\text{O}$ bond, found in both acetaldehyde and acetic acid. Both spectra show the $\text{C}-\text{O}$ stretching vibration of acetic acid at 1280cm^{-1} , indicating the formation of CH_3COOH . The bands at 1350cm^{-1} and around $1396\text{--}1410\text{cm}^{-1}$ are assigned to CH_3 in-plane bending mode and OCO stretching of adsorbed acetate, respectively. The signals of these two bands are relatively weak, which is probably due to a low product concentration. The band observed at 933cm^{-1} is assigned to $\text{C}-\text{C}-\text{O}$ asymmetric stretching of acetaldehyde. The strong band at 1598cm^{-1} is the $\text{H}-\text{O}-\text{H}$ deformation of adsorbed water molecules. The $\text{C}=\text{O}$ stretching mode of adsorbed acetaldehyde and acetyl around $1620\text{--}1635\text{cm}^{-1}$ cannot be resolved because of the presence of the strong water band. The $\text{C}-\text{H}$ wagging vibration in CH_3CHO at 1108cm^{-1} overlaps with the strong band at 1110cm^{-1} from ClO_4^- . The strong band for ClO_4^- ions is the consequence of its accumulation in the thin layer cell to compensate for the increasingly positive electrode potential. One major difference between these two spectra is the positive-going band in 2030cm^{-1} which is present in the spectra from Pt-DI, but absent from that of Pt-SP. The band is assigned to IR absorption by linearly adsorbed CO , produced by dissociative adsorption of ethanol on the catalyst surface.

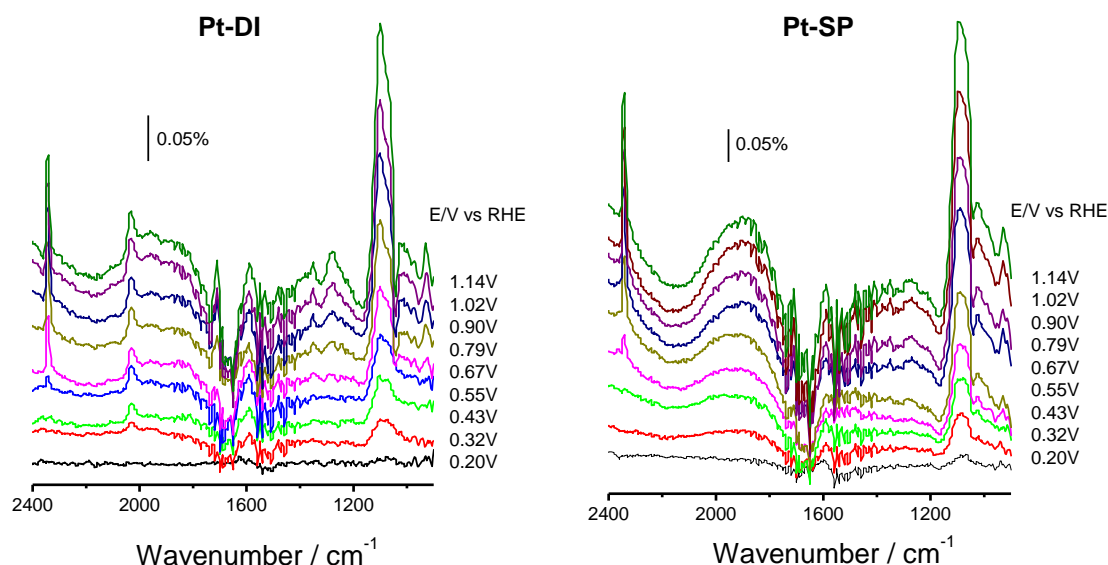


Figure 7.9: *In situ* IRRAS spectra recorded during ethanol oxidation on: (Pt-DI) 30%Pt/NbRu_yO_z ; (Pt-SP) 60% Pt/NbRu_yO_z.

Table 7.3: In situ IRRAS Spectra Band Assignments

Wavenumber/cm ⁻¹	Assignment
2343	CO ₂ asymmetric stretching ^[142]
2030	CO linear adsorption ^[142]
1705	C=O stretching of CH ₃ CHO and CH ₃ COOH in solution ^[142-144]
~1598	H-O-H deformation of adsorbed water ^[145]
1396-1410	O-C-O stretching of adsorbed acetate ^[142, 146, 147]
~1350	CH ₃ in plane bending of adsorbed acetate ^[148]
1280	C-O stretching of CH ₃ COOH in solution ^[142, 149, 150]
1368, 1108	CH ₃ symmetric deformation and C-H wagging in CH ₃ CHO ^[151-153]
1110	ClO ₄ ⁻
933	C-C-O asymmetric stretching ^[154]

Fig.7.10 shows the variation of band intensities of CO₂ (2343cm⁻¹), C=O (1705cm⁻¹) and CO (2030cm⁻¹) against the applied potentials for both Pt-DI and Pt-SP samples. On both catalysts, the amount of total oxidation product, indicated by **ICO**₂, and the amount of partial oxidation products, represented by **IC=O**, kept increasing with applied potential.

From Fig.7.10(a) we can see CO_L (linearly adsorbed CO) intensity is increasing

simultaneously with CO_2 band intensity, indicating that the CO_L formation rate is slower than its removal rate. On Pt-SP, CO_L formation was not obvious, which may suggest a higher capability for CO removal. The oxide support could supply oxygen containing species to oxidize blocking intermediate CO and promote EOR based on the bi-functional effect. The interaction between Pt nanoparticles and niobia support could alter the electronic structure of platinum and affect the reaction pathway according to the electronic effect. Therefore, the difference might be the consequence of a larger quantity of Pt-NbO_x interfaces and a stronger synergistic effect between Pt and NbRu_yO_z support in Pt-SP.

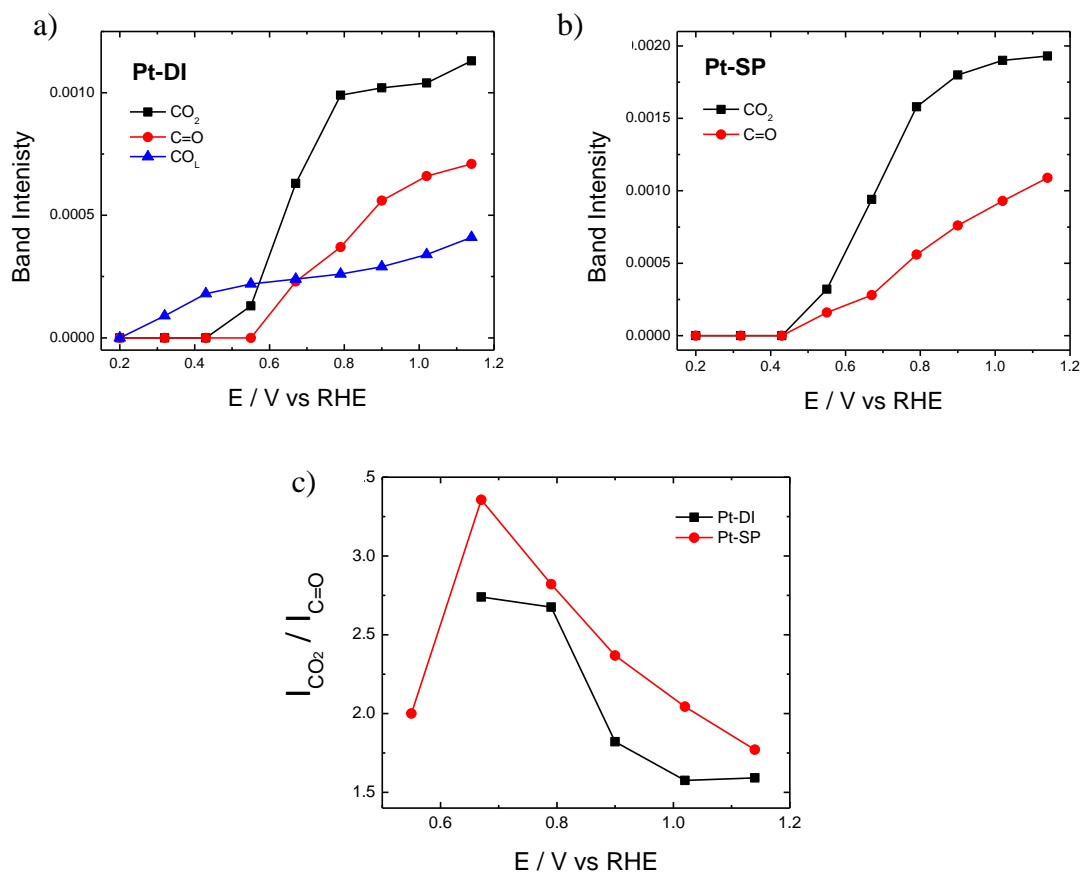


Figure 7.10: IR band intensities of CO_2 , C=O and CO_L during ethanol oxidation at different electrode potentials (data from Fig.7.9): a) Pt-DI, b) Pt-SP. c) The ratio of CO_2 band intensity to C=O band intensity versus applied potentials.

One major challenge in ethanol electrocatalysis is the breaking of the C-C bond to oxidize ethanol to CO₂. In order to better compare the selectivity of these two catalysts, we plotted the ratio between band intensity of CO₂ (**ICO**₂) and band intensity of C=O (**IC=O**) versus applied potential, and the results are shown in Fig.7.10. In the entire potential region, Pt-SP showed a higher (**ICO**₂/**IC=O**) value than Pt-DI, indicating a stronger capability to split C-C bond in ethanol molecules and promote the total oxidation pathway.

The IR results suggest that there are parallel pathways of EOR on both catalysts, while Pt-SP showed higher selectivity towards ethanol total oxidation compared with Pt-DI. This could be explained by a stronger synergy between Pt and NbRu_yO_z support in Pt-SP.

7.4.2 Reaction Kinetics

Mesoporous NbRu_yO_z as a support is intended to provide oxygen promotion, and possibly a favorable form of SMSI with Pt. To test the viability of these criteria, cyclic voltammetry was performed in 0.1M HClO₄ comparing conventional 30%Pt/XC-72 (commercial) against several Pt/NbRu_yO_z samples for ethanol oxidation. These included Pt-SP and Pt-DI, as well as a third sample, Pt-TM, which was templated by silica spheres instead of P123 surfactant.

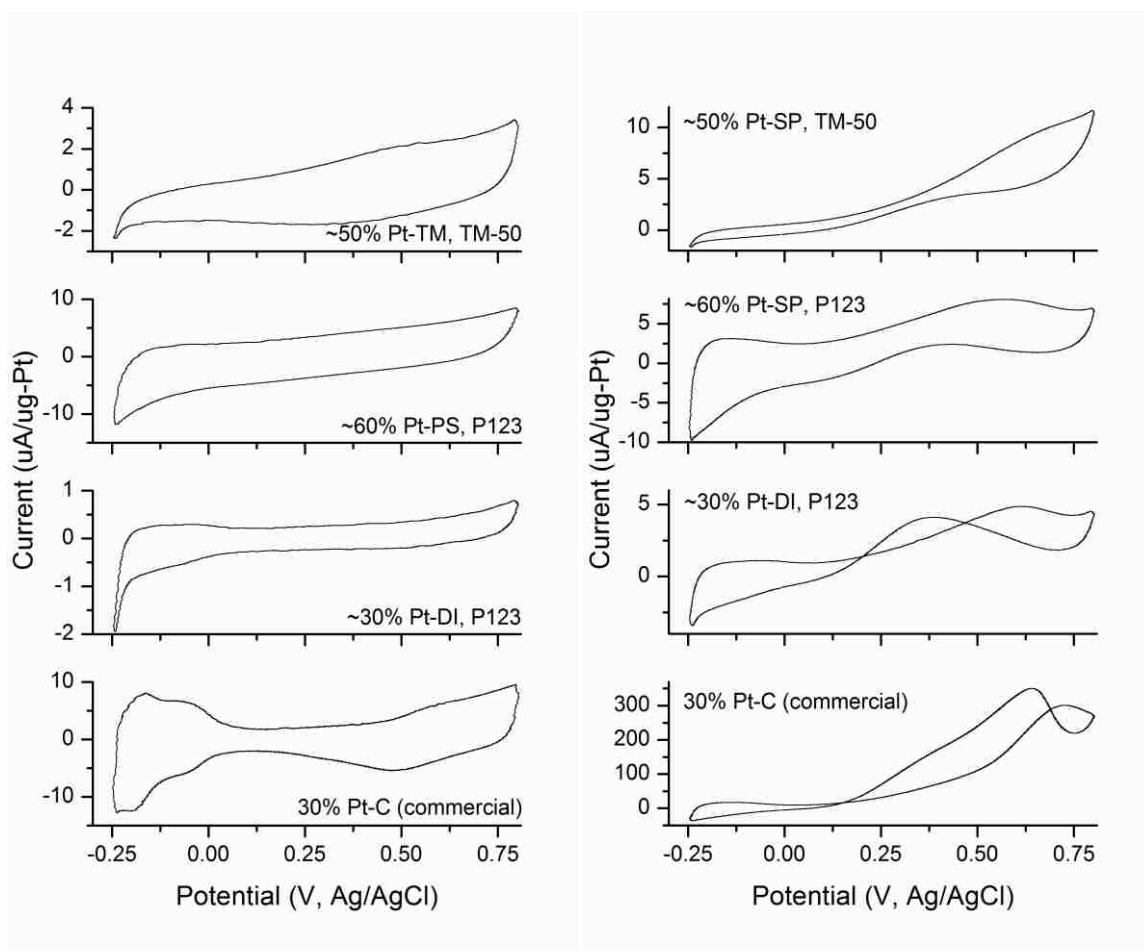


Figure 7.11: (Left) Cyclic voltammograms for Pt-C (commercial), Pt-DI, Pt-SP, and Pt-TM. Scans performed at 10mV/s in 0.1M HClO₄. (Right) Ethanol oxidation performance of the same samples at 50mV/s in 0.5M EtOH and 0.1M HClO₄.

The results shown in Fig.7.11 indicate that Pt supported on niobia exhibits a comparatively limited exchange current density. We would normally anticipate observing in all samples the similar oxidative and reductive Pt features seen for Pt/C. Yet despite having as much as twice the amount of catalyst loading, such features are absent. Unlike Pt-SP and Pt-TM, Pt-DI does exhibit subtle Pt features and less capacitance in the double layer region. If we assume that the support is interfering with catalyst activity, then this could be because the sample has larger Pt nanoparticles, and therefore, more Pt surface sites farther away from the niobia surface. However, the peak current measured

in 0.5M EtOH is still about 60x less than that of Pt/C with the same catalyst loading. There appears to be no significant improvement in current from 30% to 60%Pt/NbRu_yO_z. Nor is it clear that omitting carbon based surfactant in favor of silica improves performance. P123 surfactant, normally about 50wt% in the precursor solution, could potentially breakdown during thermal treatment into smaller carbonaceous species that poison the platinum, as mentioned earlier in the discussion of XAS. All Pt/NbRu_yO_z samples were heated to 400°C in alternating atmospheres of air and 10%H₂/N₂ for five 20min cycles, followed by 2 hrs in the latter atmosphere to account for this possibility. But no change in performance was observed. Rapid scanning in the electrochemical cell at 500mV/s and holding at lower potentials also failed to change oxidation performance.

These results suggest that lower EOR kinetics on Pt/NbRu_yO_z catalysts are not due to the poisoning by carbonaceous byproducts that is normally encountered. The only remaining carbon source in the system is the ethanol used in the initial precursor solution.

However, organic solvents are very common in the synthesis of a variety of platinum catalysts. It is also notable that mixing Pt-SP with XC-72 to attain 50wt%C did nothing to improve performance, suggesting that the electric conductivity of the sample is not inhibiting reaction kinetics. Numerous groups in the literature have observed similar deactivation behavior of Pt supported on niobia, including catalysts designed for gas phase reactions in which the electric conductivity of the material is inconsequential^{65, 125, 155-161}. Unfortunately, the exact mechanism of this fairly instantaneous deactivation has not been fully revealed, though theories have been put forth. The deactivation is most likely related to the native oxide layer niobium forms regardless of the oxidation state of

the bulk. The thickness of this layer is usually reported to be on the order of <1 to 6nm¹⁶²⁻¹⁶⁴, though this can vary significantly for niobium in various liquid electrolyte¹⁵⁸. It is not immediately clear how an oxide layer of this type would fully deactivate Pt nanoparticles 2-20nm or more in diameter, especially after the reducing treatments employed above.

7.4.3 Pt-Monolayer Deposition

Electrochemical experiments were performed in 0.1M HClO₄ as well as 1M KOH, a fresh electrode prepared for each. Before ethanol was added, some Pt features were visible in both aqueous media. Distinct oxidation regions generally appear to be more apparent in alkaline media. Changes are noticeable in the cyclic voltammograms after cationic deposition of Pt on Pt-DI (Fig.7.12A&C and Table 7.4). In acid, the total charge density of the CV decreases by 33%. Surface features of Pt hydride formation and oxidation (0-0.25mV) as well as Pt-O reduction (1-0.5V) remain characteristically broad even after deposition of additional Pt. This observation remains true at scan rates of 50mV/s. In base, these features are immediately more distinct. Here, the overall decrease in total charge density is only 7%, with most of the loss from the double layer region.

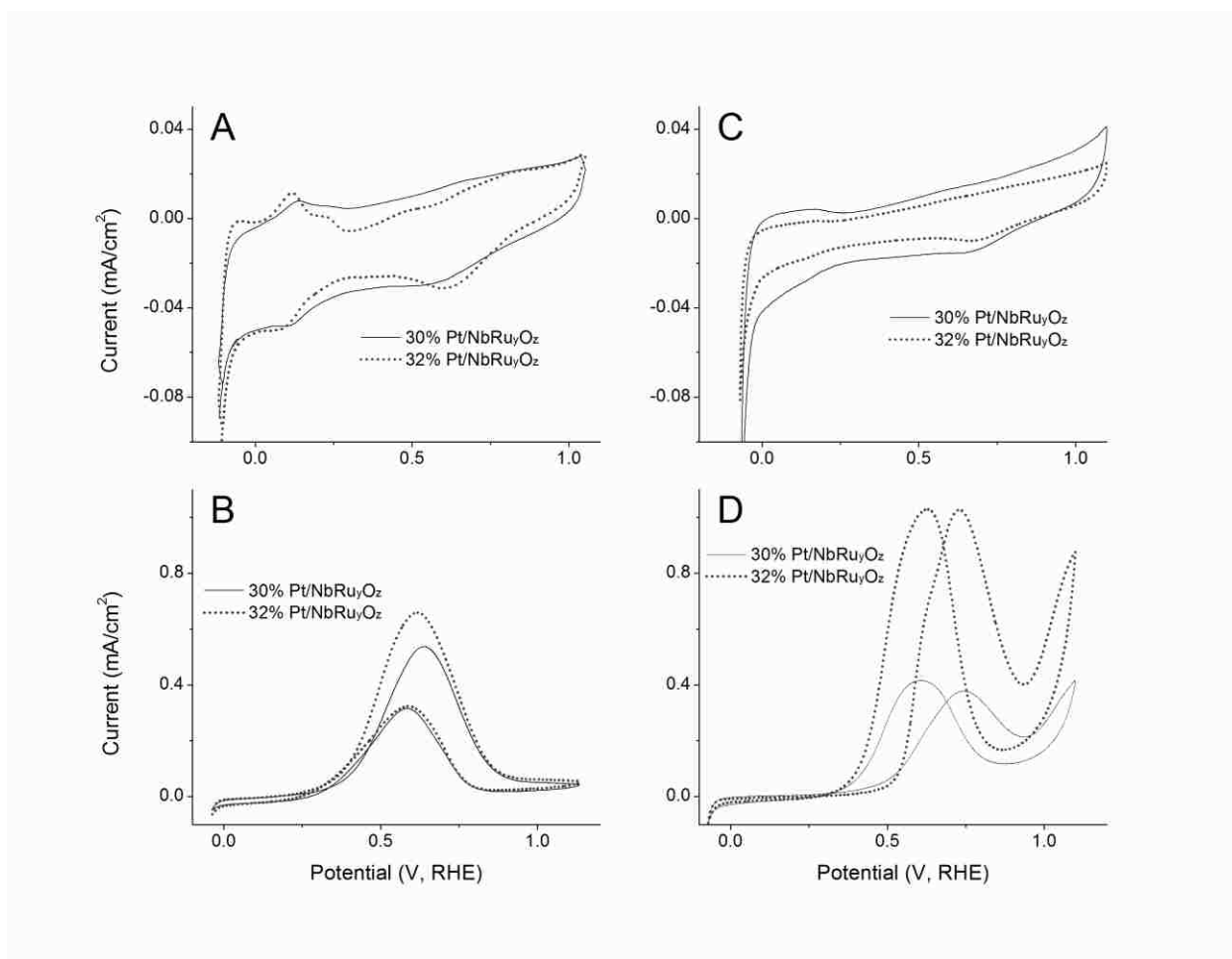


Figure 7.12: Cyclic voltammograms of Pt-DI before and after secondary Pt-monolayer deposition. (A) 50mV/s in 1M KOH. (B) 10mV/s in 1M KOH and 0.5M EtOH. (C) 10mV/s in 0.1M HClO₄. (D) 10mV/s in 0.1M HClO₄ and 0.5M EtOH.

Table 7.4: Total Charge Density and 0.5M Ethanol Oxidation Peak Dimensions (CV) Before and After Secondary Pt Deposition on Pt-DI

		Forward Sweep			Reverse Sweep		
		Sweep Area ($\mu\text{C}/\text{cm}^2$)	Peak Center (V)	Max Current (mA/cm^2)	Sweep Area ($\mu\text{C}/\text{cm}^2$)	Peak Center (V)	Max Current (mA/cm^2)
ACID	30%Pt	0.168	0.744	0.378	0.173	0.603	0.417
	32%Pt	0.374	0.728	1.027	0.350	0.625	1.030
	Δ	121.9%	-0.016	171.4%	102.2%	0.022	147.2%
BASE	30%Pt	0.170	0.638	0.538	0.097	0.587	0.316
	32%Pt	0.214	0.615	0.661	0.108	0.586	0.324
	Δ	26.5%	-0.023	22.9%	11.5%	-0.002	2.4%

Ethanol oxidation (0.5M) studies reveal further differences in the improvement of collected current. In particular, it is useful to examine the changes in EOR performance before and after ionic Pt deposition of forward (oxidizing) and reverse (reducing) sweeps independently of one another. Normally, it is preferable to compare the current of different catalysts at the same potential. In this study, attention is also given to shifts in the potential at which maximum EOR current is observed. Positive shifts are indicative of the reaction thermodynamics more similar to that of a clean Pt surface.

Characteristics of the data in Fig.7.12 are presented in Table 7.4. There is a significant increase of 171% and 147% in the total charge for EOR in acid of forward and reverse sweeps, respectively. In base, the total charge of the forward sweep improves by a more modest 23%, while the change of the reverse sweep is nearly negligible at 2.4%. In fact, the reverse peak distinguishes itself by changing remarkably little. While the position of peak centers of the forward sweeps in both media decreased by about 20mV, and the peak center of the reverse sweep increased by about the same amount, the behavior of the reverse sweep in base remains unaltered. This could indicate that the oxidizing sweep to higher potentials creates conditions that limit the Pt surface, possibly related to minor destabilization of the niobia support. This would be consistent with the observation that overall improvement is significantly better in the less oxidizing environment of 0.1M HClO₄. It also appears that Pt which is both deposited and electrochemically tested in an environment purged of oxygen can continuously recover Pt surface sites at the lowest potentials of the cycle. Ultimately, these results also suggest that the presence of oxygen

has a negative impact on the electrocatalytic activity of Pt/niobia. Although, because the electrode is still exposed to aqueous solution, these results are still subject to passivation reactions involving the decomposition of $\text{H}_2\text{O}/\text{H}_2\text{O}$ to form Nb-O_x or free oxygen.

7.4.4 Support Crystallization

In order to test the hypothesis of Pt surface inhibition from instability of niobia in highly oxidizing environments, a fresh sample was prepared consisting of Pt nanoparticles (60%) in an amorphous matrix of 10%Nb, 10%Ru and 20%O. A lower weight percent of niobium was used for several reasons. The suppression of H_2 and OH activity of platinum supported on niobia has been shown to be quite dramatic, even for gas phase reactions, necessitating the use of higher ratios of catalyst to support in order to affect observable differences in catalytic behavior. In addition, most studies in the literature involving niobia as part of an electrocatalyst have employed the metal oxide as a minor component^{61, 161, 165}. This is largely because of its relatively poor electric conductivity as Nb(V) and the difficulty in maintaining the surface in a more greatly reduced oxidation state in the presence of oxygen^{138, 162}.

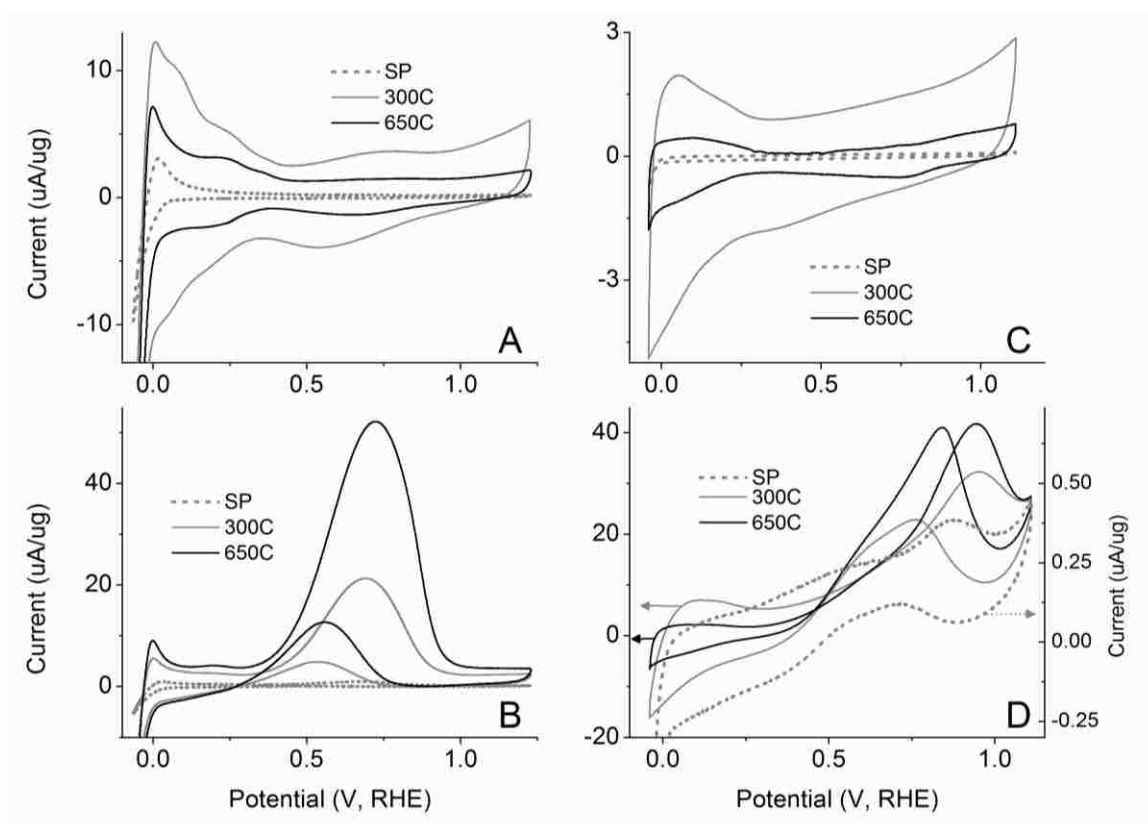


Figure 7.13: Cyclic voltammograms of Pt/NbRu_yO_z (wt% - 60:10:10:20) after different heat treatments including immediately after spray pyrolysis heating to 300 °C and 650 °C in 10% H₂/N₂ for 4hrs. (A) 50mV/s in 1M KOH. (B) 50mV/s in 1M KOH and 0.5M EtOH. (C) 10mV/s in 0.1M HClO₄. (D) 50mV/s in 0.1M HClO₄ and 0.5M EtOH.

Table 7.5: Total Charge Density and 0.5M Ethanol Oxidation Peak Dimensions (CV) for Pt/NbRu_yO_z (wt% - 60:10:10:20) Before and After Heat Treatments

		Forward Sweep			Reverse Sweep		
		Sweep Area (uC/μg)	Peak Center (V)	Max Current (uA/μg)	Sweep Area (uC/μg)	Peak Center (V)	Max Current (uA/μg)
ACID	SP	0.267	0.870	0.388	0.163	0.712	0.122
	300C	16.324	0.950	32.315	13.100	0.762	22.874
	650C	16.349	0.943	41.735	16.563	0.840	41.030
	Δ	0.2%	-0.007	29.2%	26.4%	0.078	79.4%
BASE	SP	1.621	0.667	0.986	0.931	0.520	0.090
	300C	25.216	0.693	21.314	5.135	0.539	4.721
	650C	21.928	0.722	52.206	3.890	0.558	12.709
	Δ	-13.0%	0.029	144.9%	-24.2%	0.019	169.2%

Each plot in Fig.7.13 shows three sets of cyclic voltammograms. These include performance of the powder immediately after spray pyrolysis and after thermal reduction at temperatures of 300°C (Pt-300) and 650°C (Pt-650) in 10% H₂/N₂. The first reduction at 300°C is hot enough to thermally decompose any remaining precursor complexes and activate the platinum. The second reduction occurs roughly 100°C higher than the crystallization temperature of niobia. While some limited sintering of Pt nanoparticles likely occurs, the primary difference between these samples is the presence of crystalline niobia. The results are summarized in Table 7.5.

After support crystallization, there is a substantial decrease of 74% in the total charge density of the voltammogram in acid media, nearly twice that of the same decrease in base. In acid, the total area of the forward sweep as well as the EOR peak center do not change even though the maximum current increases by 29%. This correlates with a proportional decrease in the hydrogen region. The maximum current of the reverse sweep increases by 79% and is roughly equal to the intensity of the forward sweep. Prior to support crystallization, this was not the case. Again, this could indicate that the support and related passivation reactions are more greatly stabilized as a crystalline structure and interfere less with the Pt surface at or near potentials within the oxygen region.

We see further suggestion of this behavior in base electrolyte, in which there was a comparatively dramatic increase in total charge of forward and reverse sweeps of 145% and 169%, respectively. The peak centers of both sweeps shift 20-30mV towards more positive potentials. The dramatic improvement of measured current in base compared to acid enforces the idea of inhibited surface sites of Pt supported by niobia in the presence

of oxygen. Crystallization of the niobia support appears to greatly enhance the availability of active Pt sites.

This analysis assumes that Pt nanoparticles remain relatively stable during the crystallization of niobia at 650°C for 3 hours. The sintering behavior of Pt depends upon the nature of the support ^{165, 166}. It has also been shown that heating in an oxidizing atmosphere more greatly facilitates sintering on both carbon and metal oxide supports ^{80, 88, 167-169}. We assume that changes in Pt particle size are minimal in the reducing atmosphere employed.

Orilall et al. observed relatively high mass activity for Pt and Pt-Pb supported on crystalline mesoporous niobia-carbon composites (samples contained roughly twice as much carbon within the support as those of this study) for the electro-oxidation of formic acid in 0.1M H₂SO₄. Though no amorphous support was presented, it was shown that Pt/NbO₂-C showed improved current compared to Pt/Nb₂O₅-C. In the absence of formic acid, cyclic voltammograms for both Nb(IV) and Nb(V) yielded a highly charged double layer absent of Pt redox features ¹⁷⁰. Niobia is a complex oxide with many forms, as demonstrated by the multiple polymorphs of Nb(IV) which the authors obtain by oxidizing and re-reducing the same sample. The state of the bulk does not necessarily represent the state of the surface. It is unclear how the native oxide layer varies between the two, particularly in alkaline electrolyte under various applied potentials. But the final stability of the niobia surface is likely highly variable, depending upon factors including support crystallinity, as well as pH of the electrolyte ¹⁵⁸. And though samples discussed here were heat treated in a reducing atmosphere of 10% H₂/N₂ at 400°C, we previously showed that these conditions are not sufficient to reduce bulk Nb₂O₅ to NbO₂ ¹³⁸.

In situ IRRAS results have shown that evolution of CO₂ from ethanol in 0.1M HClO₄ begins at lower potentials on Pt/NbRu_yO_z than on Pt/XC72. But it is not clear how much of the current of each sample measured in the voltammograms of Fig.7.13 is the result of complete oxidation. Yang et al. asserted that there are two competing factors for overall catalytic activity of Pt. Any increase in the average size of Pt nanoparticles during heating would adversely affect the EOR performance of the material due to lower catalyst surface area. But it has also been shown for a similar system that the oxidation of CO on Pt/Al₂O₃ is structure sensitive, improving with increasing Pt nanoparticle size⁸⁰.

Our studies here have shown that smaller Pt nanoparticles supported on amorphous niobia such as those in Pt-SP appear to be more effective at splitting the C—C bond in acid electrolyte. This is probably due to a larger Pt-NbO_x interfacial surface area. And unlike the larger Pt nanoparticles of Pt-DI, IRRAS spectra for Pt-SP indicate an absence of CO, suggesting that oxidation to CO₂ occurs very rapidly. This Pt nanoparticle size-dependent behavior found by comparing Pt-SP and Pt-DI can also be extended to the comparison of Pt-300 and Pt-650. If there was substantially greater sintering of Pt on NbRu_yO_z at 650°C compared to 300°C, then the larger nanoparticles which would result on Pt-650 should be more susceptible to CO poisoning than those of Pt-300.

Alternatively, the niobia support may stabilize Pt nanoparticles to some degree against sintering at these temperatures. Unlike Pt/Al₂O₃ gas phase catalysis, C—C scission and CO oxidation appear to be less sensitive to the extrinsic properties of Pt nanoparticles. Instead, intermediate species of EOR may bond more strongly to Pt-NbO_x interfacial sites until scission and complete oxidation are achieved.

But the total current per mass measured from EOR is extremely low. Höbel et al. observed an irreversible 50% decrease in CO gas adsorption capacity for Pd/Nb₂O₅/Cu₃Au(100) under UHV and ambient pressure after annealing above 27°C. This was due to changes in the electronic structure as opposed to catalyst sintering, which led the authors to conclude that the migration of Nb₂O₅ particles over Pd catalyst could not be responsible for the suppressed activity¹⁵⁷. For 1%Pt/Nb₂O₅ gas phase catalysis, Guerrero et al. also observed a decrease in CO adsorption capacity, but noted that it remains high in the absence of H₂. They surmised that O₂ and H₂ dissociative adsorption remained unhindered in the presence of CO, hindering CO adsorption and oxidation¹⁵⁶.

All of these observations have significant implications for Pt/NbRu_yO_z in aqueous electrolyte where the local concentrations of hydrogen and oxygen are much greater. Such selective adsorption behavior could inhibit the initial adsorption of ethanol or its partially oxidized subspecies. An additional factor unique to the electrocatalyst is the necessity for steady ion transport through the electrolyte. Under the active and selective surface conditions discussed, there is a greater potential for ions to become adsorbed or neutralized before diffusing far from the polarized double layer region.

These studies appear to confirm the prevalence of Pt-NbO_x surface sites, in which ethanol and its subspecies are more strongly bound than on Pt(111). This improves instances of C—C scission before partially oxidized species desorb from the surface. The niobia also appears to act as an oxygen promoter, facilitating CO oxidation to CO₂. But the adsorption kinetics of H₂ and O₂ species from electrolyte and atmosphere appear to dominate available catalyst surface sites, blocking adsorption of double and single carbon species and hindering the overall EOR performance. Polarization of the electrode may

induce the exchange of hydrogen and oxygen to Pt from niobia directly. In this case, the adsorption on Pt may partially proceed without the dissociation step. Such a process could explain limited kinetics of EOR.

CHAPTER 8 - Electrochemical Studies and DFT Analysis of Suppressed Exchange Current Density of Pt Supported on NbRu_yO_z

8.1 Pt/NbRu_yO_z Electrocatalyst

The electrocatalyst is primarily comprised of porous, NbRu_yO_z particles 50nm-4μm in diameter. These particles are decorated throughout the bulk and surface with platinum nanoparticles with an average diameter of 2nm. Alone, the NbRu_yO_z support particles have an average oxidation state between Nb(4-5) and a BET surface area of 167m²/g due to a mesoporous structure, with pore diameters of about 5nm. A loading of 60wt% Pt decreases the surface area to ~6m²/g. Some of the decrease results from the addition of heavier platinum, while the remainder could be the result of pores plugged by those same Pt nanoparticles. There is evidence that the strong metal support interaction between niobia and platinum in close proximity within the pores could result in the particle acting as an oxygen sponge which lowers the density of niobia near the Pt surface and eventually blocks other gasses.

8.2 Electrochemical Aging Studies

Cyclic voltammograms for Pt/XC72 (Fig.8.1A) before and after electrochemical aging show a significant decrease in early hydrogen desorption after -25mV. A second feature immediately before the double layer (presumably H-desorption from Pt(100) and Pt(111)) appears more stable. This is mirrored in the stability of the first Pt-O feature following the double layer, while oxidation at higher potentials decreases after aging. The same Pt/XC72 particles were identified on the TEM grid before and after electrochemical

aging, shown in Fig.8.2. Pt nanoparticles do not remain static on the support surface. Larger carbon particles have also shifted, though specific surface changes are unclear.

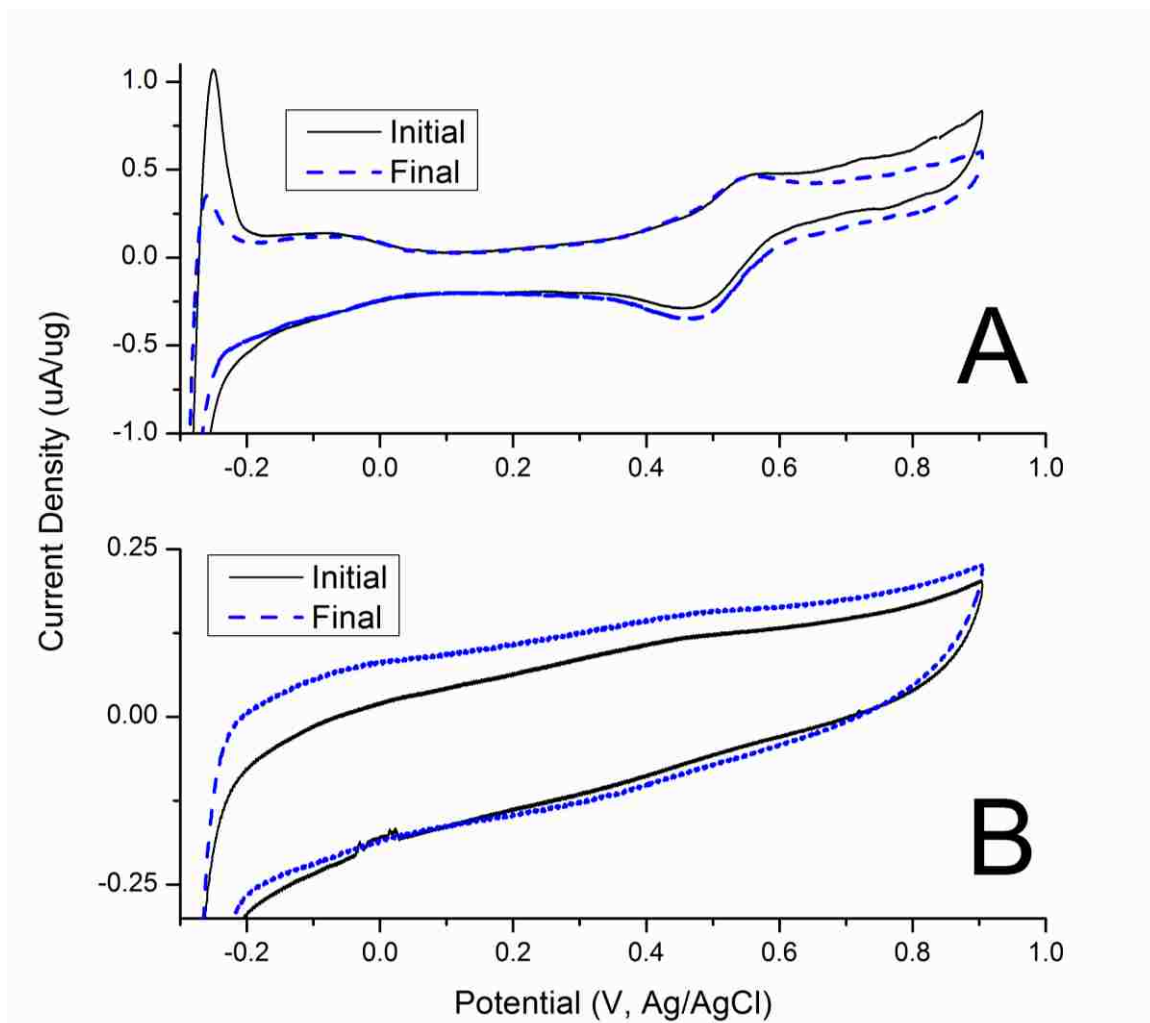


Figure 8.1: Cyclic voltammograms of (A) 30% Pt/XC-72 and (B) 60% Pt/NbRu_yO_z in 0.1M HClO₄ at a scan rate of 10mV/s (Ag/AgCl). Each plot shows the 10th cycle measured before and after the electrode was exposed to 3600 cycles at 1V/s.

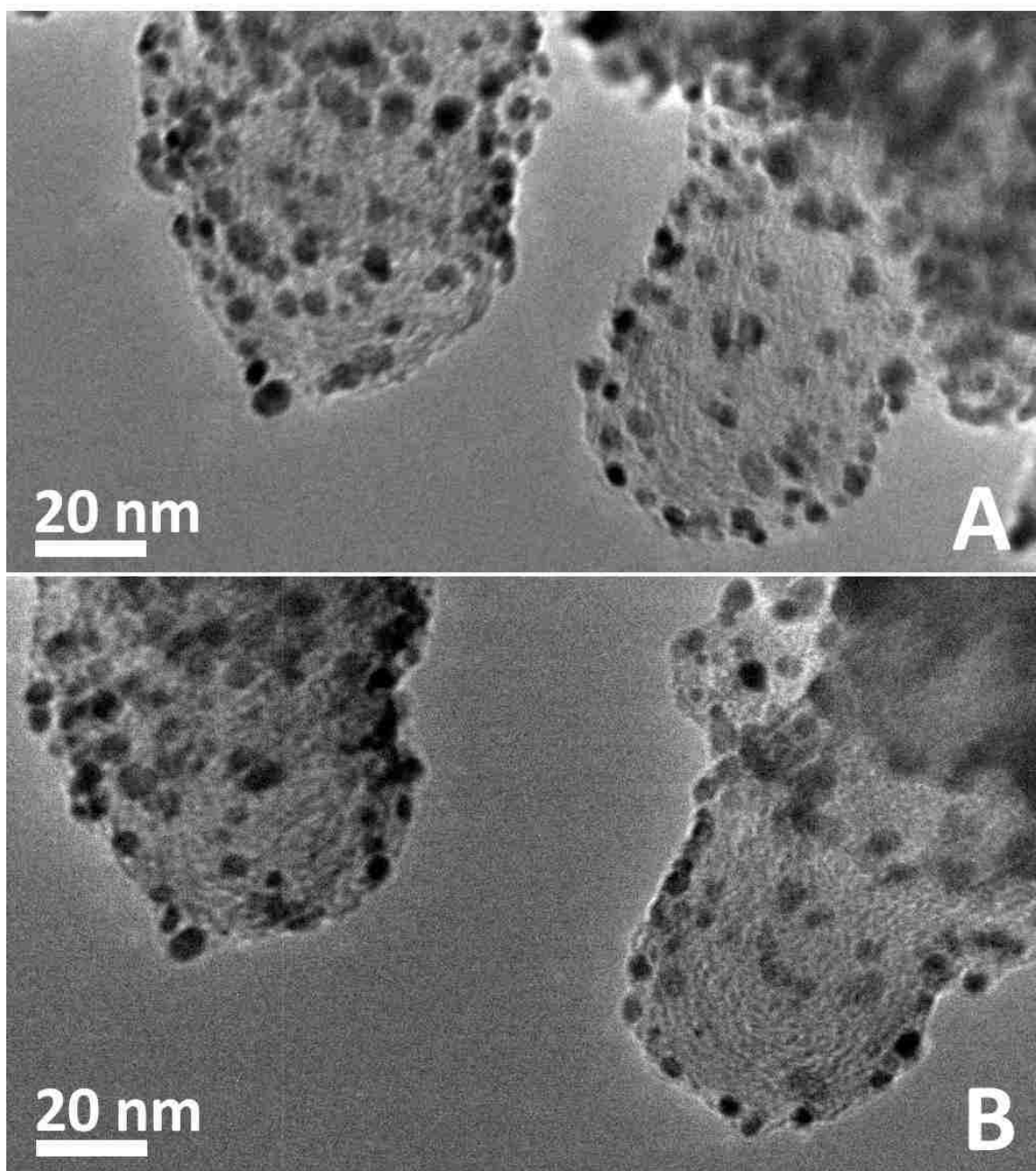


Figure 8.2: TEM images of particles of 30% Pt/XC-72 (A) before and (B) after 3600 cycles at 1V/s in 0.1M HClO₄. Migration of Pt nanoparticles after aging is apparent.

The results for Pt/NbRu_yO_z exhibit a different type of degradation. The expected features reflecting changes in Pt surface oxidation in Fig.8.1B are very subtle, but remain consistent before and after aging. Instead, there is no distinct double layer and the CV is dominated by charging. The interface of niobia with atmospheric oxygen and aqueous electrolyte is highly active. Niobium and niobia generally have a thin, native oxide layer that is subject to fluctuations in oxidation state ¹⁶². The layer is usually extremely thin and permeable to common ions, resulting in observed effects such as oxygen absorption and hydrogen intercalation. Here, a second, similar form of surface activity appears to dominate the electron exchange activity occurring on the electrode, masking or preventing features associated with platinum. The final sweep after aging is identical to the initial sweep, except for an increase in overall charging.

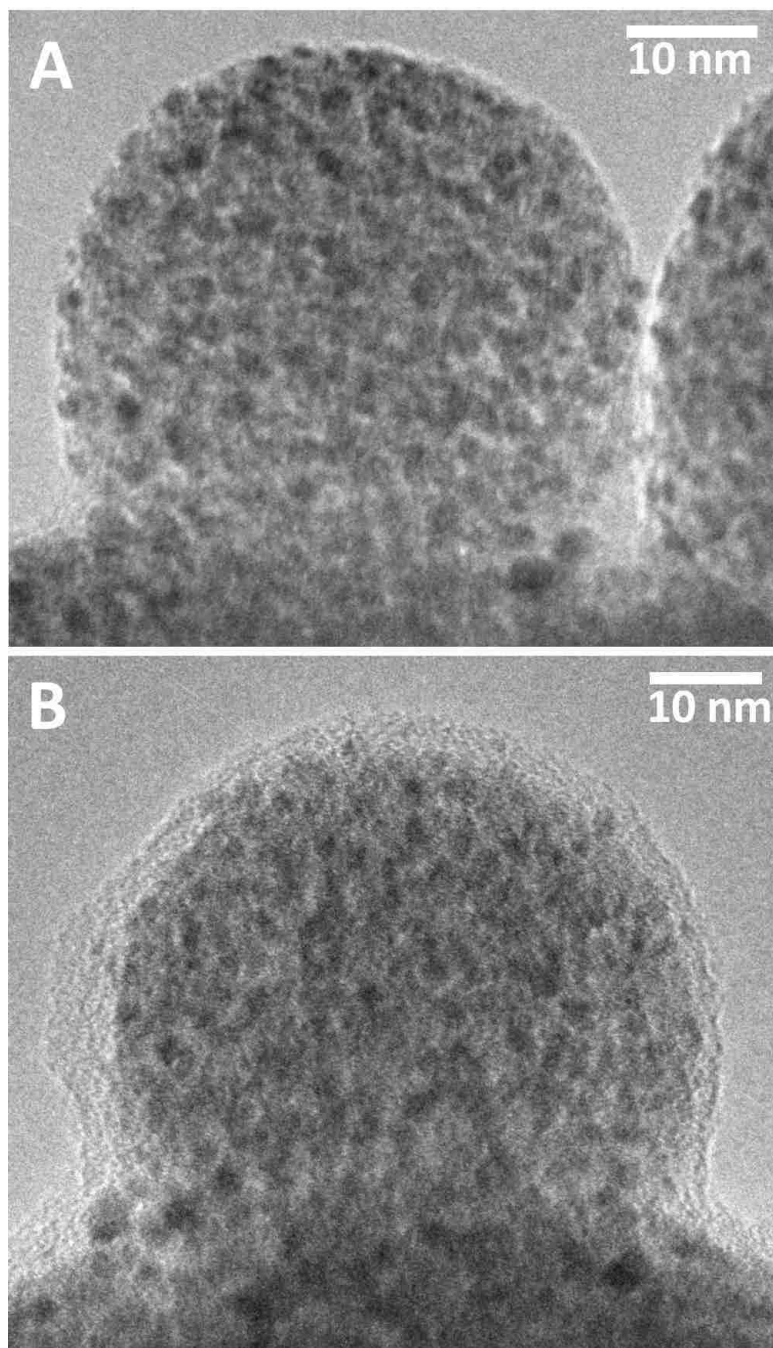


Figure 8.3: TEM images of particles of 60% Pt/NbRu_yO_z (A) before and (B) after 3600 cycles at 1V/s in 0.1M HClO₄. The aging treatment evolves a thin oxide film around the particles.

This observation is consistent with the film growth which covers the Pt/NbRu_yO_z particles after aging in Fig.8.3. The film represents a barrier to ion transfer and Pt surface sites which results in the increased capacitance shown in the corresponding CV. It is possibly an augmentation of the native oxide layer which is less dense and is sensitive to the vacuum and electron beam of the TEM.

8.3 Electron Energy Loss Spectroscopy

The catalyst underwent the same aging process as was used before in acid electrolyte, this time in 1M KOH to compare the formation of film. The film showed the same sensitivities to conditions inside the TEM as previous samples aged in acid electrolyte, preventing a quantified comparison of layer dimensions between the two from this technique.

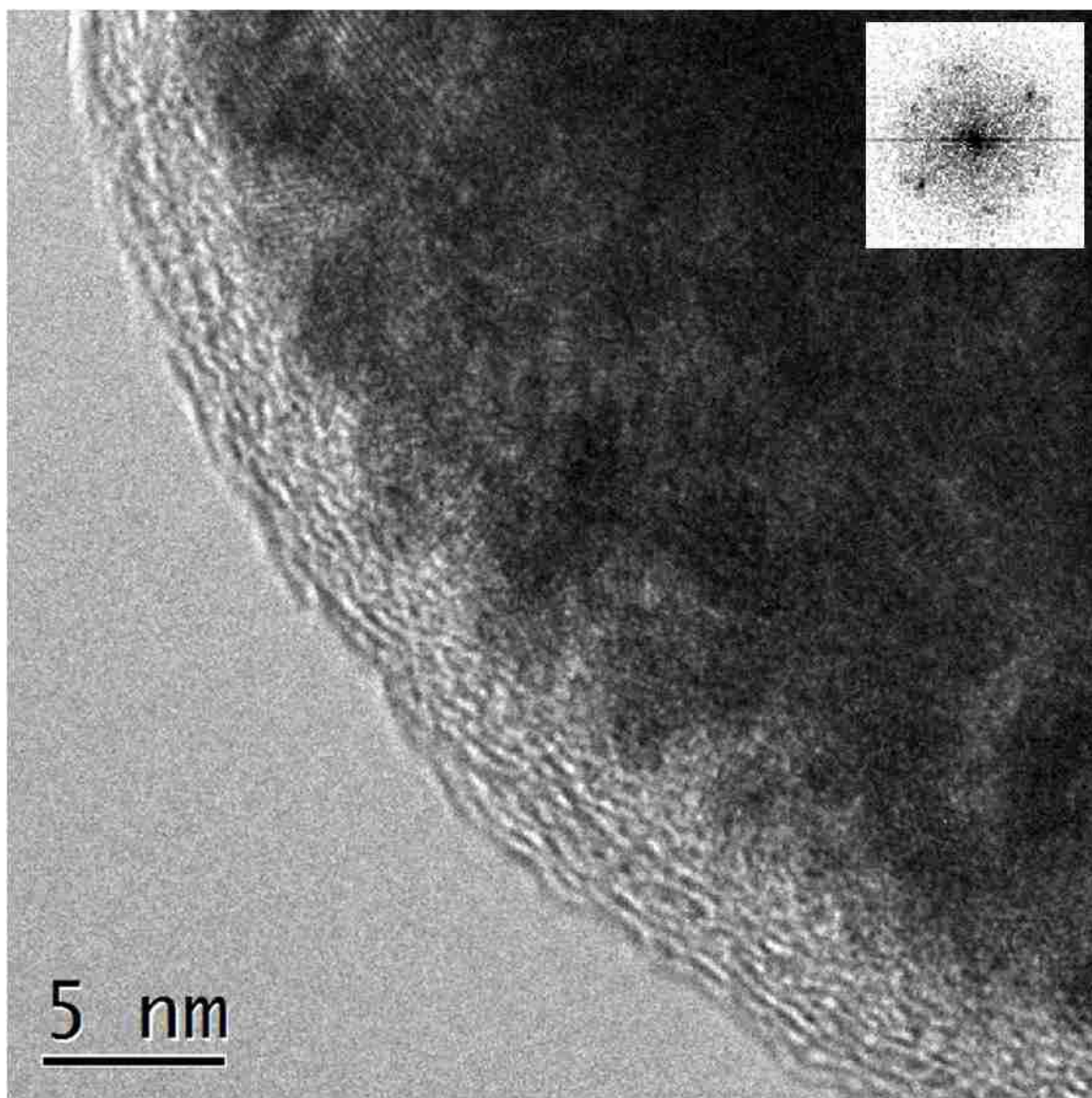


Figure 8.4: TEM image of 60%Pt/NbRu_yO_z after 3600 cycles at 1V/s in 1M KOH. The oxide film appears to form as a disordered lamellar layer growing in a traverse manner at layer edges. Inset shows the FFT pattern of darker lattice fringes, verifying the atomic spacing (2.235-2.405Å) of Pt(111).

The TEM was equipped with an Electron Energy Loss Spectrometer which was used to create a two dimensional oxygen map of the particle shown in Fig.8.4. This process stores information in each pixel describing the O-K α 2 electron count, reflecting the relative concentration of oxygen at any point in the image. This information could then

be extracted to create a linear concentration profile following a radial path from the particle's center to its surface. Multiple paths starting at the center were extracted to account for the entire circumference of the particle. These were then averaged to form the oxygen concentration profile shown in Fig.8.5. The profile indicates that the area which constitutes the film, ~35nm from the particle center, has a relatively high concentration of oxygen. This result suggests that the film is a highly oxidized form of niobia, Nb(5₂).

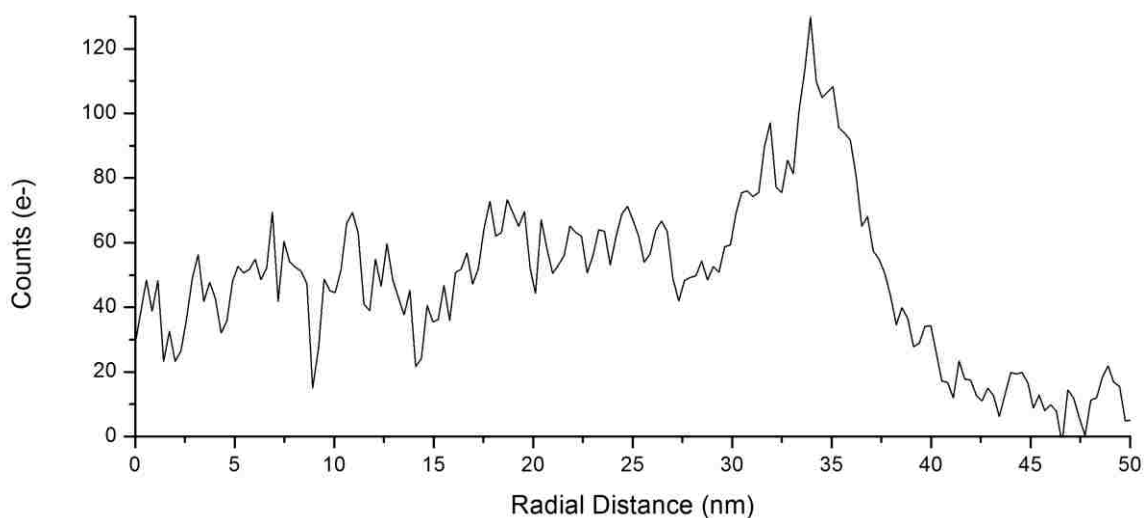


Figure 8.5: Radial oxygen concentration profile from the center (0nm) to the surface (~40nm) of the particle in Fig.8.4, measured using EELS O-K α 2.

8.4 Sequential Oxidation Cyclic Voltammetry

The oxygen-rich nature of the thin film indicated by EELS would suggest that the NbRu_yO_z support is sensitive to the presence of oxygen-containing species. Cyclic voltammetry which sequentially scans to higher potentials can reveal the relative stability of various redox features as the electrode surface spends increasing amounts of time under oxidizing conditions. The evolution of oxygen from H₂O above 1.2V represents a

threshold which, once passed, subjects the electrode to especially corrosive conditions. The graphitic surface of carbon XC72 breaks down, simultaneously destabilizing supported Pt nanoparticles. Similar treatment can also reveal oxygen sensitivity of the NbRu_yO_z support. Therefore, any differences in the redox features between increasingly anodic, stepped scans and that of increasingly cathodic, stepped scans after peaking at a maximum potential of 1.6V would indicate destabilization of the catalyst and/or support. This process was performed for 30%Pt/XC72 and 60%Pt/ NbRu_yO_z , and the results are shown in Figures 8.6-9.

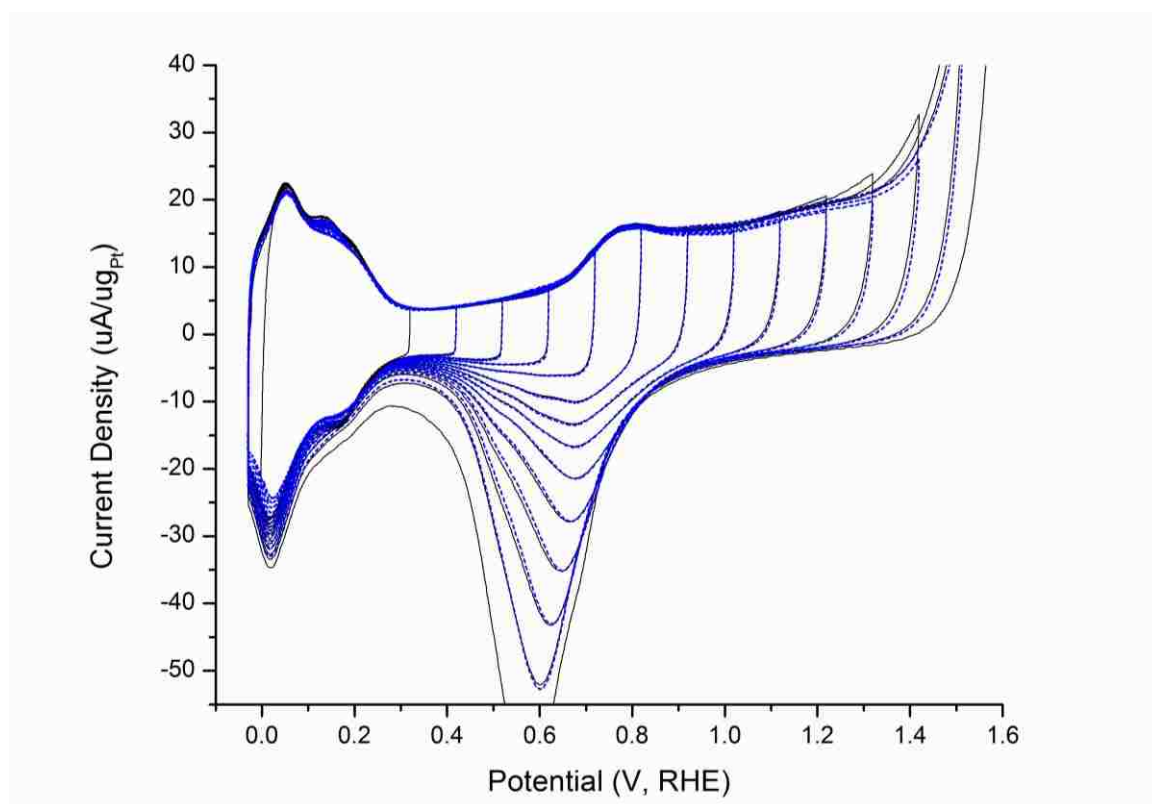


Figure 8.6: Cyclic voltammograms of 30%Pt/XC72 in 0.1M HClO_4 at a scan rate of 20mV/s with step-increases of 0.1V/cycle from 0.3V to 1.6V (solid), then back to 0.3V (dashed).

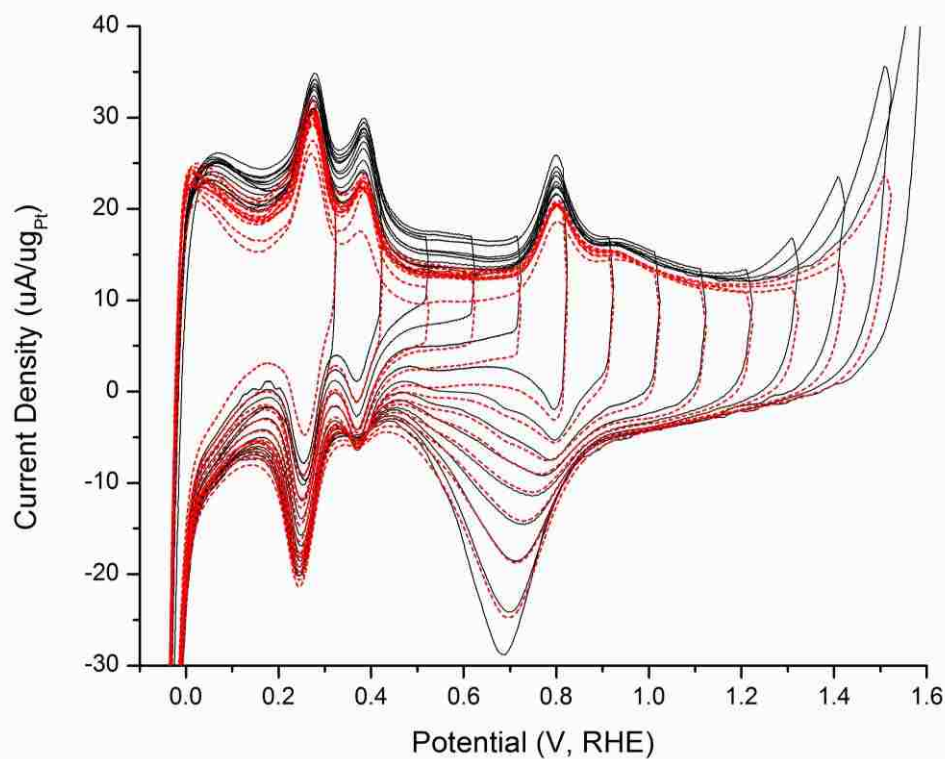


Figure 8.7: Cyclic voltammograms of 30%Pt/XC72 in 1M KOH at a scan rate of 20mV/s with step-increases of 0.1V/cycle from 0.3V to 1.6V (solid), then back to 0.3V (dashed).

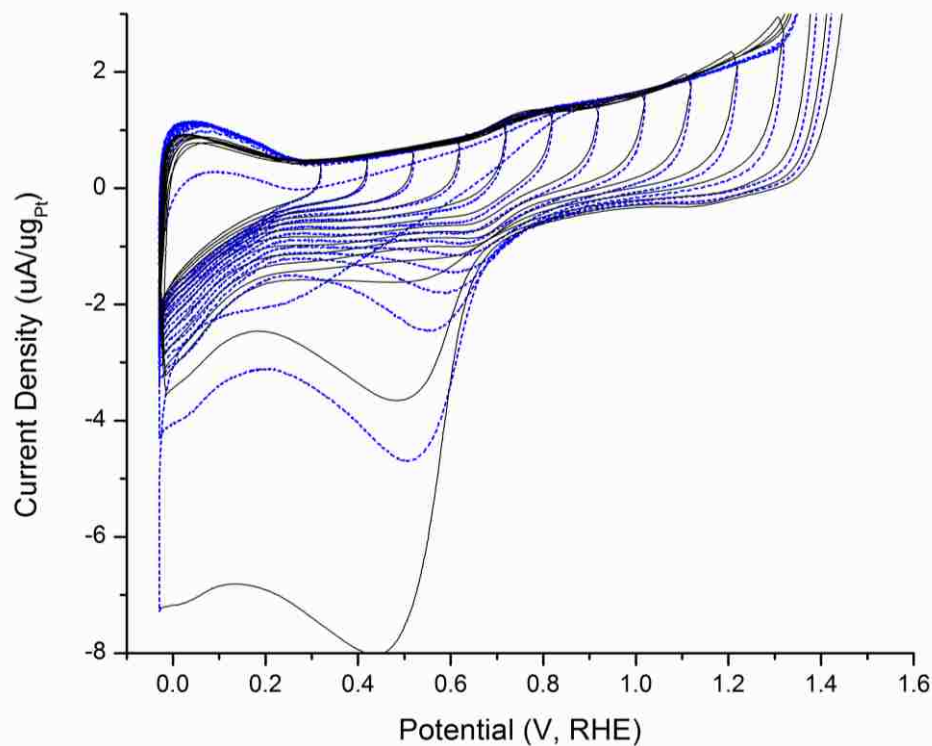


Figure 8.8: Cyclic voltammograms of 60%Pt/NbRu_yO_z in 0.1M HClO₄ at a scan rate of 20mV/s with step-increases of 0.1V/cycle from 0.3V to 1.6V (solid), then back to 0.3V (dashed).

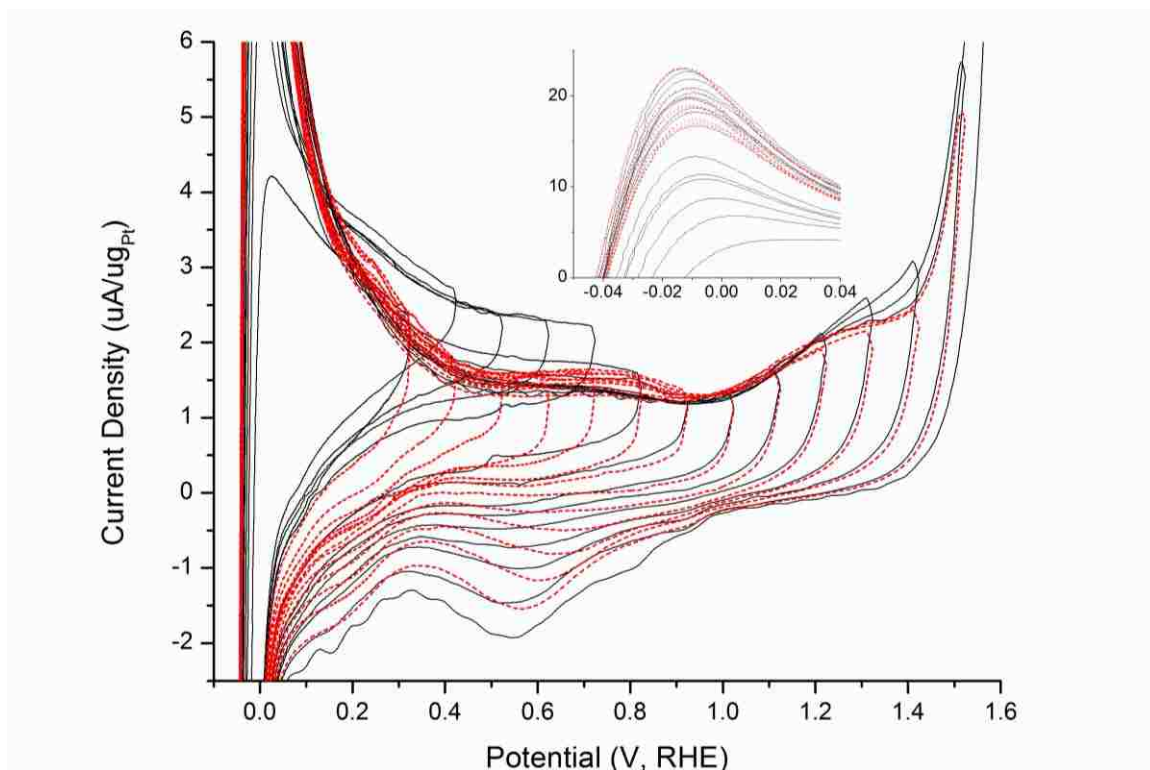


Figure 8.9: Cyclic voltammograms of 60%Pt/NbRu_yO_z in 1M KOH at a scan rate of 20mV/s with step-increases of 0.1V/cycle from 0.3V to 1.6V (solid), then back to 0.3V (dashed). Inset shows growth of the H_{des} peak.

Fig.8.6 shows that Pt/XC72 in acid remains very stable with predictable surface coverage behavior despite exposure to higher potentials. The oxygen desorption peak becomes distinguishable after 0.8V and exhibits a consistent shift to lower potentials after cycling to 1.2V_≤. This is due to the proportional growth of multilayer platinum oxide by place exchange¹⁷¹⁻¹⁷³, and represents the greater energy necessary to fully reduce the Pt-O surface. Despite this and any other effects, anodic and cathodic scans show excellent overlap indicating the stability of the catalyst. The same is true to a lesser extent for Pt/XC72 in 1M KOH. There is a very sharp peak associated with the formation of Pt-OH around 0.8V which precedes an overall shift in the double layer region to lower current densities. This shift is maintained for all progressively cathodic, stepped scans. In this

case, differences between progressively anodic and cathodic, stepped scans may be attributable to a steady state alteration in the double layer at the surface.

Fig.8.6-7 may be taken as the expected behavior of Pt without significant support contributions, and compared with the behavior of Pt/NbRu_yO_z on this basis. The Pt-O reduction peak should occur between 0.6-0.8V. Above 1.2V, the NbRu_yO_z support adsorbs a significant amount of oxygen, leading to the dramatic oxygen desorption behavior below 0.6V after scanning towards 1.6V in Fig.8.8. This behavior is likely an enhanced example of the mechanism behind the formation of the thin films observed in Fig.8.3-4. Niobia which is partially reduced, such as that at an interface with Pt or Ru, can become dissolved in electrolyte at anodic potentials, proceeding as Nb(IV) → Nb(V)_{sol} + e⁻ + V⁴_{Nb}, where V⁴_{Nb} is a cation vacancy remaining at the interface ¹⁷⁴. These vacancies could then instead be filled by more mobile H⁺ during cathodic shifts, facilitating the outward, 3D growth of the niobia film. During H⁺ adsorption, simultaneous e⁻ adsorption can reduce Nb(V) to Nb(IV) ¹⁷⁵ which suggests that a great deal of Nb(IV) could be present at Pt/Nb interfaces at low potentials. It is also possible that non-Faradaic processes are occurring farther from the electrode. Nb(IV) and Nb(V) can absorb oxygen directly, or from water according to the reaction, 2Nb(V)_{sol} + 5H₂O → Nb₂O₅ + 5H⁺.

In 1M KOH (Fig.8.9), the current density drop of the double layer at ~0.8V observed for Pt/XC72 also occurs, indicating that the phenomena is not unique to either catalyst. The Pt-O reduction peak is shifted to higher potentials during progressively cathodic sweeps which may be the result of better ion transport through a less dense surface, i.e. the niobium oxide thin film. This would also be true of the catalyst in acid. As the oxide

layer forms, Pt nanoparticles deeper in the NbRu_yO_z support particle may become increasingly exposed. The growth of the oxide layer and the resulting evolution of more Pt surface sites may be responsible for the improvement in H⁺ adsorption capacity after sweeps to higher potentials. But because these processes do not necessarily involve measureable electron exchange, it is difficult to draw conclusions from this experiment, alone. They are also inapplicable towards explaining the Pt surface deactivation observed for gas phase catalysts supported on niobia. Instead, these more likely involve reduced forms of niobia initially at Pt/Nb interfacial sites which experience a 2D growth process across the Pt surface.

8.5 Chrono-potentiostatic Analysis

Both catalysts were held for 20 min each at 0.0V, 1.2V, 0.0V in 0.1M HClO₄ and 1M KOH to monitor the cumulative surface activity during H₂ and O₂ evolution potentials. Taken from Pourbaix diagrams for each element in the system, species of certain types are more probable to be present at each potential.

At 0.0V: H₂/H₂O₂/H₂O, Pt, Nb₂O₅/NbO₃⁻, and Ru.

At 1.2V: O₂/H₂O, Pt(OH)₂/PtO₂-H₂O/PtO₃⁻, Nb₂O₅/Nb₂O₅-nH₂O/HNbO₄/NbO₄²⁻, and RuO₂-nH₂O/HRuO₄/H₂RuO₅.

These are not conclusive, and various other subspecies of niobia probably exist.

Fig.8.10A shows the charging of Pt/XC72 at 0.0V before (A1) and after (A3) holding at 1.2V (A2) for 20 min. The latter shows less surface activity, as well as a stable, less negative slope. This indicates that A2 resulted in some sintering of the Pt catalyst leading to lower surface activity. On Pt/NbRu_yO_z, the slopes of A1 and A3 are nearly identical.

The larger magnitude of A3 is likely from the rapid reduction of the thin, oxidized niobia layer built up during A2, occurring within the first few seconds. This film, formed from niobia which originated from the more dense support particle bulk, might also expose previously isolated Pt nanoparticles and form open ion pathways from the surface to the interior during the dissolution process¹⁷⁶. This would be especially conducive for greater hydrogen adsorption. If the behavior of the charge curve is defined by Pt at longer times, then the slopes of A1 and A3 for Pt/XC72 and Pt/NbRu_yO_z would seem to suggest that Pt nanoparticles are less subject to sintering on NbRu_yO_z.

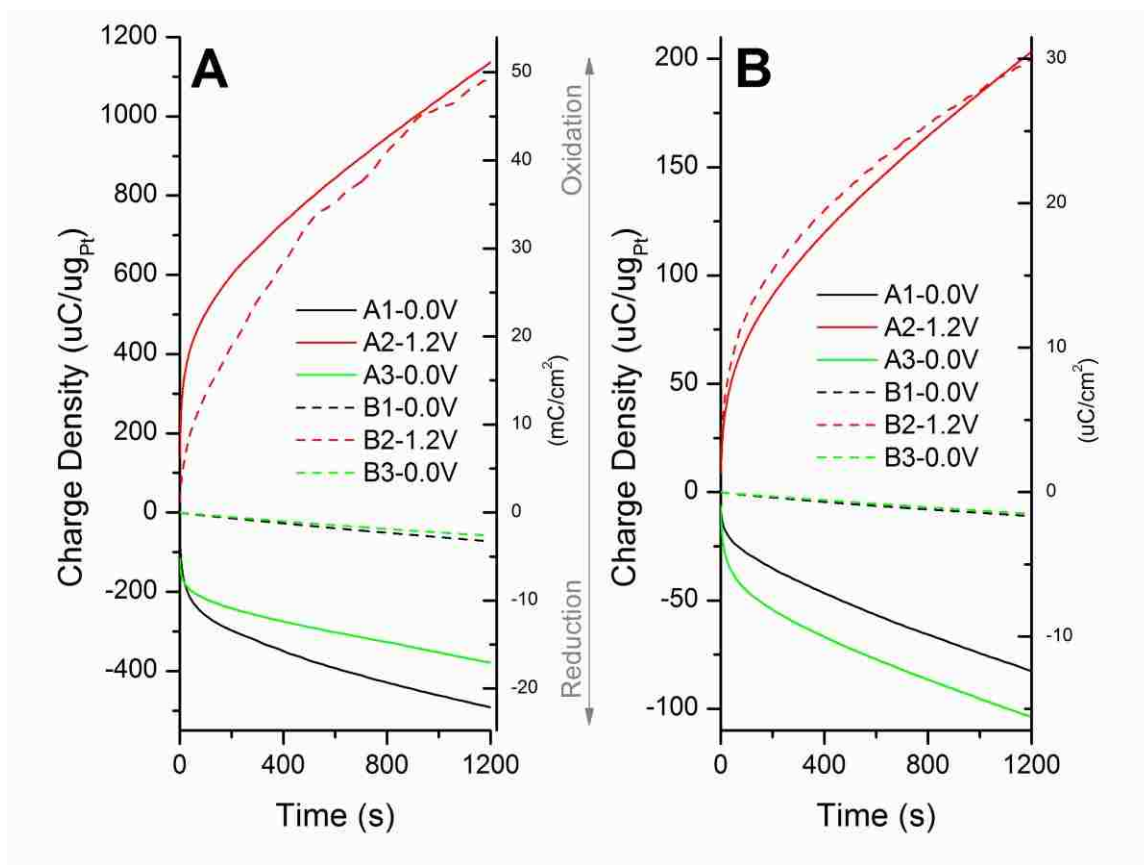


Figure 8.10: Chrono-potentiostatic coulometry measurements of (A) 30%Pt/XC72 and (B) 60%Pt/NbRu_yO_z. Electrodes were held at 0.0V, 1.2V, and 0.0V for 20 min periods in 0.1M HClO₄ (A1-A3) and 1M KOH (B1-B3).

The better stability of carbon in acid is shown by the smooth progression of A2 compared to B2 in Fig.10A. But both catalysts show roughly the same oxidation behavior in acid and base. Though, reductive charging in base is significantly less than in acid. This is consistent for a double layer with a higher concentration of anions in basic media and indicates a shift in the exchange current density at the electrode surface relative to the H_2O redox couple. It is apparent that for Pt/XC72, the relative behavior of B1 and B3 is about the same as that of A1 and A3. But this is less clear for Pt/NbRu_yO_z.

Because H^+ is the smallest ion in the system, the hydrogen desorption peaks of each catalyst taken from cyclic voltammetry performed before and after each constant-potential holding period can reveal the availability of Pt surface sites in 1M KOH. Fig.8.11 shows these peaks taken before any holding periods, as well as after B1, B2 and B3. Pt/XC72 (Fig.8.11A) behaves as expected, with greatly elevated H^+ desorption after holding at 0.0V (B1) compared to the electrode initially. After holding at 1.2V (B2), the hydrogen adsorption potential of B1 is not recovered in B3. This is due to the sintering of Pt nanoparticles observed in Fig.8.10A.

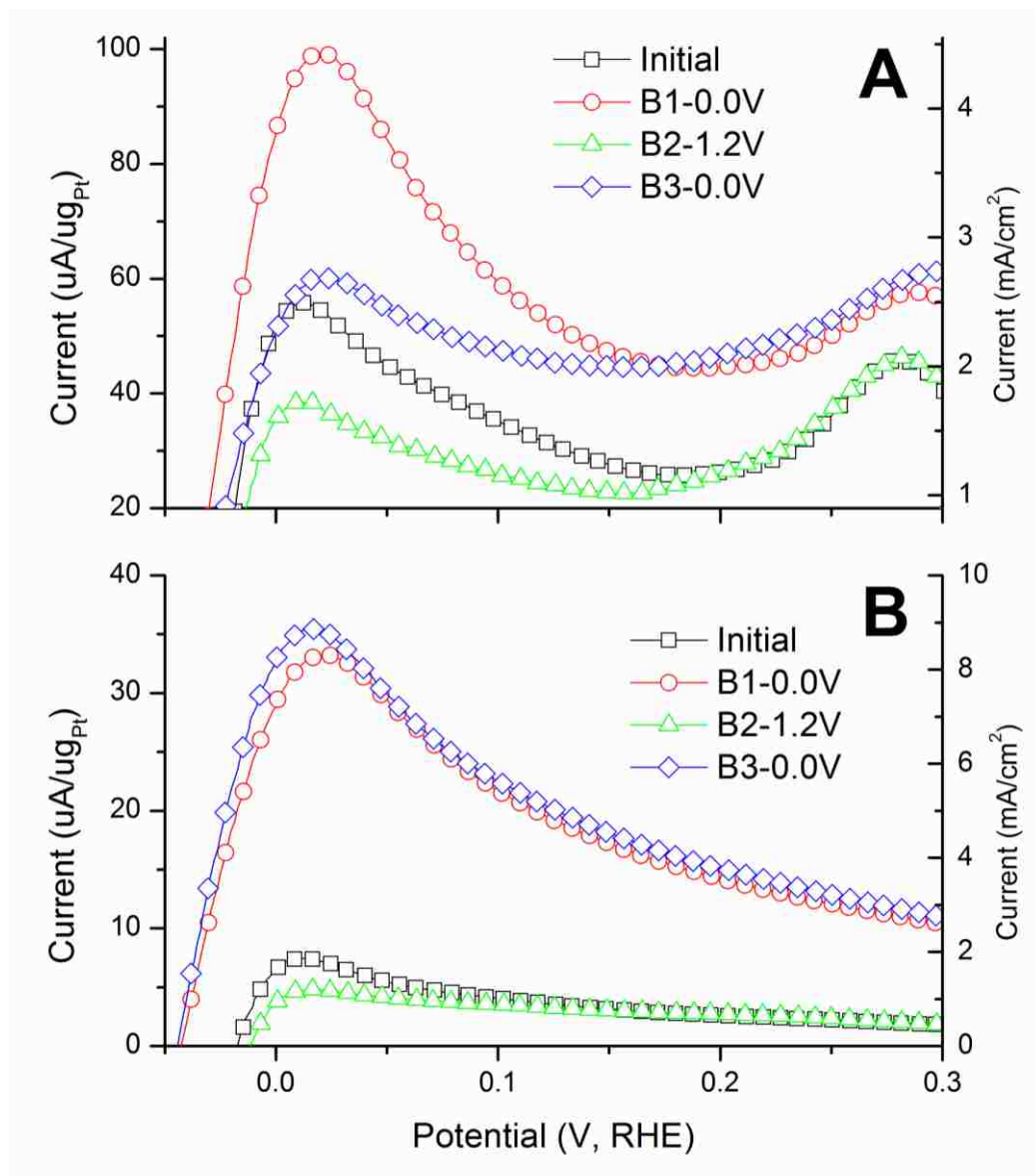


Figure 8.11: Hydrogen desorption peaks from cyclic voltammograms taken in 1M KOH at 50mV/s for (A) 30%Pt/XC72 and (B) 60%Pt/NbRu_yO_z before and after each potential holding period in Fig.8.10.

The surface of Pt/NbRu_yO_z appears to preferentially adsorb oxygen over hydrogen at open circuit potential, as shown in the near uniformity of the Initial H_{des} peak and B2 of Fig.8.11B. B3 shows increased H⁺ desorption over B1, suggesting that the adsorption potential of Pt/NbRu_yO_z in 1M KOH follows the same trend as in 0.1M HClO₄, albeit at much lower currents. As the film of oxidized niobia becomes increasingly thick, it is less clear whether formation mechanisms (especially relative to the Pt surface) are Faradaic, the result of charging, or charge separation process (especially possible from Nb(V)_{sol} at anodic potentials).

8.6 CO Stripping

CO stripping studies can help elucidate the adsorption potential of Pt surface sites from that of the absorption potential of the NbRu_yO_z support. CO is a larger molecule than H⁺/H₂, making it subject to greater diffusion resistance through the oxidized niobia film. It should also have a lesser impact on the redox behavior of niobia, instead preferentially adsorbing onto the Pt surface.

Table 8.1: Calculation of Electrochemical Surface Area on Pt for CO and H (soln) species from Fig.8.12.

	Q_{CO} ($\mu C/\mu g_{Pt}$)	Q_{H-ads} ($\mu C/\mu g_{Pt}$)	Q_{H-des} ($\mu C/\mu g_{Pt}$)	ESA_{CO-des} (m^2/g_{Pt})	ESA_{H-ads} (m^2/g_{Pt})	ESA_{H-des} (m^2/g_{Pt})	% STDev
30%Pt/XC72	356.00	153.00	157.40	84.76	72.86	74.95	8.20%
60%Pt/NbRu_yO_z	11.30	24.50	-3.28	2.69	11.67	-1.56	158.34%

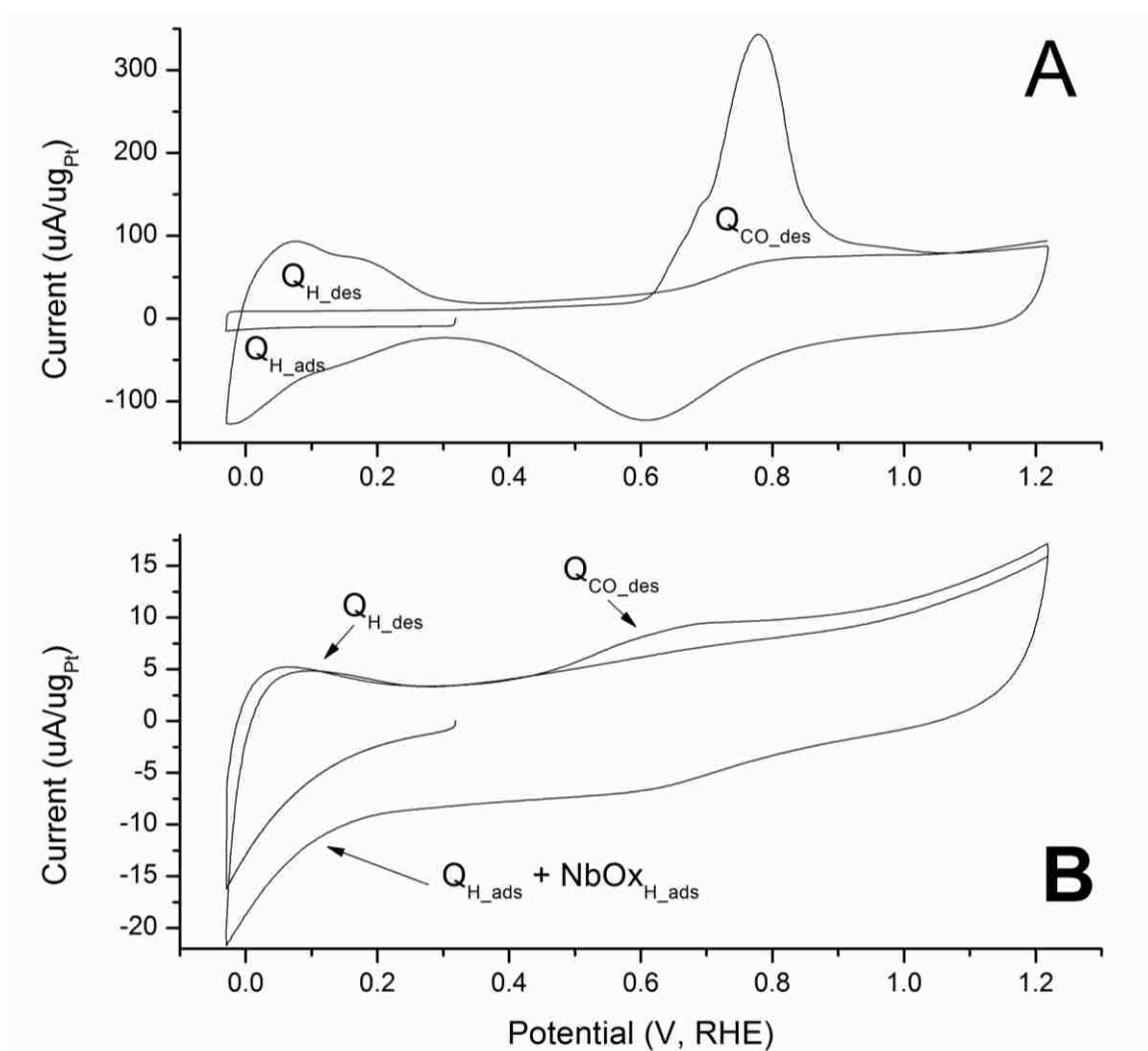


Figure 8.12: CO stripping cyclic voltammetry in 0.1M HClO₄ at 100mV/s on (A) 30%Pt/XC72 and (B) 60%Pt/NbRu_yO_z.

In Fig.8.12A, the CO desorption peak for Pt/XC72 beginning above 0.6V is characteristic of platinum on carbon, as are the hydrogen adsorption/desorption peaks and the distinguishable double layer current exchange density delineated by the first cathodic and anodic sweeps at low potential. The CO peak on Pt/NbRu_yO_z is considerably broader (Fig.8.12B). It is interesting to note that the peak begins at ~0.45V, the same potential at which we previously showed the evolution of CO₂ from 1M ethanol to begin on the

Pt/NbRu_yO_z surface using the in situ infrared reflection adsorption spectroscopy (IRRAS) technique (Ch.7).

Scans at low potentials in which all Pt sites are occupied by CO should provide a baseline against which to quantify the extent of hydrogen adsorption/desorption from subsequent scans taken after CO removal. The area of the resulting peaks can be used to calculate the electrochemically active surface area (ESA) of Pt, previously described in Ch.4.

Furthermore, the values of ESA calculated from CO_{des}, H_{ads}, and H_{des} peaks should be roughly the same for a clear Pt surface. These values are shown in Table 8.1 for both catalysts. Indeed, all peaks indicate an approximate ESA of 73-84 m²/ug_{Pt} with a small error of 8%. Values reported in the literature range from 7.8m²/g_{Pt} to 85m²/g_{Pt}¹⁷⁷⁻¹⁷⁹. It is known that a variety of factors can significantly affect the measurement, including the use or absence of Nafion on the catalyst, the purity of the sparging gas, and the cleanliness of the electrochemical cell. But all three peaks are significantly different for Pt/NbRu_yO_z and require further interpretation.

The first cathodic sweep from Pt/XC72 is relatively flat indicating a stable Pt-CO surface, whereas that of Pt/NbRu_yO_z experiences increased reduction. This could indicate the displacement of adsorbed CO with H approaching 0V, or hydrogen intercalation into the niobia. CO poisoning is largely responsible for the failure of Pt catalysts in PEM fuel cells and is usually remediated by scanning to potentials approaching or beyond 1V. This is why CO displacement is unlikely even though the net effect would be the further reduction of Pt because, unlike H, CO is known to cover multiple Pt sites¹⁸⁰. Regardless, it is difficult to discern the Pt contribution from the hydrogen region, making ESA_{CO} the most appropriate value.

8.7 Open Circuit Potential Studies in Alkaline Electrolyte

OCP studies over longer periods can further reveal differences in the surface state of both catalysts under different electrolyte conditions. It has been shown that potential shifts of niobium and niobia in basic media vary greatly with small changes in pH. The native oxide layer of niobia in open air may not be stable in electrolyte, and when it dissolves, cathodic shifts occur. Alternately, anodic shifts represent a thickening of the native oxide layer, or the formation and thickening of a new layer whose growth mechanism varies with pH¹⁵⁸.

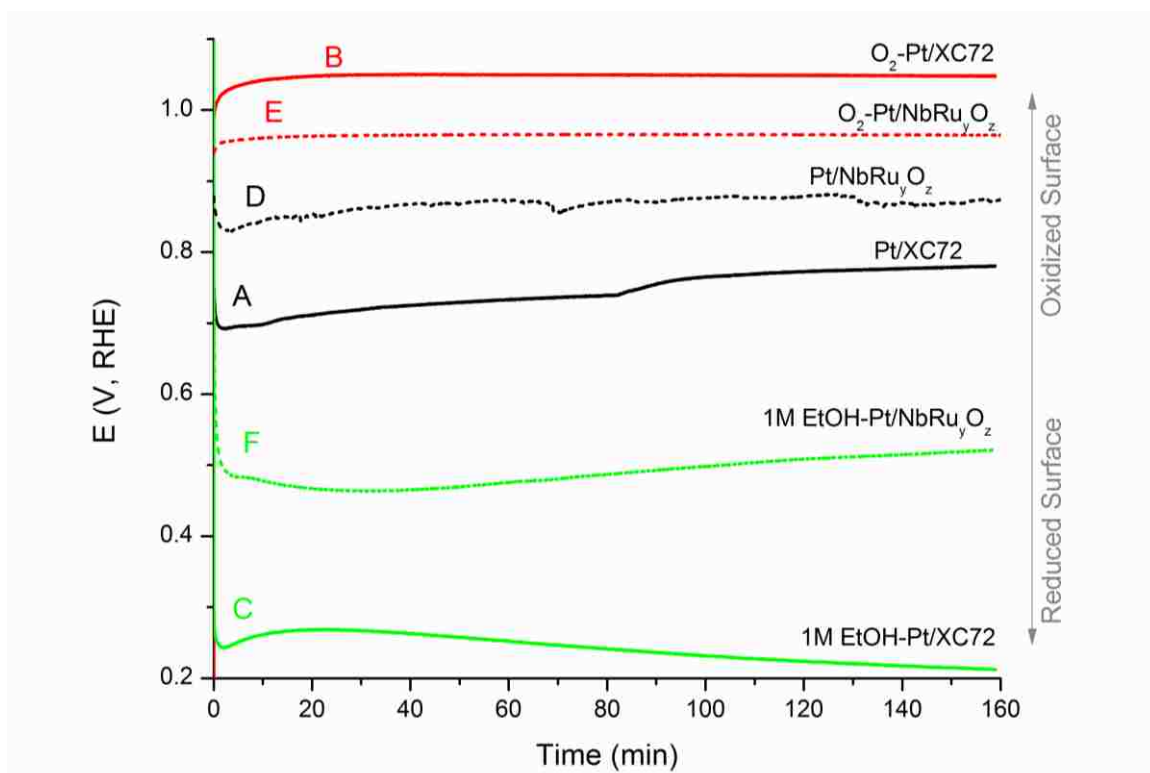


Figure 8.13: Open-circuit potential measurements in the presence of 1M KOH electrolyte, electrolyte and bubbled O₂ (sparging), and electrolyte and 1M ethanol.

The sporadic nature of Pt/NbRu_yO_z in 1M KOH is not immediately clear. It is possible that niobia dissolves into solution at the surface, causing a steady rise towards oxidative

potentials. This would occur until a local solubility limit was reached, at which point the current would suddenly exhibit a cathodic shift as a monolayer or more of niobia precipitated back onto the surface¹⁸¹. Though a similar, smoother, passivation process appears to occur on Pt/XC72 as well, the potential merely stabilizes around 83 min and never actually shifts cathodically. This occurs regardless of glassy carbon electrode surface area and whether a Pt wire or mesh is used as a counter electrode. Because the system employs no mixing and purging gas flows just above the electrolyte liquid level, this effect on Pt/XC72 might be attributed to buildup from electrolyte, alone.

These effects are not apparent for either catalyst during oxygen sparging. Instead, higher potentials are quickly reached and remain steady, indicating that both surfaces are further oxidized. The addition of 1M ethanol has the opposite effect, reducing both surfaces initially. The long term behavior would suggest that the two catalysts have different stabilities in this environment. The lower potentials caused by 1M ethanol compared to 1M KOH alone indicate a significant shift in the charge-transfer overpotential corresponding to a change in the surface concentration of electrolyte species (due to the competing presence of the alcohol). On Pt/NbRu_yO_z, the surface is initially reduced by ethanol adsorption on Pt, as well as a change in the equilibrium potential of the niobium oxide thin film seen within the first ten minutes. Reduction continues until ~0.46V, the approximate potential at which CO₂ evolution was shown to begin on this catalyst. At a potential of 0.59V at 120 min, there is a distinct change in the slope of the data from 0.56mV/min to 0.31mV/min. This decrease in the rate of change towards oxidative potentials roughly correlates with the potential at which Pt begins to adsorb H₂O onto its surface (0.5V≤). Alternately, CO adsorption is favored at lower potentials (0.4V≥). The

latter potential regime is responsible for the opposite time-behavior of Pt/XC72. A small quantity of ethanol is oxidized to acetaldehyde, acetic acid, CO or CO₂. But eventually, CO begins to accumulate as a fixed species on the surface, known as poisoning.

It is apparent that ΔE_{B-C} is much larger than ΔE_{E-F} . ΔE_{D-E} for Pt/NbRu_yO_z with the addition of oxygen is especially low and in agreement with the hydrogen desorption peak behavior (Fig.8.11B) that the surface is nearly saturated with oxygen initially. These results suggest that the anodic potential of Pt/NbRu_yO_z is limited by the intrinsic instability and corrosion/dissolution behavior of niobia near the O₂/H₂O redox couple. Alternately, the reduction potential is limited by the extrinsic decrease of free Pt adsorption sites because of an increase in Pt/NbO_x interfacial sites, possibly from a 2D NbO_x growth mechanism (see DFT). The same NbO_x species intrinsically alter the d-orbitals of Pt resulting in fewer electron vacancies. This allows ethanol subspecies to bond more strongly at these interfacial sites (Ch.7).

Cyclic voltammetry of each sample was performed at 50mV/s for 50 cycles after the 160 min OCP period to determine how each surface may have been altered. Fig.8.14 shows the results for all three stages of Pt/XC72, while those of Pt/NbRu_yO_z are shown in Fig.8.15. Arrows in each figure indicate the trend of a particular redox feature with subsequent cycles. All of the adsorption features of Pt/XC72 appear to decrease (positive current shift), except for the H_{ads} peak associated with Pt(100) at 0.22V. Desorption features also appear to decrease (negative current shift), with the exception of the ethanol oxidation peaks. All scans taken during O₂ sparging show a general decrease in current at all points, including the double layer region.

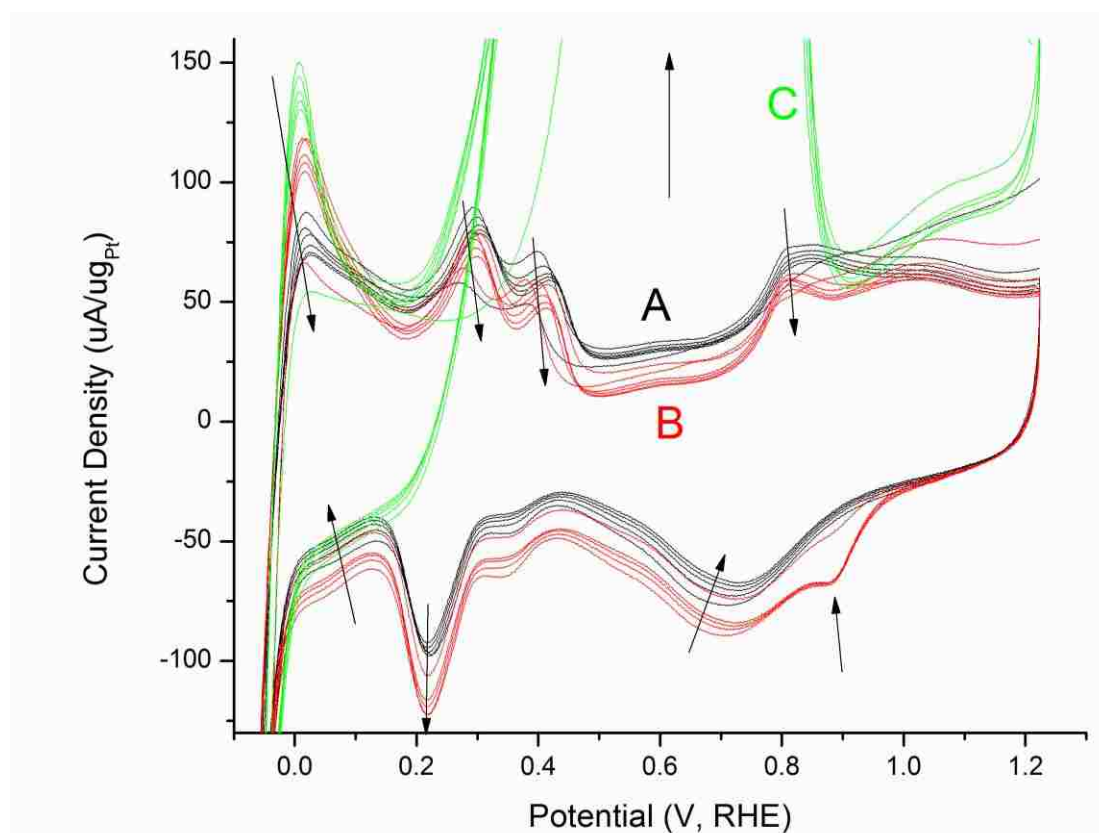


Figure 8.14: Post OCP cyclic voltammograms at 50mV/s in 1M KOH for 30%Pt/XC72. Showing cycles 1, 10, 20, 30, 40 and 50. Labels correspond to those of Fig.8.13.

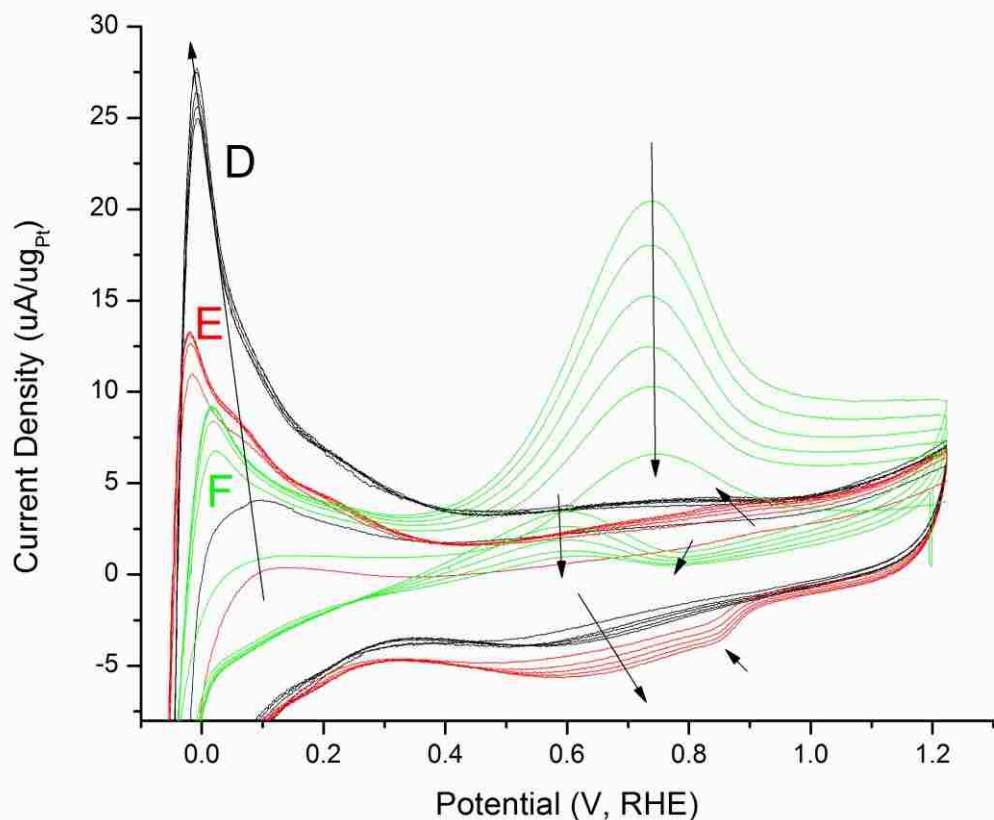


Figure 8.15: Post OCP cyclic voltammograms at 50mV/s in 1M KOH for 60%Pt/NbRu_yO_z. Showing cycles 1, 10, 20, 30, 40 and 50. Labels correspond to those of Fig.8.13.

The redox features of Pt/NbRu_yO_z appear to show the opposite behavior in all cases. The rapid decrease in the ethanol oxidation peaks indicates the deactivation of Pt adsorption sites while hydrogen adsorption and desorption both increase. The relative positions of the H_{des} peaks from electrolyte only and O₂ sparging reflect those of B1/B3 and B2 (post 0.0V and 1.2V, respectively) from Fig.8.11B. The double layer region is obscured by superimposed charging current of the niobia support/film. The two oxygen desorption peaks of the O₂ sparging cathodic sweeps in Fig.8.14 at 0.9-0.7V are also present in Fig.8.15 as a more contiguous region, possibly because of a more diffusion limited desorption behavior.

8.8 Density Functional Theory Studies Adsorbates on the Pt Surface

We used DFT type calculations to explore the energetics of surface diffusion of elemental C, O, and Nb (Fig.8.16). Carbon is seen to have the highest activation barrier (0.96 eV), followed by oxygen (0.68 eV) and niobium (0.33 eV). The transition state energies are comparable to previous work (21). Differences in activation barriers are attributed to the use of different exchange correlation functionals and different representations of nucleus electron interactions. The attempt frequency for a diffusion jump is expected to be on the same order as the vibrational frequencies, $\nu_0=10^{13}$ Hz (21,22). Taken into account the degeneracy of the diffusion path for a close packed (111) surface and a random walk model for the diffusion process, we obtain for the rms distance traveled by a particle:

$$\langle x^2 \rangle = \sqrt{\frac{2}{3} \nu_0 d^2 \exp\left(-\frac{\Delta E^*}{k_B \cdot T}\right) \cdot t}$$

Evaluating this expression for a nanoparticle of radius 10 nm at T=300 K using $d=2.812$ Å, the jump distance on the clean surface, we obtain lifetime estimates of ~1200 days, 30 minutes, and 1.2 ms, for C, O, and Nb, respectively. Comparing these results to the observed deactivation within weeks, we observe that oxygen is a likely candidate to explain the rapid deactivation of the catalyst. This is further corroborated by the previous observation that activation energies, for surface diffusion processes, obtained from DFT tend to be underestimated by ~24% on average, with a range from ~23% overestimated to 48% underestimated (21). Thus, correcting our activation energy upward by 25%, we obtain an estimated lifetime for a nano-particle of 10 nm radius of 18 days, very comparable with the experimental observations. Thus, the DFT calculations support the

deactivation mechanism that involves a transient reduced form of niobia (NbO_x) that provides the oxygen source needed for our proposed deactivation mechanism.

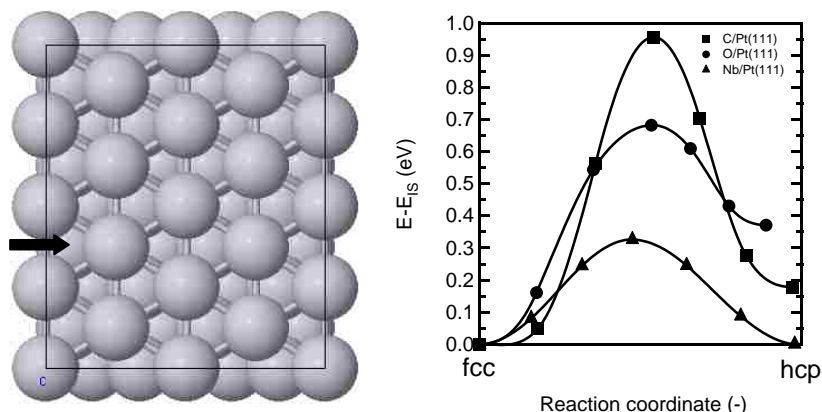


Figure 8.16: (Left) Grey spheres represent Pt atoms. The arrow indicates the transition path between the hollow fcc and hcp sites. (Right) Energetics along the transition path: squares, circles, and triangles, for surface diffusion of elemental C, O, and Nb, respectively.

8.9 60%Pt/NbRu_yO_z Treated at 300°C and 650°C

In order to determine how crystallization of the niobia support effects the results of the tests used in this study, two samples previously explored in Ch.7 were revisited here. These were based upon 6Pt:1Nb:1Ru:2O wt% and were thermally reduced at 300°C (Pt-300) and 650°C (Pt-650), the latter being ~100°C or more above the crystallization temperature of niobia. It was shown that despite the relatively low weight percent of niobium, crystallization appears to significantly reduce the charging activity (and possibly Faradaic activity associated with hydrogen intercalation) seen during standard cyclic voltammetry studies. The objective of this section is then to determine whether crystallization might shift the behavior of Pt/NbRu_yO_z towards that of Pt/C.

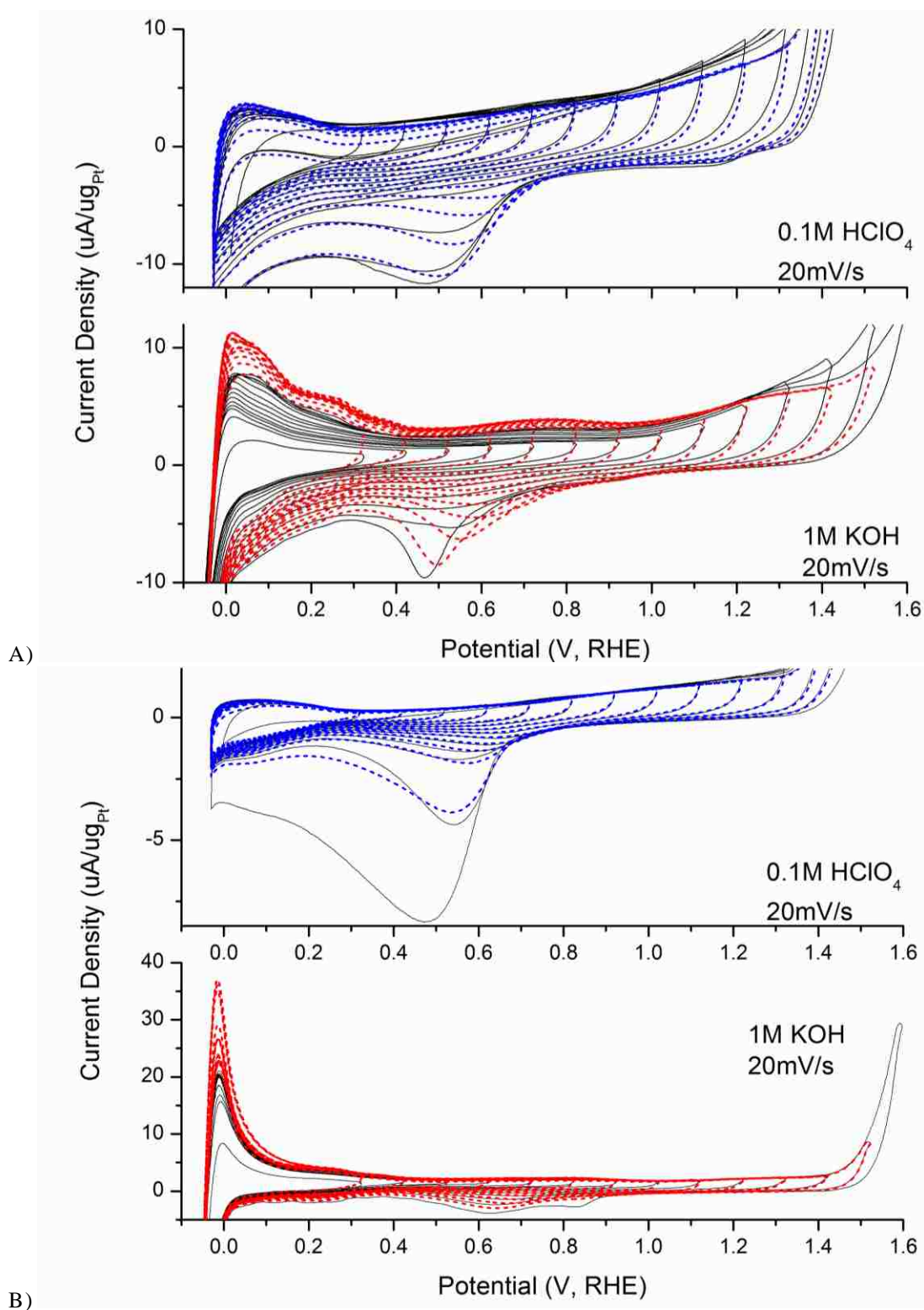


Figure 8.17: Cyclic voltammograms of Pt-300 (A) and Pt-650 (B) in 0.1M HClO_4 and 1M KOH at a scan rate of 20mV/s with step-increases of 0.1V/cycle from 0.3V to 1.6V (solid), then back to 0.3V (dashed).

Sequential oxidation studies in which cyclic voltammetry is performed with a small step-increase in the positive potential with each cycle, then followed by equal decreases to the original starting potential. The purpose was to determine the stability and reversibility of sweeps after passing the oxygen evolution potential in the aqueous electrolyte. The results show that charging in the electrochemical double layer is indeed significantly decreased after crystallization, though less-so in alkaline electrolyte. The reactivity of the material also becomes more chemically specific depending upon the media. Pt-300 appears to favor oxygen exchange, indicated by the broader adsorption and desorption peaks during anodic and cathodic scans, respectively. The opposite is true in 1M KOH, where the hydrogen adsorption/desorption activity is more greatly enhanced after exposure to higher potentials. But in both cases, the capacity for oxygen exchange is enhanced, indicating a thickening of the passive layer that can act as an oxygen sponge. After niobia crystallization, Pt-650 exhibits a decrease in oxygen desorption current, while adsorption is roughly the same in both media. Hydrogen desorption is significantly more prevalent in 1M KOH. It appears that while the hydrogen and oxygen redox features of Pt-650 are not indicative of a clean Pt surface, the material is more like Pt/C insofar as that it is significantly more reversible, and therefore, stable under harsh, oxidizing conditions at higher potentials.

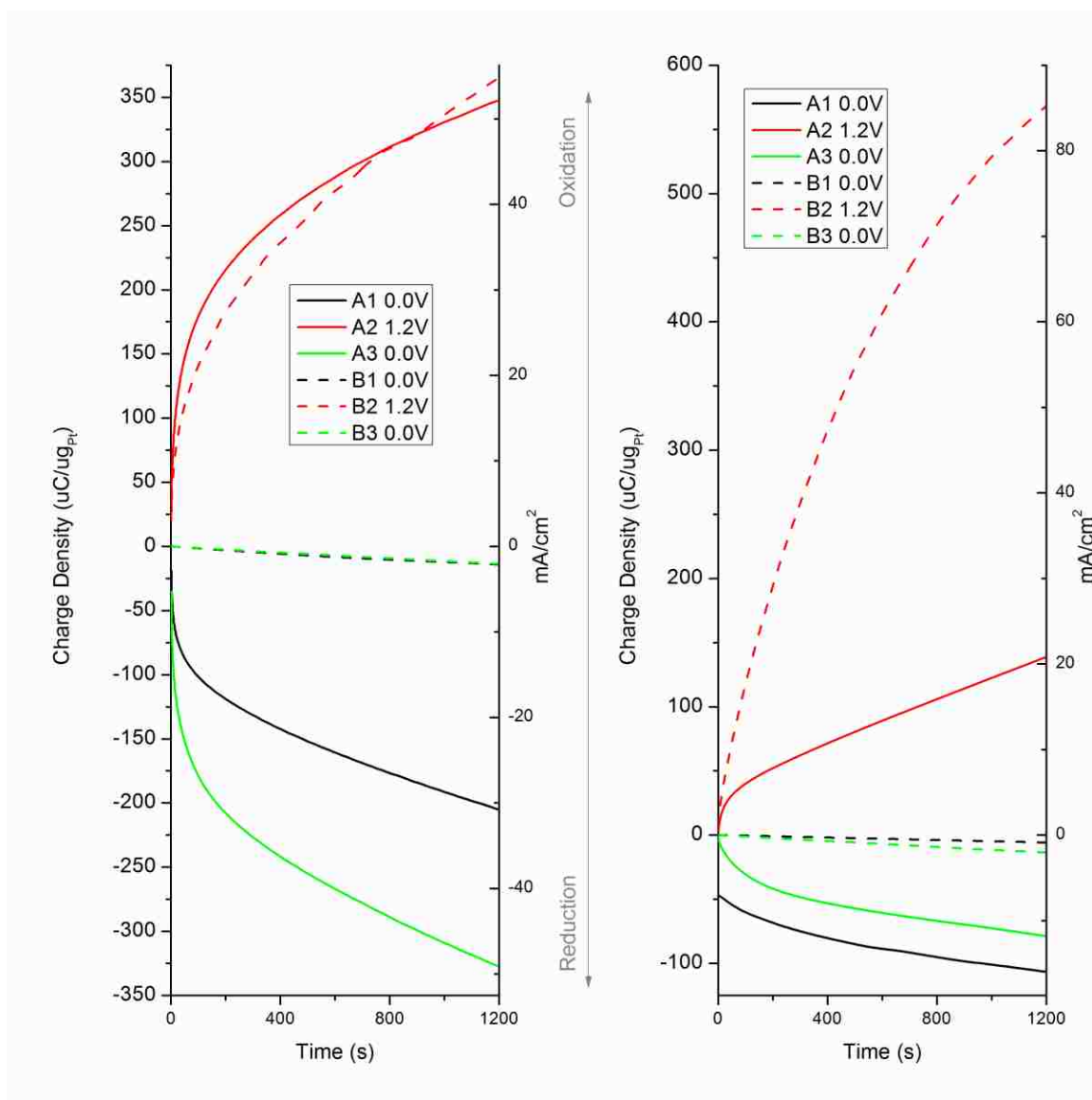


Figure 8.18: Chrono-potentiostatic coulometry measurements of Pt-300 (left) and Pt-650 (right). Electrodes were held at 0.0V, 1.2V, and 0.0V for 20 min periods in 0.1M HClO₄ (A1-A3) and 1M KOH (B1-B3).

Chrono-potentiostatic results for both samples are shown in Figure 8.18. The behavior of Pt-300 is like that of 60%Pt/NbRu_yO_z reduced at 400°C shown in Figure 8.10. Not surprisingly, there is significantly less reduction activity in basic media whereas the oxidation activity is about the same in both within the time scale considered.

Crystallization in a reducing atmosphere appears to succeed in locking the niobia into a

more reduced state. This is evident by the magnitude of B2 which is three-fold that of A2. The electrochemical surface behavior before and after crystallization also varies at 0.0V. The magnitude of the charge density is significantly lower with respect to catalyst mass and electrode surface area. For Pt-300 $|A3| > |A1|$ indicating the rapid collapse of a passive layer formed during oxidation (A2) at constant 1.2V. This trend is reversed for Pt-650, which may indicate that the native oxide layer formed at open circuit potential contained more oxygen species than the layer which was induced at 1.2V (A2). Overall, these results would seem to indicate that Pt-650 is more stable in acid electrolyte and at reducing potentials.

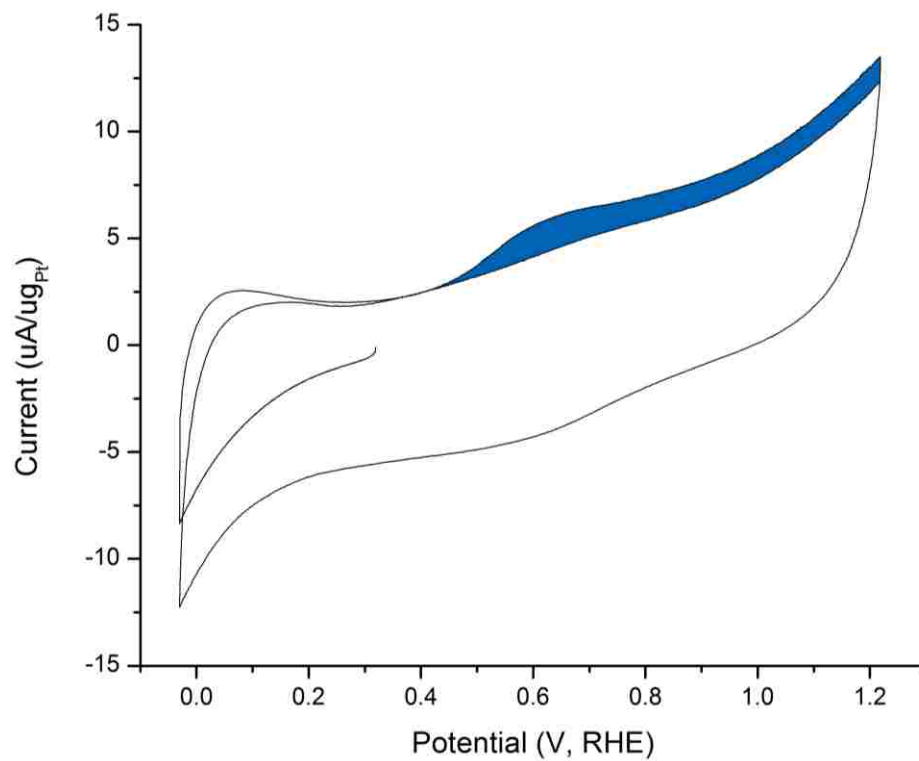
CO stripping is an especially useful method of analysis for this sample set because the formation of CO_x complexes with the niobia support or the passive oxide layer should be minimal. This is due in part to the relatively large size of CO_x species compared to O_x and H_x . But also because the polarization-induced thermodynamic shifts in the valence state of niobia should result in the formation of lower energy bonds with the latter two species. For this reason, CO adsorption might provide a clearer picture of the availability of Pt surface sites, as opposed to O_2 and H_2 which can be involved in reactions with the support.

Seen in Figure 8.19, the CO desorption peak is quite broad on Pt-300. It becomes more narrow and centered around a potential of 0.6V after crystallization. Despite more than a two-fold decrease in double layer exchange current density due to charging, the relative proportion of the CO_{des} peaks compared to the stripped CVs (taken as background) is about the same. It may be the case that the broad character of these peaks compared to that of Pt/C (Fig.8.12A) is because CO is bound more strongly on Pt/niobia. Or it may be

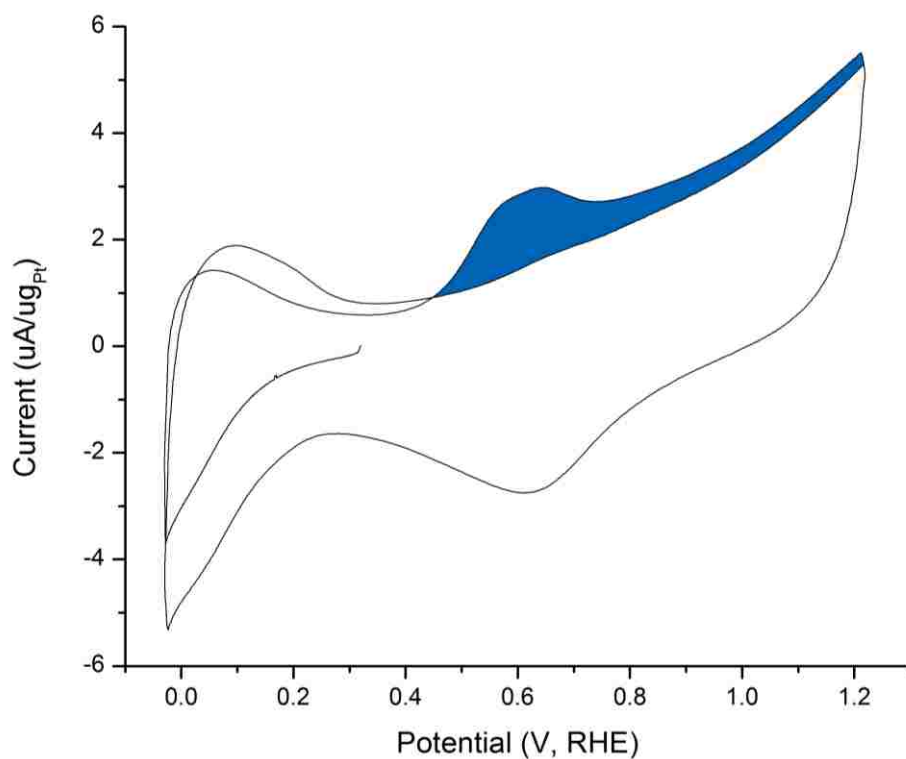
that the CO_{des} peak is overlaid with current from the formation of Pt-OH/-O or Nb₂O₅. Based upon the electronic modification of platinum by niobia shown to occur in Ch.7, as well as the decrease in charging after crystallization, both explanations are plausible. However, the latter is more likely to manifest in this type of analysis, reflected by the narrowing of the O_{des} peak in Fig.8.19B.

. Table 8.2: CO Stripping Results Calculated from Fig.8.19

	Q_{CO} ($\mu C/\mu g_{Pt}$)	ESA_{CO-des} (m^2/g_{Pt})
Pt-300	0.85	2.03
Pt-650	0.47	1.12



A)



B)

Figure 8.19: CO stripping cyclic voltammetry in 0.1M HClO₄ at 100mV/s on Pt-300 (A) and (B) Pt-650. CO_{des} peak is shaded in blue.

The calculated values of ESA from Figure 8.19 exhibit unexpected behavior and suggest that quantification of CO stripping results of Pt/niobia is not as straightforward as for Pt/C. Figure 7.13 showed that EOR is improved in acid and alkaline electrolyte after crystallization. It is possible that some unintended CO desorption occurs at potentials below 0.32V. Hydrogen intercalation activity into the niobia support may also alter the Pt surface and adsorbates. The second complete cycle which is taken in the calculations as a background after the CO stripping cycle might also behave unexpectedly. In any case, this method becomes difficult to interpret when it cannot be assumed that the Pt surface is clean, initially.

CHAPTER 9 - Non-Aerosol Synthesis of Composite Crystalline

Oxides

9.1 Electro-catalytic Value of Tin

9.1.1 Batch Deposition of Catalyst onto Supports

Platinum and ruthenium were deposited using a batch deposition technique onto several different support materials. These include mesoporous NbRu_yO_z (8:Nb:1Ru) and NbRuSnO_x (8Nb:1Ru:1Sn) which were previously synthesized using spray pyrolysis. In addition, crystalline NbO_2 nanoparticles (20-50nm) were obtained from Sigma-Aldrich. $\text{H}_2\text{PtCl}_6 \cdot 6\text{H}_2\text{O}$ and RuCl_3 were stabilized in aqueous NaOH (pH=10) as two separate solutions, one of Pt only and the other with Pt and Ru (1:1 mol). Two samples were made with each of the three support types. In the first set, the support was mixed with Pt-solution in a vial to achieve 30wt%Pt. The vial was sonicated for 30 minutes before the addition of NaBH_4 as a reducing agent. This mixture was dried overnight at 100°C . It was then mixed with DI H_2O and centrifuged three times before drying for several hours under the same conditions. The second set of supports were prepared in an identical manner, except that the catalyst loading was instead 22wt%Pt and 11wt%Ru (in addition to any Ru in the support bulk).

This process was meant to remove any differences in the amount and manner of catalyst deposition across the three supports. Cyclic voltammetry was performed in 0.1M HClO_4 and the ethanol oxidation reaction with the addition of 0.5M EtOH. The results are shown in Fig.9.1.

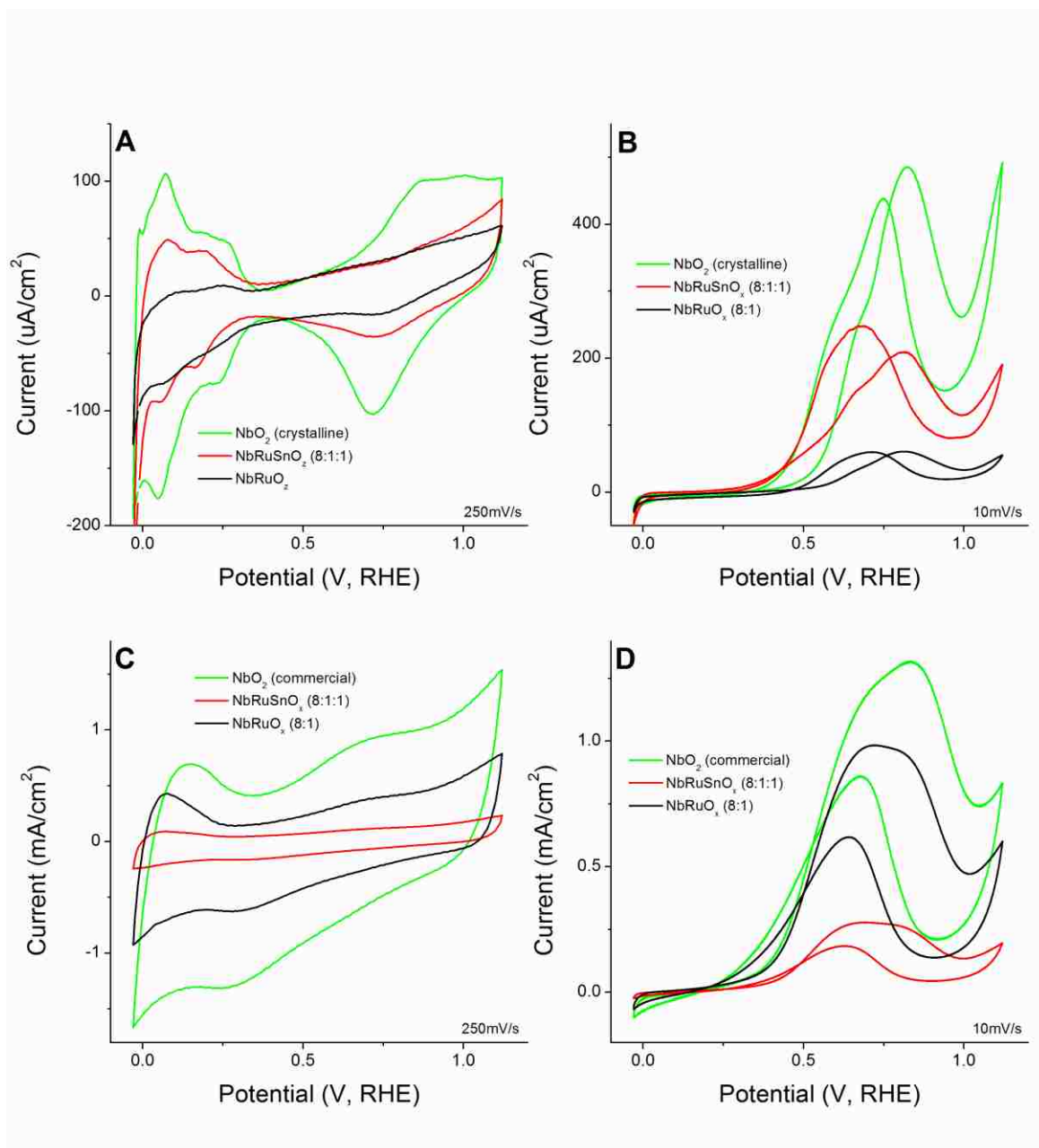


Figure 9.1: Cyclic voltammograms for 30%Pt (A,B) and 22%Pt-11%Ru (C,D) on crystalline NbO₂, NbRuSnO_x (8:1:1), and NbRuO_x (8:1). The total catalyst loading in each case was 50ug to completely cover the surface of a glassy carbon electrode.

There appears to be significantly different behavior across the three support types. But in both cases, NbO₂ appears to offer the highest exchange current density. This support benefits from the increased electrical conductivity of Nb(IV) over Nb(V), as well as stabilization of the passive oxide layer. In order to form, this layer has an additional energy barrier required to remove Nb atoms from a crystalline lattice before oxidizing at the electrolyte interface. It may be that this layer is suppressed with the presence of tin, which causes Pt/NbO₂ and Pt/NbRuSnO_x to show clearer Pt-H and Pt-OH redox features (Fig.9.1B). The EOR current activity of the former is far more comparable to commercial Pt/C than the other two. These redox features are greatly broadened with the inclusion of Ru catalyst (Fig.9.1C). Activity decreases significantly on the NbRuSnO_x support. Here, the peak current from EOR of the forward anodic sweep is nearly equal to that of the cathodic sweep in the sample with Pt-only (Fig.9.1B). This may indicate an overabundance of oxide in which the efficiency of the bi-functional effect decreases. But the benefits of this effect are still apparent on all supports due to the broad oxidation peaks, as well as the fact that the anodic sweep (compared to cathodic) of all peaks in (D) shows improved current exchange from (B).

9.1.2 IRRAS Studies

Samples with 30%Pt were further explored using in situ IRRAS to obtain FTIR spectra during EOR.

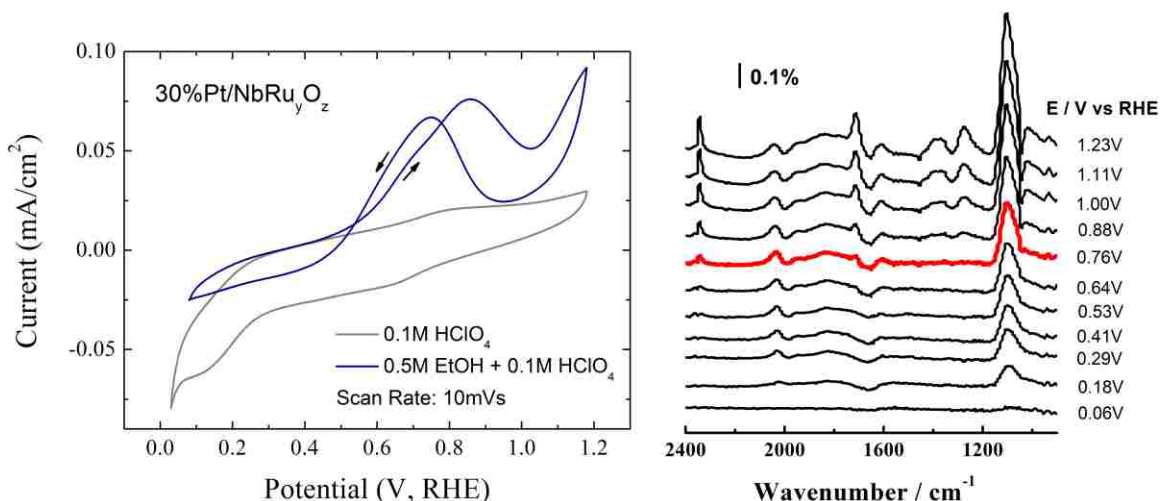


Figure 9.2: in situ IRRAS of 30%Pt/NbRu_yO_z: (Left) CVs taken at a rate of 10mV/s in 0.1M HClO₄. (Right) Corresponding FTIR time-resolved spectra (taken at 1mV/s). The red spectra indicates the start of CO₂ evolution.

30%Pt/NbRu_yO_z is essentially the same as the sample referred to as Pt-DI discussed in Ch.7. The FTIR spectra obtained is consistent between the two in that the evolution of small amounts of CO₂ begins at potentials above 0.7V, as expected for EOR on a clean Pt surface. Simultaneously, CO begins much earlier at ~0.3V. This suggests multiple reaction pathways reflecting different catalyst surface sites.

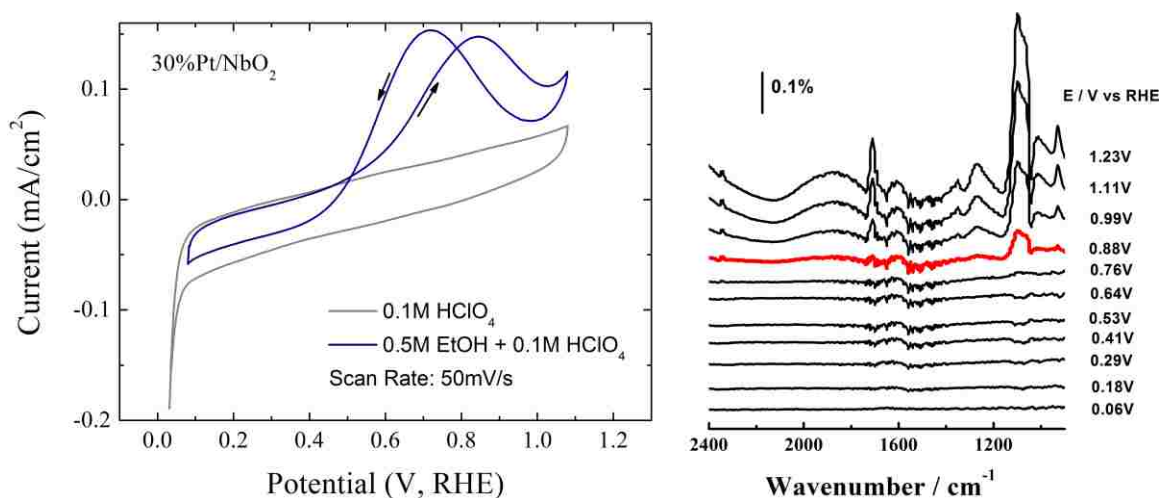


Figure 9.3: in situ IRRAS of 30%Pt/NbO₂: (Left) CVs taken at a rate of 10mV/s in 0.1M HClO₄. (Right) Corresponding FTIR time-resolved spectra (taken at 1mV/s). The red spectrum indicates the start of CO₂ evolution.

Though 30%Pt/NbO₂ (crystalline) was shown to offer the highest current density, the catalytic oxidation of ethanol is largely similar to Pt/C. The batch method of deposition of Pt is not optimal for this type of support. There are probably unsupported clusters of Pt due to the small size of NbO₂ nanoparticles which will be less effective for catalyst dispersion. The reduced form and crystalline stability of NbO₂ is also likely to result in less of a passive surface oxide film that would otherwise contribute to the formation of bi-functional Pt/NbO_x interfacial sites.

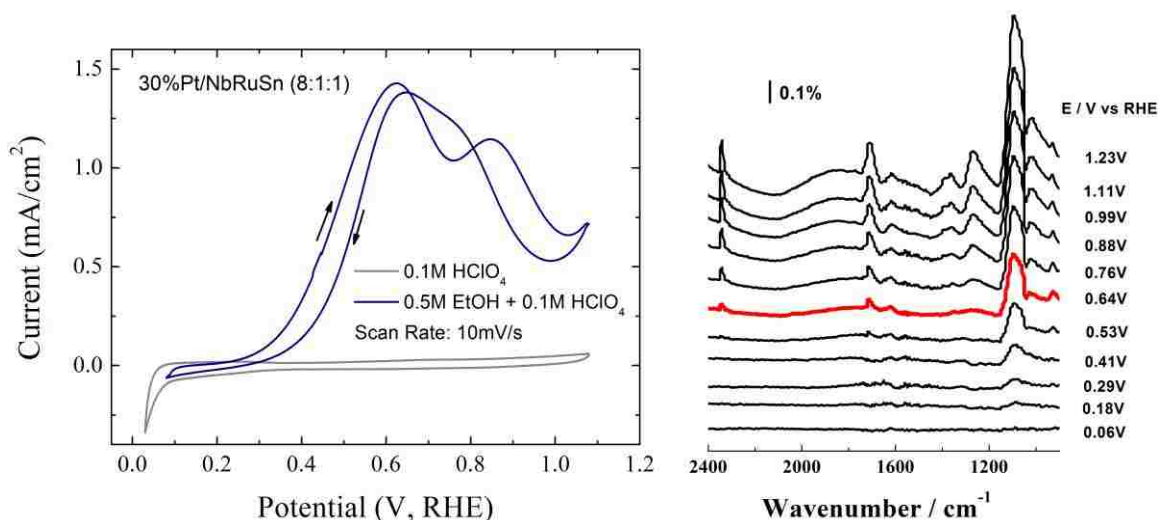


Figure 9.4: in situ IRRAS of 30%Pt/NbO₂: (Left) CVs taken at a rate of 10mV/s in 0.1M HClO₄. (Right) Corresponding FTIR time-resolved spectra (taken at 1mV/s). The red spectrum indicates the start of CO₂ evolution.

Despite the fact that batch deposition is clearly not the most effective means of forming catalyst/support interfacial sites, the addition of tin appears to enhance the total oxidation pathway of ethanol (Fig.9.4). The CO₂ asymmetric stretching peak ca. 2343cm⁻¹ appears at a slightly lower potential, while the CO linear adsorption peak normally at 2030cm⁻¹ is entirely absent. As before, this could indicate the rapid oxidation of CO to CO₂, though

in low overall yield. The presence of tin also lowers the potential at which the evolution of acetic acid and/or acetaldehyde begins by about 200mV, indicated by the peak at 1705cm^{-1} (C=O bond stretching). This behavior is typical of Pt-Sn, which is known to enhance the kinetics of EOR through a partial oxidation pathway that does not break the C—C bond.

The use of tin in these systems clearly has merit for enhancing EOR activity via multiple reaction pathways. Spray pyrolysis was used to reproduce 30%Pt/NbRuSnO_x with better Pt nanoparticles dispersion seen in Pt-SP of Ch.7. Carbon in the form of sucrose was added to enhance the electric conductivity of the final powder. Surfactant was not used in order to avoid the issues of component separation of tin seen in Ch.5 when sucrose was included. Additionally, the corrosion behavior described in Ch.8 suggests that mesopores are sufficiently small as to be blocked by the formation of a passive oxide layer from niobia. Two subsets of 30%Pt/NbRuSnO_x by spray pyrolysis were explored: one which was thermally reduced in 10% H₂/N₂ for three hours at 300°C and another at 650°C. These two temperatures were chosen due to the improvement in catalytic activity observed for 60%Pt/Nb_xRu_yO_x (1:1:2) (referred to as Pt-300 and Pt-650 in Ch.7) after crystallization of niobia.

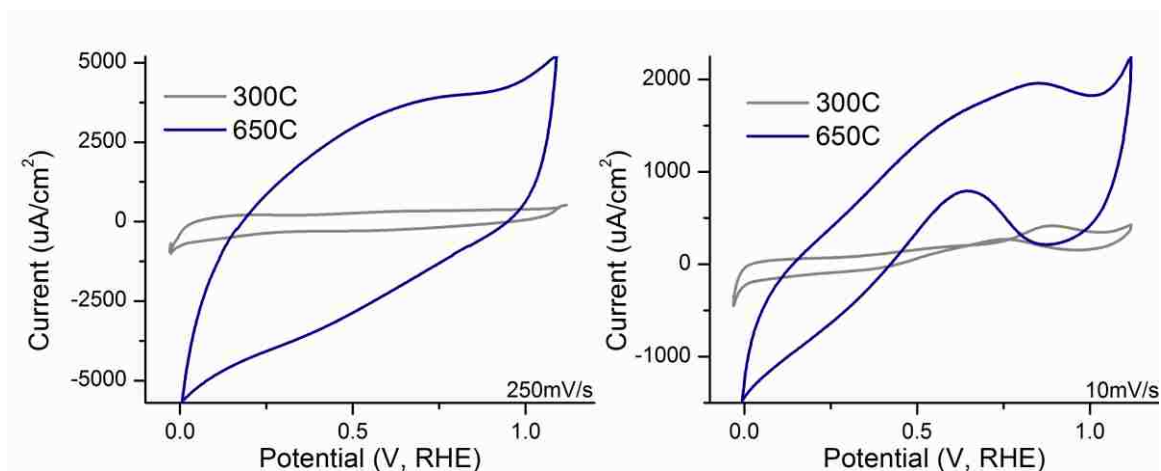


Figure 9.5: Cyclic voltammograms for 60%Pt/Nb_xRu_yO_x (1:1:2) after thermal reduction at 300°C and 650°C. (Left) 0.1M HClO₄ and (right) 0.1M HClO₄ + 0.5M EtOH.

The results are difficult to discern because of a dramatic increase in the charging current and resistivity of the system after heating to higher temperatures. Pulse voltammetry could normally be used to elucidate the faradaic current from the charging current. However, it appears from TEM analysis that the cause is probably due to component separation of Sn/SnO_x from the bulk oxide material.

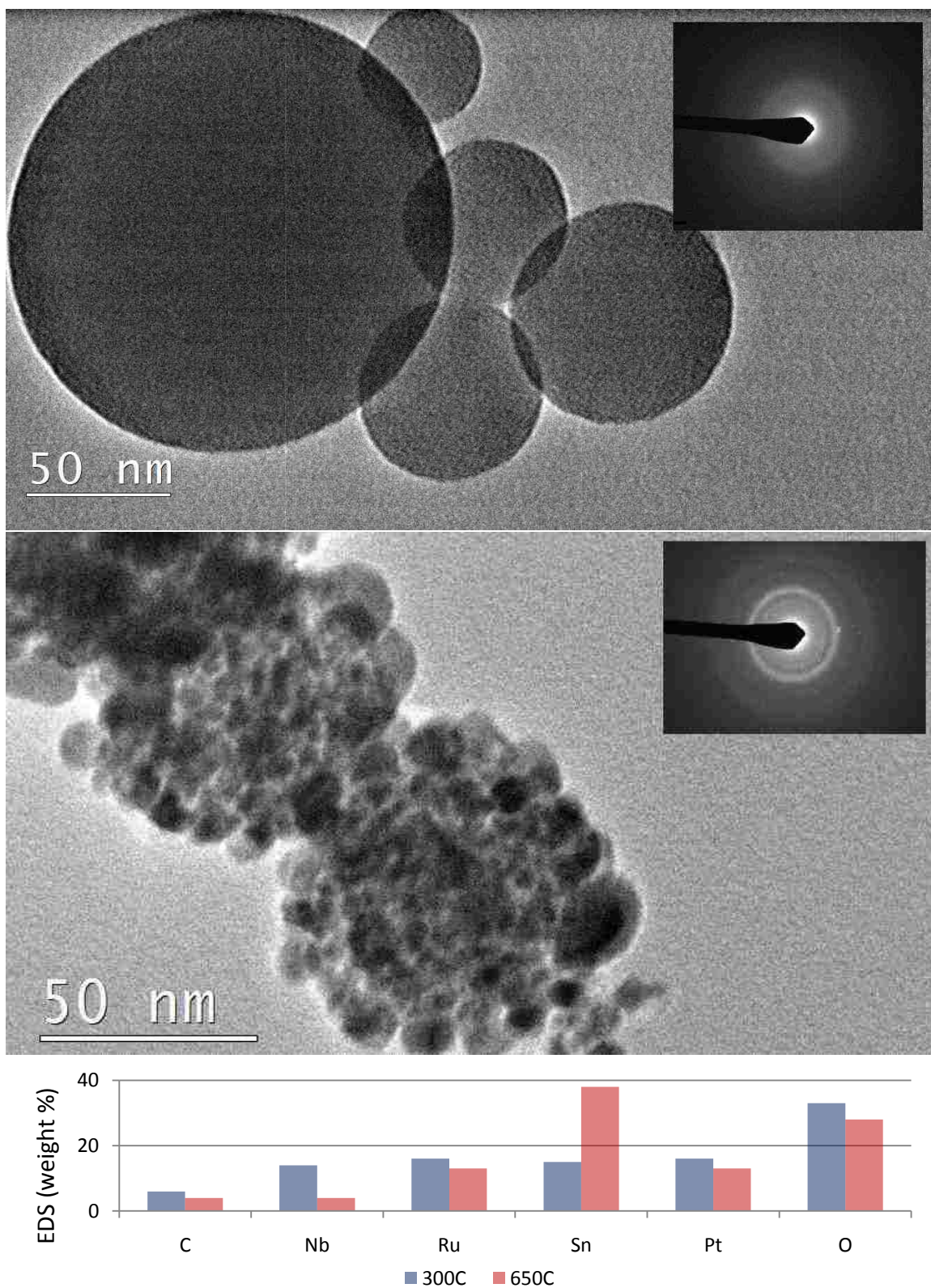


Figure 9.6: TEM analysis of 60%Pt/Nb_xRu_yO_x (1:1:2) after thermal reduction at 300°C (top) and 650°C (middle). Insets are selected area diffraction patterns which reveal the crystalline nature of the latter. Comparative EDS analysis from both samples is also shown (bottom).

This behavior was also observed for Nb-Sn in Ch.5. Even from an initially mixed state, the volatility of tin becomes too great as the metal oxide restructures from an amorphous into a crystalline form. EDS of both samples during TEM analysis reveals similar stoichiometry of all components, while the sample treated at 650°C has a dramatic increase in the counts detected from tin. The ratio of Nb to Ru, the latter being quite volatile, also appears to decrease at higher temperatures. This indicates that some Ru has migrated to the particle surface. It is reasonable to conclude that the tin shells which are shown to form at 650°C block a great deal of catalyst surface area, causing the sharp increase in charging behavior seen in Fig.9.5. The use of this material set appears to require a fixed template structure that is removed after thermal treatment in order to maintain each element homogeneously in the material. Because few surfactants remain stable above 500°C, other alternatives with preformed structures are considered.

9.2 Micro-Emulsion Silica Template

A porous silica template with desirable properties for the materials and design objectives pursued in this study was previously developed at UNM by coworkers and detailed in the literature¹⁸². An optimized synthesis process was developed using cetyltrimethylammonium bromide (CTAB), a polyether-polysiloxane/dimethicone copolyol surfactant known as ABIL EM 90 (from Degussa), tetraethylorthosilicate (TEOS), hydrochloric acid, and hexadecane. Careful mixing of the precursors results in emulsion droplets of aqueous silica precursor suspended in hexadecane. Within these droplets are smaller micro-emulsion droplets as well as micelles, both formed by CTAB. The system is essentially an oil within water within oil emulsion which, when

decomposed, yields a silica structure with a bimodal porosity. Larger pores on the order of 10-30nm are template by emulsions droplets, while smaller pores ~5nm are template by CTAB micelles. This template can be impregnated with metal precursors in the manner shown in the schematic below:

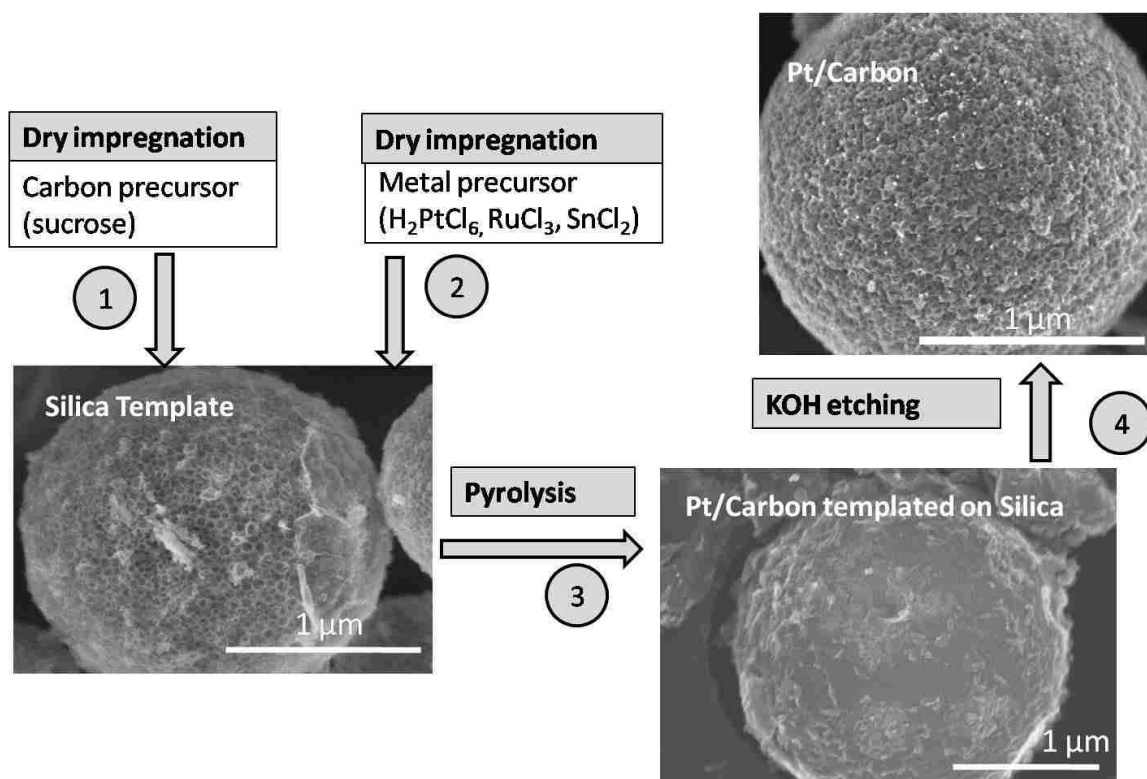


Figure 9.7: Flowchart of the impregnation process of metal precursors into the micro-emulsion silica template.

The silica template is impregnated with a solution of sucrose and metal chloride salts. The solution can be aqueous or alcoholic acetone mixture for enhanced wettability of the silica surface leading to thorough penetration of precursors into the porous structure. Once most of the volume of the template has been filled, the material is thermally decomposed under reducing conditions to breakdown the precursors. This is when mixed metal and metal-oxide materials form amidst carbonaceous scaffolding. The silica can

then be chemically removed by etching in 4-6M KOH solution for several days. This leaves a carbon metal-oxide composite with the reverse structure of the original silica template. In this way, intermetallic compounds can be formed and maintained at temperatures of 900°C or more without destruction of the pores.

9.3 Silica-Templated Pt/NbSn_xRu_yO_z

The micro-emulsion silica template is especially well suited for porous niobia-based materials. The larger pores ca. 20nm could better maintain an open porosity during the formation of a passive oxide film. Additionally, the inclusion of tin may minimize this effect so long as the tin can be stabilized with niobia and the ruthenium oxide as a mixed metal oxide.

The steps described in the previous section were followed to synthesize Pt₄Nb₁Ru₁Sn_{1.3}O₂C₂₄ (54wt% Pt, 20wt% C). The relative proportion of Sn to Nb was increased in order to match the stoichiometry of Pt₃Sn. This alloy was previously found to be the most catalytically active for EOR⁹⁸. The larger quantity of carbon was used to ensure an electrically conductive structure as well as complete filling of the silica template. A dry impregnation approach was used to add the precursors to the template. Once complete, the material was heated to 900°C for 4hrs in an atmosphere of 10% H₂/N₂ to induce crystallization and reduction of oxides. The higher temperature was necessary for the formation of Pt-Sn alloy. The resulting material is shown in the images of Fig.9.8.

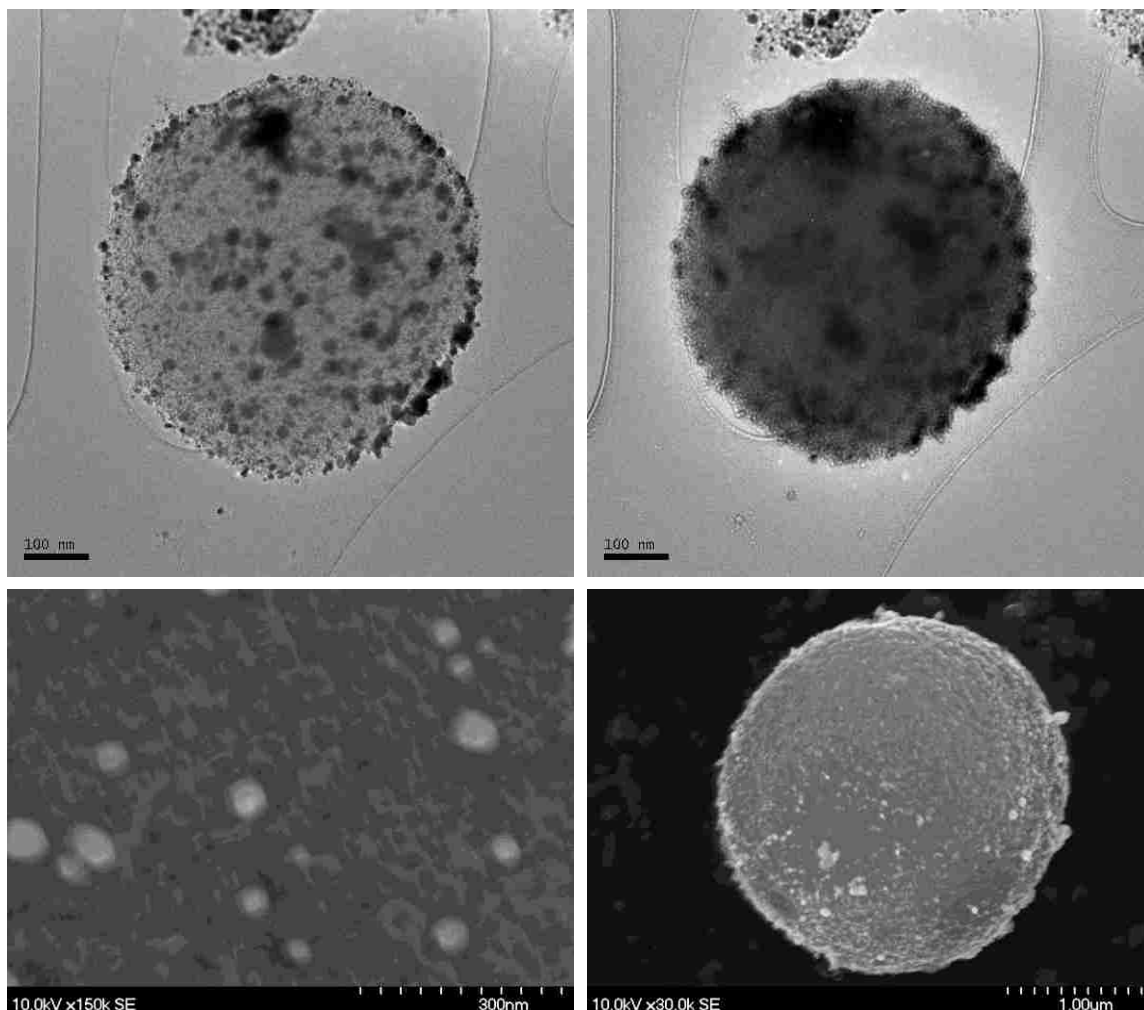


Figure 9.8: (Top) TEM bright-field (left) and dark-field (right) images of a $\text{Pt}_4\text{Nb}_1\text{Ru}_1\text{Sn}_{1.3}\text{O}_2\text{C}_{24}$ particle after thermal decomposition with the silica template still present. (Bottom) SEM images of the same material after the silica template has been etched away.

There appears to be excellent dispersion of metals before and after the removal of the silica template. It can be assumed that the majority of the porous structure is carbon based. There are a variety of particle sizes and the porosity is visible at the surface, shown in Fig.9.8 (bottom-left). These qualities are apparent in the cyclic voltammogram of ethanol oxidation.

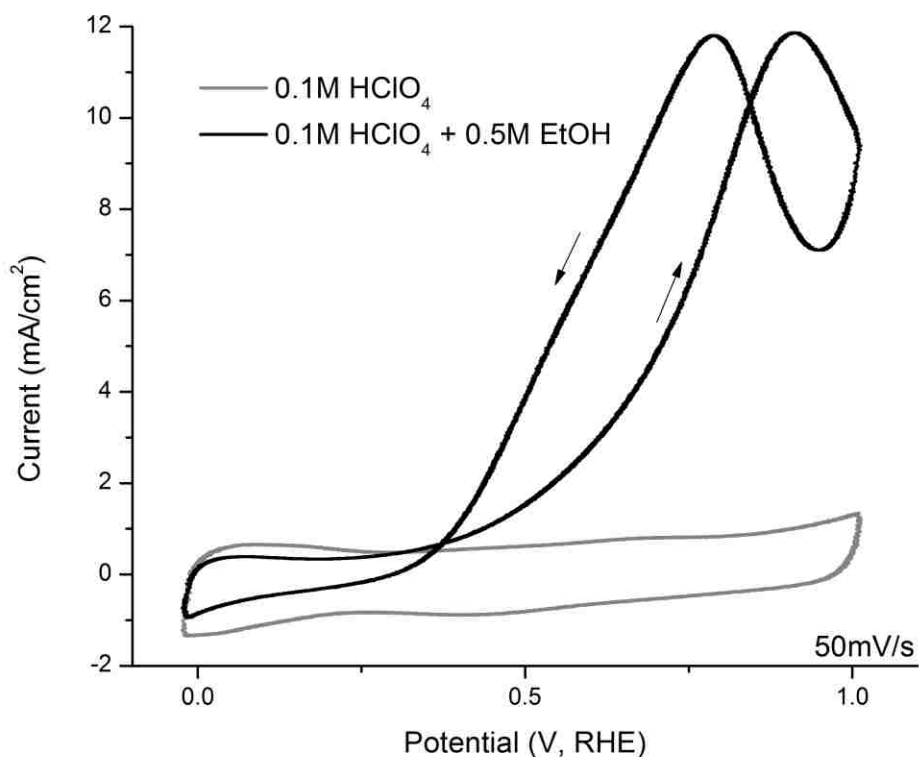


Figure 9.9: Cyclic voltammograms of Pt₄Nb₁Ru₁Sn_{1.3}O₂C₂₄ taken in 0.1M HClO₄.

Of the total metal loading, platinum accounts for 70wt%, while niobium is only 8wt%. This is relatively low compared to previous samples. However, because the metals in this sample are entirely crystalline, the affect of this loading may not be directly correlated to the electrochemical behavior of previous versions. We showed evidence that crystalline niobia may be better suited towards higher kinetics of EOR in Fig.9.1. The presence of tin has also been reported and shown here to affect EOR similarly. The discussion of Ch.2 pointed out that different forms and compositions of niobia are likely to benefit oxidation and oxygen reduction reactions to varying degrees. For example, the presence of OH species at the niobia surface might have a repulsive effect for OH forming on Pt,

which would instead allow O₂ dissociative adsorption onto platinum. Alternatively, the crystalline form of Nb(IV) or Nb(V) may be better suited for facilitating oxidation.

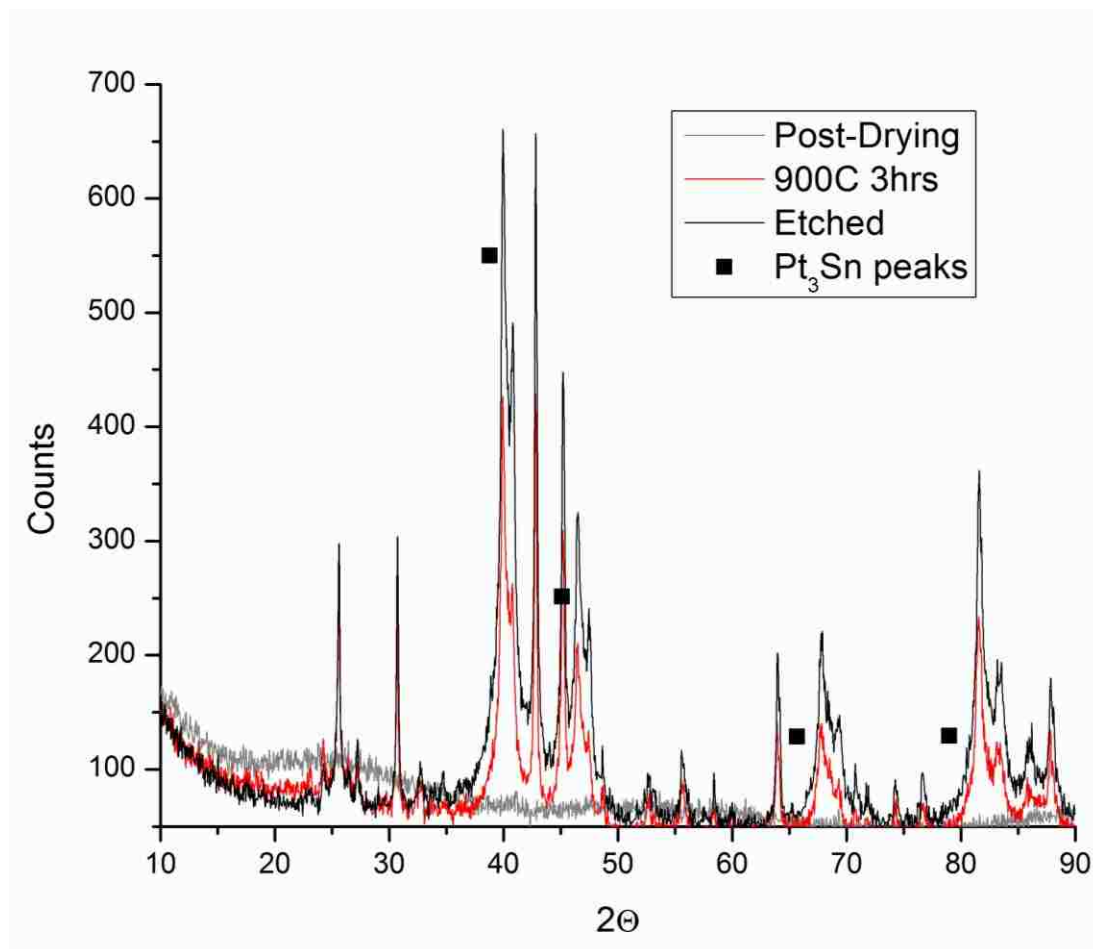


Figure 9.10: (Top) X-ray diffraction spectra of Pt₄Nb₁Ru₁Sn_{1.3}O₂C₂₄ taken after dry impregnation of sucrose and metal salts into the silica template, after heating to 900 °C for 4hrs, and after chemical removal of the silica template.

As expected, XRD spectra indicate that the crystalline structure does not change after removal of the silica template. Instead the signal from the remaining metals and metal-oxides becomes more coherent. While the spectrum is complicated, Pt₃Sn does not appear to be present in significant quantity. The addition of Sn into the Pt lattice increases the cubic unit cell from (3.93Å)³ to (4.02Å)³. This causes small decreases of 1-

2° 2 θ of the (111) and (100) faces, whereas the strong (110) and (311) peaks decrease by 3-4°. The latter two peaks are entirely absent from the sample spectra. There are indications of other Pt_xSn_y stoichiometries including Pt₃Sn₂, and PtSn. Some relevant compounds with matching peaks are identified below:

- **Pt**: 40(111), 46(100), 68(110), 82(311), 86(222) [PDF#03-065-2868(RDB)]
- **Pt_{0.996}Sn_{1.004}**: 26(100), 31(101), 34(002), 43(102), 45(110), 52(200), 56(201), 57(112), 58(103), 64(202), 71(004), 74(211), 77(104), 82(212), 84(300), 88(114) [PDF#03-065-8077(RDB)]
- **PtSn**: 25(100), 31(101), 33(002), 43(102), 45(110), 53(200), 56(201), 58(112), 59(103), 64(202), 71(202), 74(211), 76(104), 82(212) [PDF#97-004-2593(RDB)]
- **PtSn₂**: 24(111), 29(200), 40(110), 48(311), 59(400), 65(331), 72(422), 77(511) [PDF#97-06409679]
- **Pt₉Sn**: 40(111), 47(100), 68(110), 82(311), 86(222) [PDF#03-065-9538(RDB)]
- **Nb₃Pt**: 24(110), 35(100), 39(210), 43(211), 68(321) not all accounted for [PDF#97-064-5227(RDB)]
- **NbO₂**: 25(110), 34(101), 36(100), 53(211), 60(310) [PDF#97-007-5198(RDB)]
- **NbPt₃**: 25(610), 40(12,0,0), 41(502), 45(721), 53(-11,2,1) [PDF#97-010-5201]

Chrono-potentiostatic measurements in Figure 9.11 reveal interesting deviations in behavior compared to Pt/C and Pt/NbRuYz seen in Figure 8.10. After holding for 20 minutes at 0.0V, the material exhibits a large charge density at 1.2V (Fig.9.11 A2). And unlike the previous two samples, the relative behavior of each of the three holding periods in acid mirrors those of base. Sequential oxidation cyclic voltammograms (Figure 9.12) indicate that the material adsorbs more oxygen in acid media at 1.2V, and that reduction of oxidized species (Pt-O or NbO_x) occurs at lower potentials compared to basic media. The catalyst also develops a sharp hydrogen desorption peak in base after polarization to high potentials. The shape of the oxidation features in 1M KOH from 0 to 0.4V is more suggestive of the platinum surface. In addition, the current density during

cathodic sweeps before and after exposure to 1.6V appear similar, suggesting greater stability of surface reactions involving oxygen exchange. In acid media, there is a significant drop in the oxygen adsorption at 1.2V after scanning to 1.6V. This may suggest the stronger formation of a passivating niobium oxide layer in acid media which is reduced during the second holding period (third overall) at 0.0V, accounting for the difference in current density between A1 and A3 of Fig.9.11. It should be mentioned that the mass-normalized charge density at 1200s in acid is very close to that of 30%Pt/C in Fig.8.10A. Therefore, considering the high activity for ethanol oxidation in Figure 9.9, it seems reasonable to conclude that a great deal of the charge density is the result of active Pt.

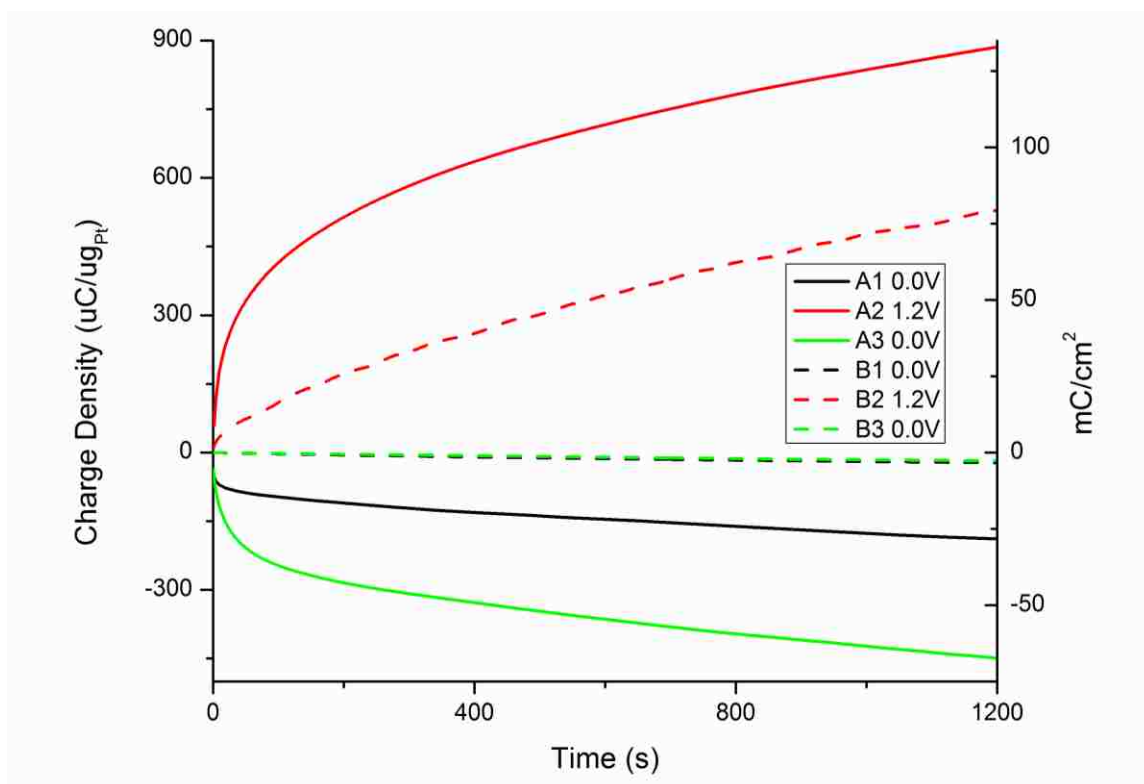


Figure 9.11: Chrono-potentiostatic coulometry measurements of Pt₄Nb₁Ru₁Sn_{1.3}O₂C₂₄. Electrodes were held at 0.0V, 1.2V, and 0.0V for 20 min periods in 0.1M HClO₄ (A1-A3) and 1M KOH (B1-B3).

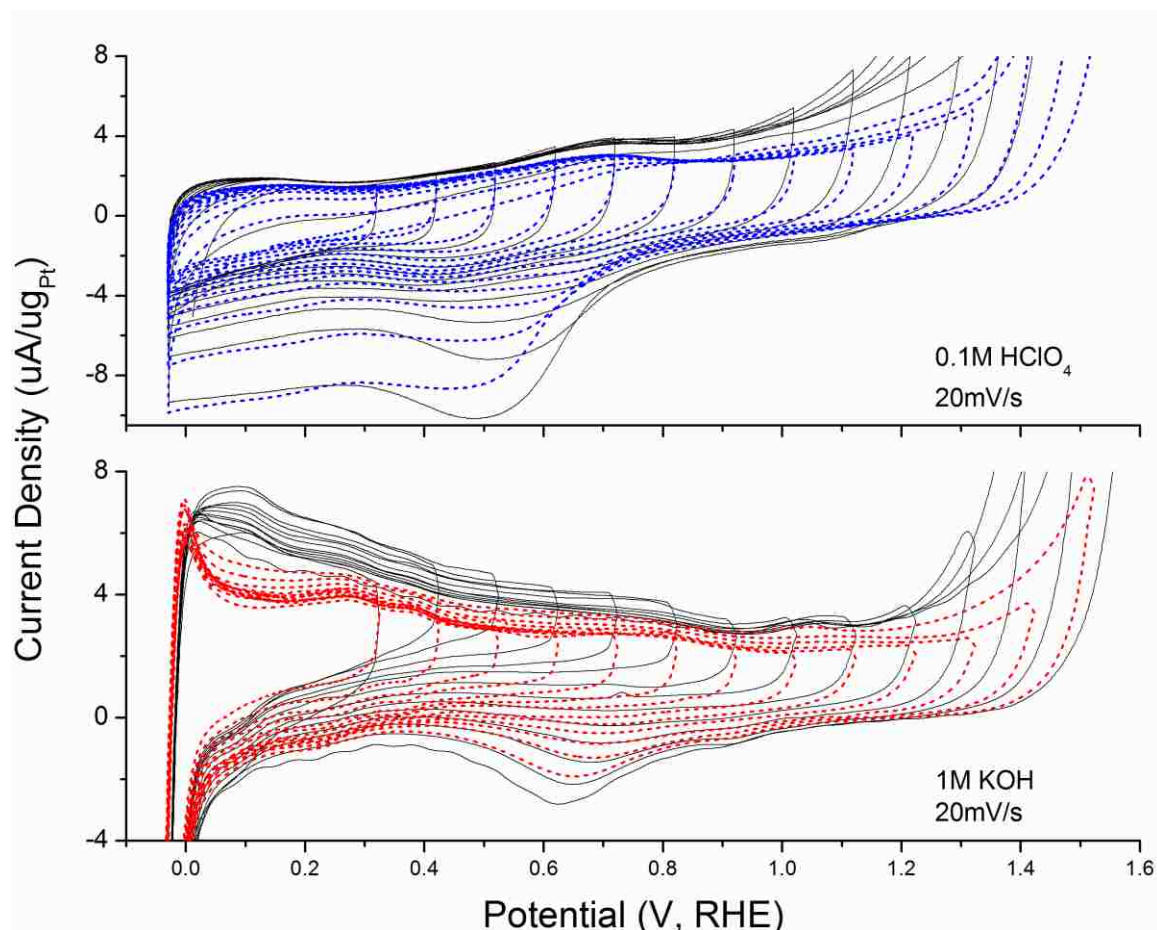


Figure 9.12: Cyclic voltammograms of Pt₄Nb₁Ru₁Sn_{1.3}O₂C₂₄ in 0.1M HClO₄ (top) and 1M KOH (bottom) at a scan rate of 20mV/s with step-increases of 0.1V/cycle from 0.3V to 1.6V (solid), then back to 0.3V (dashed).

CO stripping studies performed in 0.1M HClO₄ reveal a fairly pronounced CO_{des} peak ca. 0.7V, while simultaneously there is a great deal of charging activity from the niobia, and possibly other metals. The O_{des} peak during the cathodic scan is ca. 0.45V. The same peak in Fig.9.12 (acid) is centered just above 0.6V. Polarization studies discussed in Appendix C show that the position of the peak center is inversely proportional to the polarization rate, and so each of the aforementioned features occurs at the expected potential. The value of the current during CO adsorption at 0.32V in Fig.9.12 reveals the approximate position of the lower boundary of the electrochemical double layer.

Immediately upon commencement of cathodic scanning to lower potentials, there is a significant amount of hydrogen under-potential deposition that occurs in the form of hydrogen intercalation into the niobia. The catalyst's excellent kinetics during EOR indicate that the niobia appears to remain highly active without interfering with the platinum surface to the same degree as Pt supported on amorphous NbRu_yO_z .

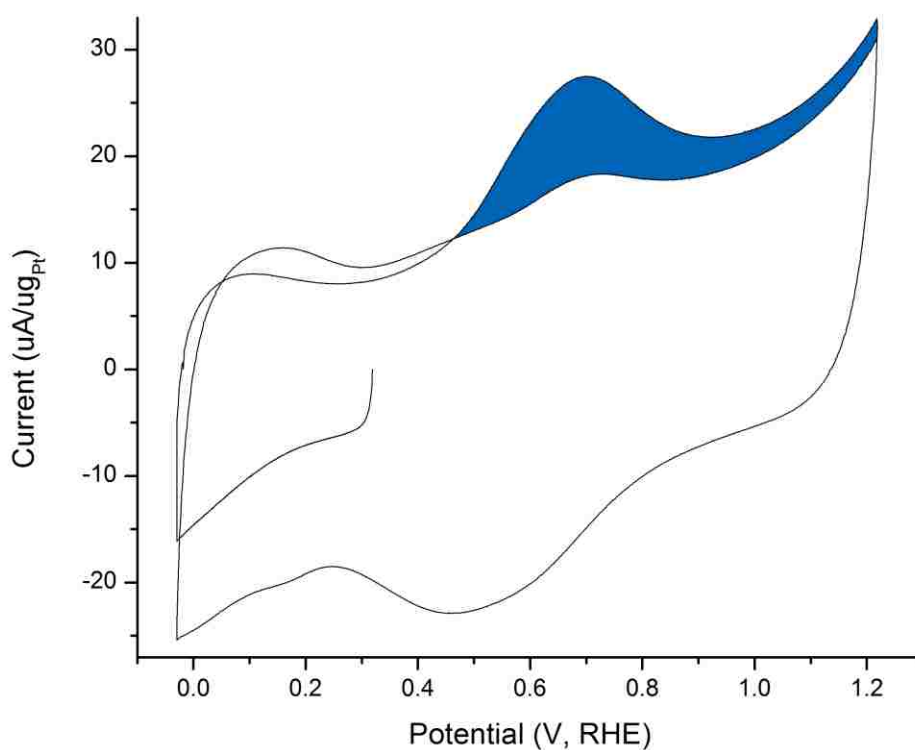


Figure 9.13: CO stripping cyclic voltammetry in 0.1M HClO_4 at 100mV/s on $\text{Pt}_4\text{Nb}_1\text{Ru}_1\text{Sn}_{1.3}\text{O}_{2.24}$. The CO desorption peak area is highlighted in blue.

Quantification of CO stripping results yield $Q_{\text{CO}} = 3.46 \text{ uC/ug}_{\text{Pt}}$ and $\text{ESA}_{\text{CO}} = 8.3 \text{ m}^2/\text{g}_{\text{Pt}}$.

As previously mentioned, the reliability of these numbers is difficult to ensure due to a variety of possible activity at the Pt- NbO_x interface. Despite the excellent EOR

performance in Figure 9.9, ESA for this sample is ten-fold lower than that calculated for 30% Pt/C, three-fold lower than that for 60%Pt/NbRu_yO_z (amorphous) in Ch.8. It is fairly clear that these results do not easily correlate to the actual EOR activity of each catalyst. This is probably because of a competition among O_x, H_x and CO_x and other ethanol subspecies for occupying Pt surface sites.

9.4 Niobium-Ruthenium-Carbide as a Support

It is clear that niobium, ruthenium, and tin oxides all have unique electrocatalytic contributions to the ethanol oxidation reaction that can be selective for partial or total oxidation pathways. While tin-modified platinum offers enhanced EOR kinetics by bringing Sn-OH species in proximity to adsorbed surface species on Pt, the resulting byproduct still contains a C—C bond and does not remain bound to the Pt surface, i.e. there is no favorable electronic modification of Pt by Sn. Alternatively, niobia has been shown here to increase the bond strength between Pt and adsorbed carbon species while simultaneously providing an oxygen source near Pt surface sites. The result is that bound ethanol subspecies follow the total oxidation pathway to CO₂ beginning at low cell potentials. However, the formation of Pt-NbO_x interfacial sites in which reduced niobia migrates on top of the Pt surface means that much of the catalyst surface area is not open to adsorbates. The bi-functional effect of ruthenium towards platinum is weaker in both functions. The deficiencies of these oxides may be minimized by creating a mixed-metal in which the concentration of niobium is reduced and simultaneously locked into a crystalline, metallic phase. This would minimize the oxide passivation layer that has been shown to evolve on all forms of niobia. Ruthenium could also dampen the strong SMSI effect between niobia and platinum. Ru also has proven solubility with Pt which eases the formation of mixed metals. Therefore, if a reduced niobia-ruthenium substrate could be produced, it might make the ideal catalyst/co-catalyst combination for the oxidation of alcohols. Furthermore, the deposition of extremely small amounts of Pt on the scale of several monolayers or less would be better achieved if the crystal structure of this niobium-ruthenium support were similar to that of platinum. The nobility of

platinum causes it to primarily form nanoparticles instead of wetting a substrate surface as a thin layer. If this behavior could be avoided, then it would open the door towards truly small amounts of supported platinum with extremely high dispersion.

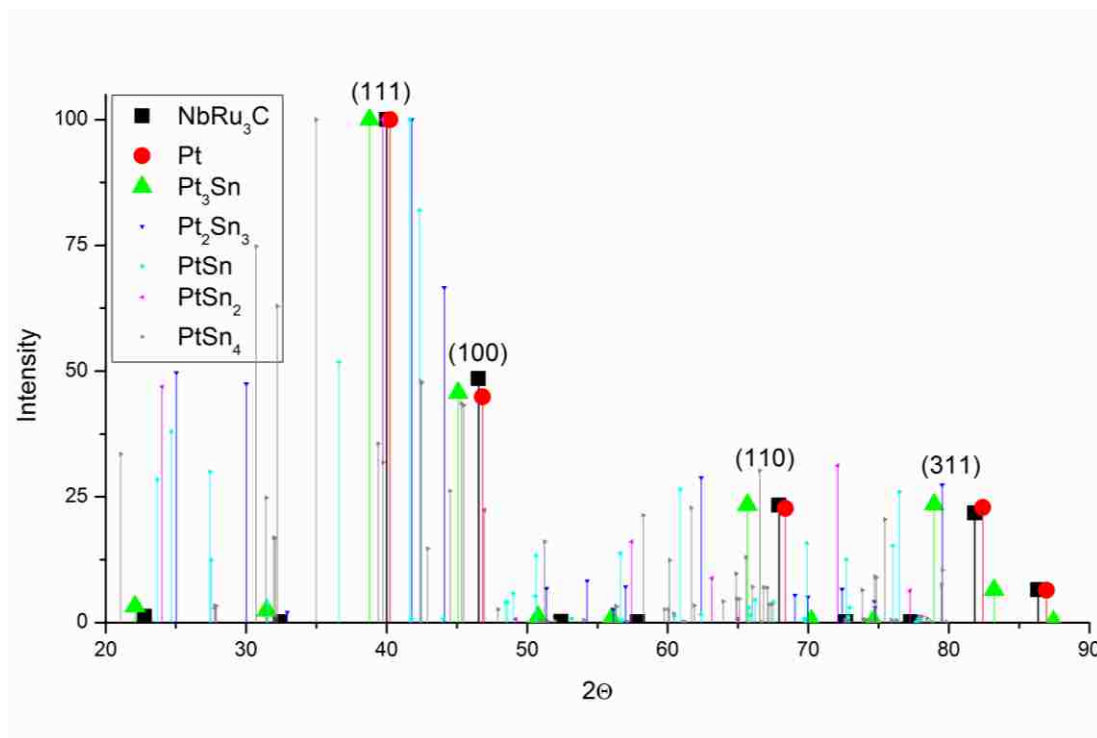


Figure 9.14: JCPDS Patterns Comparing the crystalline structure of NbRu₃C to various Pt_xSn_y species.

Table 9.1: Comparative JCPDS Structure Data of Active EOR catalysts.

Formula	Density				Structure	Cell (Å)	(deg)	%Δ Cell
	Pt:Sn	©	Mwt	Vol				
NbRu ₃ C	--	11.425	408.13	59.32	Cubic	3.9x3.9x3.9	90x90x90	0.0%
Pt	--	22.219	195.08	58.32	Cubic	3.878x3.878x3.878	90x90x90	-0.6%
Pt ₃ Sn	3.00	18.020	703.96	64.87	Cubic	4.018x4.018x4.018	90x90x90	3.0%
PtSn	1.00	13.142	313.79	79.30	Hexagonal	4.104x4.104x5.436	90x90x120	16.6%
Pt ₂ Sn ₃	0.67	11.775	746.29	210.80	Hexagonal	4.334x4.334x12.96	90x90x120	84.9%
PtSn ₂	0.50	10.891	432.50	263.70	Cubic	6.413x6.413x6.413	90x90x90	64.4%
PtSn ₄	0.25	9.510	669.92	467.80	Orthorhombic	6.397x6.397x6.397	90x90x90	64.0%

A promising material which may meet all of these criteria is NbRu_3C . As shown in Fig.9.14 and Table 9.1, XRD patterns reveal that the dominant crystal surfaces result in lattice dimensions between those of metallic Pt and Pt_3Sn . The consequence may be that true monolayers of Pt could be deposited, and that such monolayers would experience a favorable degree of strain from the support that could enhance their activity towards EOR or another useful reaction process. It is perhaps fortuitous that NbRu_3C can adapt a cubic structure when normally both niobia and ruthenium would be hexagonal, orthorhombic or similarly different from the FCC structure of Pt.

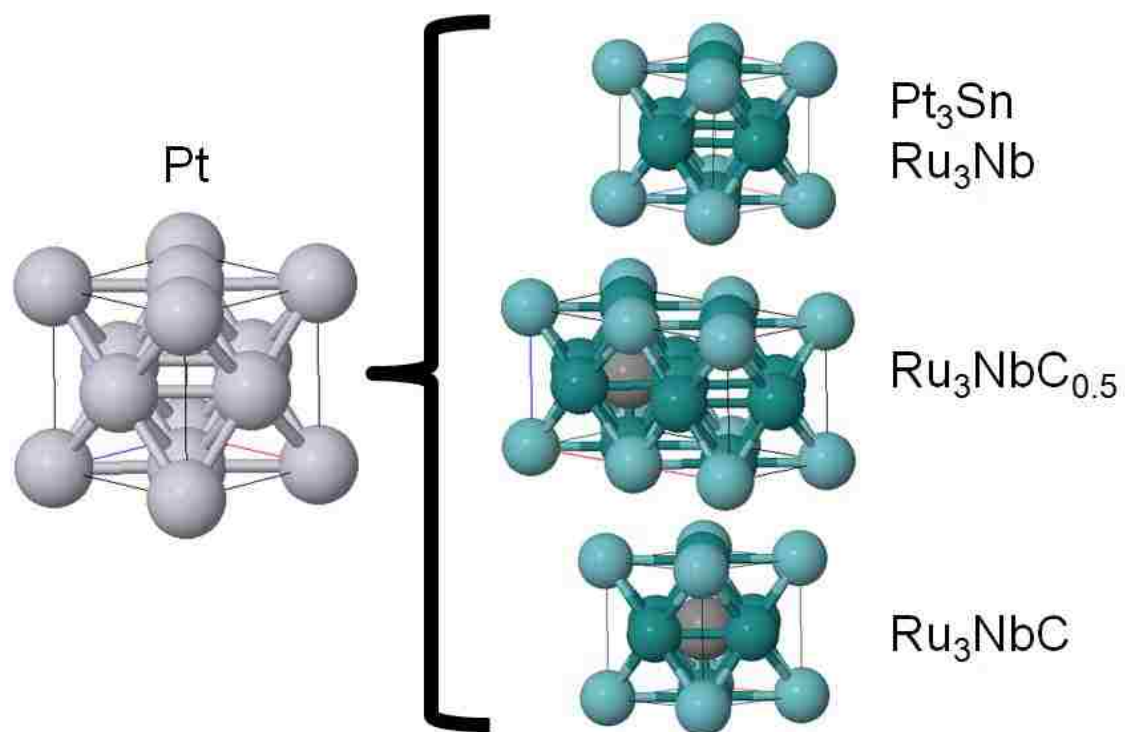


Figure 9.15: DFT calculations of relaxed structures of cubic Nb-Ru with increasing fractions of C occupying the center of the unit cell.

This material has received little attention in the literature, briefly investigated by NASA as a high-temperature tolerant metal-carbide for use as a heat shield material to protect

vehicles re-entering the earth's atmosphere. The presence of a single carbon atom per unit cell probably serves to stabilize the cubic structure of the material. If the metal-carbon compatibility is significant, it would also help anchor the material to the carbon surface of a template structure. DFT calculations were used to compare the density of electrons near the Fermi energy ($E_F=0$) of NbRu_3C_x to other catalytically active elements (Fig.9.16). The presence of electrons at or above E_F allows for electrical conductivity as well as the capacity to form bonds with adsorbed species.

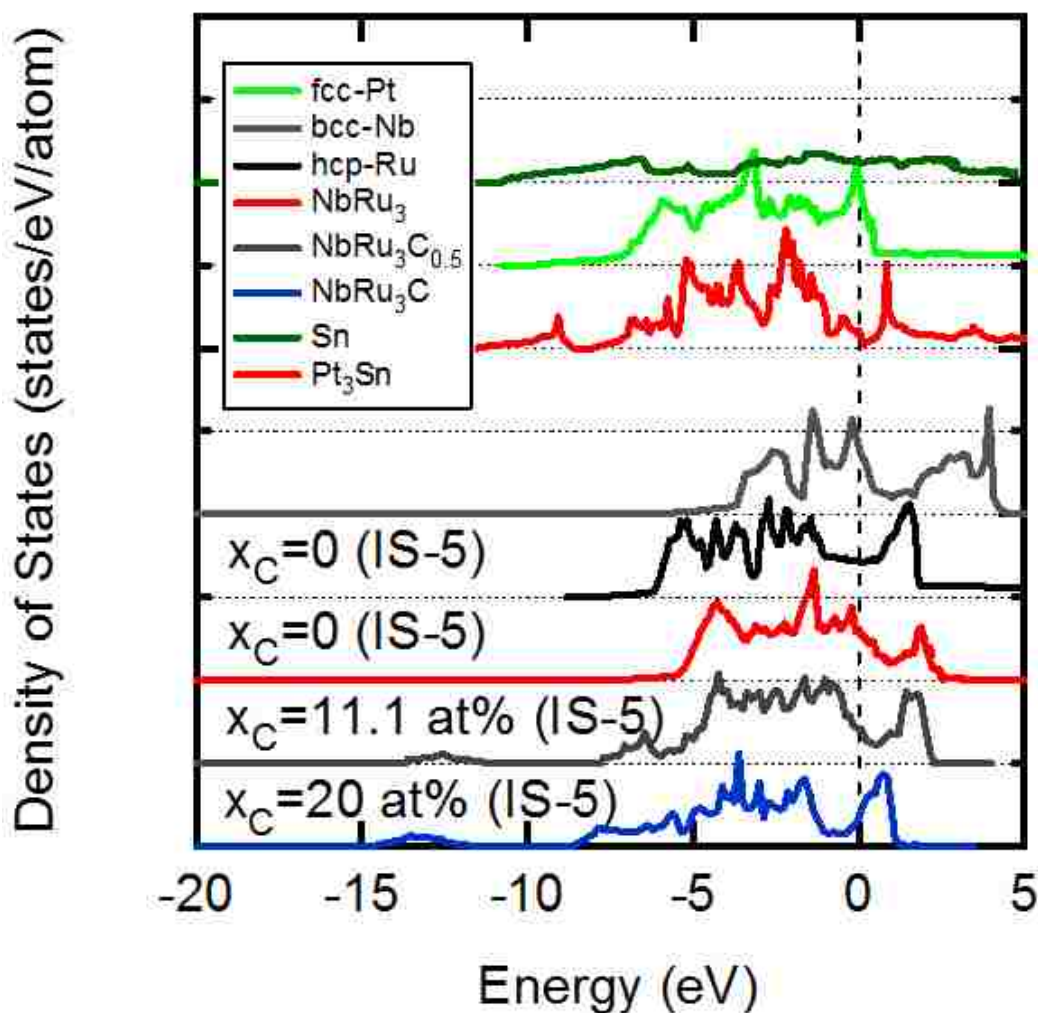


Figure 9.16: Electronic Density of States calculated for various catalyst structures using DFT.

Examining the spectra from top to bottom in Fig.9.16 reveals the nature of electronic activity in each of these metals and metal-carbides. The DOS of Sn is relatively broad above and below E_F . Alternatively, a sharp number of electrons are centered around E_F in Pt, which is expected from the noble nature of the metal. The addition of Sn into the Pt lattice to form Pt₃Sn increases the energy at which a very narrow range of valence electrons reside. This could be why acetic acid and acetaldehyde desorb quickly after formation. Niobium metal has a density of electrons around E_F similar to that of Pt, as well as a more broad range at higher energies. Availability of these higher energy electrons is responsible for the affinity of niobium to form oxygen bonds in open air or aqueous electrolyte. Below that, ruthenium has broad electron occupancy across E_F followed by a broad density at higher energies. The latter feature appears to arise from the orbital component which is dominant in subsequent NbRu₃C_x species. The difference in DOS between Nb and Ru is probably the reason why metallic phases of the latter are more stable in the presence of oxygen. As carbon is added to NbRu₃C_x, the electronic structure of ruthenium atoms appears to experience a shift in DOS towards E_F . This probably results in a more stable unit cell.

Chloride precursors of niobium and ruthenium as well as sucrose were used to impregnate the micro-emulsion silica template discussed earlier. Appropriate ratios of each precursor were used to approximate the stoichiometry of the desired material, NbRu₃C. After impregnation, the sample was slowly heated at 1°C/min to increasingly high temperatures to monitor the progression of crystalline structure formation.

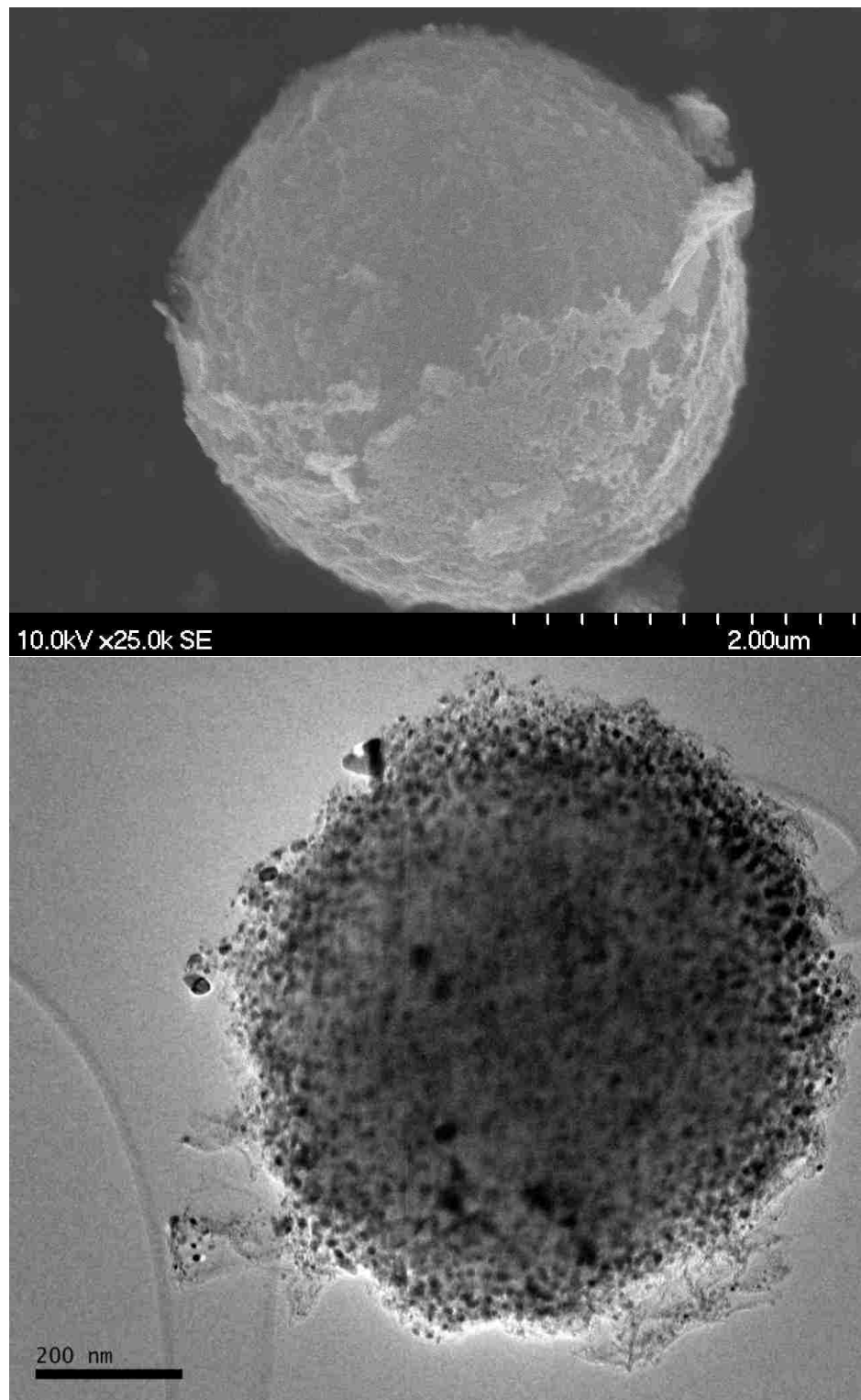


Figure 9.17: SEM and TEM of NbRu₃C after heating in 10% H₂/N₂ for 3 hrs at 600°C (top) and 800°C (bottom).

The sample appears to be stable after heating at high as 800°C despite the volatility of ruthenium. There appears to be excellent impregnation into the silica template with no significant evidence of agglomeration at the template particle surface. The films seen at the surface of particles in Fig.9.17 are also apparent in images of the template before impregnation, and so are believed to be inconsequential to the final product after all silica is chemically removed.

XRD measurements were taken after each 100°C increment in the heating process in order to determine the crystallization order of the precursor elements. While little information is available on NbRu₃C, specifically, it was previously suggested by Holleck et al.¹⁸³ that the mixed carbide does not form until temperatures between 1100-1700°C. The range is somewhat ambiguous because of the nature of the formation, which is believed to occur via a peritectic reaction⁸⁶ as $\text{Liquid}_{\text{MIXED}} + \alpha\text{-Solid}_{\text{MIXED}} \rightarrow \beta\text{-Solid}_{\text{MIXED}}$. This requires that a melting threshold temperature be crossed, sustained for a reasonable period of time, and eventually followed by a very gradual cooling rate. These temperatures are more easily achieved through the use of various arc-melting techniques, though they can result in large, heterogeneous grain structures. The small scale of the materials in this study may allow the melting to be achieved at the lower end of the mentioned range, 1100-1200°C.

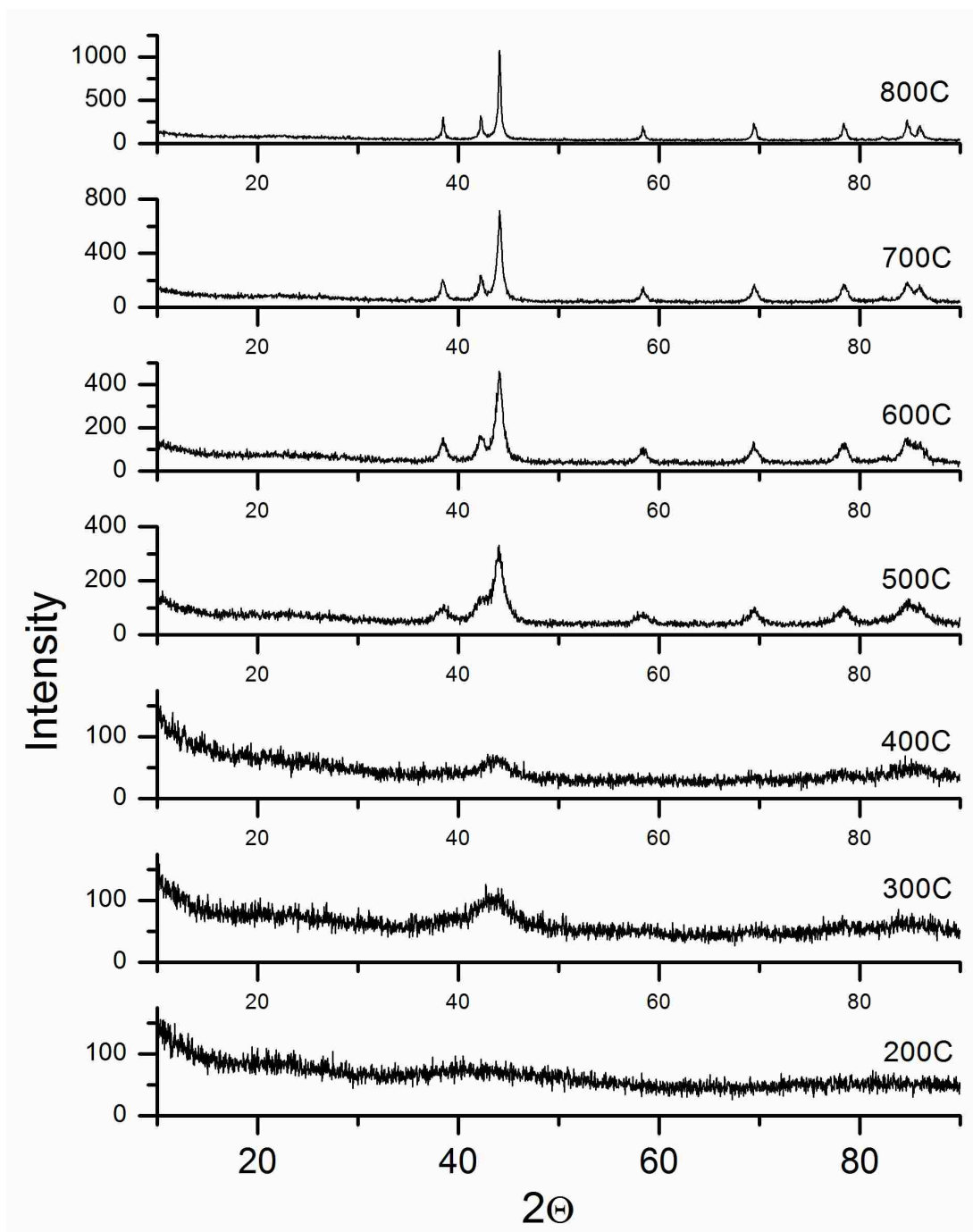


Figure 9.18: X-ray diffraction (XRD) studies of NbRu₃C crystallization after heating from 200-800°C at ramp rates of 1°C/min in 10% H₂/N₂.

XRD results show the gradual formation of hexagonal, metallic ruthenium as the dominant crystalline component at temperatures up to 800°C. The absence of any peaks

based upon niobium species is notable, but not surprising because we previously showed in Ch.6 that niobia in well-mixed Nb-Ru is stable as an amorphous material to higher temperatures than pure niobia. EDS taken from SEM analysis of NbRu₃C after 800°C verifies retention of the original stoichiometry of the sample.

These results are consistent with those of Holleck et al. that higher temperatures are needed to induce the peritectic phase transformation to the cubic metal-carbide. The volatility and toxicity of ruthenium at high temperatures, even under a reducing atmosphere, requires that a well sealed reactor system capable of ~1400°C or less be setup before the study is continued. At such temperatures, the stability of the silica template must be considered. But ideally, the cubic structure could form at temperatures at or below 1200°C. Once attained and the template removed, a variety of techniques could be pursued to deposit ultra-low amounts of Pt catalyst. A promising method for this task would be galvanic ion deposition of Pb/Pt explored in Ch.7. Such a could fully utilize Pt towards theoretical limits while taking advantage of a mixed-metal support tailored for the ethanol oxidation reaction or other equally important half-reactions for fuel cells.

CHAPTER 10 - Conclusions

Synthesis of Mixed Metal Oxides

Computational multi-physics simulations of the conditions for an aerosol during thermal decomposition inside a tube furnace revealed significant variation of velocity and heat flux proportional to tube volume. A droplet with solvated precursors will lose most of its liquid solution shortly before or after the furnace entrance regardless of tube dimensions. But the stream velocity and heat flux are much more important for the thermal decomposition process, especially when volatile precursors are used. Larger tubes offer a more narrow velocity range and therefore a more uniform residence time, but with a much more broad temperature range. Both systems would benefit from increased mixing inside the tube.

Preliminary aerosol synthesis experiments show that mixed, multi-component materials with niobia are difficult to achieve when more than one volatile component is present. These include sucrose, P123 surfactant, and metals with significantly lower energies of vaporization such as Ru, Ti, Ni, and Sn. For Sn, in particular, lower reactor temperatures are not an effective means of avoiding component separation from niobia because the energy of thermal decomposition (halide) appears close to the volatilization energy.

Mesoporous Niobia Supports

Thermal aerosol synthesis (spray pyrolysis) was used to synthesize mesoporous niobium oxide, and ruthenium-modified niobium oxide. Evaporation-induced self-assembly of the pluronic surfactant P123 led to poorly ordered mesoporous particles with BET surface areas as high as $\sim 180 \text{ m}^2/\text{g}$, and pore diameters in the 3.5-4 nm range. An acid etching

treatment was needed to open up internal surface area, and several variations of post-processing involving acid washing and heating under different atmospheres have been explored.

The final morphological, compositional, and electrical properties of the end product have been reported relative to manipulation of these post-treatments. Most notably, acid wetting of powders produced from a Nb/12 wt % Ru precursor mixture, followed by reduction in N₂/10% H₂ at 400°C, resulted in a promising material that possessed 167 m²/g surface area and had low electrical resistance (2.3 Ω). This material, which apparently consists of Ru integrated into the niobium oxide matrix, was also tested for electrochemical behavior and found to have activity for the oxidation of methanol in the absence of platinum catalyst. The intrinsic properties of this NbRu_yO_z material suggest that it can be utilized in fuel cells as a reactive support for electrocatalyst.

Platinum Catalyst on NbRu_yO_z

NbRu_yO_z support synthesized by spray pyrolysis underwent different means of platinum deposition. *Pt-DI* supported 30%Pt deposited by dry impregnation, while the other, *Pt-SP*, supported 60%Pt by a complex nucleation-condensation process to form Pt nanoparticles during pyrolysis. XAS results indicate that the d-band of Pt-SP contains additional electrons, possibly strengthening its adsorption potential.

In situ IRRAS studies have shown that CO₂ evolution during EOR begins above an applied potential of 0.4V (RHE) on Pt/NbRu_yO_z, about 0.37V lower than Pt(111) alone. The smaller Pt nanoparticles of Pt-SP appear to make it a more effective electrocatalyst for C—C scission as well as CO oxidation. These results indicate that niobia is a

promising component of more efficient electrocatalysts for EOR. But even with twice the loading of Pt, these catalysts yielded about 60x smaller current exchange density during EOR than commercially available 30%Pt on carbon, indicating that the expected surface area of Pt supported on niobia is somehow inhibited.

Deposition of monolayer amounts of fresh Pt onto existing Pt surfaces in Pt-DI and EOR-CV studies showed that much of the original Pt can be recovered in the absence of atmospheric oxygen. But peak currents equivalent to Pt/C are not achieved.

Crystallization of the niobia support appears to decrease the overall charge density and improve the EOR performance significantly in both 0.1M HClO₄ and 1M KOH, suggesting that the niobia is somehow stabilized.

These studies appear to confirm the prevalence of Pt-NbO_x surface sites, in which ethanol and its subspecies are more strongly bound than on Pt(111). This improves instances of C—C scission before partially oxidized species desorb from the surface. The niobia also appears to act as an oxygen promoter, facilitating CO oxidation to CO₂. But the adsorption kinetics of H₂ and O₂ species from electrolyte and atmosphere appear to dominate available catalyst surface sites, blocking adsorption of double and single carbon species and hindering the overall EOR performance. Polarization of the electrode may induce the exchange of hydrogen and oxygen to Pt from niobia directly. In this case, the adsorption on Pt may partially proceed without the dissociation step. Such a process could explain limited kinetics of EOR.

***Electrochemical Studies and DFT Analysis of Suppressed Exchange Current
Density of Pt Supported on NbRu_yO_z***

The catalytic deactivation of platinum supported on niobia occurs progressively from the moment of synthesis to complete suppression within several weeks time in the open atmosphere. Aging studies in which Pt/NbRu_yO_z on a gold grid was rapidly cycled between anodic and cathodic potentials has shown the 3D growth of a thin film of niobia covering support and catalyst particles. It appears that this film may increasingly inhibit ion transport from the catalyst surface in 0.1M HClO₄ and 1M KOH with continued growth. EELS analysis shows that the film is more oxygen-rich than the bulk support particle. Density Functional Theory calculations for the surface diffusion of available atomic species, C, O, and Nb across the Pt(111) surface corroborate the experimental finding that the mechanism of deactivation is likely related to the local concentration of oxygen which reacts with niobia. Sources of oxygen include the open atmosphere, aqueous electrolyte, and possibly also the breakdown of Nb₂O₅ into more reduced forms of NbO_x.

Chrono-potentiostatic measurements of amorphous and crystalline NbRu_yO_z of various compositions reveal that thermal treatment can increase the stability of the support in acid and alkaline media at potentials near the hydrogen and oxygen evolution boundaries of water. More specifically, the stability is usually biased towards one potential range and electrolyte pH over the other, giving credence to the idea that the final properties of niobia based catalysts depend largely upon the methods of preparation. Niobia supports may indeed be tailored during synthesis processing so as to be co-catalytically active for the ethanol oxidation reaction or the oxygen reduction reaction.

Non-Aerosol Synthesis of Composite Crystalline Materials

The best activity for ethanol oxidation was shown to be catalyzed by a silica-templated sample that was thermally reduced at 900°C with the final atomic composition $\text{Pt}_4\text{Nb}_1\text{Ru}_1\text{Sn}_{1.3}\text{O}_2\text{C}_{24}$. Though it was not clear that the most active intermetallic for EOR (Pt_3Sn) was formed, it was evident that the composition and structure yielded an effective electrocatalyst with excellent exchange current density. Higher contents of ruthenium, tin and carbon may suppress substantial 3D growth (thick films) of the passivating niobium oxide layer while still allowing the formation of 2D Pt-NbO_x interfacial sites that facilitate the total oxidation pathway of ethanol at lower potentials.

It appears that tin with platinum co-catalyzes the partial oxidation pathway of ethanol at a high kinetic rate. Therefore, an alternative to the use of Sn may be found in the development of an alternative niobium-ruthenium-carbide, NbRu_3C . The crystalline and metallic nature of the support would limit the formation of a passivating niobium oxide layer. This material also exhibits a cubic lattice structure with atomic spacing between those of Pt and Pt_3Sn . Such structural similarity could make this metal-carbide an excellent substrate for the deposition of Pt catalyst on the order of several monolayers or less due to minimal lattice strain at the catalyst-support interface. This process should be pursued using a mesopore-templating material which is stable to temperatures ~1200°C so that the peritectic formation of the cubic structure could form without loss of the pore structure. Once achieved, the galvanic-ionic deposition method could be used to deposit minelayers of Pt throughout the structure. In this way, a tailored electrocatalyst for the total oxidation pathway of ethanol with well-dispersed, ultra-low loadings of Pt might be achieved.

Appendix A:

Paper Version Authors: *Pylypenko, S., Blizanac, B.B., Olson, T.S., Konopka, D., Atanassov, P.*

Corrosion Stability of Ruthenium Oxide Materials

The search for alternative energy is recognized as a very important part of the efforts toward sustainability. Fuel cells are currently explored for automotive, stationary, and portable applications. There has been a substantial acceleration of the research in fuel cell power systems to meet the established targets toward these applications.

Improvement of electrocatalytic materials for fuel cells is envisioned mainly through the improvement in their activity and durability and the reduction of catalyst costs. Carbon blacks are used as supports for the catalytically active phase in state-of-the-art, low-temperature polymer electrolyte membrane (PEM) and phosphoric acid fuel cell (PAFC) electrocatalysts. As such, they are an important component of electrocatalytic layers.

Corrosion of the carbon support on the cathode side of a fuel cell has been identified as one of the major detrimental factors in the durability of electrocatalysts and, subsequently, entire fuel cell-based power devices. The carbon corrosion process is facilitated by the highly corrosive environment of the fuel cells, and also by transient conditions during start-up and shutdown cycles, resulting in cathode voltage excursions to high anodic/oxidative overpotentials. Under such conditions, carbon corrosion is even more pronounced in the presence of a platinum phase, known to catalyze carbon oxidation¹⁸⁴. Earlier studies of carbon corrosion were centered around the PAFCs^{55, 185-188}. The stability of the carbon supports in PEM fuel cells is the focus of the latest work in this area^{184, 189-191}. Increased stability and durability of platinum electrocatalysts

supported on carbon is possible through enhancement of the platinum-carbon support interaction by using more corrosion-resistant carbon supports and/or by using platinum alloys¹⁸⁴. Another route to improving the durability of fuel cell systems is to use novel corrosion-resistant noncarbonaceous supports, such as metal oxides.

There are a number of requirements that the new materials have to meet to be considered as catalyst supports in proton-exchange fuel cells. They have to provide good electrical and structural properties at low cost. There have been several reports on the investigations of conductive metal oxides for application as supports^{18, 61, 63, 192-194}.

Sasaki et al. have shown the utilization of metal oxide supports for low-content platinum electrocatalysts^{18, 63}. They have demonstrated an improved performance of these materials toward oxygen reduction and methanol oxidation. Scheiba et al. have reported the results of their study of hydrous ruthenium oxide as a support for electrocatalysts in DMFCs that showed an increased proton conductivity and catalyst utilization in monoethanolamine (MEA) testing along with limited promotion of carbon monoxide and methanol oxidation¹⁹³. The previous investigations of the corrosion stability of hydrous and anhydrous ruthenium oxides were done in the context of their application for the electrolytic evolution of chlorine and oxygen from aqueous solutions¹⁹⁵⁻¹⁹⁷. The anodic corrosion of these materials was linked to the hydrous component, and it was reported that mild heat treatment of the oxide improves the stability and electrocatalytic activity of these materials^{195, 197}. The majority of the literature reporting the physical characterization of ruthenium oxide materials was done in the context of their application as capacitors^{198, 199}. The information about the effect of the structure and morphology on the corrosion stability of ruthenium oxide materials as supports for fuel cell

electrocatalysts is very limited. The cost of alternative fuel cell catalyst support materials, such as ruthenium oxide, is a concern. Therefore, increasing the utilization of noncarbonaceous fuel cell catalyst supports should be targeted as a main engineering objective. In the current work, we aim to elucidate potential advantages in the performance characteristics of metal oxide fuel cell catalyst supports.

In this study, we have investigated the corrosion stability of commercially available and produced-in-house ruthenium oxide materials. We have developed a procedure for making gas-diffusion electrodes (GDEs) that contain ruthenium oxide material in the active layer. The performance of ruthenium oxide-based GDEs toward oxygen reduction and the impact of material corrosion on the oxygen reduction performance are evaluated. Conclusions on the effect of the bulk and surface compositions, surface area, and surface morphology on the corrosion stability of the ruthenium oxide materials are discussed.

Experimental Approach

Ruthenium oxide material was produced at Cabot by flame pyrolysis. Another two ruthenium oxide powder materials were obtained from ESPI Metals and J&J Materials. The materials were characterized as received and after postreduction in a hydrogen environment at 250°C for 2 h. 10% Pt/Vulcan XC- 72 was purchased from ETEK.

Gas-diffusion electrodes (GDEs) were made in a two-step procedure. First, the gas-diffusion layer (GDL) was made by pressing of the 35 wt% Teflon-modified Vulcan XC-72 (XC-35) at 125°C and 16,000 lb of pressure for 10 min. Next, the ink was prepared as follows: 30 mg of RuO₂, 250 mg of a 5% Nafion solution, and 650 mg of de-ionized (DI) water were sonicated for 5 min; then 12 mg of XC-35 and isopropyl alcohol were added

and sonicated for another 5 min. The ink was then applied to the GDL layer using a Los Alamos painting technique at 75°C. Also, electrodes were made using the ink formulation without the carbon, and in this case, the ink was made of RuO₂, Nafion, and DI water only. The GDEs were electrochemically evaluated using a EG&G Princeton Applied Research potentiostat/galvanostat model 273A. Steady-state polarization curves were obtained in galvanostatic mode at room temperature in a 2M H₂SO₄ liquid electrolyte. For anodic polarization tests, currents ranging from 10 to 30 mA were applied. An acceptable steady-state transient was achieved in 10 min. O₂ was supplied to the air-breathing side of the GDE at atmospheric pressure. For all GDEs, the loading of Ru was 6.7 mg, assuming pure RuO₂. The electrode area was 9.61 cm², translating to a RuO₂ loading of 2.1 mg/cm². The electrochemically active surface area was calculated by using the specific capacitance for RuO₂ of C) 85 μF/cm². In inductively coupled plasma atomic emission spectrometry (ICP-AES) measurements, the acceptable relative standard deviation (RSD) is up to 5.00%. R² of calibration standards is 99.896%. The minimum acceptable R² value is 99.5%.

X-ray photoelectron spectroscopy (XPS) analysis was performed on a Kratos Axis Ultra X-ray photoelectron spectrometer with a monochromatic Al KR source operated at 300 W. Data analysis quantification was performed using CasaXPS software. The Ru 3d spectrum has two spin-orbit components corresponding to Ru 3d5/2 [lower binding energy (BE) side of Ru 3d] and Ru 3d3/2 (higher BE side). The separation between these components is 4.2 eV. The data were fitted with a series of mixed Gaussian-Lorentzian functions. The full-width at half maximum of the 3/2 components is larger than that of the 5/2 components. The ratio of the primary spin-orbit components and the satellite

components was constrained to be 0.67. An asymmetric function was used to curve-fit the RuO₂ component of the Ru 3d peak and the O₂- component of the O 1s peak²⁰⁰. The asymmetric function was used to reflect the fact that the positive hole created by the photoelectric effect interacts with the mobile conduction electrons. C 1s components then were added to complete the curve-fit. X-ray diffraction (XRD) data of samples were acquired with a Bruker D8 Advance powder diffractometer. The angular resolution in 2 θ scans was 0.02° for the wide-angle 2 θ scans from 20° to 90°. Thermogravimetric analysis (TGA) was performed on a TA Instruments SDT Q600 TGA/DSC. High-resolution transmission electron microscopy (HRTEM) micrographs were obtained on a JEOL 2010 200 kV transmission electron microscope. Scanning electron microscopy (SEM) images were acquired using a Hitachi S-5200 scanning electron microscope.

Results and Discussion

Physical Characterization

XRD experiments on powdered RuO₂ materials were carried out to identify the phases present in the materials. The XRD measurements on three different ruthenium oxide parent metal oxides are shown in Figure A.1. When compared to the reference (library) data, all three samples are shown to consist of a rutile RuO₂ phase. Significant differences in the diffraction line broadening indicate materials with different crystallite size, translating to differences in the Brunauer-Emmett-Teller (BET) surface area, also indicated in Table A.2. The XRD pattern of the reduced Cabot ruthenium oxide material has peaks due to two phases, metallic ruthenium and ruthenium oxide. Quantification of ruthenium oxide versus metallic ruthenium phases, however, is difficult because of the different scattering cross sections for these two phases. Also, it is important to note that

XRD is a bulk technique while corrosion processes occur on the surface. A detailed discussion of the surface species is further presented.

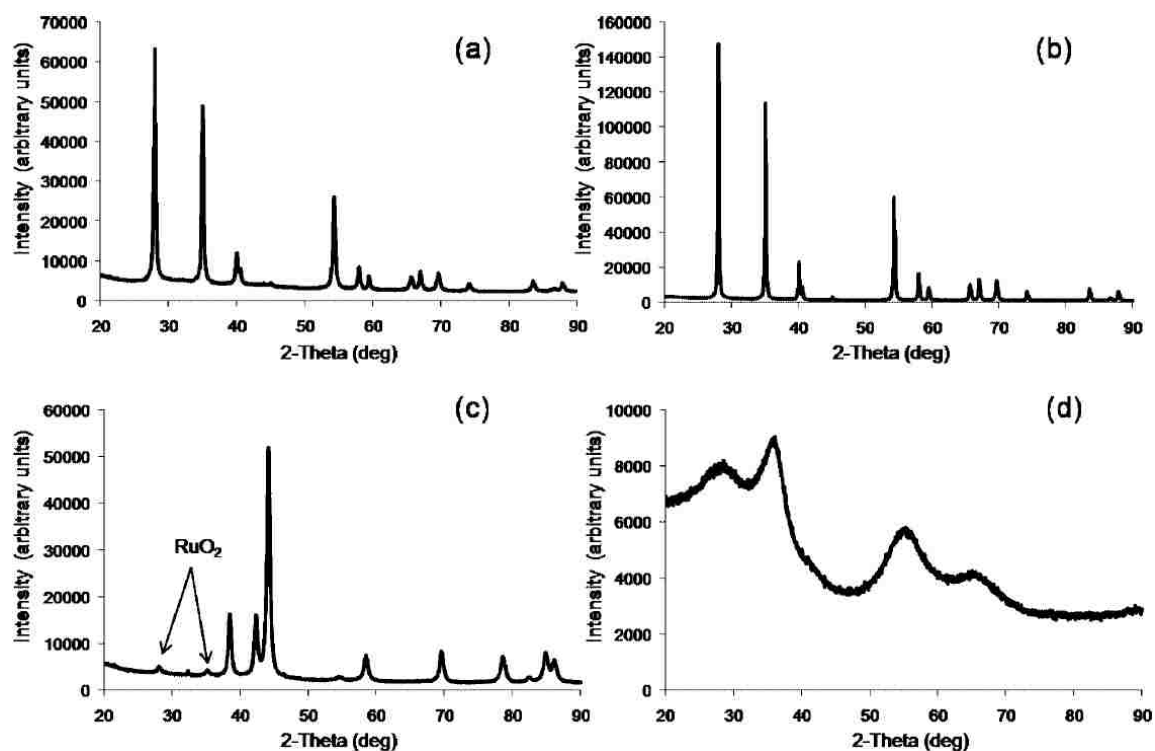


Figure A.1: XRD patterns of ruthenium oxide materials from (a) Cabot, (b) Cabot, reduced in a hydrogen environment at 250°C for 2 h, (c) ESPI Metals, and (d) J&J Materials.

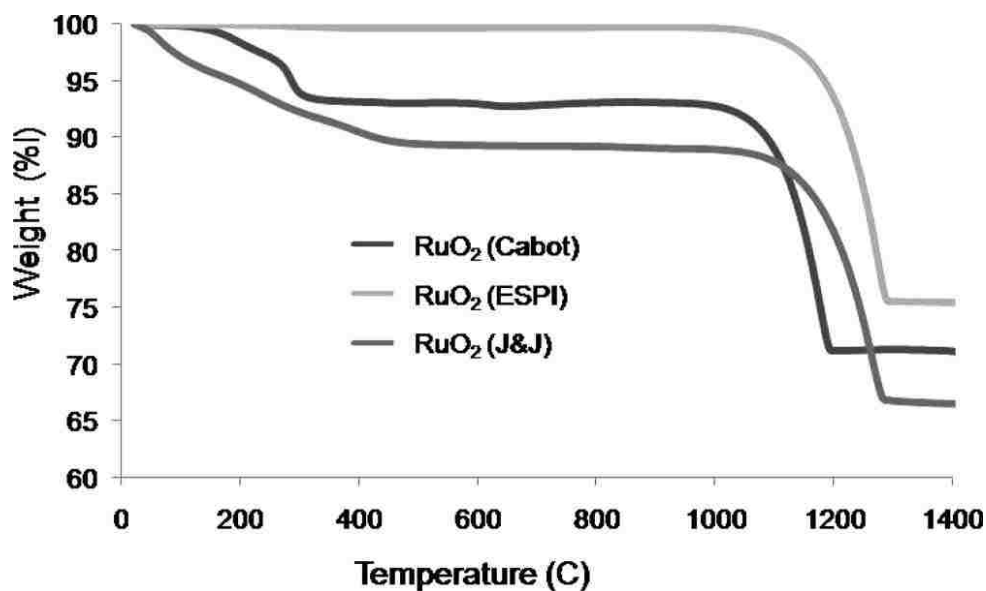


Figure A.2: TGA analysis of ruthenium oxide materials under nitrogen. Ramp rate 10°C/min.

Figure A.2 shows TGA data collected under a nitrogen atmosphere for the ruthenium oxide materials. There are two distinctive regions of mass loss in the analyzed temperature range, suggesting that there are two types of processes. The weight loss in the temperature range above 1000°C corresponds to the decomposition of RuO₂ to Ru metal. The weight percent loss measured for all materials in this temperature range is close to the value calculated based on the loss of two oxygen atoms per ruthenium atom. This indicates that ruthenium oxide materials predominantly consist of RuO₂ and do not contain metallic ruthenium. The weight losses observed in the temperature range of 25-500°C for Cabot and J&J Materials ruthenium oxide materials are most likely due to desorption of bound H₂O and OH groups. On the basis of the weight percent loss in this temperature range, we can speculate that the hydrous content of ruthenium materials is close to 0% for ESPI Metals material, about 7% for Cabot material, and about 11% for J&J Materials ruthenium oxide.

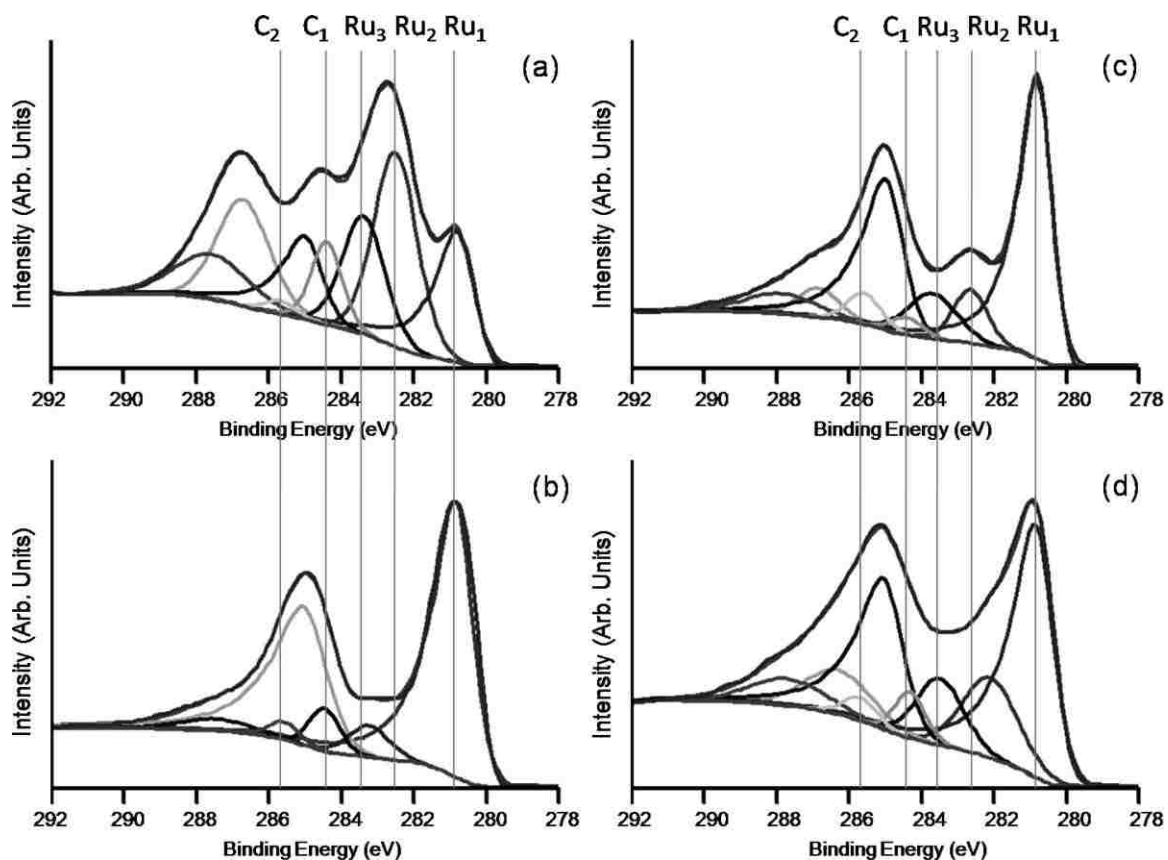


Figure A.3: High-resolution Ru 3d XPS spectra of ruthenium oxide materials from (a) Cabot, (b) Cabot, reduced in a hydrogen environment at 250°C for 2 h, (c) ESPI Metals, and (d) J&J Materials.

Table A.1: Curve Fit of High-Resolution Ru 3d XPS Spectra

sample	Ru ₁ , % RuO ₂ screened final state	Ru ₂ , % RuO ₂ · nH ₂ O	Ru ₃ , % RuO ₂ unscreened final state
RuO ₂ (ESPI Metals)	66	15	19
RuO ₂ (J&J Materials)	54	27	19
RuO ₂ (Cabot) + XC-35	24	47	28
reduced RuO ₂ (Cabot) + XC-35	88	0	12

The conductivity of the ruthenium oxide powders was evaluated using a built-in-house device that allowed measurement of the resistance, while controlling the mass and thickness of the oxide layer. Considering that the bulk of the material consists of ruthenium in the 4+ oxidation state, all three materials should display significant (metal-

like) electronic conductivity. Ruthenium oxide materials (ESPI Metals and J&J Materials) have electric resistivity below the detection limit of the multimeter used, indicating sufficient conductivity of these materials. It may seem surprising that for the Cabot ruthenium oxide the XRD measurements confirm the existence of an electronically conductive phase, but electronic conductivity measurements indicate the significant dielectric nature of the material. The reason lies in fact that the XRD measurements are bulk property measurements and almost insensitive to the surface composition. TGA, while providing information about the water content, does not allow one to differentiate the surface content from the bulk. Therefore, a surface-sensitive tool, such as XPS, has been employed to investigate the surface composition that may be different from the bulk composition.

High-resolution Ru 3d XPS spectra acquired from ruthenium oxide materials shown in Figure A.3 demonstrate that surface ruthenium in all materials is in the mixed state. Six components in the Ru 3d spectrum correspond to ruthenium components. Components at 280.8 eV (5/2 component) and 285 eV (3/2 component) are due to RuO₂. The second doublet is around 282.5 eV (5/2 component) and 286.7 eV (3/2 component). A recently published assignment of the peak at 282.5 eV to crystalline ruthenium was based on the visual analysis of the shoulder of the spectrum rather than deconvolution of the spectrum²⁰¹. As demonstrated here, deconvolution of the spectrum reveals more than one doublet on as-received ruthenium oxide materials. The changes in the amount of the peak at 282.5 eV are accompanied by the changes in the overall water content determined by TGA and by XPS analysis of oxygen spectra, supporting its assignment to RuO₂ · nH₂O. Thus, after reviewing available literature regarding the nature of the species within the BE

range of the second component in the ruthenium spectra, we assign this component to hydrous ruthenium oxide (RuO_xH_y or $\text{RuO}_2 \cdot n\text{H}_2\text{O}$). The third doublet is around 283.5 eV (5/2 component) and 287.7 eV (3/2 component). The nature of the peak at 283.5 eV has been the subject of debate in the literature²⁰⁰. Some believe that this component is due to ruthenium oxide in higher oxidation states, while others attribute this peak to the unscreened final state, shifted to higher BEs as compared to the screened final state at around 281.3 eV. Table A.1 shows the relative amounts of species, corresponding to combined 5/2 and 3/2 components of Ru 3d peaks. Among the three materials, ruthenium oxide from ESPI Materials has the highest amount of ruthenium in the RuO_2 form and the lowest amount (15%) in the form of $\text{RuO}_2 \cdot n\text{H}_2\text{O}$. Ruthenium oxide (J&J Materials) has a somewhat higher content of $\text{RuO}_2 \cdot n\text{H}_2\text{O}$ (27%). The main form of ruthenium in Cabot material is $\text{RuO}_2 \cdot n\text{H}_2\text{O}$ (47%). Five components were used to curve-fit O 1s spectra (not shown). The component at 529.4 eV is due to O_2^- species (oxygen bound to ruthenium). The component at 530.6 eV can be due to RuO_3 and/or OH^- . The peak at 531.6 eV is attributed to OH^- species. The last two components, at 532.8-534 eV, can be assigned to adsorbed H_2O and/or CO and CO_2 species (21). OH^- and H_2O are dominating the structure of the untreated ruthenium oxide (Cabot) material. Generally, water can be bound to the RuO_2 surface as a chemically bound layer and/or physically adsorbed within the micropores²⁰¹. The physically adsorbed water is expected to evaporate under UHV conditions and, therefore, is not detected in the O 1s XPS signal.

Post-reduction in a hydrogen atmosphere was used to convert ruthenium to valence IV. After reduction in a hydrogen atmosphere at 250°C, the amount of RuO_2 significantly increases (Figure A.3b). After reduction at 250°C, concentrations of peaks due to RuO_2 in

screened and unscreened final states are 88% and 12%, respectively. $\text{RuO}_2 \cdot n\text{H}_2\text{O}$ was effectively converted to RuO_2 . Analysis of O 1s spectra has revealed a significant increase in O_2 - species and a decrease in OH- and H_2O . Therefore, the important conclusion is that materials produced on the flame pyrolysis platform with aqueous precursor solutions show bulk conversion to the conductive phase of RuO_2 , but the surface composition corresponds to an insulating hydrated state, $\text{RuO}_2 \cdot n\text{H}_2\text{O}$. The increased electronic conductivity of materials exposed to a reducing atmosphere is due to bulk conversion to metallic ruthenium (XRD) and surface conversion to RuO_2 (XPS).

The BET surface area of the Cabot ruthenium oxide was measured to be $38 \text{ m}^2/\text{g}$. However, the BET surface area of the reduced material is $17 \text{ m}^2/\text{g}$, which is about 2 times lower than the BET of the pristine ruthenium oxide (Cabot). One of the possible explanations of the decrease in the BET surface area can be adherence of the particles to each other. The BET surface area of the ruthenium oxide (ESPI Metals) is $7 \text{ m}^2/\text{g}$, which is about 5 times less than the BET surface area of Cabot ruthenium oxide. The ruthenium oxide material obtained from J&J Materials has a much higher surface area than other materials tested in this work. The measured BET surface area is $122 \text{ m}^2/\text{g}$.

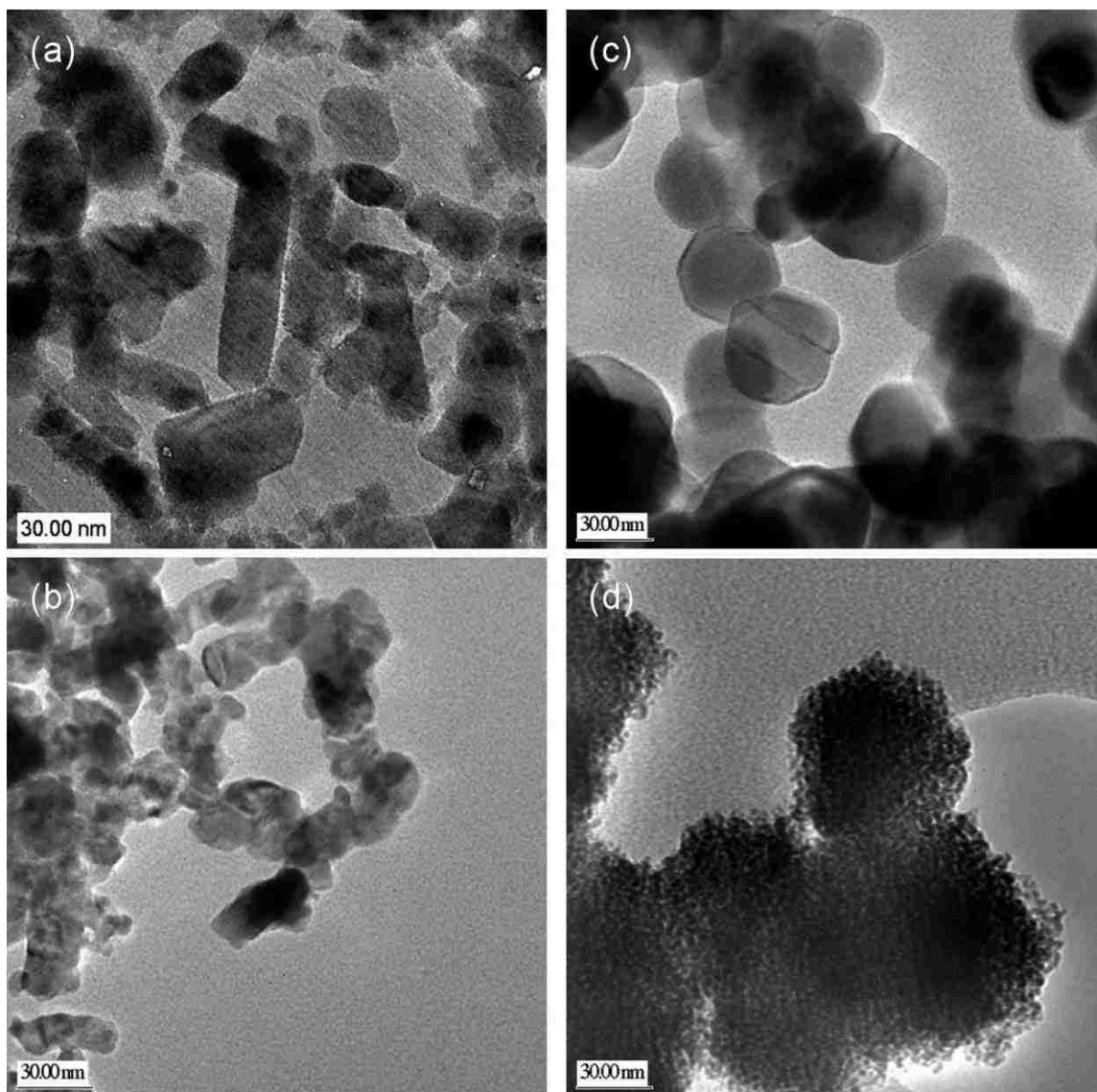


Figure A.4: HRTEM images of ruthenium oxide materials from (a) Cabot, (b) Cabot, reduced in a hydrogen environment at 250°C for 2 h, (c) ESPI Metals, and (d) J&J Materials.

TEM micrographs of ruthenium oxide powders are presented in Figure A.4. TEM micrographs demonstrate various morphologies and particle sizes of these materials. Ruthenium oxide (Cabot) powder consists of particles of elongated shape with lengths in the range of 20-120 nm. The elongated shape of the particles is also observed in a high magnification SEM image (not shown). TEM micrographs of the ruthenium oxide from

Cabot, reduced at 250°C in a hydrogen atmosphere, indicate that upon reduction the asymmetric shape of the crystallites becomes less pronounced and the size of the particles decreases significantly, although the particles fuse together to form more complex aggregate structures. The morphology of the ruthenium oxide (ESPI Metals) material is drastically different from the morphology of the Cabot material. Contrary to the elongated shape of the particles in the Cabot material (Figure A.4a), the ESPI Metals material is relatively monodispersed, hexagonally shaped particles with a diameter of about 50 nm (Figure A.4c). The TEM micrograph (Figure A.4d) and high magnification SEM image (not shown) of the ruthenium oxide (J&J Materials) demonstrate that the surface roughness in this material is much higher than that for other RuO₂ materials, leading to a significantly higher BET surface area. Figure A.5, representing low-magnification SEM images of ruthenium oxide materials, shows that smaller ruthenium oxide particles form large agglomerates.

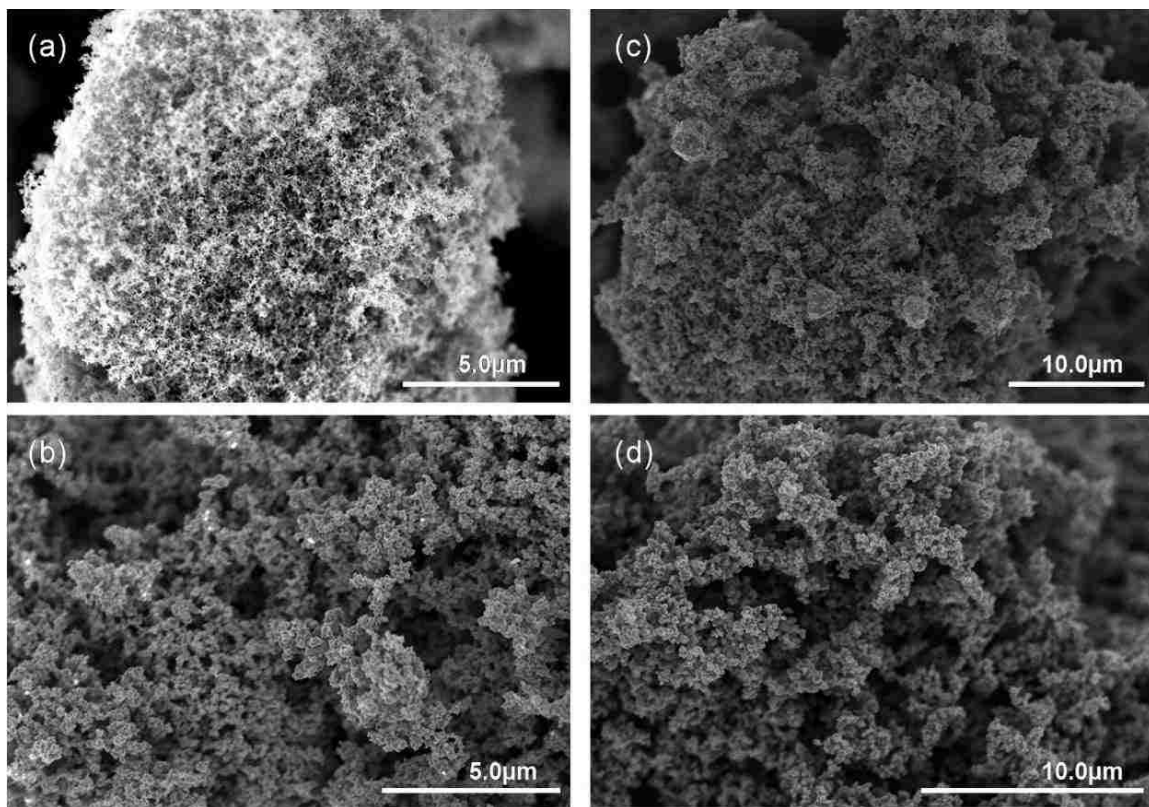


Figure A.5: SEM images of ruthenium oxide materials from (a) Cabot, (b) Cabot, reduced in a hydrogen environment at 250°C for 2 h, (c) ESPI Metals, and (d) J&J Materials.

Electrochemical Characterization

Currently, there are no procedures developed for testing the corrosion stability of noncarbon supports. Subsequently, there are no metrics that would indicate what the corrosion stability requirement is, i.e., what is “good enough”. In this work, the methodology borrowed from carbon corrosion testing was modified and applied to noncarbon materials. The results of corrosion evaluation are shown in Figure A.6. Two cathodic polarization curves for each tested material are shown. The first curve demonstrates the initial performance. The second curve is obtained after the anodic polarization of the GDE. This anodic polarization was performed to accelerate the corrosion processes that occur during fuel cell operation. The losses in the oxygen

reduction performance are result of corrosion of the electrode material. To be able to quantify the material loss during corrosion measurements, after the full corrosion protocol was applied, the liquid solution was filtered and submitted for ICP analysis. Filtration was necessary to prevent inclusion of the material lost during the physical deterioration of the electrode and to account for only the part resulting from RuO_2 corrosion dissolution. The results of the corrosion measurements, along with the ICP data, are shown in Table A.2.

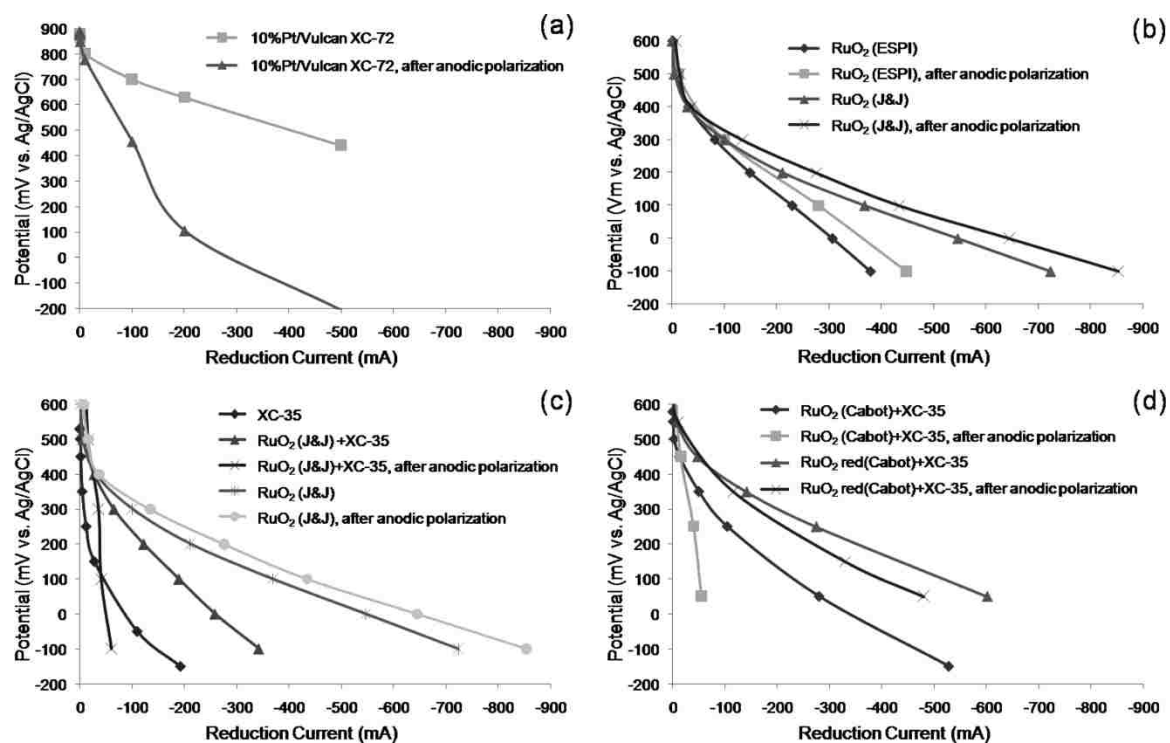


Figure A.6: Corrosion testing in a gas-diffusion cell in a liquid electrolyte, O_2 , 0 psi. Cathodic polarization curves for (a) 10% Pt/Vulcan XC-72 (ETEK), (b) ruthenium oxide materials from ESPI Metals and J&J Materials, (c) ruthenium oxide material from J&J Materials, demonstrating the effect of Teflon-modified carbon, and (d) ruthenium oxide from Cabot, demonstrating the effect of post-reduction in hydrogen.

Table A.2: Results of the Corrosion Stability Measurements of Ruthenium Oxide Materials: Values of Corrosion Current and ICP-AES Analysis

sample	BET, m ² /g	<i>I</i> at 1.2 V RHE, mA	<i>I</i> /mass, mA/mg	<i>I</i> /BET, mA/m ²	<i>I</i> /ESA, mA/m ²	concn, mg/L	RSD of three replicates, %	Ru loss, %
RuO ₂ (ESPI Metals)	7	8.4	1262	156.5	30.5	0.179	1.74	0.5
RuO ₂ (J&J Materials)	122	24	3605	30.3	11.9	0.184	1.72	0.6
RuO ₂ (Cabot) + XC-35	38	5.4	811	25.4	38.1	2.69	0.8	8.1
Reduced RuO ₂ (Cabot) + XC-35	17	8	1202	72.1	100.0	1.089	0.47	3.3

The oxygen reduction performances before and after anodic polarization of 10% Pt/Vulcan XC-72 (ETEK) and ruthenium oxide (J&J Materials and ESPI Metals) materials are shown in Figure A.6a,b. 10% Pt/Vulcan XC-72 tested under the same conditions has shown higher reduction currents compared to ruthenium oxide materials; however, it exhibited lower reduction currents than RuO₂ samples after anodic polarization. The higher overall cathodic (Figure A.6b) and anodic (Table A.2) currents obtained on ruthenium oxide supplied by J&J Materials compared to the sample provided by ESPI Metals are not due to the intrinsic corrosion stability but are due to the higher BET surface area of the J&J Materials sample. When the anodic current, measured at 1.2V versus reversible hydrogen electrode scale (RHE), is normalized to the BET surface area and electrochemically accessible surface area (ESA), currents due to corrosion of these two materials are close. Moreover, both of these materials demonstrated no decrease in the oxygen reduction performance associated with corrosion of RuO₂. Slightly higher currents observed after anodic polarization are probably associated with changes in the ESA and/or more complete surface conversion of hydrated RuO₂ · *n*H₂O to RuO₂. ICP-AES analysis confirmed that the loss of ruthenium due to corrosion is less than 1%. Thus, the corrosion test has shown that ruthenium oxide materials exhibit high corrosion stability. We expect a significant improvement in the oxygen reduction

performance of ruthenium oxide upon platinum deposition as well as the preserved corrosion stability of the ruthenium oxide support. Figure A.6c demonstrates the differences in the performance of the electrodes made of ruthenium oxide (J&J Materials) with and without the addition of a carbon component (XC-35, Teflon-modified XC-72) in the ink. Significantly lower cathodic currents are observed for the electrode made of ruthenium oxide mixed with Teflon-modified carbon. Reduction of the cathodic current is, however, not due to the RuO_2 dissolution (corrosion) but the physical loss in the ruthenium oxide powder as a result of corrosion of the teflonized carbon matrix within the GDE. This became apparent after the visual inspection of the working solution, where ruthenium oxide precipitate was observed. After the carbon materials were completely excluded from the GDE preparation, the loss of RuO_2 due to the corrosion was much smaller. Figure A.6d displays the cathodic polarization curves for Cabot ruthenium oxide. These electrodes were made using a mixture of ruthenium oxide and Teflon-modified carbon, resulting in lower oxygen reduction currents and deterioration of the electrode. However, when the as-received ruthenium oxide (Cabot) and postreduced ruthenium oxide (Cabot) are compared, several observations can be made. The sample made in-house in which incomplete surface conversion to RuO_2 , i.e., surface in the hydrated state, was confirmed by XPS measurements showed initially a high corrosion loss, ca. 8%. A postreduction step in hydrogen at 250°C after 2 h resulted in a significant improvement in the corrosion stability, as evidenced by cathodic polarization curves and ICP-AES analysis.

Conclusion

Ruthenium oxide materials with a higher surface concentration of RuO_2 showed superior corrosion stability. The loss of ruthenium during the corrosion tests was less than 1% for these samples. We have found that conversion of hydroxo groups present at the surface of ruthenium oxide materials to the RuO_2 phase by postreduction in a hydrogen atmosphere leads to improved conductivity and corrosion stability. The tested ruthenium oxide materials exhibited higher corrosion stability compared to carbon used to form GDE. When carbon-containing GDEs were subjected to corrosion measurements, false characterization originated from corrosion of the carbon powder in the electrode and a loss in the interfacial contact between the teflonized carbon and metal oxide. At this stage, it has been assumed that a loss of less than 5% ruthenium, after the full corrosion stability protocol, is sufficient for DMFC cathode applications. This assumption, as well as the performance of platinum supported on ruthenium oxide, will have to be verified in MEA measurements, by evaluating the effect of corrosion on the MEA and membrane performance.

Appendix B:

Paper Version Authors: *Bliznac, B.B., Pylypenko, S., Olson, T.S., Konopka, D., Atanassov, P.*

Niobium Oxide as a Cathode Catalyst

The performance of the oxygen reduction reaction (ORR) at the cathode in Direct Methanol Fuel Cells (DMFCs) is increasingly inhibited by the migration of un-oxidized methanol from the anode crossing the ionomer membrane as the fuel cell is run over time. Increasing the thickness of the membrane to increase resistance to methanol migration is usually a very limited solution since ion transport also becomes limited. Because platinum conventionally serves as the primary catalyst at the cathode and as bifunctional PtRu at the anode, the relative affinity for methanol adsorption and oxidation, including the adsorption of the partially reacted intermediates, is somewhat similar between the two. Thus, in presence of methanol, as a result of cross-over and competing reactions of oxygen reduction and methanol oxidation, a mixed potential is established at the cathode, where methanol oxidation also causes a decrease in the circuit potential between the electrodes. Oxygen reduction is further inhibited when Pt at the cathode becomes poisoned with CO, an intermediate of electro-oxidation.

One route to increase methanol tolerance is through design of methanol tolerant electrocatalyst at the cathode⁸. Similar to anode side platinum-based alloys, such as PtRu and PtSn, platinum alloys with Co and/or Cr were applied on the cathode side²⁰²⁻²⁰⁴. As alternative to platinum-based materials, a number of materials, based on transition metal macrocycles, sulfides and chalcogenides were explored as methanol tolerant cathode electrocatalyst²⁰⁵⁻²⁰⁹. Similar to transition metal-based materials, Ru electrocatalysts

supported on carbon provide methanol tolerance but at sacrificed activity towards ORR²¹⁰. In the practical design of robust DMFC's, where small levels of methanol migration are unavoidable, and where the most active catalysts for methanol oxidation and oxygen reduction are based upon a similar set of noble metals, the catalytic support is the other available component suitable for modification to differentiate and enhance the anode and cathode towards their respective, desired catalysis. This is achieved by two means: modification of the supported catalyst and of the catalyst's environment. In the case of the former, platinum catalyst experiences some level of electronic interaction with the support, intrinsically altering the distribution of electron density of Pt available for participation in adsorption & desorption of reactants and intermediates^{62, 156, 211}. A computational DFT study by Shao et al. demonstrated how the electronic structures of Pd & Pt as alloys and as surface layers could be altered so as to slightly weaken the Pd-O bond affinity and better desorb reaction intermediates while still achieving O-O bond cleavage for oxygen reduction²¹¹. In the latter, the catalyst might remain unaltered, but is surrounded by an environment whose surface chemistry or degree of oxidation is most conducive to fuel oxidation or oxygen reduction. While platinum remains the most active catalyst for both reactions, greater flexibility of the supports can allow for the anode and cathode to become well distinguished.

The relative degree of dispersion of catalyst on the support surface is an important factor in the overall performance of the cathode^{63, 212}. If the support is able to favorably enhance platinum towards improved ORR kinetics and ensure suppression to MeOH/CO adsorption, then a prevalence of Pt-support interfaces (or good dispersion of Pt nanoparticles) must be formed and maintained throughout electrochemical performance.

Without this, one might fail to observe any ORR enhancing effects which might otherwise be present. Therefore, high dispersion of supported platinum nanoparticles is a prerequisite to any ORR cathode system that may be considered.

The oxygen-promoting effect of metal-oxides (MO) as anodic, catalytic supports has been well identified throughout the literature. Because of the oxygen-rich surface of an MO support, oxidation of species adsorbed on platinum is further facilitated as compared to conventional platinum on carbon. But the impact and degree of the effect varies with different transition metals ⁴⁶, and the exact nature and its implications when applied towards ORR are much less clear in the literature, with the exception of Pt-Ru based catalysts in which ruthenium provides corrosion resistance and tolerance to CO due to the formation of surface hydroxyl sites near the Pt-Ru interface ^{52, 212}. One of the most highly oxidizing and corrosion resistive MO's reported upon in the literature is Nb₂O₅/NbO₂. A study by Guerrero et al. found that platinum's behavior in the presence of CO could be varied greatly with adjustments made to a Nb₂O₅ support. In particular, it was shown that in an atmosphere of CO (0.8%), O₂ (0.8%), H₂ (51%) and He, oxidation and adsorption of CO was greatly inhibited on 1%Pt on Nb₂O₅ as compared to unsupported Pt, while oxidation of H₂ remained very high. Alternatively, 1%Pt on 5%Nb/Al₂O₃ showed greatly enhanced CO activity compared to unsupported Pt ⁶⁵. This suggests that niobia could be used to develop CO-tolerant Pt supports for ORR.

Another study by Sasaki et al. measured a three-fold increase in the oxygen reduction activity of Pt on carbon supported NbO₂ nanoparticles over commercial Pt/C ⁶³. This is attributed to the greater reduction of Pt-OH to Pt, due to a lateral repulsion between Pt-OH and oxide surface species. The study also revealed that the 4-electron reduction

pathway of O_2 was dominant reaction mechanism for Pt/NbO₂/C. But this was not the case with Pt/Nb₂O₅/C, in which a greater electronic interaction between niobia and platinum is suggested and greater formation of H₂O₂ is of concern. Similar observations were made by Park et al., who attributed enhanced ORR activity of Pt/Nb-TiO₂ over commercial Pt/C to better dispersion of Pt nanoparticles and beneficial catalyst-support interactions⁶².

These studies and others suggest the potential for a wide range of catalytic supports based upon niobia in DMFCs^{18, 61, 121}. The effects of platinum-niobia interaction and platinum dispersion, as well as performance relative to all manner of observed deviations among niobia phases are of particular interest. These phases include crystalline and amorphous forms of niobia, and Nb(IV) which tends to form varying degrees of Nb(V) surface layers. Such deviations can impact the electrochemical performance profoundly.

We discuss the oxygen reduction performance of platinum deposited on Nb_xO_y supported on carbon black Vulcan XC-72R (Pt/Nb_xO_y/C) in the presence of methanol. These results, along with thorough physical characterization of all materials employed, are discussed with regard to the principles mentioned above. Further conclusions about the relationship between platinum and niobia are elucidated from the data which should provide valuable insight for future studies.

Experimental

Composite materials were prepared in two-steps. In the first step, niobium oxide was supported by precipitation on Vulcan XC72R (from Cabot Corp.). NbCl₅ (from Sigma-Aldrich) was dissolved in absolute ethanol and added to carbon, suspended in absolute

ethanol. Next, combined dispersion was sonicated for 5 minutes, and then stirred at room temperature for 3 hours. After solvent evaporation, resulting powder was pyrolyzed in nitrogen atmosphere at 500°C for 4 hours (temperature ramp, from room temperature, was 3°C per minute). In the second step, composite Nb_xO_y/XC72R powder, obtained in step one, was re-dispersed in DI water. Platinum precursor, H₂PtCl₆ (from Sigma-Aldrich) was dissolved separately, in the equal amount of DI water, while stirred and heated at 40°C. The pH was adjusted to 5 with the addition of KOH solution. Formic acid was mixed with DI water, and this solution was titrated to the H₂PtCl₆ solution, drop by drop. After the titration was completed, the final solution was stirred for 5 minutes and then added to the Nb_xO_y/VXC72R dispersion. This final dispersion was stirred for 1.5 hours, until the solution turned from yellow to clear. Subsequently, the dispersion was filtrated; the collected powder was washed four times with DI water and dried in oven at 70°C. Composite Pt/NbO_x/VXC72R with two different Pt loadings, namely 10 and 50 wt.% were prepared using this procedure. The same protocol was used to make a reference 50 wt.% Pt/VXC72R.

High-resolution transmission electron microscopy (HRTEM) micrographs were obtained on a JEOL 2010 200 kV microscope. X-ray diffraction (XRD) patterns were acquired with a Scintag Pad V diffractometer in the range from 10° to 90° 2θ with 0.02° angular resolution.

All electrochemical measurements are conducted in a thermostated three-compartment electrochemical cell. The reference electrode is a saturated calomel electrode (SCE), separated from the working electrode compartment by a closed electrolyte bridge in order to avoid chloride contamination. All the potentials in this study, however, refer to that of

the reversible hydrogen electrode (RHE) in the same electrolyte. Calibration of the reference electrode, in the given electrolyte and the given temperature, on the reversible hydrogen electrode scale is done by measuring the hydrogen oxidation/evolution polarization curves in hydrogen saturated solution on a polycrystalline bulk Pt electrode. All gases used in this study are Research Purity Grade, purchased from Matheson Tri-Gas. The potentiostat is PAR BiStat and is computer controlled. The rotator unit is manufactured by Pine Instruments, model MSR.

Results and Discussion

Materials Characterization

The TEM image of Nb_xO_y supported onto Vulcan XC72R is shown in Figure 1. The morphologies of the Nb_xO_y /Vulcan XC72R and Vulcan XC72R (not shown) are very similar suggesting the amorphous nature of the niobium oxide. XRD analysis, however, revealed small fraction of crystalline Nb_2O_5 . TEM images of Pt/ Nb_xO_y /Vulcan XC72R composite materials are shown in Figure 1 (b-d). Based on the TEM micrographs, Pt is uniformly distributed over the surface of support. The crystal size is on the larger side (ca. 5-10 nm), but what is also observable is existence of asymmetric shapes. In this case, elongated shapes of crystallites indicate formation of Pt crystal aggregates, composed of two or more Pt crystals fused together. In order to prevent this aggregation, the BET surface of the support and the metal loading have to be carefully balanced.

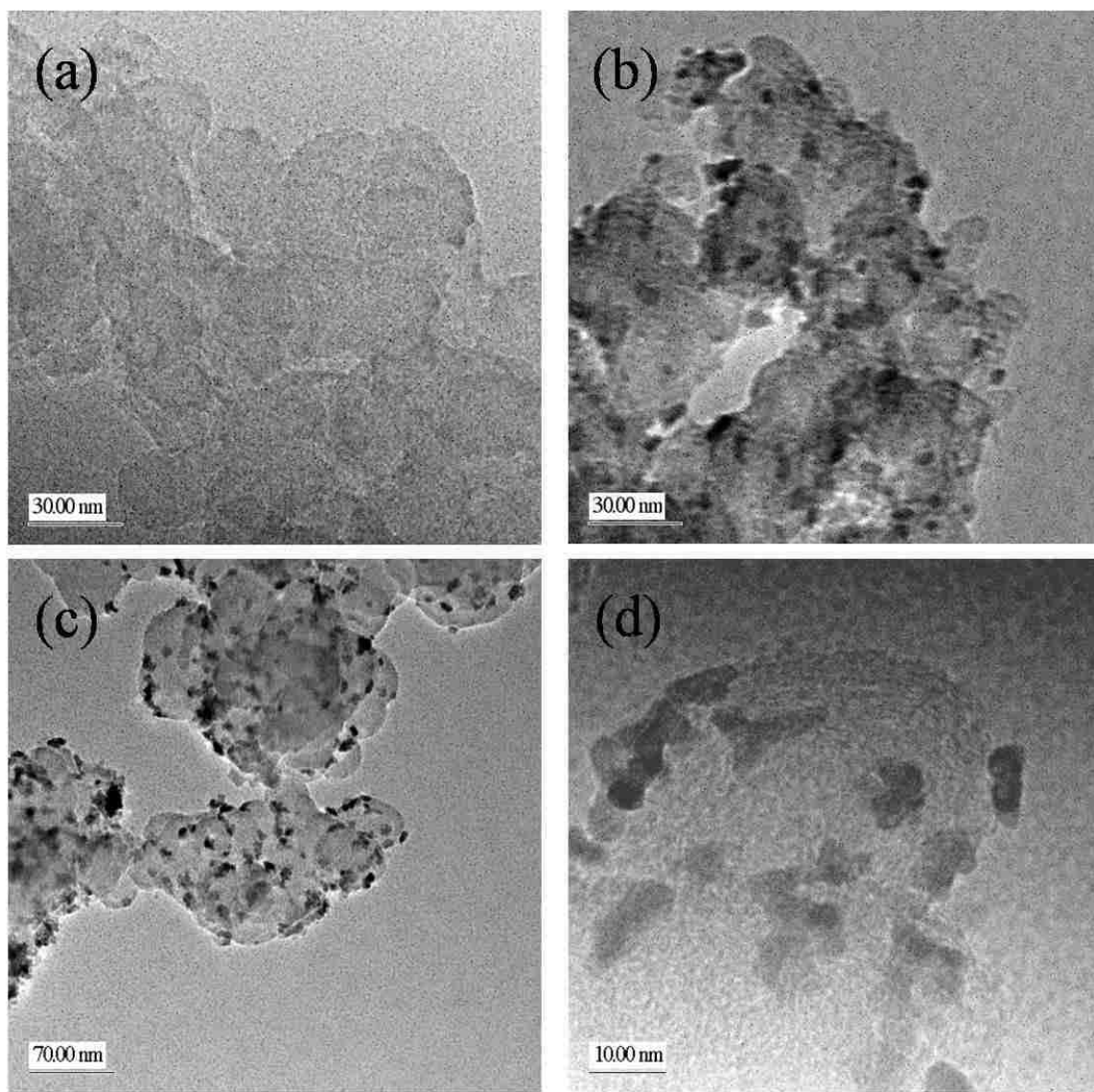


Figure B.1: HRTEM images of a) $\text{Nb}_x\text{O}_y/\text{VXC72R}$, b) 10 wt.% $\text{Pt}/\text{Nb}_x\text{O}_y/\text{VXC72R}$, c) 50 wt.% $\text{Pt}/\text{Nb}_x\text{O}_y/\text{VXC72R}$, d) 50 wt.% $\text{Pt}/\text{Nb}_x\text{O}_y/\text{VXC72R}$ under higher magnification.

The BET for this powder, 50 wt.% $\text{Pt}/\text{Nb}_x\text{O}_y/\text{VXC72R}$, was determined to be $75 \text{ m}^2/\text{g}$.

Figure B2 shows the XRD characterization data for the same sample. As expected, five peaks, characteristic for the fcc phase of Pt are observed in the spectrum, with the reflection from (111) crystallographic plane as the most intense. When this XRD pattern is compared with the pattern corresponding to 50 wt.% Pt supported on Vulcan XC72R in the absence of Nb_xO_y , extra features in the XRD spectrum of composite material in

$20^\circ < 2\theta < 30^\circ$ range, are attributed to the reflection from Nb_2O_5 . The position of the Pt XRD peaks is almost the same, and there is no shift that would indicate (measurable) Pt/Nb alloying.

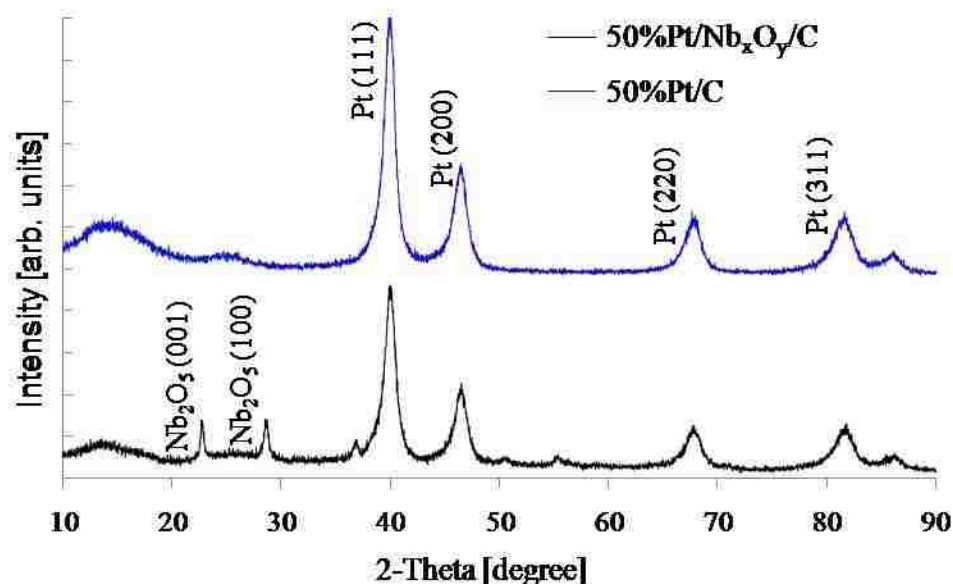


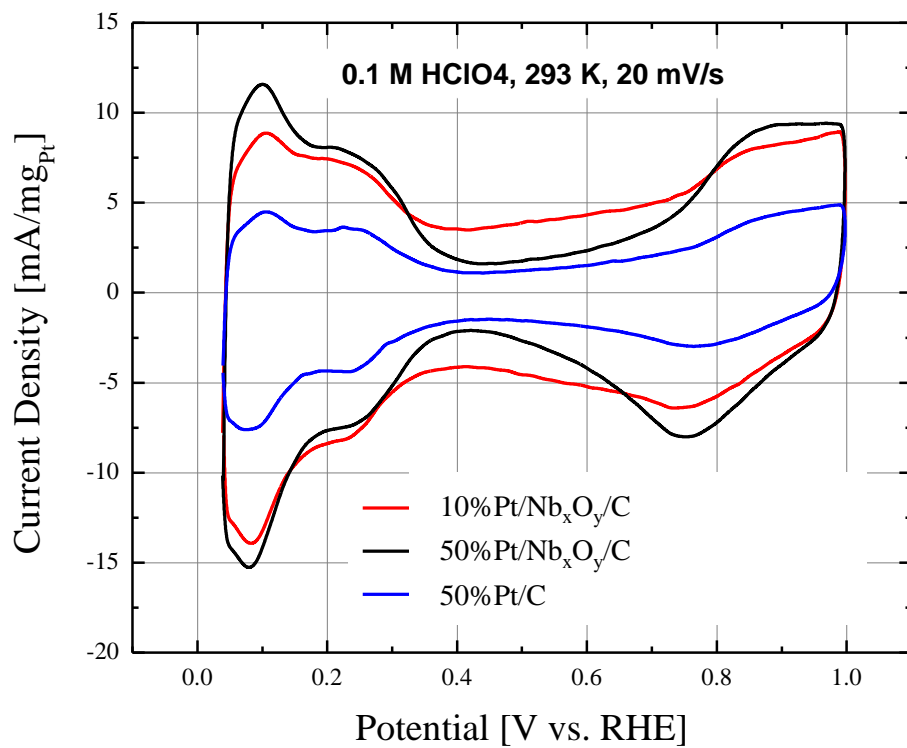
Figure B.2: XRD patterns of 50 wt.% Pt/VXC72R and 50 wt.% Pt/ Nb_xO_y /VCX72.

Electrochemical Characterization

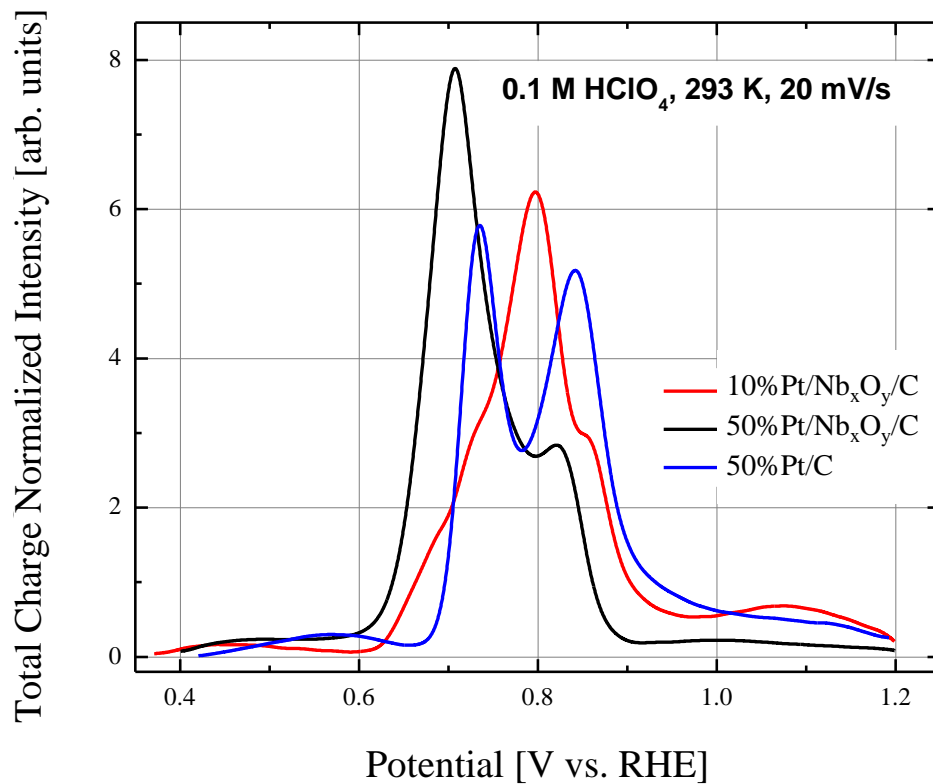
For subsequent electrochemical characterization three powders were used, namely 10 wt.% Pt/ Nb_xO_y /VXC72R, 50 wt.% Pt/ Nb_xO_y /VXC72R, and as a baseline 50 wt.% Pt/VXC72R obtained under identical preparation conditions. The first electrochemical measurements involved ex-situ characterization in thin-film-rotating-disk electrode (TFRDE) configuration. Cyclic voltammograms (CV's), indicative of the catalyst/electrolyte (water) interface and interfacial adsorption phenomena is given in Figure B.3a. All three cyclic CV's have features characteristic for Pt on carbon supported materials. Starting from negative potential limit, characteristic hydrogen (underpotential)

adsorption/desorption phenomena, $0 < E < 0.3$ V, is followed by capacitance dominantly under influence of support materials, $0.6 < E < 1$ V, further followed by water activation, $E < 0.6$ V, resulting in oxide formation/reduction region. As expected, the sample with only 10 wt.% Pt and the highest support (carbon + niobium oxide) mass contribution shows the most pronounced pseudo-capacitive features.

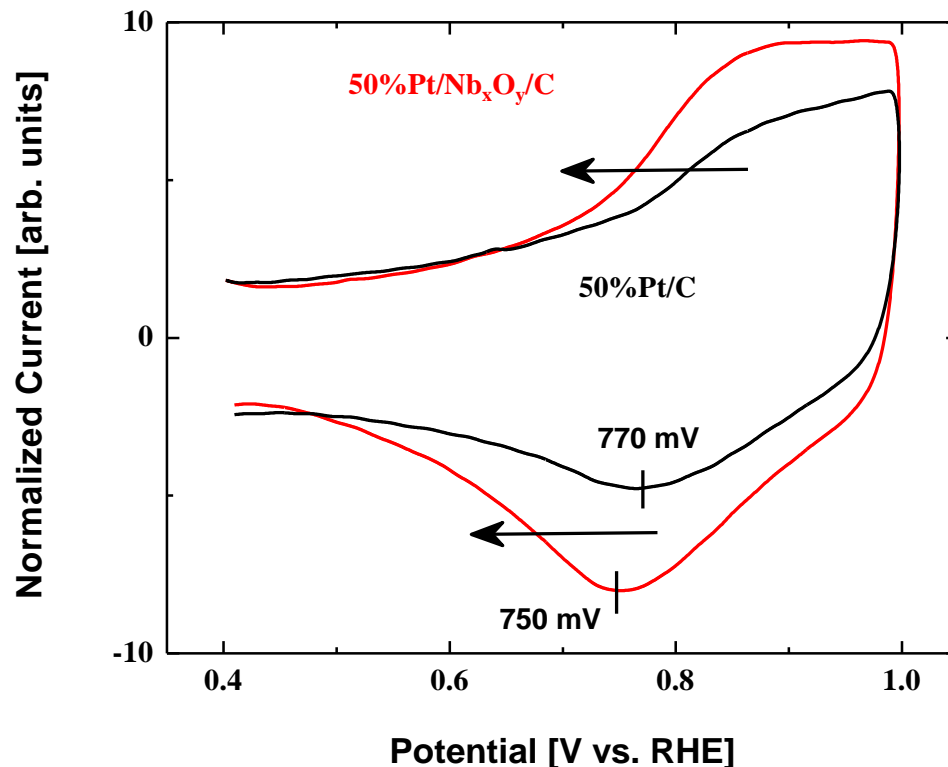
Hydrogen adsorption/desorption phenomena were further utilized to calculate the electrochemically active surface area (ECSA). The ECSA was obtained by integrating the hydrogen desorption region, after correction for pseudo-capacitive contribution, and by assuming that every $210 \mu\text{C}$ of integrated charge corresponds to 1 cm^2 of electrochemically active surface area of platinum. The ECSA, alternatively, was also calculated by using the oxidation of pre adsorbed CO_{ad} layer on the electrode surface, the so-called CO-stripping ECSA, now assuming that every $420 \mu\text{C}$ charge corresponds to 1 cm^2 of electrochemically active surface. The CO stripping curves, corrected for the capacitive features obtained in the second consecutive (after CO stripping) polarization sweep is shown in Figure B.1b.



(a)



(b)

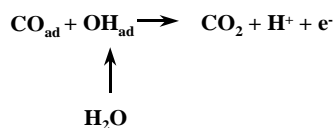


(c)

Figure B.3: a) Cyclic voltammograms in 0.1 M HClO₄ at 293K, b) CO stripping curves after subtraction of second consecutive positive sweep, c) The potential range of the cyclic voltammograms indicating the negative shift in water activation and oxide formation on composite 50 wt.% Pt/Nb_xO_y/VXC72R vs. 50 wt.% Pt/VXC72R. The current density was normalized to emphasize these features.

Appearance of multiple peaks during the oxidation of pre-adsorbed CO_{ad} layer, indicates the highly heterogeneous surface in terms of adsorption/oxidation sites, and this might originate from the multimodal crystal size distribution, or by existence of the grain boundary between oxide and Pt particles. In the case of the latter, the reaction of CO oxidation starts at the grain boundary and propagates to the remainder of the Pt crystallite surface. Alternatively, multiple peaks in CO stripping experiments might originate from complex- overlapping diffusion patterns as a result of high Pt-metal loading and low BET of the support material, resulting in high lateral density of Pt crystallites. In addition to

the calculation of ECSA based on oxidation of pre-adsorbed CO layer, CO stripping experiments are also insightful in terms of potential of zero total charge (pztc), and related to this parameter the ability of surface to dissociate water and form OH_{ad}, the so-called surface oxides. The reaction sequence of CO oxidation can be given by next equation:



Based on this equation, after the initial adsorption of CO on the surface, the oxidative removal of CO occurs as a Langmuir-Hinshelwood type reaction, requiring that in addition to CO_{ad} there are adsorbed surface oxide species, in electrochemical jargon called OH_{ad}. These surface oxides are the result of water dissociation (in acid media). Therefore, the onset potential for CO oxidation will depend on the ability of surface to dissociate water at given potential. The more negative potential where water dissociation occurs, the more negative onset potential for oxidative removal of pre-adsorbed CO. Based on Figure B.3b, both composite electrodes consisting the Nb_xO_y have the onset of CO oxidation shifted toward more negative potentials compared to the sample where Pt is supported only on carbon. This result is also well aligned with observed features in CV (Figure B.3a). Considering the difference in Pt dispersion, in the Figure B.3c, voltammetric features are normalized to show different potentials of water dissociation and subsequent shift in oxide reduction peak. As can be seen from this figure, in the presence of Nb_xO_y, formation of surface oxides (and subsequent transformation to bulk oxides) starts at potentials shifted 20-40 mV to more negative values. Obviously, the

presence of Nb_xO_y results in more hydrophilic nature of these powders. This effect is not expected to promote the intrinsic oxygen reduction activity, quite the opposite, but it is expected to facilitate the removal of CO_{ad} intermediate in CH_3OH oxidation as a result of methanol crossover in DMFC.

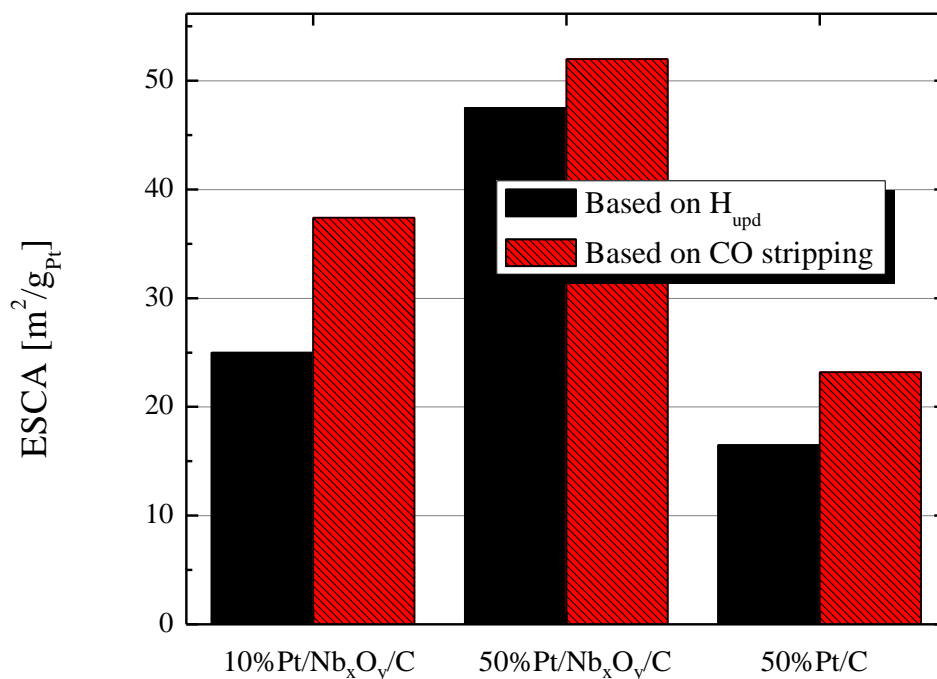
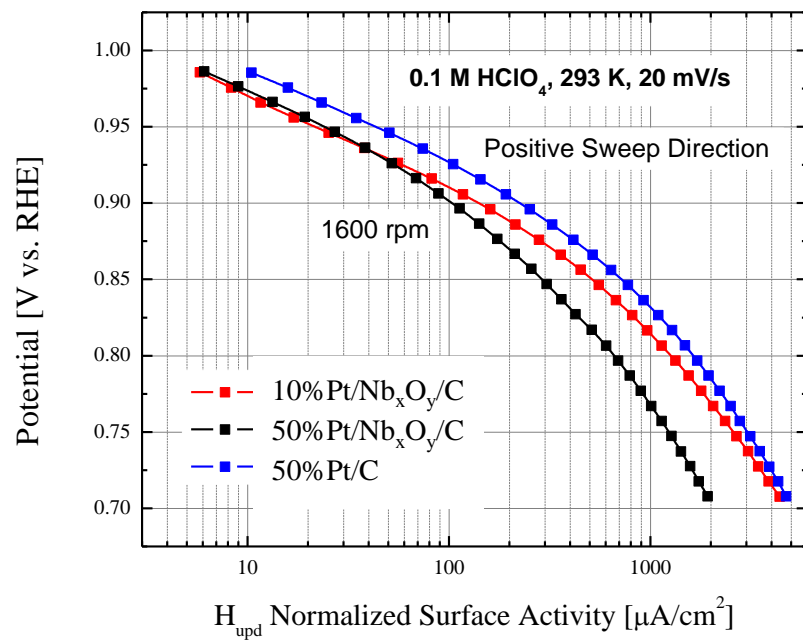


Figure B.4: Chart presenting electrochemically active surface area (ECSA) values obtained from hydrogen desorption and CO stripping.

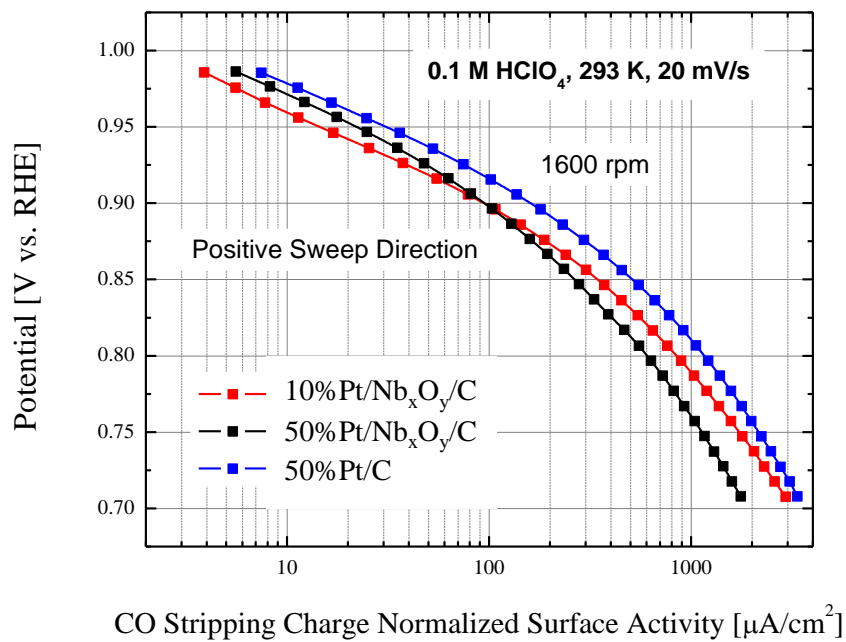
The ECSA determined by utilizing both the hydrogen desorption and CO stripping is shown in Figure B.4. The major observation from Figure B.4 is much higher Pt dispersion in the presence of Nb_xO_y for both low and high Pt loadings. For the same Pt loading of 50 wt.%, ECSA in the presence of Nb_xO_y is double of that where Pt is supported only on Vulcan XC72R. Although the synthetic chemistry can be further

optimized, this is important result. This additional confirmation of improved Pt dispersion in the presence of oxides should be investigated further as a method of improved Pt dispersion, particularly for catalysts requiring high Pt loading as a way of controlling the catalysts layer thickness in H₂/Air Fuel Cells. The selection of oxides as dispersing agents for these applications should be also based on how easy is to remove oxides after Pt dispersion is locked and desired dispersion is achieved.

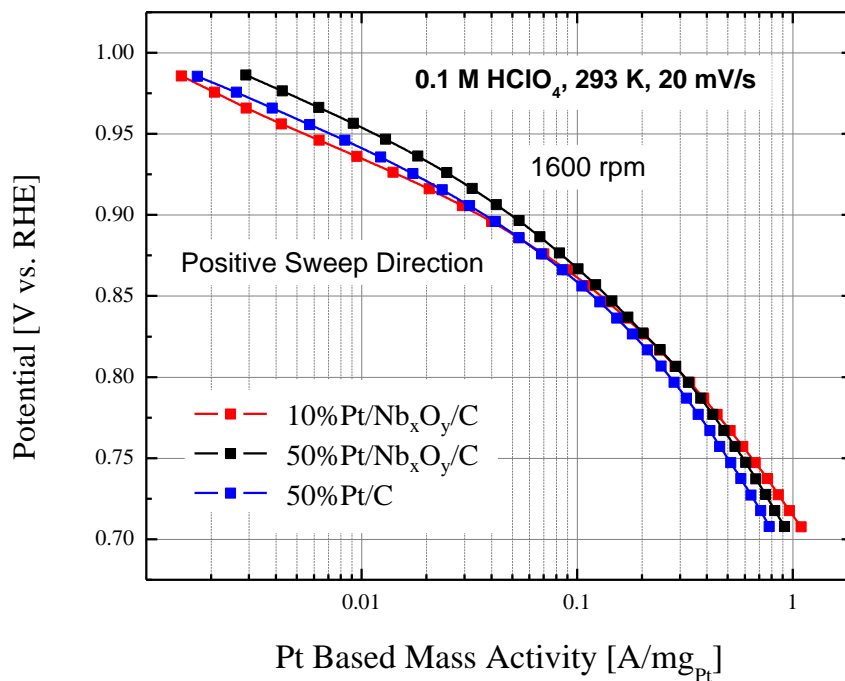
After this initial electrochemical characterization, the intrinsic catalytic activity toward the oxygen electroreduction, i.e. in the absence of methanol, was measured. There are several ways to express the intrinsic catalytic activity. From the fundamental-catalytic perspective, kinetic current, corrected for the diffusion limitations, when expressed as surface normalized activity enables comparison of different catalysts based on their fundamental catalytic properties- the concentration of surface active sites and the turnover frequency (TOF). Alternatively, catalytic activity can be expressed as a mass normalized activity (normalized over the mass of Pt), and from the practical point this normalization is more meaningful as it defines how much of the expensive Pt has to be used to achieve desired absolute performance. However, these normalized activities are interconnected, i.e. mass activity is the product of surface normalized activity and the Pt dispersion (dispersion of the active phase), and therefore both should be used in catalysts design and optimization. Kinetic currents, corrected for diffusion limitations, normalized over ECSA obtained from electrochemical hydrogen desorption and CO stripping, are shown in Figure B.5.



(a)



(b)



(c)

Figure B.5: Diffusion corrected ORR currents a) normalized to ESCA obtained from hydrogen desorption, b) normalized to ESCA obtained from CO stripping, c) normalized to Pt mass.

Based on Figure B.5, although the presence of Nb_xO_y acts as a promoter for Pt dispersion it, somewhat, inhibits the intrinsic catalytic activity for oxygen reduction reaction. This is expected based on previous discussion, and can be explained by facilitated water dissociation on niobium oxide in the immediate vicinity of Pt crystallites, and diffusion of these surface oxides to the surface of Pt phase. Presence of surface oxides on platinum decreases the concentration of active sites available for molecular oxygen adsorption, intermediate in oxygen electro-reduction reaction. In this case, Nb_xO_y acts as an inhibitor for the oxygen electroreduction. Mass activity, however, will depend on both the surface normalized activity, where Nb_xO_y acts as an inhibitor, and Pt dispersion, where Nb_xO_y

acts as a promoter. Mass normalized kinetic current for these three samples are shown in Figure B.5c. Now, the 50 wt.% Pt/Nb_xO_y/VXC72R is the most active catalysts, more active than 50 wt.% Pt/VXC72R. From here it is clear that initially lower intrinsic catalytic activity for ORR is compensated with much better Pt dispersion, so that the overall Pt mass utilization, measured as mass normalized ORR activity surpasses the mass activity without the Nb_xO_y.

Conventional way in comparing the intrinsic catalytic activity of different catalysts is at fixed potential, the most frequently at 0.9 V, where diffusion restrictions are assumed to be negligible. Intrinsic catalytic activities for these three materials: surface (ECSA), and mass normalized are shown in next figure (Figure B.6).

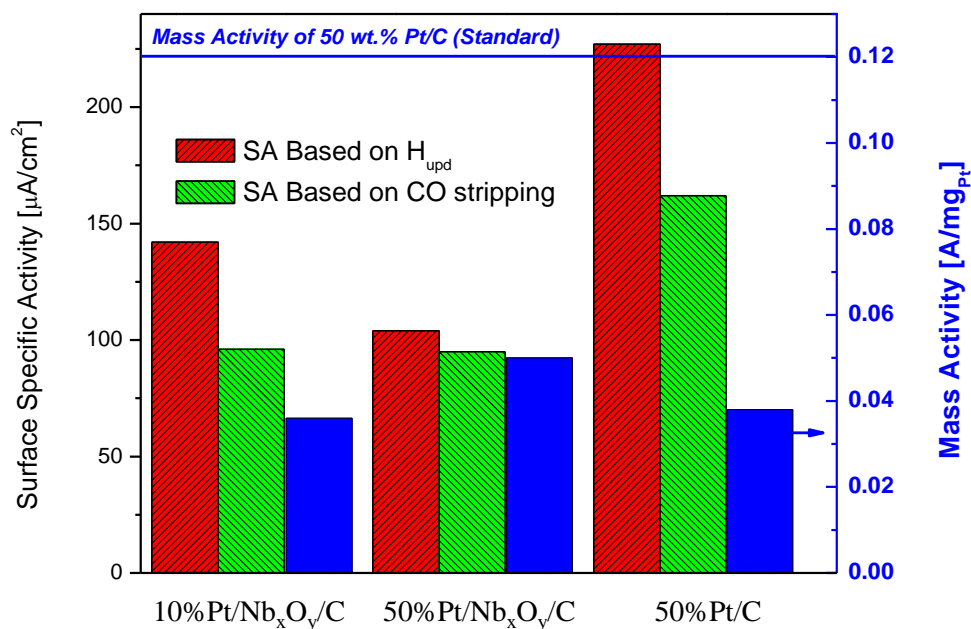
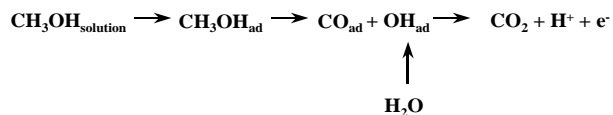


Figure B.6: ORR activity at 0.9 V; ECSA normalized values are shown on left y-axis and mass normalized values are shown on right y-axis.

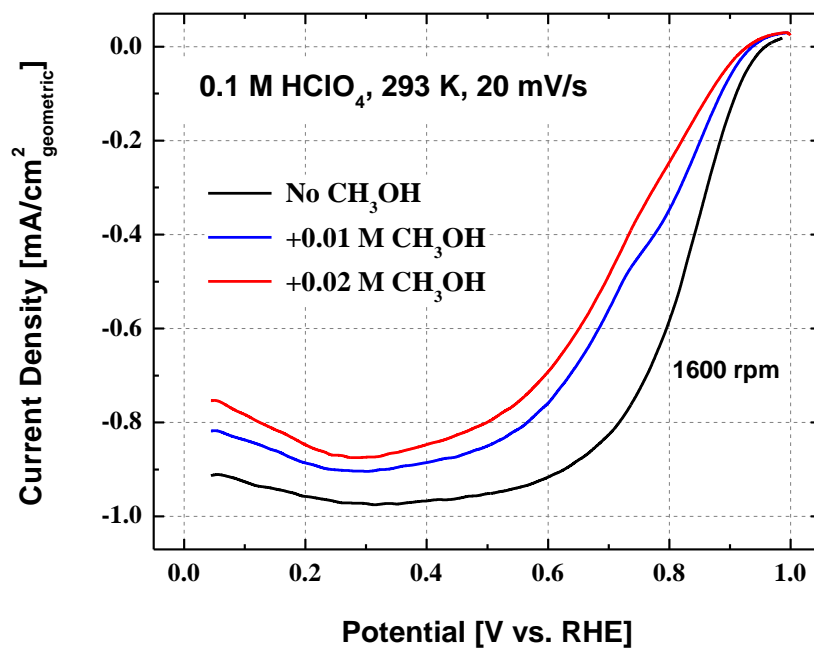
The horizontal line at 0.12 A/mg_{Pt} in Figure B.6 represents the baseline- 50 wt.% Pt/Ketjen Black catalysts. Although, measured catalytic activities for three samples in this study are much lower than the baseline, it should be mentioned, however, that they are close (within 20-30%) to catalysts consisting of 60-65 wt.% Pt on Ketjen Black. Considering the difference in BET surface area between Vulcan XC72R and Ketjen Black, higher weight loading on Ketjen Black is closer/better comparison. It also suggests that the Pt metal loading has to be closely and carefully balanced for each BET of the support.

Oxygen Reduction Reactivity in the Presence of Methanol

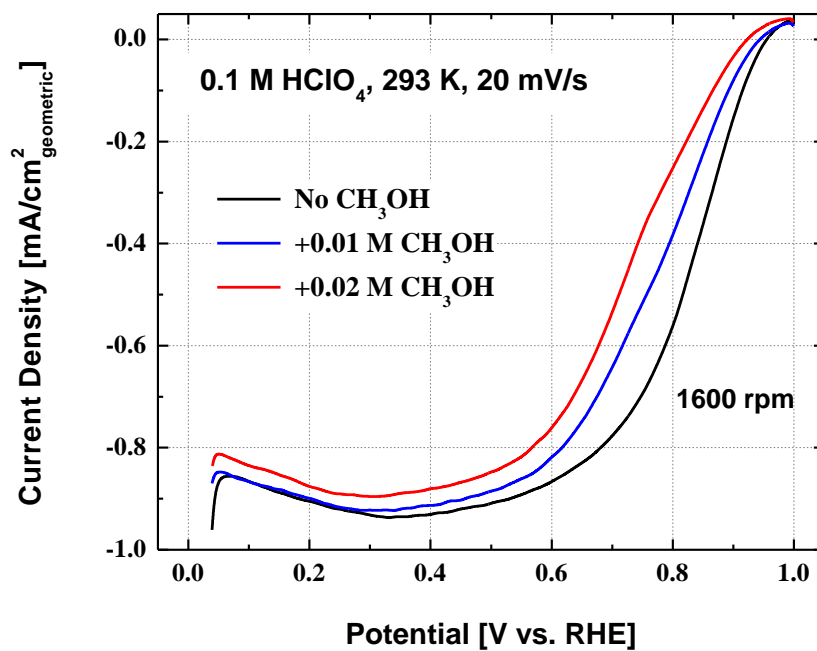
The last stage in ex-situ catalysts characterization consisted of ORR activity measurement in the presence of methanol- the so-called “methanol tolerance”. For comparison clarity, two samples with the same Pt loading without and in the presence of Nb_xO_y were used. The methanol concentration in these experiments might seem too low. However, since all the polarization curves were obtained when electrodes were rotated at 1600 rotations per minute, the concentration gradients (the driving force for the diffusion) correspond to concentration gradients in the presence of at least the order of magnitude higher methanol concentrations on stationary electrodes (DMFC cathodes). In this case the methanol concentration would correspond to quite realistic 10-20% methanol crossover in DMFC. The general features of ORR on both electrodes are similar (Figure B.7). Addition of methanol to the solution results in shift of oxygen reduction currents to higher ORR overpotentials. However, there are significant differences. To explain the differences we need to know the mechanism/pathway for CH₃OH oxidation. This pathway is given by next equation:



The first step in methanol oxidation is the methanol adsorption on the surface. The intermediate formed after partial methanol oxidation (dehydrogenation step) is CO_{ad} which, as we have seen previously, can only be removed at sufficiently high positive potentials where water dissociation occurs and OH_{ad} forms on the surface. These potentials are significantly more positive for Pt/VXC72R sample, compared to the Pt/ NbO_x /VXC72R. As a result, without the Nb_xO_y to supply the OH_{ad} at low potentials, methanol oxidation intermediates have more irreversible poisoning effect. This can be observed from Figure B.7. On 50 wt.% Pt/VXC72R, the diffusion limiting currents are decreasing when methanol concentration is increasing. This is the result of irreversible (within the experimental potential range and potential sweep rate) “contamination” of Pt surface by intermediates of methanol oxidation (both CH_3OH , and CO_{ad}). The same effect can be observed, although smaller in magnitude, on composite Pt/ Nb_xO_y /VXC72R electrode only at high methanol concentrations. CH_3OH concentration of 0.01 M, in the diffusion-limiting region, has almost no effect on composite electrode.



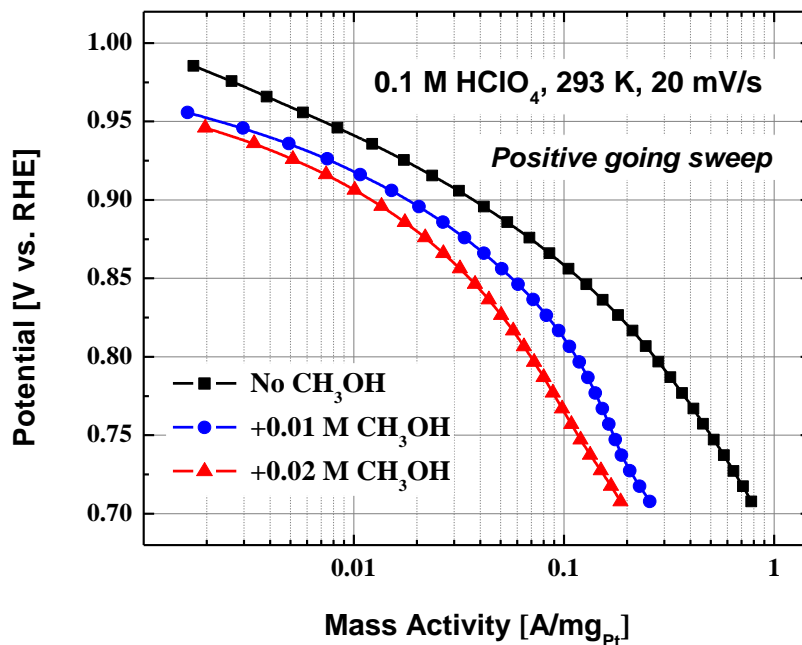
(a)



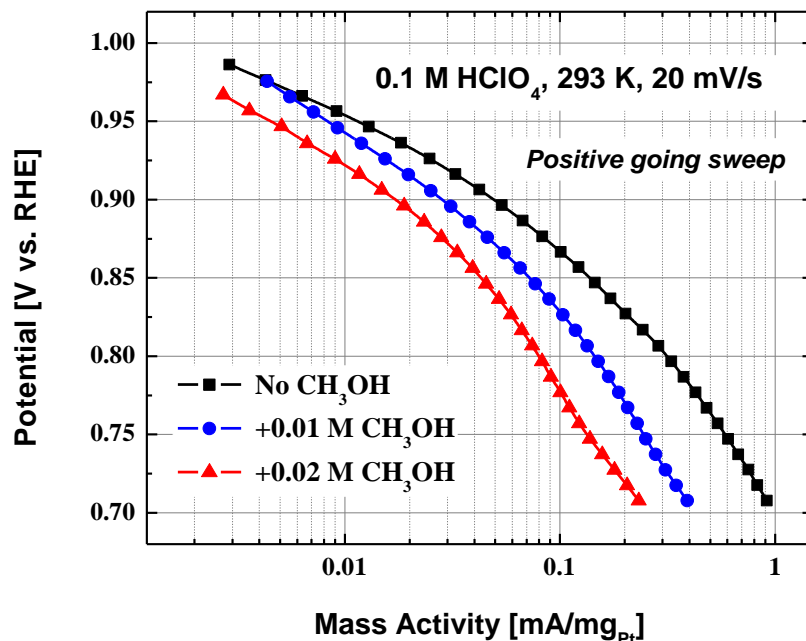
(b)

Figure B.7: ORR polarization curves at 1600 rpm, without and in the presence of methanol on a) 50 wt.% Pt/VXC72R, b) 50 wt.% Pt/Nb_xO_y/VXC72R.

Comparison of kinetic currents, corrected for diffusion, mass normalized and as a function of methanol concentration is given in Figure B.8. From here it can be seen that the impact of methanol is more gradual on composite electrode, whereas on Pt/VXC72R even the small methanol concentration already results in steep deactivation in ORR activity.



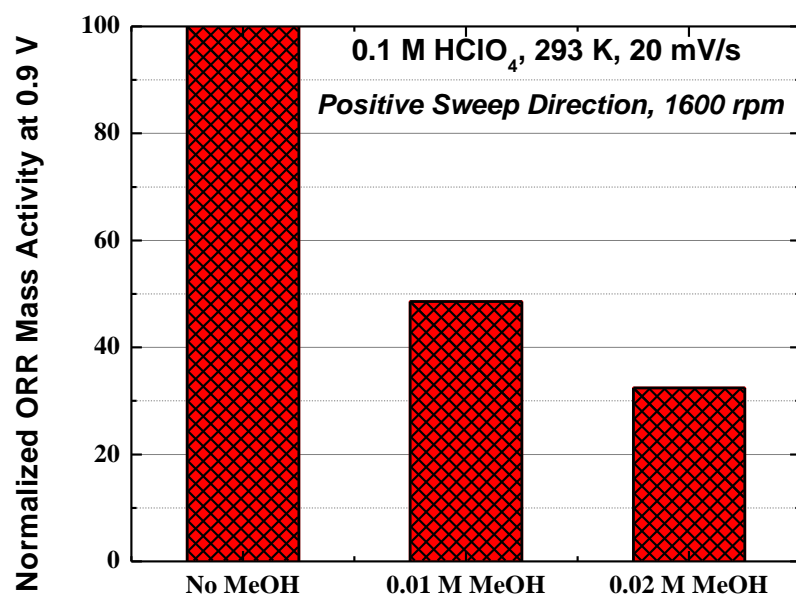
(a)



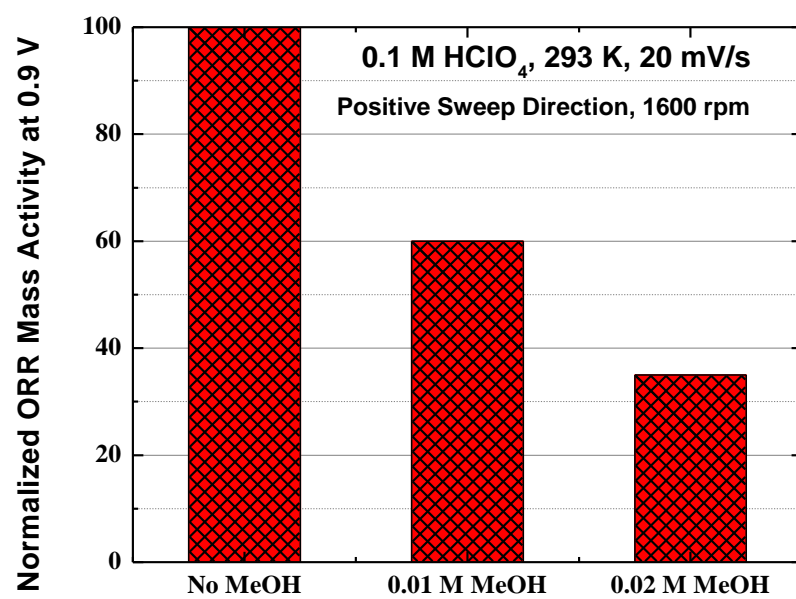
(b)

Figure B.8: Diffusion corrected ORR currents, mass normalized, without and in the presence of methanol, on a) 50 wt.% Pt/VXC72R, b) 50 wt.% Pt/Nb_xO_y/VXC72R.

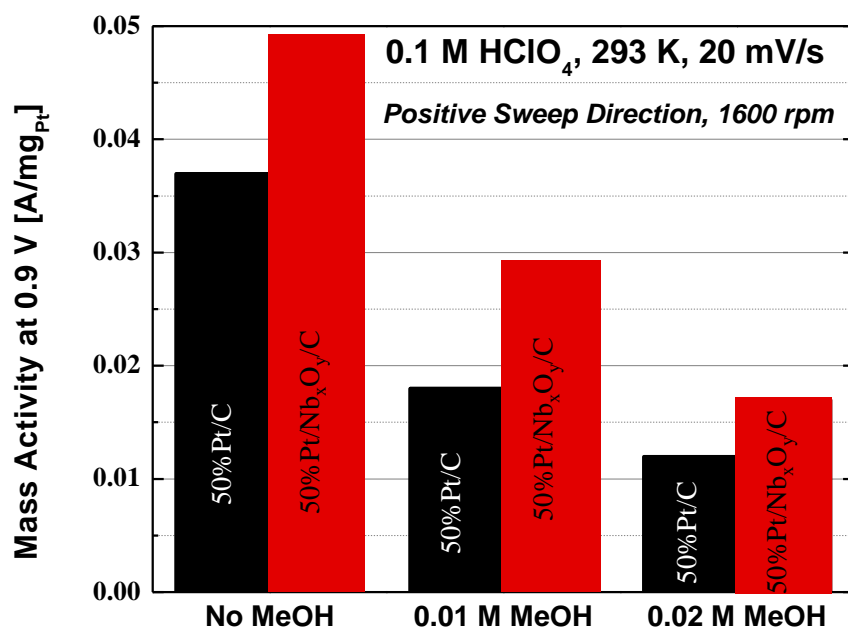
This can be better observed in next figure (Figure B.9). Here the ORR mass activities at 0.9 V are normalized to the mass activity without the methanol in the solution. With the addition of 0.01 M CH₃OH, the composite Pt/Nb_xO_y/VXC72R retains 60% of initial ORR activity, compared to less than 50% of the initial activity in the absence of Nb_xO_y on Pt/VXC72R electrode. With the addition of even more methanol, the difference in deactivation between the composite and Pt/VXC72R is still favoring the composite Pt/Nb_xO_y/VXC-72R, although the benefit in relative terms is less pronounced. It seems that this can be even further optimized by simultaneous optimization between the Pt loading, Nb_xO_y loading and the BET of the carbon support.



(a)



(b)



(c)

Figure B.9: Effect of methanol concentration on ORR activity at 0.9 V, expressed as a per cent of the initial activity without methanol in the solution on a) 50 wt.% Pt/VXC72R, b) 50 wt.% Pt/Nb_xO_y/VXC72R, c) mass activity toward the oxygen electroreduction at 0.9 V without and in the presence of methanol.

The absolute mass normalized ORR performance at 0.9 V for these two catalysts compositions is shown in Figure B.9c. Here it is obvious that benefit of having the Nb_xO_y extends over all CH₃OH concentration. Furthermore, the initial mass activity ratio between these two catalysts of 1.3, jumps to 1.6 in favor of composite catalysts in the presence of 0.01 M CH₃OH, and although it drops to 1.4 at 0.02 M CH₃OH, it is still higher than the initial activity ratio proving the enhanced methanol tolerance in the presence of Nb_xO_y.

Conclusions

Electrocatalysts consisting of Pt deposited on Nb_xO_y/Vulcan XC72R composite support were synthesized and characterized. Electrochemical activity data for composite materials suggests that advanced ORR catalysts development can proceed in two directions. First direction is development of methanol tolerant ORR catalysts (bi-functional catalysts). In this case, although the addition of metal-oxides is inhibiting for intrinsic catalytic activity (H₂O activation and surface oxide diffusion to the Pt phase occurs at more negative potentials) the resulting activity in the presence of methanol is superior compared to Pt supported only on carbon. This result suggests that it is not of paramount importance to control Pt deposition to any particular phase, i.e. carbon or metal-oxide. The other direction, to improve the intrinsic catalytic activity, imposes more stringent requirements on selective Pt deposition. Here, it seems that to have controlled Pt deposition exclusively on the metal-oxide phase is of paramount importance. This is dictated by two main reasons. First one is related to modifications of electronic properties of Pt phase when deposited on the oxide, as a result of different electron donor/acceptor properties of the Pt-oxide interface and possibly of the strain effect. The other reason for necessary Pt deposition on the oxide support is related to the oxide passivation when covered with Pt, and therefore suppressed parasitic ORR activity. In both cases, Pt has to go on the surface of the oxide, and the metal-oxide surface exposed to the electrochemical environment has to be minimized. It seems worthwhile to explore oxides as dispersing agents, particularly when high Pt loading catalysts compositions are considered. In the pursuit of state of the art mass activity, the chemical nature and BET of support and the metal loadings should be carefully balanced. After that, MEA optimization has to emphasize the operation

under low relative humidity, where higher hydrophilicity of composite materials are expected to be beneficial.

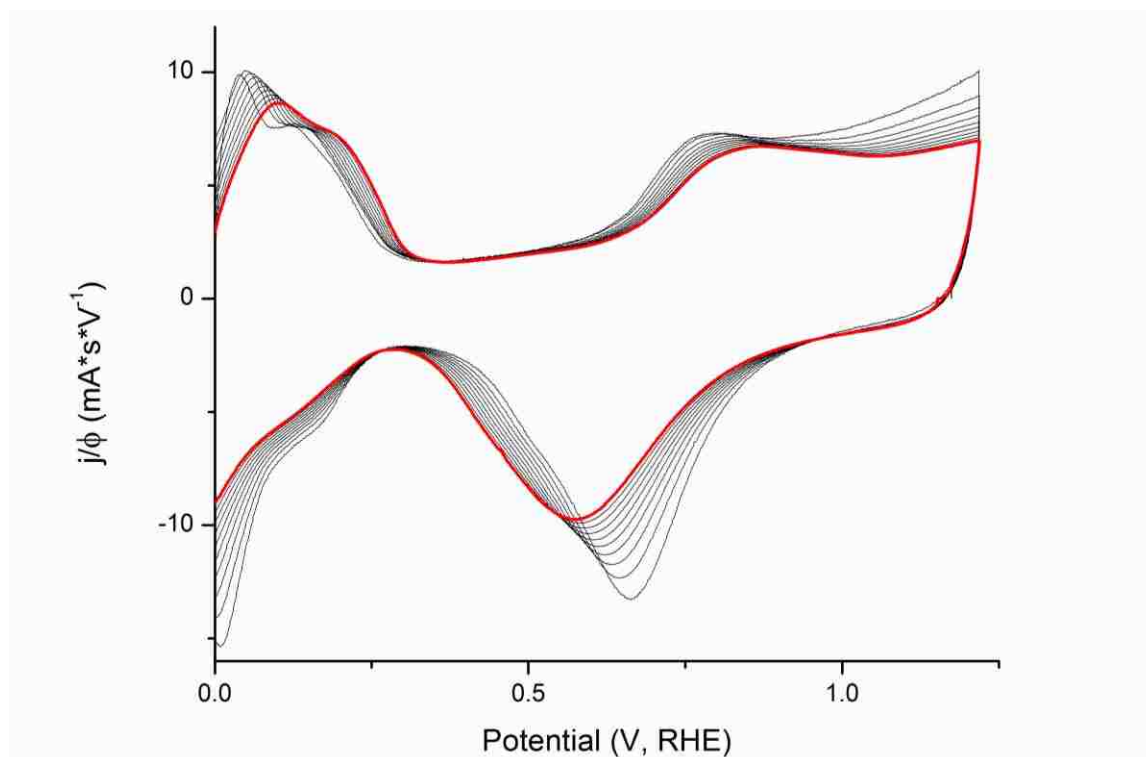
Appendix C:

Cyclic Voltammetry: Charging Response to Increasing Polarization Rates

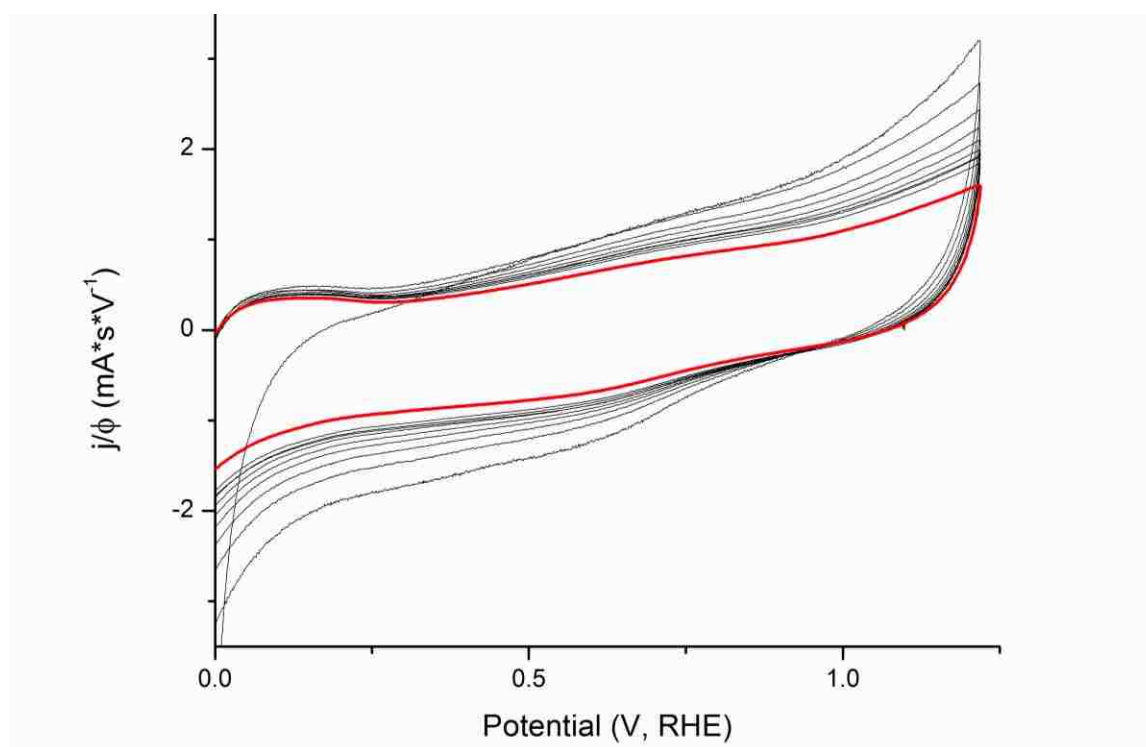
The shape of redox features is influenced by the polarization rate of the electrode (ϕ) in cyclic voltammetry studies. Therefore, it is important to understand how catalyst materials respond at different values of ϕ for the purpose of comparing separate plots of cyclic voltammograms measured at different polarization rates. The polarization rate affects the amount of time the electrode spends within a potential regime. For example, a higher value of ϕ might mean that an electrode with an initially reduced metal spends less time at potentials near oxygen evolution in aqueous media. There are instances of materials in this study when redox features will not be visible unless higher polarization rates are applied. Usually this pertains to redox reactions occurring to a small degree, very rapidly, or both. However, slower polarization rates such as $\phi = 1\text{-}50\text{mV/s}$ are typically considered to yield a reliable picture of the most prevalent redox processes occurring on the electrode and are most commonly encountered in literature publications.

Several samples which are especially important in this study underwent continuous cycles in 0.1M HClO_4 at increasing polarization rates from 20mV/s to 200mV/s with $\Delta\phi=20\text{mV/s}$ with each new cycle. The measured current of each cycle was then normalized to its respective polarization rate. Shifts in the most important redox features with increasing ϕ can be clearly observed. The red data set in each plot represents the final cycle at $\phi = 200\text{mV/s}$.

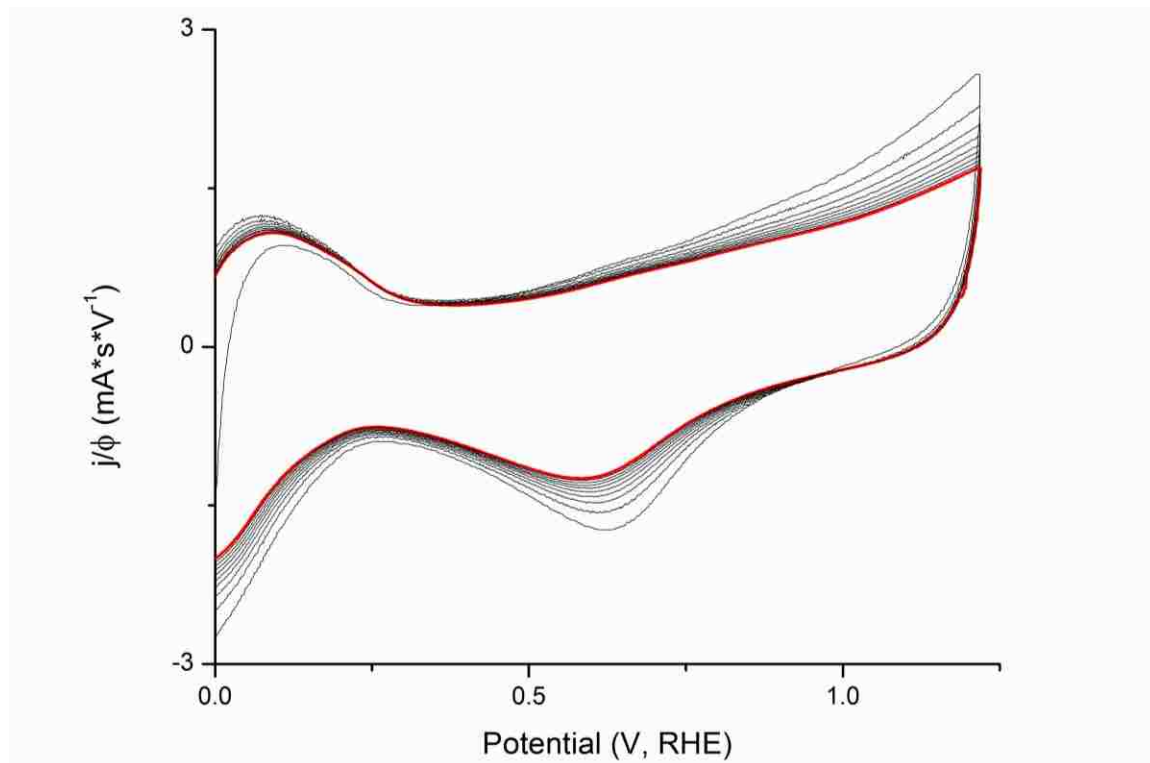
30wt% Platinum Supported on XC-72 (commercial, Etek)



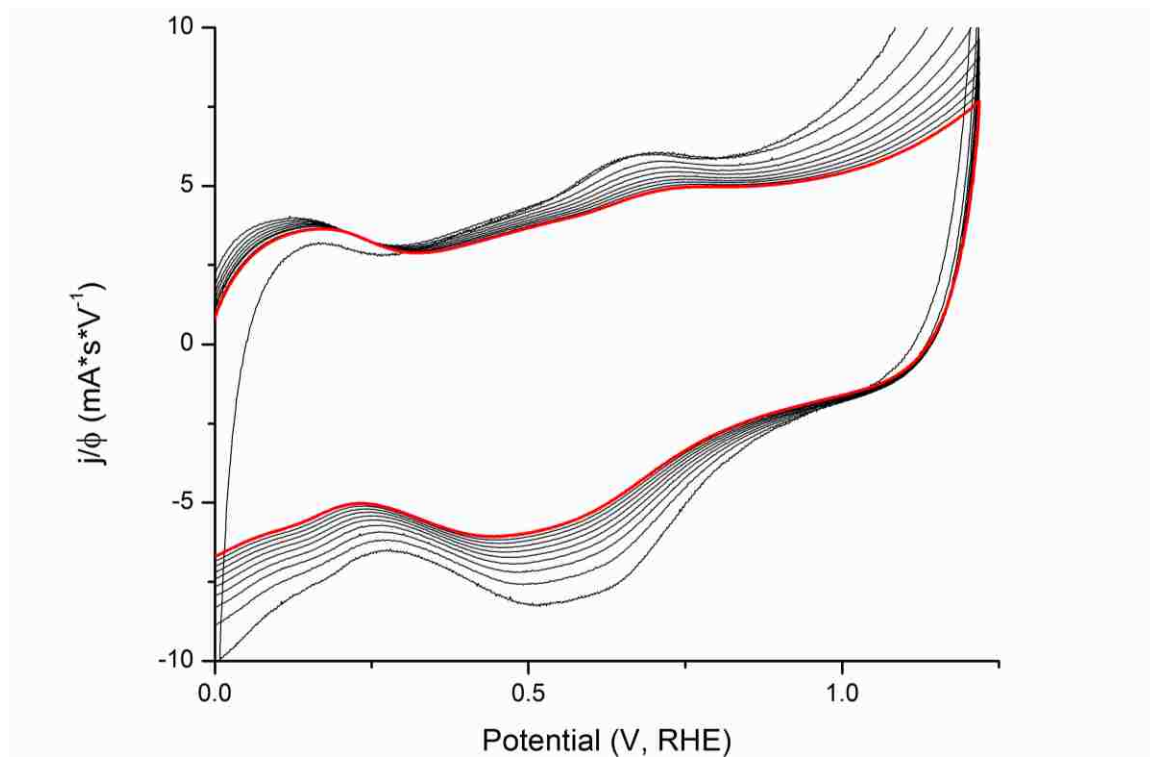
60wt% Pt/NbRu_yO_z Treated to 300°C



60wt% Pt/NbRu_yO_z Treated to 650°C



60wt% Pt/NbRu_yO_z (silica templated) Treated to 900°C



References

1. Thomas, S.; Zalbowitz, M., Fuel Cells - Green Power. Los Alamos National Laboratory: 2006.
2. Fitzgerald, J.; O'Bryan, N., Fuel Cells: A Better Energy Source for Earth and Space. 2005.
3. *Potential Oil Production from the Coastal Plain of ANWR*; 2001.
4. Lamy, C.; Belgsir, E. M.; Leger, J. M., Electrocatalytic oxidation of aliphatic alcohols: Application to the direct alcohol fuel cell (DAFC). *Journal of Applied Electrochemistry* **2001**, 31 (7), 799-809.
5. Bogdanovic, B.; Schwickardi, M., Ti-doped alkali metal aluminium hydrides as potential novel reversible hydrogen storage materials. *Journal of Alloys and Compounds* **1997**, 253, 1-9.
6. Sakintuna, B.; Lamari-Darkrim, F.; Hirscher, M., Metal hydride materials for solid hydrogen storage: A review. *International Journal of Hydrogen Energy* **2007**, 32 (9), 1121-1140.
7. Schlapbach, L.; Züttel, A., Hydrogen-storage materials for mobile applications. *Nature* **2001**, 414 (6861), 353-358.
8. Aricò, A. S.; Srinivasan, S.; Antonucci, V., DMFCs: From Fundamental Aspects to Technology Development. Fuel Cells. *Fuel Cells* **2001**, 1 (2), 133-161.
9. Dillon, R.; Srinivasan, S.; Aricò, A. S.; Antonucci, V., International activities in DMFC R&D: status of technologies and potential applications. *Journal of Power Sources* **2004**, 127 (1-2), 112-126.
10. Lwin, Y.; Daud, W. R. W.; Mohamad, A. B.; Yaakob, Z., Hydrogen production from steam-methanol reforming: thermodynamic analysis. *International Journal of Hydrogen Energy* **2000**, 25 (1), 47-53.
11. Geissler, K.; Newson, E.; Vogel, F.; Truong, T.; Hottinger, P.; Wokaun, A., Autothermal methanol reforming for hydrogen production in fuel cell applications. *Phys.Chem.Chem.Phys.* **2001**, 3, 2001.
12. Ertl, G., *Catalysis, Science and Technology*. Springer-Verlag: 1983; Vol. 4.
13. Christensen, C. H.; Jørgensen, B.; Rass-Hansen, J.; Egeblad, K.; Madsen, R.; Klitgaard, S. K.; Hansen, S. M.; Hansen, M. R.; Andersen, H. C.; Riisager, A., Formation of Acetic Acid by Aqueous-Phase Oxidation of Ethanol with Air in the Presence of a Heterogeneous Gold Catalyst. *Angewandte Chemie International Edition* **2006**, 45 (28), 4648-4651.
14. Rass-Hansen, J.; Falsig, H.; Jørgensen, B.; Christensen, C. H., Bioethanol: fuel or feedstock? *Journal of Chemical Technology and Biotechnology* **2007**, 82 (4), 329-333.

15. Gasteiger, H. A.; Kocha, S. S.; Sompalli, B.; Wagner, F. T., Activity benchmarks and requirements for Pt, Pt-alloy, and non-Pt oxygen reduction catalysts for PEMFCs. *Applied Catalysis B-Environmental* **2005**, *56* (1-2), 9-35.
16. Ando, Y. J.; Sasaki, K.; Adzic, R., Electrocatalysts for methanol oxidation with ultra low content of Pt and Ru. *Electrochemistry Communications* **2009**, *11* (6), 1135-1138.
17. Sasaki, K.; Wang, J. X.; Naohara, H.; Marinkovic, N.; More, K.; Inada, H.; Adzic, R. R., Recent advances in platinum monolayer electrocatalysts for oxygen reduction reaction: Scale-up synthesis, structure and activity of Pt shells on Pd cores. *Electrochimica Acta* **2010**, *55* (8), 2645-2652.
18. Sasaki, K.; Adzic, R. R., Monolayer-level Ru- and NbO₂-Supported platinum electrocatalysts for methanol oxidation. *Journal of the Electrochemical Society* **2008**, *155* (2), B180-B186.
19. Tang, J. M.; Jensen, K.; Li, W.; Waje, M.; Larsen, P.; Ramesh, P.; Itkis, M. E.; Yan, Y.; Haddon, R. C., Carbon nanotube free-standing membrane of Pt/SWNTs as catalyst layer in hydrogen fuel cells. *Australian Journal of Chemistry* **2007**, *60* (7), 528-532.
20. Minteer, S., *Alcoholic Fuels*. CRC Publishing: 2006.
21. Kotrba, R., STATE LEGISLATION Roundup and Review. *Ethanol Producer Magazine* 2005, pp 52-55.
22. Shapouri, H.; Duffield, J. A.; Graboski, M. S. *Estimating the Net Energy Balance of Corn Ethanol*; U.S. Department of Agriculture, Economic Research Service, Office of Energy: 1995.
23. Wang, M.; Saricks, C.; Santini, D. *Effects of Fuel Ethanol Use on Fuel-Cycle Energy and Greenhouse Gas Emissions*; Center for Transportation Research, Energy Systems Division, Argonne National Laboratory: Argonne, Il, 1999.
24. *National Geographic* September, 2008, p 144.
25. Lindsey, R. *Looking for Lawns*; NASA: November 8, 2005.
26. Kodas, T. T.; Hampdensmith, M. J., *Aerosol Processing of Materials*. Wiley-VCH: New York, 1999; p 656.
27. Lu, Y. F.; Fan, H. Y.; Stump, A.; Ward, T. L.; Rieker, T.; Brinker, C. J., Aerosol-assisted self-assembly of mesostructured spherical nanoparticles. *Nature* **1999**, *398* (6724), 223-226.
28. Chandler, C. D.; Roger, C.; Hampden-Smith, M. J., Chemical aspects of solution routes to perovskite-phase mixed-metal oxides from metal-organic precursors. *Chemical Reviews* **1993**, *93* (3), 1205-1241.
29. Cho, S. Y.; Lee, J. H.; Park, S. J., Preparation of Spherical Zr_{0.8}Sn_{0.2}TiO₄ Powder by Ultrasonic Spray-Pyrolysis. *Journal of Materials Science* **1995**, *30* (12), 3274-3278.

30. Moser, W. R.; Lennhoff, J. D., A New High-Temperature Aerosol Decomposition Process for the Synthesis of Mixed Metal-Oxides for Ceramics and Catalysts and Their Characterization. *Chemical Engineering Communications* **1989**, 83, 241-259.
31. Messing, G. L.; Zhang, S. C.; Jayanthi, G. V., Ceramic Powder Synthesis by Spray-Pyrolysis. *Journal of the American Ceramic Society* **1993**, 76 (11), 2707-2726.
32. Hinds, W. C., *Aerosol technology: Properties, behavior, and measurement of airborne particles*. 1 ed.; Wiley-Interscience: New York, 1982; p 442.
33. van der Lijn, J. Simulation of heat and mass transfer in spray drying. Proefschrift Wageningen, Pudoc, Wageningen, 1976.
34. Nesic, S.; Vodnik, J., Kinetics of Droplet Evaporation. *Chemical Engineering Science* **1991**, 46 (2), 527-537.
35. Pourbaix, M., *Atlas d'équilibres électrochimiques*. 2 ed.; National Association of Corrosion Engineers: Houston, TX, 1974; p 644.
36. Helmholtz Double-Layer. New Mexico State University.
37. Vassos, B.; Ewing, G., *Electroanalytical Chemistry*. John Wiley & Sons: 1983; p 255.
38. Rahim, M. A. A.; Hameed, R. M. A.; Khalil, M. W., Nickel as a catalyst for the electro-oxidation of methanol in alkaline medium. *Journal of Power Sources* **2004**, 134 (2), 160-169.
39. Rahim, M. A. A.; Hameed, R. M. A.; Khalil, M. W., The role of a bimetallic catalyst in enhancing the electro-catalytic activity towards methanol oxidation. *Journal of Power Sources* **2004**, 135 (1-2), 42-51.
40. Rao, V.; Hariyanto; Cremers, C.; Stimming, U., Investigation of the ethanol electro-oxidation in alkaline membrane electrode assembly by differential electrochemical mass spectrometry. *Fuel Cells* **2007**, 7 (5), 417-423.
41. Tripkovic, A. V.; Popovic, K. D.; Grgur, B. N.; Blizanac, B.; Ross, P. N.; Markovic, N. M., Methanol electrooxidation on supported Pt and PtRu catalysts in acid and alkaline solutions. *Electrochimica Acta* **2002**, 47 (22-23), 3707-3714.
42. Lopezatalaya, M.; Morallon, E.; Cases, F.; Vazquez, J. L. K.; Perez, J. M., Electrochemical Oxidation of Ethanol on Pt(Hkl) Basal Surfaces in Naoh and Na2co3 Media. *Journal of Power Sources* **1994**, 52 (1), 109-117.
43. Spendelow, J. S.; Wieckowski, A., Electrocatalysis of oxygen reduction and small alcohol oxidation in alkaline media. *Physical Chemistry Chemical Physics* **2007**, 9 (21), 2654-2675.
44. Schulze, A.; Gulzow, E., Degradation of nickel anodes in alkaline fuel cells. *Journal of Power Sources* **2004**, 127 (1-2), 252-263.
45. Verma, L. K., Studies on methanol fuel cell. *Journal of Power Sources* **2000**, 86 (1-2), 464-468.

46. Antolini, E., Catalysts for direct ethanol fuel cells. *Journal of Power Sources* **2007**, *170* (1), 1-12.
47. El-Shafei, A. A.; El-Maksoud, S. A. A.; Moussa, M. N. H., Effect of some ad-atoms on the electrocatalytic oxidation of ethanol on a platinum electrode in alkaline medium. *Journal of Electroanalytical Chemistry* **1992**, *336* (1-2), 73-83.
48. Shen, P. K.; Xu, C., Alcohol oxidation on nanocrystalline oxide Pd/C promoted electrocatalysts. *Electrochemistry Communications* **2006**, *8* (1), 184-188.
49. Hu, F. P.; Chen, C. L.; Wang, Z. Y.; Wei, G. Y.; Shen, P. K., Mechanistic study of ethanol oxidation on Pd-NiO/C electrocatalyst. *Electrochimica Acta* **2006**, *52* (3), 1087-1091.
50. Xu, C.; Shen, P. K.; Ji, X.; Zeng, R.; Liu, Y., Enhanced activity for ethanol electrooxidation on Pt-MgO/C catalysts. *Electrochemistry Communications* **2005**, *7* (12), 1305-1308.
51. Xu, C. W.; Shen, P. K.; Liu, Y. L., Ethanol electrooxidation on Pt/C and Pd/C catalysts promoted with oxide. *Journal of Power Sources* **2007**, *164* (2), 527-531.
52. Pylypenko, S.; Blizanac, B. B.; Olson, T. S.; Konopka, D.; Atanasov, P., Composition- and Morphology-Dependent Corrosion Stability of Ruthenium Oxide Materials. *Acs Applied Materials & Interfaces* **2009**, *1* (3), 604-611.
53. Rolison, D. R.; Hagans, P. L.; Swider, K. E.; Long, J. W., Role of hydrous ruthenium oxide in Pt-Ru direct methanol fuel cell anode electrocatalysts: The importance of mixed electron/proton conductivity. *Langmuir* **1999**, *15* (3), 774-779.
54. Borup, R.; Meyers, J.; Pivovar, B.; Kim, Y. S.; Mukundan, R.; Garland, N.; Myers, D.; Wilson, M.; Garzon, F.; Wood, D.; Zelenay, P.; More, K.; Stroh, K.; Zawodzinski, T.; Boncella, J.; McGrath, J. E.; Inaba, M.; Miyatake, K.; Hori, M.; Ota, K.; Ogumi, Z.; Miyata, S.; Nishikata, A.; Siroma, Z.; Uchimoto, Y.; Yasuda, K.; Kimijima, K. I.; Iwashita, N., Scientific aspects of polymer electrolyte fuel cell durability and degradation. *Chemical Reviews* **2007**, *107* (10), 3904-3951.
55. Kinoshita, K., *Carbon : Electrochemical and Physicochemical Properties*. Wiley: New York, 1988.
56. Mayrhofer, K. J. J.; Ashton, S. J.; Meier, J. C.; Wiberg, G. K. H., Non-destructive transmission electron microscopy study of catalyst degradation under electrochemical treatment. *Journal of Power Sources* **2008**, *185*, 734-739.
57. Bi, W.; Fuller, T. F., Temperature effects on PEM fuel cells Pt/C catalyst degradation. *Journal of the Electrochemical Society* **2008**, *155* (2), B215-B221.
58. Colon-Mercado, H. R.; Popov, B. N., Stability of Platinum Based Alloy Cathode Catalysts in PEM Fuel Cells. *Journal of Power Sources* **2005**, *155*, 253-263.
59. Antolini, E.; Gonzalez, E. R., Ceramic materials as supports for low-temperature fuel cell catalysts. *Solid State Ionics* **2009**, *180* (9-10), 746-763.

60. Vettraiño, M.; Trudeau, M.; Antonelli, D. M., Synthesis and characterization of a new family of electroactive alkali metal doped mesoporous Nb, Ta, and Ti oxides and evidence for an Anderson transition in reduced mesoporous titanium oxide. *Inorganic Chemistry* **2001**, *40* (9), 2088-2095.
61. Garcia, B. L.; Fuentes, R.; Weidner, J. W., Low-temperature synthesis of a PtRu/Nb_{0.1}Ti_{0.9}O₂ electrocatalyst for methanol oxidation. *Electrochemical and Solid State Letters* **2007**, *10* (7), B108-B110.
62. Park, K. W.; Seol, K. S., Nb-TiO₂ supported Pt cathode catalyst for polymer electrolyte membrane fuel cells. *Electrochemistry Communications* **2007**, *9* (9), 2256-2260.
63. Sasaki, K.; Zhang, L.; Adzic, R. R., Niobium oxide-supported platinum ultra-low amount electrocatalysts for oxygen reduction. *Physical Chemistry Chemical Physics* **2008**, *10* (1), 159-167.
64. Bansal, N. P., Synthesis and Thermal Evolution of Structure in Alkoxide-Derived Niobium Pentoxide Gels. *Journal of Materials Science* **1994**, *29* (17), 4481-4486.
65. Guerrero, S.; Miller, J.; Wolf, E. E., Activity and selectivity control by niobium for the preferential oxidation of CO on Pt supported catalysts. *Applied Catalysis A-General* **2007**, *328* (1), 27-34.
66. Santen, R. A.; Neurock, M., *Molecular heterogeneous catalysis: a conceptual and computational approach*. Wiley-VCH: 2006; p 488.
67. Jaksic, J. M.; Krstajic, N. V.; Vracar, L. M.; Neophytides, S. G.; Labou, D.; Falaras, P.; Jaksic, M. M., Spillover of primary oxides as a dynamic catalytic effect of interactive hypo-d-oxide supports. *Electrochimica Acta* **2007**, *53*, 349-361.
68. Shao, M. H.; Huang, T.; Liu, P.; Zhang, J.; Sasaki, K.; Vukmirovic, M. B.; Adzic, R. R., Palladium monolayer and palladium alloy electrocatalysts for oxygen reduction. *Langmuir* **2006**, *22* (25), 10409-10415.
69. Wendt, H., Electrocatalysis and electrocatalysts for low temperature fuel cells: fundamentals, state of the art, research and development. *Quím. Nova* **2005**, *28* (6).
70. Chorkendorff, I.; Niemantsverdriet, J. W., *Concepts of modern catalysis and kinetics*. Wiley-VCH: 2003; p 457.
71. Kandoi, S.; Greeley, J.; Sanchez-Castillo, M. A.; Evans, S. T.; Gokhale, A. A.; Dumesic, J. A.; Mavrikakis, M., Prediction of experimental methanol decomposition rates on platinum from first principles. *Topics in Catalysis* **2006**, *37* (1), 17-28.
72. Greeley, J.; Mavrikakis, M., Competitive paths for methanol decomposition on Pt(111). *Journal of the American Chemical Society* **2004**, *126* (12), 3910-3919.
73. Colmati, F.; Antolini, E.; Gonzalez, E. R., Effect of temperature on the mechanism of ethanol oxidation on carbon supported Pt, PtRu and Pt₃Sn electrocatalysts. *Journal of Power Sources* **2006**, *157* (1), 98-103.

74. Neophytides, S. G.; Murase, K.; Zafeiratos, S.; Papakonstantinou, G.; Paloukis, F. E.; Krstajic, N. V.; Jaksic, M. M., Composite hypo-hyper-d-intermetallic and interionic phases as supported interactive electrocatalysts. *Journal of Physical Chemistry B* **2006**, *110* (7), 3030-3042.
75. Neophytides, S. G.; Zafeiratos, S.; Papakonstantinou, G. D.; Jaksic, J. M.; Paloukis, F. E.; Jaksic, M. M., Extended Brewer hypo-hyper-d-interionic bonding theory - I. Theoretical considerations and examples for its experimental confirmation. *International Journal of Hydrogen Energy* **2005**, *30* (2), 131-147.
76. Neophytides, S. G.; Zafeiratos, S.; Papakonstantinou, G. D.; Jaksic, J. M.; Paloukis, F. E.; Jaksic, M. M., Extended Brewer hypo-hyper-d-interionic bonding theory II. Strong metal-support interaction grafting of composite electrocatalysts. *International Journal of Hydrogen Energy* **2005**, *30* (4), 393-410.
77. Clavilier, J.; Rodes, A.; Elachi, K.; Zamakhchari, M. A., Electrochemistry at Platinum Single-Crystal Surfaces in Acidic Media - Hydrogen and Oxygen-Adsorption. *Journal De Chimie Physique Et De Physico-Chimie Biologique* **1991**, *88* (7-8), 1291-1337.
78. Asselin, E.; Ahmed, T. M.; Alfantazi, A., Corrosion of niobium in sulphuric and hydrochloric acid solutions at 75 and 95 °C. *Corrosion Science* **2007**, *49* (2), 694-710.
79. Yuan, L.; Gulians, V. V., Mesoporous niobium oxides with tailored pore structures. *Journal of Materials Science* **2008**, *43* (18), 6278-6284.
80. Yang, P. D.; Zhao, D. Y.; Margolese, D. I.; Chmelka, B. F.; Stucky, G. D., Block copolymer templating syntheses of mesoporous metal oxides with large ordering lengths and semicrystalline framework. *Chemistry of Materials* **1999**, *11* (10), 2813-2826.
81. Brinker, C. J.; Lu, Y. F.; Sellinger, A.; Fan, H. Y., Evaporation-induced self-assembly: Nanostructures made easy. *Advanced Materials* **1999**, *11* (7), 579-+.
82. Romero, R.; Ramos-Barrado, J. R.; Martin, F.; Leinen, D., Nb₂O₅ thin films obtained by chemical spray pyrolysis. *Surface and Interface Analysis* **2004**, *36* (8), 888-891.
83. Senzaki, Y.; Hampdensmith, M. J.; Kodas, T. T.; Hussler, J. W., Preparation of Metal Ruthenates by Spray-Pyrolysis. *Journal of the American Ceramic Society* **1995**, *78* (11), 2977-2983.
84. Smith, W. H., *Foundations of Materials Science and Engineering*. 3 ed.; McGraw-Hill: 2004; p 908.
85. Bell, W. E.; Tagami, M., HIGH-TEMPERATURE CHEMISTRY OF THE RUTHENIUM-OXYGEN SYSTEM. *The Journal of Physical Chemistry* **1963**, *67* (11), 2432-2436.
86. Rard, J. A., Chemistry and thermodynamics of ruthenium and some of its inorganic compounds and aqueous species. *Chemical Reviews* **1985**, *85* (1), 1-39.

87. Kaga, Y.; Abe, Y.; Yanagisawa, M.; Sasaki, K., Ru and RuO₂ Thin Films by XPS. *Surface Science Spectra* **1999**, 6 (1), 68.
88. Graham, G. W.; Jen, H. W.; Chun, W.; Sun, H. P.; Pan, X. Q.; McCabe, R. W., Coarsening of Pt Particles in a Model NO_x Trap. *Catalysis Letters* **2004**, 93 (3), 129-134.
89. Wynblatt, P.; Gjostein, N. A., Supported metal crystallites. *Prog Solid State Chem* **1975**, 9, 21-58.
90. Fletcher, J. M.; Gardner, W. E.; Hooper, E. W.; Hyde, K. R.; Moore, F. H.; Woodhead, J. L., Anhydrous ruthenium chlorides. *Letter to Nature* **1963**, 199, 1089-1090.
91. Ravel, B. *Hephaestus*, 2008.
92. Brunauer, S.; Deming, L. S.; Deming, W. E.; Teller, E., On a Theory of the van der Waals Adsorption of Gases. *Journal of the American Chemical Society* **1940**, 62 (7), 1723-1732.
93. Hohenberg, P.; Kohn, W., Inhomogeneous Electron Gas. *Physical Review* **1964**, 136 (3B), B864.
94. Perdew, J. P.; Burke, K.; Ernzerhof, M., Generalized Gradient Approximation Made Simple. *Physical Review Letters* **1996**, 77 (18), 3865.
95. Kresse, G.; Furthmüller, J., Efficient iterative schemes for ab initio total-energy calculations using a plane-wave basis set. *Physical Review B* **1996**, 54 (16), 11169.
96. Kresse, G.; Hafner, J., Ab initio molecular dynamics for open-shell transition metals. *Physical Review B* **1993**, 48 (17), 13115.
97. Wang, J., *Analytical Electrochemistry*. 3 ed.; Wiley: 2006; p 272.
98. Switzer, E. E. **NANOSTRUCTURED ELECTROCATALYSTS FOR FUEL CELLS BASED ON AEROSOL TEMPLATING SYNTHESIS TECHNIQUES**. University of New Mexico, Albuquerque, 2008.
99. Goeke, R. **MODEL ELECTRODE STRUCTURES FOR STUDIES OF ELECTROCATALYST DEGRADATION**. University of New Mexico, Albuquerque, 2010.
100. Castillo, I.; Munz, R. J., Transient modeling of heat, mass and momentum transfer of an evaporating cerium nitrate solution droplet with a surrounding shell in a rf thermal argon-oxygen plasma under reduced pressure. *International Journal of Heat and Mass Transfer* **2007**, 50 (21-22), 4468-4487.
101. Weddemann, A.; Auge, A.; Wittbracht, F.; Herth, S.; Hütten, A. In *Interactions of Magnetic Particles in a Rotational Magnetic Field*, Proceedings of the COMSOL Conference, Hannover, Hannover, 2008.
102. Richardson, J. F.; Harker, J. H.; Backhurst, J. R., *Coulson and Richardson's Chemical Engineering - Particle Technology and Separation Processes*. 5 ed.; Elsevier: 2002; Vol. 2.

103. Dros, A. B.; Grosso, D.; Boissière, C.; Soler-Illia, G. J. d. A. A.; Albouy, P.-A.; Amenitsch, H.; Sanchez, C., Niobia-stabilised anatase TiO₂ highly porous mesostructured thin films. *Microporous and Mesoporous Materials* **2006**, *94* (1-3), 208-213.
104. Chen, D.; Hsieh, C., Synthesis of nickel nanoparticles in aqueous cationic surfactant solutions. *Journal of Materials Chemistry* **2002**, *12*, 2412-2415.
105. Gadalla, A. M.; Yu, H. F., Preparation of fine, hollow, spherical NiFe₂O₄ powders. *Journal of the Materials Research Society* **1990**, *5* (12), 2923-2927.
106. Criado, J. M.; Ortega, A.; Real, C., Mechanism of the thermal decomposition of anhydrous nickel nitrate. *Reactivity of Solids* **1987**, *4* (1-2), 93-103.
107. Lewandowska, A.; Monteverdi, S.; Bettahar, M.; Ziolk, M., MCM-41 mesoporous molecular sieves supported nickel--physico-chemical properties and catalytic activity in hydrogenation of benzene. *Journal of Molecular Catalysis A: Chemical* **2002**, *188* (1-2), 85-95.
108. Ko, E. I.; Hupp, J. M.; Rogan, F. H.; Wagner, N. J., Preparation, reduction, and chemisorption behavior of niobia-supported nickel catalysts. *Journal of Catalysis* **1983**, *84* (1), 85-94.
109. Tauster, S. J.; Fung, S. C.; Garten, R. L., Strong metal-support interactions. Group 8 noble metals supported on titanium dioxide. *Journal of the American Chemical Society* **1978**, *100* (1), 170-175.
110. Jasik, A.; Wojcieszak, R.; Monteverdi, S.; Ziolk, M.; Bettahar, M. M., Study of nickel catalysts supported on Al₂O₃, SiO₂ or Nb₂O₅ oxides. *Journal of Molecular Catalysis A: Chemical* **2005**, *242*, 81-90.
111. Chary, K. V. R.; Sri, K.; Venkat, P.; Rao, R.; Seetha, K.; Rao, R.; Papadaki, M., Characterization and catalytic properties of niobia supported nickel catalysts in the hydrodechlorination of 1, 2, 4-trichlorobenzene. *Journal of Molecular Catalysis A: Chemical* **2004**, *223*, 353-361.
112. Liu, B. H.; Li, Z. P.; Suda, S., Electrocatalysts for the anodic oxidation of borohydrides. *Electrochimica Acta* **2004**, *49* (October 2003), 3097-3105.
113. Carbucicchio, M.; Centi, G.; Forzatti, P.; Trifirò, F.; Villa, P. L., Propylene oxidation to acrolein on Fe---Sb---Ti---O catalysts. *Journal of Catalysis* **1987**, *107* (2), 307-316.
114. Bayu, A.; Nandiyanto, D.; Kaihatsu, Y.; Iskandar, F.; Okuyama, K., Rapid synthesis of a BN / CNT composite particle via spray routes using ferrocene / ethanol as a catalyst / carbon source. *Materials Letters* **2009**, *63* (21), 1847-1850.
115. Kamalakaran, R.; Lupo, F.; Grobert, N., In-situ formation of carbon nanotubes in an alumina "nanotube composite by spray pyrolysis. *Carbon* **2003**, *41*, 2737-2741.
116. Kamalakaran, R.; Terrones, M.; Seeger, T.; Ru, M.; Kim, Y. A.; Hayashi, T.; Endo, M., Synthesis of thick and crystalline nanotube arrays by spray pyrolysis. *Applied Physics Letters* **2000**, *77* (21), 3385-3387.

117. Osva, Z.; Kerte, K.; Sa, Z.; Darabont, A.; Biro, L. P., Diameter and morphology dependence on experimental conditions of carbon nanotube arrays grown by spray pyrolysis. *Carbon* **2005**, *43*, 970-977.
118. Trong On, D.; Nguyen, S. V.; Hulea, V.; Dumitriu, E.; Kaliaguine, S., Mono- and bifunctional MFI, BEA and MCM-41 titanium-molecular sieves. Part 1. Synthesis and characterization. *Microporous and Mesoporous Materials* **2003**, *57* (2), 169-180.
119. van der Waal, J. C.; van Bekkum, H., Zeolite titanium beta: A versatile epoxidation catalyst. Solvent effects. *Journal of Molecular Catalysis A: Chemical* **1997**, *124* (2-3), 137-146.
120. Nowak, I.; Ziolk, M., Niobium Compounds: Preparation, Characterization, and Application in Heterogeneous Catalysis. *Chemical Reviews* **1999**, *99* (12), 3603-3624.
121. Papageorgopoulos, D. C.; Keijzer, M.; Bruijn, F. A. D., The inclusion of Mo, Nb and Ta in Pt and PtRu carbon supported electrocatalysts in the quest for improved CO tolerant PEMFC anodes. *Electrochimica Acta* **2002**, *48*, 197-204.
122. Jiang, L.; Zhou, Z.; Li, W.; Zhou, W.; Song, S.; Li, H.; Sun, G.; Xin, Q., Effects of Treatment in Different Atmosphere on Pt₃Sn/C Electrocatalysts for Ethanol Electro-oxidation. *Energy & Fuels* **2004**, *18* (3), 866-871.
123. Li, G.; Pickup, P. G., Decoration of carbon-supported Pt catalysts with Sn to promote electro-oxidation of ethanol. *Journal of Power Sources* **2007**, *173* (1), 121-129.
124. Lee, E.; Park, I.-s.; Manthiram, A., Synthesis and Characterization of Pt-Sn-Pd / C Catalysts for Ethanol Electro-Oxidation Reaction. *Journal of Physical Chemistry C* **2010**, *114*, 10634-10640.
125. Marques, P.; Ribeiro, N. F. P.; Schmal, M.; Aranda, D. A. G.; Souza, M. M. V. M., Selective CO oxidation in the presence of H₂ over Pt and Pt-Sn catalysts supported on niobia. *Journal of Power Sources* **2006**, *158* (1), 504-508.
126. Lee, B.; Yamashita, T.; Lu, D. L.; Kondo, J. N.; Domen, K., Single-crystal particles of mesoporous niobium-tantalum mixed oxide. *Chemistry of Materials* **2002**, *14* (2), 867-875.
127. Lee, B.; Lu, D. L.; Kondo, J. N.; Domen, K., Three-dimensionally ordered mesoporous niobium oxide. *Journal of the American Chemical Society* **2002**, *124* (38), 11256-11257.
128. Kondo, J. N.; Takahara, Y.; Lee, B.; Lu, D. L.; Domen, K., Synthesis and property of mesoporous tantalum oxides. *Topics in Catalysis* **2002**, *19* (2), 171-177.
129. Antonelli, D. M.; Nakahira, A.; Ying, J. Y., Ligand-assisted liquid crystal templating in mesoporous niobium oxide molecular sieves. *Inorganic Chemistry* **1996**, *35* (11), 3126-3136.

130. Skadtchenko, B. O.; Antonelli, D. M., 2005 Pure or Applied Inorganic Chemistry Award Lecture - Host-guest inclusion chemistry of electroactive, mesoporous transition metal oxides oxidation and 1-D confinement in one step and why amorphous is better. *Canadian Journal of Chemistry-Revue Canadienne De Chimie* **2006**, 84 (3), 371-383.
131. Brayner, R.; Bozon-Verduraz, F., Niobium pentoxide prepared by soft chemical routes: morphology, structure, defects and quantum size effect. *Physical Chemistry Chemical Physics* **2003**, 5 (7), 1457-1466.
132. Lenzmann, F.; Shklover, V.; Brooks, K.; Gratzel, M., Mesoporous Nb₂O₅ Films: Influence of Degree of Crystallinity on Properties. *Journal of Sol-Gel Science and Technology* **2000**, 19 (1-3), 175-180.
133. Jehng, J. M.; Wachs, I. E., Structural Chemistry and Raman-Spectra of Niobium Oxides. *Chemistry of Materials* **1991**, 3 (1), 100-107.
134. McQueen, T.; Xu, Q.; Andersen, E. N.; Zandbergen, H. W.; Cava, R. J., Structures of the reduced niobium oxides Nb₁₂O₂₉ and Nb₂₂O₅₄. *Journal of Solid State Chemistry* **2007**, 180 (10), 2864-2870.
135. Waldron, J. E. L.; Green, M. A.; Neumann, D. A., Structure and electronic properties of monoclinic Nb₁₂O₂₉. *Journal of Physics and Chemistry of Solids* **2004**, 65 (1), 79-86.
136. Jaksic, J. M.; Lacnjevac, C. M.; Krstajic, N. V.; Jaksic, M. M., INTERACTIVE SUPPORTED ELECTROCATALYSTS AND SPILLOVER EFFECT IN ELECTROCATALYSIS FOR HYDROGEN AND OXYGEN ELECTRODE REACTIONS. *Chemical Industry & Chemical Engineering Quarterly* **2008**, 14 (2), 119-136.
137. Massalski, T. B.; Okamoto, H., *Binary Alloy Phase Diagrams*. ASM International: Materials Park, 1990.
138. Konopka, D. A.; Pylypenko, S.; Atanassov, P.; Ward, T. L., Synthesis by Spray Pyrolysis of Mesoporous NbRuyOz as Electrocatalyst Supports in Fuel Cells. *Acs Applied Materials & Interfaces* **2009**, 2 (1), 86-95.
139. Kowal, A.; Li, M.; Shao, M.; Sasaki, K.; Vukmirovic, M. B.; Zhang, J.; Marinkovic, N. S.; Liu, P.; Frenkel, A. I.; Adzic, R. R., Ternary Pt/Rh/SnO₂ electrocatalysts for oxidizing ethanol to CO₂. *Nat Mater* **2009**, 8 (4), 325-330.
140. Liang, Y.; Li, J.; Xu, Q.-c.; Hu, R.-z.; Lin, J.-d.; Liao, D.-w., Characterization of composite carbon supported PtRu catalyst and its catalytic performance for methanol oxidation. *Journal of Alloys and Compounds* **2008**, 465, 296-304.
141. Hammer, B.; Nørskov, J. K.; Bruce C. Gates, H. K., Theoretical surface science and catalysis--calculations and concepts. In *Advances in Catalysis*, Academic Press: 2000; Vol. Volume 45, pp 71-129.
142. Socrates, G., *Infrared Characteristic Group Frequencies*. Wiley: New York, 1966.

143. Xia, X. H.; Liess, H. D.; Iwasita, T., Early stages in the oxidation of ethanol at low index single crystal platinum electrodes. *Journal of Electroanalytical Chemistry* **1997**, *437* (1-2), 233-240.
144. Shao, M. H.; Adzic, R. R., Spectroscopic Identification of the Reaction Intermediates in Oxygen Reduction on Gold in Alkaline Solutions. *The Journal of Physical Chemistry B* **2005**, *109* (35), 16563-16566.
145. Ataka, K.-i.; Yotsuyanagi, T.; Osawa, M., Potential-Dependent Reorientation of Water Molecules at an Electrode/Electrolyte Interface Studied by Surface-Enhanced Infrared Absorption Spectroscopy. *The Journal of Physical Chemistry* **1996**, *100* (25), 10664-10672.
146. Shin, J.; Tornquist, W. J.; Korzeniewski, C.; Hoaglund, C. S., *Surface Science* **1996**, *364*, 122.
147. Rodes, A.; Pastor, E.; Iwasita, T., Structural effects on CO₂ reduction at Pt single-crystal electrodes. Part 1. The Pt(110) surface. *Journal of Electroanalytical Chemistry* **1994**, *376*, 109.
148. Gao, Q.; Hemminger, J. C., A vibrational spectroscopy study of CH₃COOH, CH₃COOD and ¹³CD₃COOH(D) adsorption on Pt(111): I. Surface dimer formation and hydrogen bonding. *Surface Science* **1991**, *248* (1-2), 45-56.
149. Leung, L. W. H.; Weaver, M., Real-time FTIR spectroscopy as a quantitative kinetic probe of competing electrooxidation pathways for small organic molecules. *Journal of Physical Chemistry* **1988**, *92* (14), 4019-4022.
150. Corrigan, D. S.; Krauskopf, E. K.; Rice, L. M.; Wieckowski, A.; Weaver, M. J., Adsorption of acetic acid at platinum and gold electrodes: a combined infrared spectroscopic and radiotracer study. *The Journal of Physical Chemistry* **1988**, *92* (6), 1596-1601.
151. Lamy, C.; Rousseau, S.; Belgsir, E. M.; Coutanceau, C.; Léger, J. M., Recent progress in the direct ethanol fuel cell: development of new platinum-tin electrocatalysts. *Electrochimica Acta* **2004**, *49* (22-23), 3901-3908.
152. Iwasita, T.; Rasch, B.; Cattaneo, E.; Vielstich, W., A sniftirs study of ethanol oxidation on platinum. *Electrochimica Acta* **1989**, *34* (8), 1073-1079.
153. Wu, J., *Modern Fourier Transform Infrared Spectroscopy Techniques and their Applications*. Scientific and Technical Document Publishing House: Beijing, 1994.
154. Gao, P.; Chang, S.-C.; Zhou, Z.; J. Weaver, M., Electrooxidation pathways of simple alcohols at platinum in pure nonaqueous and concentrated aqueous environments as studied by real-time ftir spectroscopy. *Journal of Electroanalytical Chemistry* **1989**, *272* (1-2), 161-178.
155. Serrano-ruiz, J. C.; Dumesic, J. A., Catalytic Processing of Lactic Acid over Pt / Nb 2 O 5. *Chemsuschem* **2009**, *2*, 581-586.
156. Guerrero, S.; Miller, J. T.; Kropf, A. J.; Wolf, E. E., In situ EXAFS and FTIR studies of the promotion behavior of Pt-Nb₂O₅/Al₂O₃ catalysts during the preferential oxidation of CO. *Journal of Catalysis* **2009**, *262* (1), 102-110.

157. Höbel, F.; Bandara, A.; Freund, H.-j., Deactivation of Pd particles supported on Nb₂O₅ / Cu₃Au (1 0 0): SFG and TPD studies from UHV to 100 mbar Frank Ho. *Surface Science* **2006**, 600, 963-970.
158. Mickova, I.; Prusi, A.; Grcev, T.; Arsov, L., Electrochemical Passivation of Niobium in KOH Solutions. *Croatica Chemica Acta* **2006**, 79 (4), 527-532.
159. Passos, F. B.; Aranda, D. A. G.; Schmal, M., The state of Tin on Pt-Sn / Nb₂O₅ catalysts. *Catalysis Today* **2000**, 57, 283-289.
160. Passos, F. B.; Aranda, D. A. G.; Soares, R. R.; Schmal, M., Effect of preparation method on the properties of Nb₂O₅ promoted platinum catalysts. *Catalysis Today* **1998**, 43, 3-9.
161. Aranda, D. A. G.; Ramos, L. D.; Passos, F. B.; Schmal, M., Characterization and dehydrogenation activity of Pt / Nb₂O₅ catalysts. *Catalysis Today* **1996**, 28, 119-125.
162. Bach, D.; Schneider, R.; Gerthsen, D.; Verbeeck, J.; Sigle, W., EELS of Niobium and Stoichiometric Niobium-Oxide Phases—Part I: Plasmon and Near-Edges Fine Structure. *Microscopy and Microanalysis* **2009**, 15 (6), 505-523.
163. Bach, D.; Schneider, R.; Gerthsen, D., EELS of Niobium and Stoichiometric Niobium-Oxide Phases?Part II: Quantification. *Microscopy and Microanalysis* **2009**, 15 (06), 524-538.
164. Arsova, I.; Prusi, A., Ellipsometric study of anodic oxide films formed on niobium surfaces. *Journal of Solid State Chemistry* **2003**, 7, 217-222.
165. Chhina, H.; Campbell, S.; Kesler, O., Ex Situ and In Situ Stability of Platinum Supported on Niobium-Doped Titania for PEMFCs. *Journal of the Electrochemical Society* **2009**, 156 (10), 1232-1237.
166. Wikander, K.; Ekstrom, H.; Palmqvist, A.; Lindberg, G., On the influence of Pt particle size on the PEMFC cathode performance. *Electrochimica Acta* **2007**, 52, 6848-6855.
167. Adams, K. M.; Graham, G. W., Impact of redox conditions on thermal deactivation of NO_x traps for diesel. *Applied Catalysis B-Environmental* **2008**, 80, 343-352.
168. Croy, J. R.; Mostafa, S.; Hickman, L.; Heinrich, H.; Cuenya, B. R., Bimetallic Pt-Metal catalysts for the decomposition of methanol : Effect of secondary metal on the oxidation state , activity , and selectivity of Pt. *Applied Catalysis a-General* **2008**, 350, 207-216.
169. Wanke, S. E.; Flynn, P. C., The Sintering of Supported Metal Catalysts. *Catalysis Reviews: Science and Engineering* **1975**, 12 (1), 93 - 135.
170. Orilall, M. C.; Matsumoto, F.; Zhou, Q.; Sai, H.; Abrunlfa, H. c. D.; DiSalvo, F. J.; Wiesner, U., One-Pot Synthesis of Platinum-Based Nanoparticles Incorporated into Mesoporous Niobium OxideâCarbon Composites for Fuel Cell Electrodes. *Journal of the American Chemical Society* **2009**, 131 (26), 9389-9395.

171. Angerstein-Kozłowska, H.; Conway, B. E.; Sharp, W. B. A., The real condition of electrochemically oxidized platinum surfaces: Part I. Resolution of component processes. *Journal of Electroanalytical Chemistry* **1973**, *43* (1), 9-36.
172. Zolfaghari, A.; Conway, B. E.; Jerkiewicz, G., Elucidation of the effects of competitive adsorption of Cl- and Br- ions on the initial stages of Pt surface oxidation by means of electrochemical nanogravimetry. *Electrochimica Acta* **2002**, *47* (8), 1173-1187.
173. Jerkiewicz, G.; Vatankhah, G.; Lessard, J.; Soriaga, M. P.; Park, Y.-S., Surface-oxide growth at platinum electrodes in aqueous H₂SO₄: Reexamination of its mechanism through combined cyclic-voltammetry, electrochemical quartz-crystal nanobalance, and Auger electron spectroscopy measurements. *Electrochimica Acta* **2004**, *49* (9-10), 1451-1459.
174. Bojinov, M.; Cattarin, S.; Musiani, M.; Tribollet, B., Evidence of coupling between film growth and metal dissolution in passivation processes. *Electrochimica Acta* **2003**, *48*, 4107-4117.
175. Mujawar, S. H.; Inamdar, A. I.; Betty, C. A.; Ganesan, V.; Patil, P. S., Effect of post annealing treatment on electrochromic properties of spray deposited niobium oxide thin films. *Electrochimica Acta* **2007**, *52*, 4899-4906.
176. Jouve, G., Electrochemical breakdown in thin Nb₂O₅ films. *Philosophical Magazine B-Physics of Condensed Matter Statistical Mechanics Electronic Optical and Magnetic Properties* **2000**, *80* (8), 1507-1515.
177. Teng, Z.-H.; Wang, G.; Wu, B.; Gao, Y., High activity Pt/C catalyst for methanol and adsorbed CO electro-oxidation. *Journal of Power Sources* **2007**, *164* (1), 105-110.
178. Zhai, Y.; Zhang, H.; Xing, D.; Shao, Z.-G., The stability of Pt/C catalyst in H₃PO₄/PBI PEMFC during high temperature life test. *Journal of Power Sources* **2007**, *164* (1), 126-133.
179. **Krishnamurthy, B.; Deepalochani, S., Performance of Platinum Black and Supported Platinum Catalysts in a Direct Methanol Fuel Cell. *Int. J. Electrochem. Sci.* **2009**, *4*, 386-395.**
180. Giorgi, L.; Pozio, A.; Bracchini, C.; Giorgi, R.; Turtù, S., H₂ and H₂/CO oxidation mechanism on Pt/C, Ru/C and Pt–Ru/C electrocatalysts. *Journal of Applied Electrochemistry* **2001**, *31* (3), 325-334.
181. Hamann, C. H.; Hamnett, A.; Vielstich, W., *Electrochemistry*. Wiley-VCH: 2007.
182. Carroll, N. J.; Pylypenko, S.; Atanassov, P. B.; Petsev, D. N., Microparticles with Bimodal Nanoporosity Derived by Microemulsion Templating. *Langmuir* **2009**, *25* (23), 13540-13544.
183. Holleck, H., Die Konstitution ternärer Systeme der Ubergangsmetalle der 4., 5, und 6. Gruppe mit Rhenium oder Platinmetallen und Kohlenstoff - I. *Metallwissenschaft und Technik* **1983**.

184. Yu, X.; Ye, S., Recent advances in activity and durability enhancement of Pt/C catalytic cathode in PEMFC: Part II: Degradation mechanism and durability enhancement of carbon supported platinum catalyst. *Journal of Power Sources* **2007**, *172* (1), 145-154.
185. Giordano, N.; Antonucci, P. L.; Passalacqua, E.; Pino, L.; Aricò, A. S.; Kinoshita, K., Relationship between physicochemical properties and electrooxidation behaviour of carbon materials. *Electrochimica Acta* **1991**, *36* (13), 1931-1935.
186. Gruver, G. A., The Corrosion of Carbon Black in Phosphoric Acid. *Journal of the Electrochemical Society* **1978**, *125* (10), 1719-1720.
187. Kinoshita, K.; Bett, J., Electrochemical oxidation of carbon black in concentrated phosphoric acid at 135°C. *Carbon* **1973**, *11* (3), 237-247.
188. Antonucci, P. L.; Romeo, F.; Minutoli, M.; Alderucci, E.; Giordano, N., Electrochemical corrosion behavior of carbon black in phosphoric acid. *Carbon* **1988**, *26* (2), 197-203.
189. Aricò, A. S.; Stassi, A.; Modica, E.; Ornelas, R.; Gatto, I.; Passalacqua, E.; Antonucci, V., Performance and degradation of high temperature polymer electrolyte fuel cell catalysts. *Journal of Power Sources* **2008**, *178* (2), 525-536.
190. Dowlapalli, M. R.; Atanassov, P.; Xie, J.; Rice, G., Electrochemical Oxidation Resistance of Carbonaceous Materials. *ECS Transactions* **2006**, *1* (8), 41-50.
191. Maass, S.; Finsterwalder, F.; Frank, G.; Hartmann, R.; Merten, C., Carbon support oxidation in PEM fuel cell cathodes. *Journal of Power Sources* **2008**, *176* (2), 444-451.
192. Chen, G.; Bare, S. R.; Mallouk, T. E., Development of Supported Bifunctional Electrocatalysts for Unitized Regenerative Fuel Cells. *Journal of the Electrochemical Society* **2002**, *149* (8), A1092-A1099.
193. Scheiba, F.; Scholz, M.; Cao, L.; Schafrank, R.; Roth, C.; Cremers, C.; Qiu, X.; Stimming, U.; Fuess, H., On the Suitability of Hydrous Ruthenium Oxide Supports to Enhance Intrinsic Proton Conductivity in DMFC Anodes. *Fuel Cells* **2006**, *6* (6), 439-446.
194. Ioroi, T.; Senoh, H.; Yamazaki, S.; Siroma, Z.; Fujiwara, N.; Yasuda, K., *Journal of the Electrochemical Society* **2008**, *155*, 321-326.
195. McMurray, H. N., Hydrothermal modification of electrocatalytic and corrosion properties in nanosize particles of ruthenium dioxide hydrate. *Journal of Materials Chemistry* **1994**, *4* (8), 1283-1287.
196. Mill, A.; Gidding, S.; Pate, I., *J.Chem.Soc. Faraday Trans.* **1987**, *83*, 2317-2329.
197. Mill, A.; Lawrenc, C.; Eno, R., *J.Chem.Soc.Chem., Chem.Communic.* **1984**, *1984*, 1436-1438.
198. Fang, W.-C.; Huang, J.-H.; Chen, L.-C.; Su, Y.-L. O.; Chen, K.-H., Effect of temperature annealing on capacitive and structural properties of hydrous ruthenium oxides. *Journal of Power Sources* **2006**, *160* (2), 1506-1510.

199. Sugimoto, W.; Yokoshima, K.; Murakami, Y.; Takasu, Y., Charge storage mechanism of nanostructured anhydrous and hydrous ruthenium-based oxides. *Electrochimica Acta* **2006**, 52 (4), 1742-1748.
200. Rochefort, D.; Dabo, P.; Guay, D.; Sherwood, P. M. A., XPS investigations of thermally prepared RuO₂ electrodes in reductive conditions. *Electrochimica Acta* **2003**, 48 (28), 4245-4252.
201. Foelske, A.; Barbieri, O.; Hahn, M.; Kotz, R., An X-Ray Photoelectron Spectroscopy Study of Hydrous Ruthenium Oxide Powders with Various Water Contents for Supercapacitors. *Electrochemical and Solid-State Letters* **2006**, 9 (6), A268-A272.
202. Mukerjee, S.; Srinivasan, S., Enhanced electrocatalysis of oxygen reduction on platinum alloys in proton exchange membrane fuel cells. *Journal of Electroanalytical Chemistry* **1993**, 357 (1-2), 201-224.
203. Mukerjee, S.; Srinivasan, S.; Soriaga, M. P.; McBreen, J., Effect of Preparation Conditions of Pt Alloys on Their Electronic, Structural, and Electrocatalytic Activities for Oxygen Reduction - XRD, XAS, and Electrochemical Studies. *The Journal of Physical Chemistry* **1995**, 99 (13), 4577-4589.
204. Paffett, M. T.; Beery, J. G.; Gottesfeld, S., Oxygen Reduction of Pt sub 0.65 Cr sub 0.35 , Pt sub 0.2 Cr sub 0.8 and Roughened Platinum. *Journal of the Electrochemical Society* **1988**, 135 (6), 1431-1436.
205. Reeve, R. W.; Christensen, P. A.; Hamnett, A.; Haydock, S. A.; Roy, S. C., Methanol Tolerant Oxygen Reduction Catalysts Based on Transition Metal Sulfides. *Journal of the Electrochemical Society* **1998**, 145 (10), 3463-3471.
206. Vante, N. A.; Tributsch, H., Energy conversion catalysis using semiconducting transition metal cluster compounds. *Nature* **1986**, 323 (6087), 431-432.
207. Sun, G. Q.; Wang, J. T.; Savinell, R. F., Iron(III) tetramethoxyphenylporphyrin(FeTMPP) as methanol tolerant electrocatalyst for oxygen reduction in direct methanol fuel cells. *Journal of Applied Electrochemistry* **1998**, 28 (10), 1087-1093.
208. Jiang, R.; Chu, D., Remarkably Active Catalysts for the Electroreduction of O₂ to H₂O for Use in an Acidic Electrolyte Containing Concentrated Methanol. *Journal of the Electrochemical Society* **2000**, 147 (12), 4605-4609.
209. Olson, T. S.; Blizanac, B.; Piela, B.; Davey, J. R.; Zelenay, P.; Atanassov, P., Electrochemical Evaluation of Porous Non-Platinum Oxygen Reduction Catalysts for Polymer Electrolyte Fuel Cells. *Fuel Cells* **2009**, 9 (5), 547-553.
210. Schmidt, T.; Paulis, U.; Gasteiger, H. A.; Alonso-Vante, N.; Behm, R. J., *Journal of the Electrochemical Society* **2000**, 147, 2620.
211. Shao, M.; Liu, P.; Zhang, J.; Adzic, R., Origin of Enhanced Activity in Palladium Alloy Electrocatalysts for Oxygen Reduction Reaction. *The Journal of Physical Chemistry B* **2007**, 111 (24), 6772-6775.

212. Stolbov, S.; Ortigoza, M. A.; Adzic, R.; Rahman, T. S., High CO tolerance of Pt/Ru nanocatalyst: Insight from first principles calculations. *Journal of Chemical Physics* **2009**, *130*.